Titre: Title:	Simulating Shot Peen Forming with Eigenstrains
Auteur: Author:	Pierre Faucheux
Date:	2019
Type:	Mémoire ou thèse / Dissertation or Thesis
Référence: Citation:	Faucheux, P. (2019). Simulating Shot Peen Forming with Eigenstrains [Ph.D. thesis, Polytechnique Montréal]. PolyPublie. https://publications.polymtl.ca/4189/

URL de PolyPublie: PolyPublie URL:	https://publications.polymtl.ca/4189/
Directeurs de recherche: Advisors:	Frederick Gosselin, & Martin Lévesque
Programme: Program:	Génie mécanique

POLYTECHNIQUE MONTRÉAL
affiliée à l'Université de Montréal

Simulating shot peen forming with eigenstrains

PIERRE FAUCHEUX
Département de génie mécanique

Thèse présentée en vue de l'obtention du diplôme de *Philosophiæ Doctor*
Génie mécanique

Décembre 2019

POLYTECHNIQUE MONTRÉAL
affiliée à l'Université de Montréal

Cette thèse intitulée :

Simulating shot peen forming with eigenstrains

présentée par **Pierre FAUCHEUX**
en vue de l'obtention du diplôme de *Philosophiæ Doctor*
a été dûment acceptée par le jury d'examen constitué de :

René MAYER, président
Frédérick P. GOSSELIN, membre et directeur de recherche
Martin LÉVESQUE, membre et codirecteur de recherche
Alexander KORSUNSKY, membre
Emmanuelle ROUHAUD, membre externe

ACKNOWLEDGEMENTS

First and foremost, I would like to thank my co-advisors, Pr. Frédérick Gosselin and Martin Lévesque. Frédérick propelled me into research seven years ago when he offered me, as a summer project, to model a micro-extrusion process that he was working on at the time. While I had initially approached him for advice on industrial internships, a most convincing presentation of his work and his enthusiasm made me reconsider my plans. The understanding we now have of peen forming owes a lot to the way he approaches research, drawing parallel with seemingly unrelated problems and pushing for simple physics where brute force computations could have sufficed. Equally important to the success of this project was Martin's long-lasting effort to build one of the most dynamic research team on campus. The many students he trains at LM2—effectively in-house experts on subjects ranging from residual stress characterization to advanced composite modeling—the state-of-the-art facilities he manages, and his tireless administering are the foundations on which research is getting done.

I am indebted to Pr. A. Korsunsky, E. Rouhaud, and R. Mayer, for having accepted to be the members of my thesis committee on such a short notice.

This work was funded by Airbus and received additional support from the Rio Tinto group through a graduate scholarship. At Airbus, I am especially grateful to M. van der Veen for overseeing this work, providing technical guidance, and ensuring that we got a glimpse of how our work found applications in production.

Dr. Hongyan Miao supported this project from the very start. Having drafted the research contract well before I joined the lab, she ensured that its practical aspects went smoothly. Her many contacts in the peening industry saved us precious time.

Among my colleagues at LM2, I would especially like to thank Thierry, Wassime, and Shibo for insightful discussions and helping me on several occasions with tricky experiments. I also had the chance to supervise four interns: Elie, Michael, Erik and Olivier—two of which are now pursuing a PhD. All generated ideas that have been actively shaping our research since.

While not directly involved in the project, the team of the Centre Technologique en Aérospatiale provided us with much needed help on experimental setup design, metrology, and robotics. I am especially grateful to M. Aubé, J. F. d'Aigle, M. Barrette, and M. C. Caya.

Finally, I must thank misters C. Cuy y Mola and J. Cathala for having, many years ago, provided me with opportunities that opened the path I am currently following.

And my family for everything else.

RÉSUMÉ

Les tôles d'aluminium qui couvrent les ailes de la plupart des avions sont mises en forme par grenaillage. Ce procédé consiste à bombarder une tôle avec un jet de billes d'acier, de verre, ou de céramique dont le diamètre excède rarement un millimètre. Lorsqu'une bille frappe la tôle, elle comprime le matériau dans la direction normale à la surface et l'étire dans la direction parallèle à la surface. Pour accommoder ces déformations, la tôle s'alonge et plie. Lorsque combiné à un choix judicieux des conditions de grenaillage, cet effet permet de donner à une tôle initialement plane une forme complexe. Bien que plusieurs modèles du procédé aient été proposés dans la littérature, tous doivent être calibrés dans des conditions proches de celles utilisées en production, ce qui limite leurs capacités prédictives. Par conséquent, la plupart des séquences de grenaillages sont, encore aujourd'hui, développées par essai-erreur.

Cette thèse vise à développer de nouveaux outils pour simuler et optimiser la mise en forme par grenaillage. Tous les développements présentés reposent sur le concept d'eigenstrains (déformations libres) où l'effet du grenaillage est modélisé par une expansion permanente des couches superficielles de matière. Dans un premier temps, on rappelle comment identifier ces eigenstrains à partir de mesures réalisées sur de petits coupons représentatifs, puis, comment les transférer vers des modèles éléments finis de grandes structures pour estimer contraintes résiduelles et déformations induites par grenaillage. On présente ensuite les résultats d'une campagne expérimentale lors de laquelle trente-six tôles d'aluminium 2024–T3 de 4.9 mm d'épaisseur et de longueur comprise entre 1 et 0.5 m ont été mises en forme. Toutes les tôles ont été grenaillées uniformément sur une face avec le même traitement. Certaines étaient libres de se déformer tandis que d'autres étaient précontraintes dans un montage de flexion 4-points. L'une des principales conclusions est que, pour les géométries considérées, les contraintes résiduelles de présentes avant grenaillage comme celles induites par le traitement thermique T3 peuvent, même si elles sont de faible amplitude, affecter significativement la forme finale des tôles. On montre également comment une instabilité élastique explique que certaines tôles adoptent une déformée 'sphérique', avec la même courbure dans toutes les directions, alors que d'autres adoptent une déformée 'cylindrique', avec une courbure dans une seule direction. Enfin, on montre comment la procédure de simulation proposée peut être couplée à des algorithmes d'optimisation usuels pour déterminer automatiquement des séquences de grenaillages permettant de fabriquer une géométrie imposée. Bien qu'elles ne soient validées que sur des plaques rectangulaires d'épaisseur uniforme, les procédures proposées peuvent être adaptées à d'autres géométries et traitements de surface, par exemple le grenaillage laser.

ABSTRACT

Aluminum skins that cover the wings of most aircraft are usually shaped using shot peen forming. The process consists in bombarding the initially flat skins with a stream of hard shot—usually steel sphere about one millimeter in diameter—in order to plastically deform a thin layer of material. In this layer, repeated impacts compress the material in the direction normal to the surface and stretch it in the direction tangent to the surface, and the strain incompatibility with the underlying material that results causes the whole skin to deform. When faced with a new design, process engineers can control the type of shot, the intensity of the treatment, and which areas to peen to achieve the desired shape. However, because of a lack of robust models of the process, peening sequences are still being developed by trial and error, which often requires scrapping several parts before finding an appropriate sequence.

This thesis aims at developing simulation procedures to predict the final shape of metal sheets subjected to known peening treatment. The proposed strategy relies on the concept of eigenstrains (stress-free strains) to model peening induced loads as permanent growth in the peening affected layer. First, we show how to identify these loads experimentally from limited strain and residual stress measurements performed on small representative coupons. Once identified, the loads are mapped onto finite element models of larger parts to compute distortions. This approach is then used to analyze the results of peen forming experiments conducted on 4.9 mm thick and about 1 m long rectangular 2024–T3 aluminum sheets of various aspect ratios uniformly shot peened on one face with the same low intensity treatment. Some specimens were free to deform during peening while others were elastically prestressed in a four-point bending jig. Our results show that the progressive deformation of unconstrained specimens amounts to an externally applied prestress and that constraining conditions significantly affect the shape of peen formed parts. We also found that, for the geometries and peening treatment investigated, low intensity initial stresses present in the specimen did control the direction along which the specimens preferentially bent. Furthermore, we clarify how an elastic instability causes uniformly shot peened plates to transition from spherical to cylindrical deformed shape as the intensity of the treatment is increased. Finally, we demonstrate how the proposed simulation procedure can be interfaced with off-the-shelf optimization algorithms to automatically identify peening patterns and process parameters required to form metal sheets into desired target shapes. Although validation is limited to rectangular aluminum sheets of uniform thickness, the proposed approach is generic and can be adapted to other geometries and surface treatments, such as laser peening.

TABLE OF CONTENTS

LIST OF TABLES

LIST OF FIGURES

LIST OF APPENDICES

CHAPTER 1 INTRODUCTION

Imagine bombarding a metal plate with a stream of hard steel shot about one millimeter in diameter. As each shot hits the surface, it plastically deforms a small volume of material which, if the treatment continues for a sufficiently long time, results in a plastically deformed layer. In this layer, the material is compressed in the direction perpendicular to the surface and stretched in the directions parallel to the surface. The underlying material, on the other hand, is not, and the strain incompatibility that results causes the plate to bend—in the same way that a bilayer made of two materials with different coefficients of thermal expansion bends when heated. Although sometimes seen as an unwanted consequence of peening and sandblasting processes (Tolentino, 2013), this effect can be harnessed to shape thin metal parts.

Its first recorded use in a production environment was as a process control indicator where the deflection of normalized steel strips was used to monitor the intensity delivered by peening equipment (Almen, 1944). The potential of shot peening as a forming process was then quickly realized by the Lockheed Corporation which adopted it in the early 1950s to form integrally stiffened wing panels for the Lockheed Constellation aircraft (Simmons, 1952; Baughman, 1970; O'Hara, 2006). Since then, peen forming has been used to shape wing panels for most commercial aircraft (Kopp and Schulz, 2006). These panels are usually machined from thick aluminum plates from the 2xxx or 7xxx series to thicknesses of few millimeters, feature complex distributions of thicknesses, and can exceed 30 m in length and 3 m in width (Blackwell et al., 2004; Levers, 2010). Figure 1.1a shows final adjustments being performed on a typical wing panel with an air blasting machine after the panel was formed in an automated peening cabinet and figure 1.1b shows a typical shot stream produced by an air blasting machine. Other applications of the process include forming fuselage panels for commercial aircraft as well as panels and tank bulkheads for the Ariane launchers of the European Space Agency, one example of which is shown in figure 1.1c–d (Meyer et al., 1987; Hornauer and Köhler, 1990; Merino et al., 2017).

The main advantage of peen forming is that it can form integrally stiffened, tapered, and pocketed panels that would otherwise be too challenging or prohibitively expensive to form with more conventional forming processes such as press or stretch forming (Baughman, 1970). Because the same equipment can be used to shape many different contours, peen forming is especially adapted to small series or large parts for which investing in heavy tooling is not justified. Since it is a cold forming process, it also enables to form parts directly in

Figure 1.1 Peen forming of wing panels and tank bulkheads. (a) Final shape corrections being applied to a wing panel with a portable compressed air peening machine at Sonaca Montréal. The initially flat panel had previously been peen formed in an automated peening cabinet. Reproduced with permission from Sonaca. (b) Shot propelled onto a metal strip with a compressed air machine. Reproduced with permission from Fraunhofer IWM (© Felizitas Gemetz / Fraunhofer IWM). (c–d) Tank bulkheads for the Ariane 5 launcher made of eight initially flat trapezoidal segments peen formed to their final shape then welded together. Reproduced with permission from MT Aerospace.

their heat-treated state (Ramati et al., 1999). Finally, whereas most forming processes that involve stretching operations induce tensile residual stresses that can be detrimental to the fatigue behavior of the parts and promote stress corrosion cracking, peening leaves the outer surface of treated parts in a state of compression, which has the opposite effect. On the other hand, peen forming can only form smooth contours, without sudden breaks, and, while it is possible to form very thin parts to tights radii of curvature (Johnson et al., 1981), radii of curvature that can be achieved on typical wing panels rarely go below one meter. For these reasons, creep forming is sometimes preferred to peen forming for thick or challenging wing designs (Levers, 2010).

Although companies that dominate the peen forming market have acquired a deep understanding of the process and sometimes developed their own numerical models (Friese et al., 2002; Levy, 2018), this knowledge remains mostly confidential. As a result, new entrants and smaller businesses are often reduced to develop peening sequences by trial and error. This process takes time and often requires scrapping several parts before finding an appropriate sequence. Furthermore, because of low production rates, there was, until recently, little incentive to optimize a peening sequence once it delivered the desired shape. In fact, the very flexibility of the process might explain why little effort has been devoted to developing peen forming models, both in the industry and in the scientific literature. Indeed, whereas there are huge incentives to develop accurate models for forming processes that involve heavy tooling and costly dies, no such incentives exist for peen forming as localized peening in strategic areas is often all it takes to correct the shape of a warped panel.

But things are changing due to the increasing availability of laser peening systems. Instead of shot, laser peening utilizes pressure waves generated by the confined expansion of a plasma to plastically deform the target. Long under development, this technology has steadily been deployed in production since the 1990s when high power and high repetition rate laser sources small enough to be compatible with a production environment became available.[1] For example, laser peening has been chosen to form some of the wing sections of the Boeing 747–8 in 2008 (Penning, 2010; Hackel et al., 2017). Although it requires large investments compared to shot peening, the process can plastically deform material over a much larger depth, which enables to form panels much thicker than what would be possible with conventional peen forming. A compelling example is the ongoing effort to demonstrate that laser peening can form thick steel panels for the naval industry (Hackel et al., 2017). There is, therefore, a need to develop predictive tools to clarify what designs can (or cannot) be formed with conventional shot peen forming to help process engineers select the right process for the right application. Developing such tools is the primary objective of this thesis.

The manuscript is structured as follows. Chapter 2 presents a critical literature review focused on numerical models of the peen forming process. It opens with a summary of the mechanics of peen forming, proceeds by reviewing existing models, and ends by introducing the concept of eigenstrains on which the rest of the analysis is based. Chapter 3 summarizes the limitations of prior research and defines the project's research objectives. Chapter 4 explores how the concept of eigenstrains can be harnessed to simulate peen forming and presents several improvements to existing inverse procedures used to experimentally identify eigenstrains in shot peened parts. Three articles resulting from this work are then presented in chapters 5 through 7. Chapter 5 presents the methods and results of a peen forming experimental campaign conducted on 2024–T3 aluminum sheets. Chapter 6 analyses these experimental results within the framework of the theory of eigenstrains. The main findings are then integrated in chapter 7 where we demonstrate how eigenstrain simulations coupled with off-the-shelf optimization algorithms enable to automatically determine peening patterns and treatments required to form a flat sheet into a desired shape. Chapter 8 presents additional optimization results generated during the course of the project. Finally, chapter 9 discusses limitations of the proposed models and outlines recommendations for future work.

---

[1] For a comprehensive history of laser peening, see Clauer (2019) and Dane and Hackel (1997).

CHAPTER 2 LITERATURE REVIEW

2.1 Peen forming mechanics

2.1.1 Before an impact

For a given target, the outcome of an impact depends on the type of shot and the impact velocity. The impact velocity, in turn, depends on the type of propelling system (air pressure; centrifugal wheel; gravity; see Kopp and Schulz, 2006), on process parameters, and on interactions between shot and their environment. In particular, collisions between incident and reflected shot, as well as rebounds, result in a distribution of impact velocities (Hong et al., 2008). Several models relying on granular materials and fluid dynamics simulations have been proposed to estimate these distributions (Micoulaut et al., 2007; Badreddine et al., 2014; Nguyen et al., 2014). Alternatively, they can be measured experimentally, either directly, with appropriate sensors, or indirectly, by correlating impact diameters or the deflection of normalized strips with reference experiments or simulations (Nordin and Alfredsson, 2016). Once available, this information, alongside material properties, geometry, and boundary conditions enables to investigate the response of the target under impacts.

2.1.2 Isolated impact

Shot used for peen forming operations are usually steel spheres about 1 mm in diameter propelled at several tens of meters per second (say $40\,\mathrm{m\,s^{-1}}$). Under these conditions, the impact of a single shot on a target very large in comparison to the shot can be considered as quasi-static (see sections 11.4 and 11.5 of Johnson, 2003 and section 6.5 of Stronge, 2004). This makes it possible to use Hertz's theory of elastic contact to estimate what impact velocities are required to initiate plasticity. For a steel shot hitting an aluminum half space, the theory predicts that yield first occurs for impact velocities of the order of $10^{-2}\,\mathrm{m\,s^{-1}}$, the reason for such low values being that, since the duration of an impact is very short, large loads can develop even for low velocity impacts (Johnson, 2003; Stronge, 2004). At low impact velocities, only a small amount of plastic deformation occurs below the peened surface, with the plastically deformed region being surrounded by elastic material. For higher impact velocities, the extent of the plastically deformed region increases until it reaches the surface and encompasses the contact area. This regime of indentation is called 'fully plastic' (Sharp et al., 1993; Mesarovic and Fleck, 1999). It is in this regime that peen forming usually operates, as is illustrated in figure 2.1 which shows the distribution of equivalent

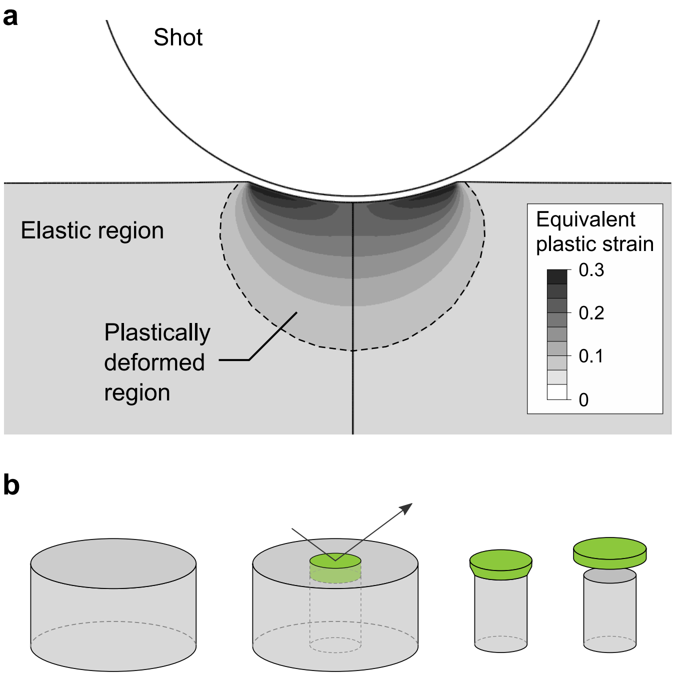

Figure 2.1 Distribution of plastic strains after a single impact. (a) Contour map of equivalent plastic strain in a 2024–T3 aluminum target struck at 40 m s^{-1} by a rigid shot 0.71 mm in diameter. The map was obtained by three-dimensional finite element simulation for the material model described in Prime (2013), a rigid shot, and frictionless contact. (b) The effect of a single impact on residual stresses and distortions can be visualized by idealizing the distribution of plastic strains as a cylindrical inclusion with homogeneous plastic strains. If the inclusion could be removed from the part, it would expand in the direction parallel to the surface and contract in the direction normal to the surface. Since the inclusion is slightly larger than the cavity it was removed from, inserting it back induces compressive stresses in the inclusion in the direction parallel to the surface and a slight downward bending as the structure elastically deforms to accommodate the inclusion. Adapted from Ballard (1991).

plastic strains after the impact of a 0.71 mm in diameter steel shot propelled at 40 m s^{-1} on a 2024–T3 aluminum target. This map was obtained by finite element simulations assuming a rigid shot, frictionless contact, and the same material model as in Prime (2013).

To visualize what residual stresses and distortions a single impact induces, it is convenient to idealize the distribution of plastic strains of figure 2.1a as a shallow cylinder coming up to the surface in which plastic strains are uniformly distributed, as shown schematically in figure 2.1 (Ballard, 1991). This cylinder can be thought of as an inclusion. If the inclusion could be removed without altering the distribution of plastic strains, it would contract in the direction perpendicular to the surface and expand in the directions parallel to the surface (since plastic flow conserves volume). In this configuration, the system is stress-free. Inserting the inclusion back into its cavity requires performing the inverse sequence of operations, that is, compressing it in the direction parallel to the surface and stretching it in the transverse direction. This results in compressive residual stresses in the inclusion in the direction parallel to the surface and a slight downward bending of the overall system as the latter deforms elastically to accommodate the inclusion.

2.1.3 Multiple impacts

Now consider a plate of uniform thickness being repeatedly struck by shot until its surface is fully covered by dents. Since the location of impacts and impact velocities are stochastic, material points located near the peened surface experience a complex load path with sudden changes in the magnitude and direction of contact loads. At the scale of a shot, the stress and strain fields that result present sharp local variations and the surface is rough, as illustrated in figures 2.2a and b. The former shows a scanning electron micrograph of the surface of a 7050 aluminum specimen shot peened with steel shot with a treatment typical of those encountered in the aircraft industry. The latter shows a distribution of in-plane residual stresses in a $76 \times 19 \times 2.39$ mm steel strip peened with 2 mm diameter rigid shot propelled at $75\,\mathrm{m\,s^{-1}}$ computed by Chen et al. (2014) with finite element impact simulations. Although local variations of mechanical fields can play an important role in determining the fatigue behavior of a part (Musinski and McDowell, 2015; Castro Moreno, 2017), such variations are of secondary importance for peen forming. Indeed, the process operates at the scale of the structure at which local variations in the distribution of plastic strains have little to no influence on the obtained deformed shapes. The latter rather depend on *average* plastic strains.

When averaged in the directions parallel to the peened surface over a region whose extent is large compared to the depth of the plastically deformed layer, all mechanical fields must, by translational invariance, only depend on the coordinate normal to the surface. Furthermore, shear components must be zero. In the rectangular x, y, z–coordinate system of figure 2.3, this implies that the distribution of plastic strains, $\boldsymbol{\varepsilon}^{pl}$, is of the form

$$\boldsymbol{\varepsilon}^{pl}(z) = \begin{pmatrix} \varepsilon^{pl}_{xx}(z) & 0 & 0 \\ 0 & \varepsilon^{pl}_{yy}(z) & 0 \\ 0 & 0 & \varepsilon^{pl}_{zz}(z) \end{pmatrix}. \tag{2.1}$$

Furthermore, the fact that plastic deformations take place at constant volume requires that $\varepsilon^{pl}_{zz} = -(\varepsilon^{pl}_{xx} + \varepsilon^{pl}_{yy})$. Figure 2.2c–d shows typical in-plane plastic strain and residual stress profiles in 2024–T3 aluminum alloy peened with 0.5 mm in diameter steel shot in conditions

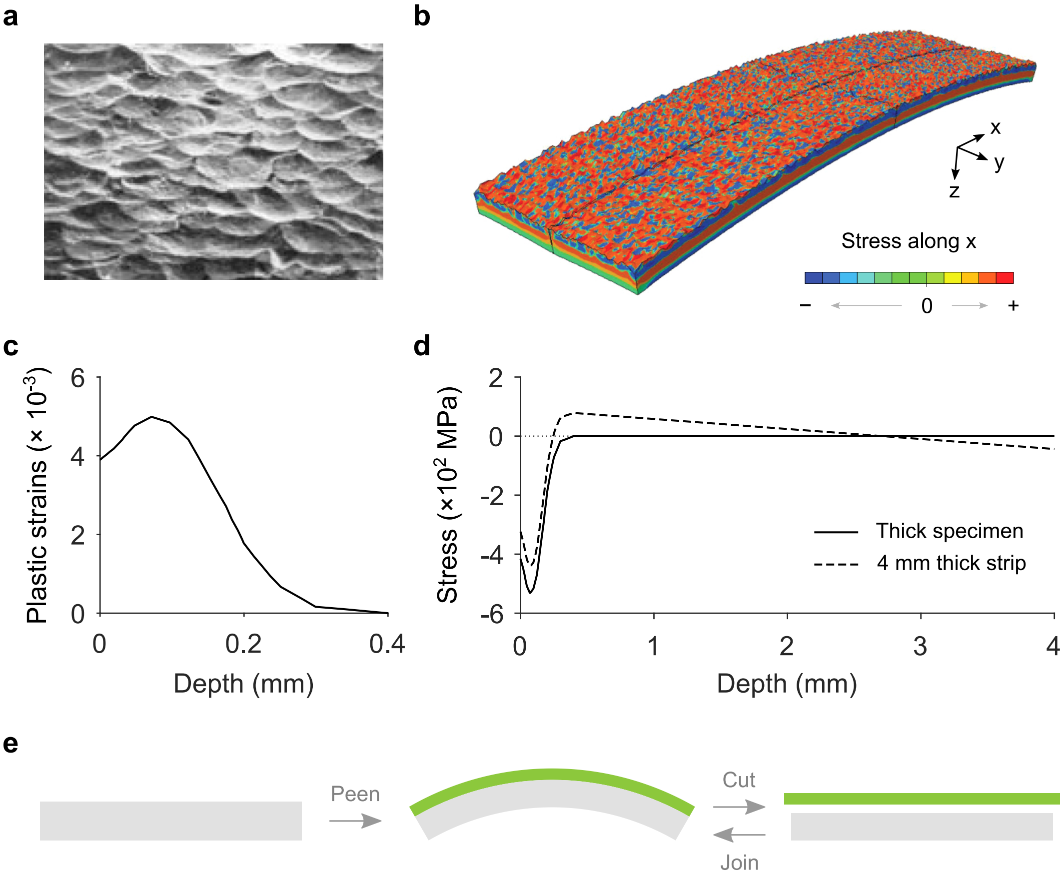

Figure 2.2 Typical surface finish, residual stresses, and plastic strains after many peening impacts. (a) Scanning electron micrograph showing the surface of 7050 aluminum alloy peened with steel shot. Adapted from Sharp and Clark (2001). (b) Finite element simulation showing residual stresses in a $76 \times 19 \times 2.39$ mm steel strip peened with rigid shot 2 mm in diameter propelled at 75 m s^{-1}. While the magnitude of residual stresses near the rough peened surface varies significantly from point to point, residual stresses deeper into the material display a clear ‘layered’ structure with compressive stresses near the peened face and the back face, and tensile stresses in-between. Adapted from Chen et al. (2014) with permission from the American Society of Mechanical Engineers. (c–d) Typical in-plane plastic strain and residual stress profiles for shot peened 2024–T3 aluminum. Residual stresses in the thick specimen are from Levers and Prior (1998) (the thickness of the specimen is not available). Residual stresses in the thin specimen and plastic strains are from Korsunsky (2005). The latter were reconstructed from the stresses in the thick specimen as described in the article then used as loads in a plate model to estimate residual stresses in the thin specimen. In this case, the peening affected layer is about 0.4 mm thick. Residual stresses below this layer vary linearly owing to the bending and stretching of the specimens. For thick specimens that do not deform significantly, residual stresses are almost zero in this region. (e) The effect of multiple impacts on residual stresses and distortions can be visualized by idealizing the distribution of plastic strains as a layer with homogeneous plastic strains. If this layer could be separated from the bulk, it would expand in the direction parallel to the surface. Because of strain incompatibility, gluing the layers back together induces compressive stresses in the upper layer, tensile residual stresses immediately below the transition (the upper layer stretches the bulk) and causes the structure to bend.

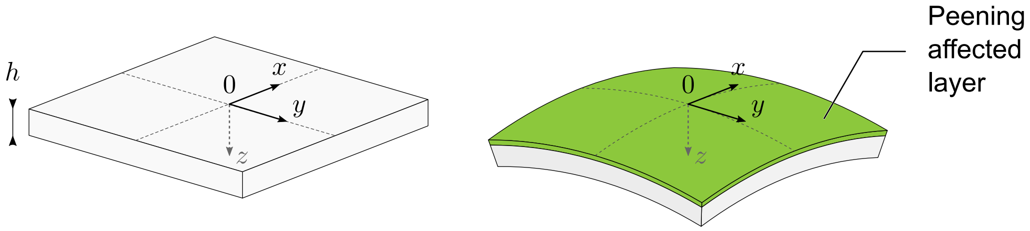

Figure 2.3 Rectangular x, y, z–coordinate system used throughout the thesis.

typical of those used to peen form wing skin panels. In this case, the peening affected layer is about 0.4 mm thick. In this layer, plastic strains are positive (the upper layer is stretched) and residual stresses are negative (the underlying material resists the expansion of the upper layer). Note that the same layered structure is predicted by the finite element simulations of figure 2.2b.

To visualize what residual stresses and distortions a peening treatment does induce, it is convenient to imagine that plastic strains are uniformly distributed in a thin layer of uniform thickness parallel to the peened surface, as illustrated in figure 2.2e. If this layer could be separated from the bulk, it would expand in the direction parallel to the surface to reach a stress-free configuration. Gluing back the layers together requires compressing the upper layer and/or stretching the bulk. When all external constraints are released, the system spontaneously bends into an equilibrium configuration that is a compromise between the rest configurations of the two layers taken separately.

2.2 Modeling peen forming

At the scale of an impact, the response of the material is highly non-linear. It involves contact between the shot and the target, (visco-)plastic deformations, and large displacements and rotations for points close to the surface, which are characteristics of forming processes. On the other hand, at the scale of the structure, the response following the introduction of incompatible plastic strains is usually elastic with large displacements and large rotations but small strains (Chen et al., 2014). Computing the final deformed shape of a peen formed part can therefore be seen as a springback analysis. Finally, one must consider how the local and global scales interact and whether some form of coupling between the two is required.

In this section, we review existing peen forming models in order of complexity, starting with detailed models where every impact is explicitly modeled and ending with idealized models calibrated using small scale experiments.

2.2.1 Simulating every impact

One strategy to model the peen forming process consists in modeling the entire structure and simulating explicitly every single impact. One early example of this approach was presented in Wang et al. (2002) where the authors simulated up to 1000 impacts on models of a quarter of 20 × 20 × 4 mm aluminum coupons. More recently, Chen et al. (2014) simulated 1500 impacts of 2 mm shot on a model of one quarter of a 76 × 19 × 2.4 mm aluminum coupon held into an Almen holder. In both cases, impacts were simulated with a dynamic explicit finite element analysis followed by a springback analysis to obtain the final deformed shape of the coupons after all external constraints were removed. However, while both models qualitatively predict the expected shape for deflection curves, residual stress, and equivalent plastic strain profiles, neither was validated.

The main merit of these simulations is that they naturally include the coupling between the local and global scales. Furthermore, although prohibitively high computing times limits their use to small structures, they show a detailed view of the mechanics of the process. For example, for the conditions investigated, Wang et al. (2002) observed that plastic strains after numerous impacts were organized in layers of equal intensity parallel to the surface and Chen et al. (2014) observed that no reverse yielding occurred during springback, which corroborated similar conclusions that had previously been reached based on the analysis of simpler models, experimental data, and insight.

2.2.2 Local/global models

Another modeling strategy, which is in no way specific to peen forming, consists in using distinct models to deal with local and global scales. To the best of our knowledge, no peen forming model has been published that considers the coupling between the local and global scales. Instead, the analysis proceeds sequentially as follows. First, a local model is used to simulate the response of the target when it is subjected to the peening treatment. Because the interactions between the shot and the target are highly local, these simulations are usually performed on small representative volumes—usually small blocks a few millimeters on each side. The results of these simulations are then post-processed to obtain an averaged response; for example, average plastic strain or residual stress profiles, or resulting axial loads and bending moments. Finally, these averaged loads are transferred to a model of the entire structure to compute its final deformed shape.

Models that include the progressive deformation of the structure

One of the first local-global model of the process was proposed by Cao et al. (1995). To compute peening induced loads, the authors used a semi-analytical model described in Khabou et al. (1989). This model returns the residual stresses that a peening treatment would induce in a half space made of the same material as the treated part and peened until it reaches a steady-state cycle (adaptation or shakedown). These profiles, which are zero outside of the peening affected layer, were then used as an initial stress state for springback simulations. When transferred to a model of a structure of finite thickness, these stresses become unbalanced and they redistribute, causing the structure to deform. The deformed shape computed in this way can be thought of as the shape that the peened part would assume if it was perfectly constrained during peening then released. However, this one-step approach underestimates the deformation of parts that are free to deform during peening. To include the effect of the progressive deformation of a part, the authors proposed an iterative procedure where, after having solved for equilibrium, residual stresses in the peening-affected layer are 'reset' to their original value, as illustrated in the last step of figure 2.4a. This process is then repeated until convergence. It amounts to assuming that the peening treatments sets the distribution of residual stresses in the peening-affected layer and to compute the elastic deformations needed to equilibrate these stresses. Note that this procedure provides no information about the shape of the part at intermediate stages of the treatment; it only returns its final deformed shape once deformations have saturated. In Cao et al. (1995), this procedure was implemented using a linear strength-of-materials plate model and validated against peen forming experiments conducted on imperfectly constrained Almen A strips. Computed residual stresses and deflections were close to experimental measurements for all types of shot and shot velocities considered in the study.

A model to compute the response of a peen formed part at any stage of the peening sequence was proposed by Gariépy et al. (2011) and further improved in Gariépy et al. (2013c). Like Cao's model, Gariépy's model used unbalanced residual stresses as loads and relied on an iterative procedure where near-surface stresses were reset after each equilibrium computation. However, unlike Cao et al. (1995), the iterations were not continued until convergence. Instead, three-dimensional finite element simulations were first used to obtain unbalanced stress profiles for different peening times at regularly spaced time intervals. Then, a few iterations of the loading scheme were conducted for each time step. Finite element shell models that included geometric nonlinearities were used to compute the deformed shape of the peened part. The main limitation of this approach is that there is no clear physical basis for choosing the number of iterations per time step. Consequently, this parameter must

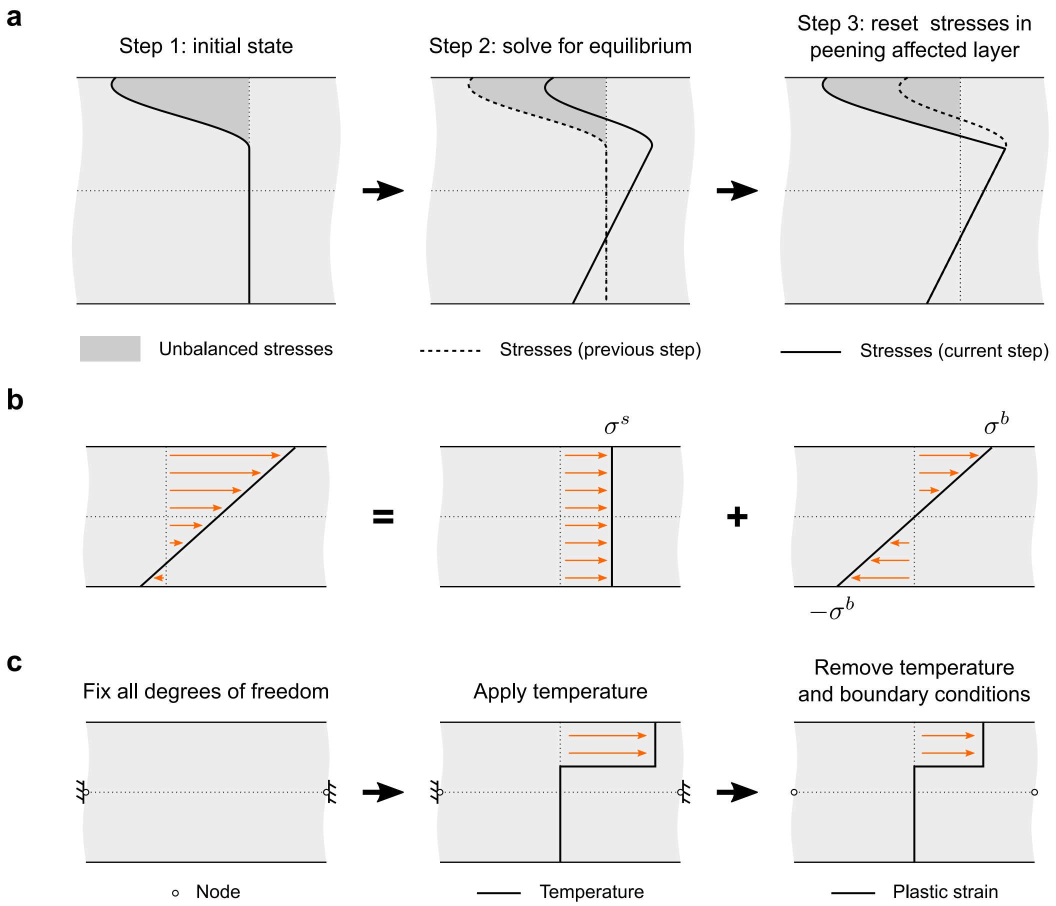

Figure 2.4 Loading schemes for peen forming simulations. (a) Unbalanced residual stresses computed in a half-space with a local peening model are input into a model of thin-walled structure. Stress rebalancing causes the structure to deform. To simulate multiple peening passes, residual stresses in the peening affected layer are reset to their original value and the process is repeated. (b) Idealized unbalanced stresses obtained by combining a constant stretching term of magnitude σ^s with a linear bending term of magnitude σ^b. The former controls the amount of stretching while the latter controls the amount of bending. (c) Procedure to input plastic strain profiles in thin shell finite element models. After having fixed all degrees of freedom, the thermal expansion coefficient is set to a negative value and a temperature profile is applied to the entire model. Temperature is increased until thermal stresses exceed the yield limit, which induces a distribution of plastic strains having the same shape as the temperature profile.

be calibrated against experimental data, which undermines the predictive capabilities of the model.

In Gariépy et al. (2011), loads were applied uniformly to the entire structure, which was deemed appropriate to simulate parts peened uniformly over the course of many cycles. Each time step therefore corresponded to the peening nozzle traveling once over the entire surface of the part. In Gariépy et al. (2013c), smaller time steps were used to simulate a peening nozzle traveling at low velocity over the part. As a validation exercise, the authors simulated peen forming tests conducted on $76 \times 76 \times 1.6$ mm 2024–T3 aluminum plates peened in a single pass with parallel strokes spaced 6 mm apart. The size of the time steps and the number of increments were calibrated based on the deflection of $76 \times 19 \times 1.6$ mm strips made of the same material and peened in the same conditions. The error on deflection between simulations and experiments ranged from -2 to 20 %. However, the authors acknowledge that the overall good results could be due to the calibration having been conducted on specimens similar to those used for validation. Whether this modeling strategy can successfully be scaled up to model large structures remains to be validated.

Models that neglect the progressive deformation of the structure

Peen forming models that neglect the progressive deformation of the part during peening include those of Han et al. (2002) and Chaise et al. (2012).

Han et al. (2002) used impact simulation on small representative volumes to obtain peening-induced loads which were then mapped to a finite element model of the part meshed with solid elements to compute deformed shapes. The discrete element method was used to model shot and shot-target interactions and the finite element method was used to compute the response of the target. Although the main advantage of discrete element simulations is that it can capture multiple interactions such as those that occur between shot, thus leading to realistic distributions of impact speeds and locations (Hong et al., 2008; Badreddine et al., 2014), shot-shot interactions were not included in the analysis. The authors also insist on the necessity to map either residual stress or strain fields, as well as hardening variables. The latter is, in fact, only required if the springback analysis is followed by further forming simulations; it is otherwise unnecessary.

Chaise et al. (2012) used a semi-analytical impact model to compute the distribution of plastic strains induced by peening in a half space then mapped average plastic strains profiles to a finite element model of the part meshed with solid elements to compute deformed shapes. The semi-analytical model was an extension to that presented in Jacq et al. (2002). This model is limited to normal frictionless impacts and small strains but can otherwise simulate any sequence of impacts on a half-space with a computational time about one order of magnitude lower than equivalent finite element simulations. Plastic strain profiles were input as thermal strains by augmenting the material properties of each layer of elements parallel to the peened surface with coefficients of thermal expansion $\boldsymbol{\alpha}$ equal to the average plastic strain $\boldsymbol{\varepsilon}^{pl}$ at that depth and by applying a unit increment of temperature, $\Delta T = 1$, such that the resulting thermal strains,

$$\boldsymbol{\varepsilon}^{th} = \boldsymbol{\alpha}\Delta T, \tag{2.2}$$

yielded the desired incompatible strains. More details about the validity of this loading strategy can be found in Hill (1996) and in latter sections.

2.2.3 Models calibrated using small scale peen forming tests

All simulation procedures presented so far were fully numerical. Most of them were developed for academic research projects that aimed at investigating the mechanics of peen forming. All relied on complex local models of the process and validation was limited to small strips and small deflections. Another class of models, some of which have been deployed in engineering departments of major wing manufacturers, only rely on a global model of the structure loaded with ‘equivalent’ idealized loads that mimic the effect of the peening treatment. These loads are derived from small scale peen forming experiments conducted on representative coupons.

One of these models was developed by Homer (1989) as part of a wider research program on peen forming initiated by Boeing (see Harburn and Miller, 1982; Homer and VanLuchene, 1991; VanLuchene et al., 1995; VanLuchene and Cramer, 1996). The authors used a thin shell finite element model loaded with idealized unbalanced residual stress profiles like that shown in figure 2.4b, which were obtained by combining a constant stretching term of magnitude σ^s with a linear bending term of magnitude σ^b. The former parameter controls the amount of in-plane stretch while the later controls the amount of curvature. Their values were obtained experimentally by peening elongated strips of constant thickness uniformly on one face and by measuring their curvature and in-plane stretch, as explained in VanLuchene et al. (1995).

Another approach, proposed by Grasty and Andrew (1996) and also discussed in Levers and Prior (1995), consisted in meshing the geometry with solid elements and by squeezing the layers closest to the peened surface until plastic yielding occurred by applying pressure loads on the upper and lower face of these layers. When the pressure was removed, plastic strains remained and caused the model to deform. While the thickness of the squeezed layer was chosen based on the depth of the plastically deformed volume obtained from single impact finite element simulations, the magnitude of the pressure loads was calibrated for each peening treatment by comparing simulated curvatures to those experimentally obtained on small representative coupons. Once identified, the loads were stored into databases for later use in large scale peen forming simulations.

This strategy was extended to thin shell models by Wang et al. (2006). Like Grasty et al., the authors used plastic strains as loads. The loading scheme, however, differed. First, all degrees of freedom of the model were set to zero and a profile of temperature similar to that shown in figure 2.4c, with no increase of temperature outside of the peening-affected layer, was applied to the entire model. The magnitude of the profile was increased until plastic yielding occurred. It was then ramped down to zero and the constraints were removed for the springback analysis. In this procedure, the plasticity model, thermal expansion coefficients, and variation in temperature are fictitious properties: their only purpose is to obtain the desired distribution of plastic strains. Like in Grasty and Andrew (1996), the depth of the plastically deformed layer was chosen based on numerical or theoretical considerations and the magnitude of the loads was calibrated experimentally.

Both Grasty and Andrew (1996) and Wang et al. (2006) suggested to perform several iterations of the proposed loading scheme to model parts that were free to deform during peening, using the final state of one step as the initial state for the next. This procedure requires additional calibration to relate the number of iterations to the peening time.

The works of Grasty and Andrew (1996) and Wang et al. (2002) were part of a larger research effort on peen forming carried out at Cambridge University during the 1990s and early 2000s. Related work include Gardiner (2001) for stress peen forming and Wang et al. (2002) for the design of blanks, among others. Most of this research was supported by BAe Airbus and built upon ideas presented in Levers and Prior (1998). Instead of inducing plastic strains in surface layers of material to mimic the effect of peening treatments, Levers and Prior (1998) proposed to use thermal strains as loads. For a given thermal expansion coefficient, through-thickness profiles of temperature were computed from experimental peening-induced residual stress profiles such that, when input into a model of the specimens used for measurements, these profiles induced the same residual stresses as those that were measured. Once identified, the profiles were input into finite element shell models in which enough through-thickness integration points were used to accurately discretize the profiles. Even though the loads were derived from experimental data, a final calibration step was performed where small coupons were peened in the same condition as the part to be simulated and the thermal expansion coefficient was used as a scale factor on the loads to ensure that simulations matched calibration experiments. Finally, while they acknowledge that unbalanced residual stress profiles could be input directly into finite element models, the authors reject this approach because “this instantaneous application of the residual stress can be difficult to analyze successfully, especially if the structures [. . .] undergo large distortions” and because “this method does not simulate very closely the physical behavior of a structure undergoing the real peening process, which occurs over a period of time”. Although this might have been true at the time of writing, this is no longer the case as most modern finite element codes include procedures to equilibrate unbalanced initial residual stress profiles. Usually, stresses are progressively ramped from zero in much the same way that thermal loads would be applied (Abaqus 6.14, 2014). Both approaches enable approximately the same level of control on the solution procedure and we show in latter sections that they are, in fact, equivalent. In the original article, only a proof of concept for an 11 m long wing panel was presented, without validation. The authors nevertheless demonstrated the potential of the method by simulating an actual peening sequence with the appropriate peening treatment and peening patterns on each face of the panel. Additional information about later developments of this method at Airbus UK are available in Blackwell et al. (2004).

Several models similar to those discussed above, where peen forming tests performed on small coupons are used to calibrate the thickness and amount of extension in an active layer, have also been patented for peen forming and distortion correction applications. See for example Mika et al. (2006) and Zarka (2017).

2.2.4 Summary

Table 2.1 summarizes the main features of the models reviewed in the previous sections and table 2.2 lists the characteristics of local impacts models whenever one is used. Note that table 2.2 only lists local models used in peen forming simulations. Many other local models have been developed for shot peening simulations as evidenced by the reviews of Rouhaud et al. (2005) and Zimmermann et al. (2010). Such models could be substituted to those listed here without altering the sequence of simulations.

2.3 Eigenstrain simulations

2.3.1 Unbalanced residual stress versus plastic strains

Most peen forming models reviewed in section 2.2 use residual stresses as loads. More precisely, they use unbalanced residual stresses profiles that a peening treatment *would* induce in a half space made of the same material as the treated part either directly as loads or as an intermediate step to compute equivalent loads—for example, resulting forces and moments in Cao et al. (1995), and temperature profiles in Levers and Prior (1998). This probably

Table 2.1 Summary of numerical models of the shot peen forming process published in the open literature.

Type of model	Reference(s)	Comments	Global model							Parameters used for simulations presented in the articles					Validated against . . .
			Type	Loads	Loads obtained from . . .	Includes peening trajectory	Includes progressive deformation	Includes initial stresses	Requires calibration	Target material	Target dimensions (mm)	Constraining conditions	Type of shot (diameter; in mm)	Shot velocity (m/s)	
Simulates every impact	Chen et al. (2014)	[10]	FEA; solid	-	Computed directly	-	Yes	No	No	SAE 1070 steel	76 × 19 × 2.4	Almen holder	Steel (2)	50–75	-
	Wang et al. (2002)	[11]	FEA; solid	-	Computed directly	-	Yes	No	Yes [4]	Aluminum 2024–T351	20 × 20 × 4	Free to deform	Steel; S660 (≃ 1.9)	21–35	Curvatures in one direction
Local/global	Cao et al. (1995)	-	Strength of materials	Forces and moments [7]	Local model	No	Yes [1]	No	No	SAE 1070 steel	76 × 19 × 1.3	Almen holder	Steel; S110, S170, S230, S330 (0.3–0.6)	20–80	Arc height and residual stress profiles in both directions for some conditions
	Chaise et al. (2012)	-	FEA; solid	Plastic strains	Local model	No	No	No	No	Inconel 600	60 × 18 × 2 [9]	Similar to Almen holder	Steel; ball bearings (4)	4	Residual stresses in both directions and deformed shapes
	Gariépy et al. (2011)	[12]	FEA; shell	Unbalanced stress profiles	Local model	No	Yes	Yes	Yes [3]	Aluminum 2024–T3	76 × 19 × 1.6	Almen holder	Ceramic (0.4–0.6)	34–66	Arc height and residual stress profiles in one direction only
	Gariépy et al. (2013c)	[13]	FEA; shell	Unbalanced stress profiles	Local model	Yes	Yes	Yes	Yes [3]	Aluminum 2024–T3	76 × 19 × 1.6 76 × 76 × 1.6	Clamped on two edges	Ceramic (0.4–0.6)	34	Deflection and radii of curvature in both directions
	Han et al. (2002)	-	FEA; solid	Stress and plastic strain	Local model	No	No	No	No	Aluminum 7050–T7651	150 × 40 × 4	-	Steel; S550 (1.4)	36 and 46.5	Arc height
Calibrated	Grasty and Andrew (1996)	-	FEA; solid	Plastic strains	Calibration	No	Yes [3]	Yes [8]	Yes [2]	Aluminum 5251	50 × 10 × 0.9 strip and 0.9 mm thick disc, 25 mm in diam.	Free to deform	Cast iron (≃ 1)	19	Deflection and surface strain for the disc
	Homer (1989) and Homer and VanLuchene (1991)	-	FEA; shell	Unbalanced stress profiles	Peening tests on small coupons	No	No	Yes [8]	No	Aluminum	10000 × 1000 × 5 plates and wing panel	Free to deform	-	-	-
	Levers and Prior (1998)	-	FEA; shell	Thermal expansion	Peening stress profiles databases plus calibration	-	-	Yes [8]	Yes [2]	Aluminum	150 × 50 × 4 strips and wing panel	-	(0.5)	-	-
	Wang et al. (2006)	[14]	FEA; shell	Plastic strains	Calibration	No	Yes [4]	Yes [8]	Yes [2]	Aluminum 5251	76 × 19 × 3	Free to deform	Steel; S660 (≃ 1.9)	-	Arc height [6]

[1] Stabilized state only.
[2] Loads to simulate the deformation of large structures are obtained by calibrating simulations against small scale peening experiments.
[3] Calibration required to relate the number of iterations to the actual peening time.
[4] Calibration required to relate simulation time to the actual peening time.
[5] Only the central 19 × 19 mm area was peened.
[6] It is unclear which data were used for calibration and which were used for validation.
[7] Derived from unbalanced residual stress profiles computed with the local model.
[8] Indirectly via the calibration.
[9] See Chaise (2011) for the dimensions of the strips.
[10] Considers 1400 randomly distributed impacts on a model of one quarter of the structure.
[11] Considers 1000 randomly distributed impacts on a model of one quarter of the structure.
[12] Adapts the model of Cao et al. (1995) to finite element simulations.
[13] Extends the model of Gariépy et al. (2011) to simulate the incremental deflection of a part as a peening nozzle travels over it.
[14] Extends the model of Grasty and Andrew (1996) to shell models.

Table 2.2 Summary of local impact models used by the local-global simulations listed in table 2.1.

Reference	Type of model	Hardening model			Shot behavior	Impacts sequence	Includes friction	Boundary conditions
		Hardening law	Strain rate dependence	Cyclic hardening				
Cao et al. (1995)	Semi-analytical [3]	No [2]	No	No	Elastic	-	No	Half space
Chen et al. (2014)	Finite elements	Isotropic	Yes	No	Rigid	Stochastic	Yes	Symmetry BCs on two faces; Prescribed displacements to model bolts; Rigid support
Chaise et al. (2012)	Semi-analytical	Isotropic	No	No	Elastic	Deterministic	No	Half-space
Gariépy et al. (2011) and Gariépy et al. (2013c)	Finite elements	Combined kinematic/isotropic	No	Yes	Rigid [1]	Stochastic	Yes	Symmetry BCs on lateral faces; Bottom face fixed
Han et al. (2002)	Combined discrete and finite elements	-	No	No	Rigid	Deterministic	Yes	Symmetry BCs on lateral faces; Bottom face fixed
Wang et al. (2002)	Finite elements	-	-	No	Rigid	Stochastic	-	Symmetry on two faces; Rigid support with friction

[1] Random diameter.
[2] Stabilized state only.
[3] See cited references for details.

stems from the fact that most studies about shot peening are concerned with how the process affects the fatigue behavior of treated parts and that, in such studies, it is natural to characterize the effect of peening treatments primarily in terms of residual stresses. For peen forming simulations, however, using unbalanced residual stresses as loads requires an abstraction effort as these stresses are at no point present in a structure. Indeed, residual stresses continuously redistribute. One exception is the case where a thick plate is perfectly constrained against stretching and bending, shot peened, then released (VanLuchene et al., 1995). In this scenario, residual stresses just before the constraints are released are a close approximation of the unbalanced stresses. In any other case, unbalanced stresses can only exist in a virtual configuration where they are equilibrated by some distribution of fictitious loads. This virtual configuration actually corresponds to the initial state of the finite element simulations of Gariépy et al. (2011, 2013b,c).

Unlike residual stresses, plastic strains do not evolve when a structure deforms—unless the yield stress is exceeded. Furthermore, because they result from highly localized interactions between the shot and the target, plastic strains induced by the same peening treatment in parts of different geometries should be almost identical, provided that the peened surface is smooth and that the parts are sufficiently thick, such that geometry does not to affect the outcome of an impact. This intuition, which is illustrated schematically in figure 2.5, was confirmed experimentally by Coratella et al. (2015) on laser peened 7050 aluminum specimens. Zhang et al. (2008) also demonstrated that plastic strains in shot peened 17–4 PH steel strips were independent of the thickness of the strips for the peening parameters considered in the study, which lead the authors to suggest that this result might hold for a variety of materials and peening conditions. Similar observations by Achintha and Nowell (2011) on laser peened Ti–6Al–4V support Zhang and collaborators' hypothesis. Taken together, these results suggest that loading schemes where plastic strain obtained on a half space are mapped onto models of parts of finite thickness are physically justified. Despite its advantages, this approach was only followed by Chaise et al. (2012) even though almost all authors acknowledge that plastic strains are the physical source of distortions. In particular Wang et al. (2006) noticed that "it has been believed that if the fundamental principle, such as the creation of plasticity by shot peening, can be included in the model, it can simulate the reality more accurately".

2.3.2 From plastic strains to eigenstrains

There exists a general framework to study the relationship between incompatible strains, residual stresses, and distortions called the theory of eigenstrains (Korsunsky, 2017). The

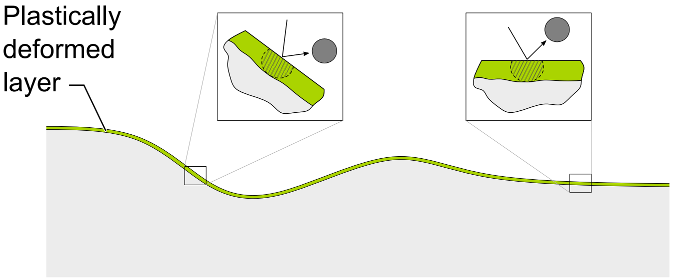

Figure 2.5 Schematic illustration of impacts on a curved surface. At the scale of a shot, impact sites indistinguishable from one another if the local radii of curvature of the peened surface are much larger than the radius of a shot. When this is the case, the distribution of plastic strains in the direction normal to the surface is expected to be the almost same everywhere.

term eigenstrains was introduced by Mura (1987) to designate all permanent nonelastic strains present in a structure. Thus, for small strains,

$$\boldsymbol{\varepsilon} = \boldsymbol{\varepsilon}^{el} + \boldsymbol{\varepsilon}^{*}, \tag{2.3}$$

where $\boldsymbol{\varepsilon}$ are total strains, $\boldsymbol{\varepsilon}^{el}$ are elastic strains, and $\boldsymbol{\varepsilon}^{*}$ are the eigenstrains. The eigenstrains themselves can be additively decomposed into thermal strains $\boldsymbol{\varepsilon}^{th}$, plastic strains $\boldsymbol{\varepsilon}^{pl}$, and any other volumetric strains such as those caused by the converse piezoelectric effect or phase changes here denoted by $\boldsymbol{\varepsilon}^{v}$, that is,

$$\boldsymbol{\varepsilon}^{*} = \boldsymbol{\varepsilon}^{th} + \boldsymbol{\varepsilon}^{pl} + \boldsymbol{\varepsilon}^{v}. \tag{2.4}$$

In the special case of shot peened parts, plastic strains are the only source of nonelastic strains and, therefore, plastic strains and eigenstrains are one and the same quantity.

In one of the first studies to use the concept of eigenstrains to model shot peening (Korsunsky, 2005), Korsunsky addressed the forward problem (also called direct problem) that consists in determining residual stresses and distortions that arise due to a known distribution of eigenstrains. Closed form solutions were presented for uniformly shot peened plates as well as for the special case of a non-uniform treatment when the problem is axisymmetric. Although the analysis was limited to thin plates within the context of the linear theory of elasticity, the proposed framework is general and can be extended with little modifications to complex geometries, non-uniform peening treatments, and geometric nonlinear problems by using the finite element method, or any other appropriate numerical method.

Apart from a series of papers on laser peen forming by Hu and collaborators (see for example

Hu et al., 2010, 2015) and limited results obtained on 60 × 18 × 2 mm Inconel 600 strips presented in Chaise et al. (2012), very few studies considered using eigenstrain simulations to predict peening-induced distortions. This is all the more surprising since these tools are widely used in other fields of residual stress engineering, in particular for welding simulations where they provide a cost-effective alternative to complete simulations of the process (Luo et al., 1999; Liang et al., 2005) and for laser peening simulations where they are commonly used to estimate residual stresses induced in massive components (DeWald and Hill, 2009a; Achintha and Nowell, 2011; Coratella et al., 2015).

2.3.3 Characterizing eigenstrains

Solving the forward problem requires knowing what eigenstrains are present in a part. If a local model of the process is available, then eigenstrains can be extracted from the results of the simulations. Otherwise, they must be characterized experimentally.

About impact simulations

Although widely used, local impact simulations remain a challenge to implement, primarily owing to the complex material models they require. In particular, since impacts encountered during peen forming treatments are usually fully plastic, particular attention must be paid to accurately modeling the plastic behavior of the materials.

Conventional isotropic, kinematic, or combined kinematic-isotropic hardening law are appropriate for simulations of single impacts or low coverage peening treatments with little interactions between individual impacts as, in these conditions, strains are moderate and the principal stress directions do not suddenly change during the analysis. These models, however, cannot capture the distortion of the yield surface that is likely to occur when the material is subjected to complex nonproportional loading paths such as those encountered near the surface of heavily shot peened parts. Modeling these effects calls for special models (François, 2001; Lemaitre et al., 2009). In particular, 2024 aluminum has been shown to be sensitive to nonproportional effects (Benallal et al., 1989).

The known plastic anisotropy of 2024–T3 aluminum alloy (Bron and Besson, 2004) should also be taken into account as it can significantly affect the outcome of indentation simulations, as illustrated in the following series of articles by Prime and collaborators: Pagliaro et al. (2009); Prime (2013); Merson et al. (2016); Prime (2017).

Next, consider the temperature dependence of material properties. Apart from Rouquette et al. (2009), most studies neglect this effect. However, single impact simulations conducted with the material model reported in Prime (2013) for 2024–T3 aluminum showed that, for shot diameters and velocity typical of those encountered during typical peen forming operation, the duration of an impact was only a few microseconds. These events are much shorter than the duration required for thermal diffusion to transfer energy away from the point of contact: taking the average diameter of a dent $\phi = 200\,\mu\mathrm{m}$ as a characteristic length and $D \simeq 5 \times 10^{-5}\,\mathrm{m}^2/\mathrm{s}$ as the thermal diffusivity of 2024–T3 aluminum yields a characteristic time $\tau = \phi^2/D \simeq 8 \times 10^{-4}\,\mathrm{s}$ for thermal diffusion. This suggests that the material might heat, and that temperature dependence and viscosity might have to be included in the model.

From the same simulations, strain rates about $10^5\,\mathrm{s}^{-1}$ were obtained below the indenter over a volume of the size of the dent and strain rates about $10^6\,\mathrm{s}^{-1}$ were obtained immediately below the advancing contact line. These values are typical of those reported in the literature, all alloys and peening conditions taken together (Meguid et al., 2002, 2007). Since Seidt and Gilat (2013) showed that 2024–T3 aluminum is strain rate sensitive for strain rates above $5 \times 10^3\,\mathrm{s}^{-1}$, this suggests that rate-dependent yield should be included in impact simulations. However, the highest strain rates that can be reached on laboratory equipment are of the order of $10^4\,\mathrm{s}^{-1}$ on split-Hopkinson bar setups, which raises the issue of material parameters identification.

Another experimental issue concerns the identification of material parameters on metal sheets, which requires special precautions to prevent the specimens from buckling during uniaxial tests or, if more representative load paths are desired, indentation tests (Cao et al., 2009; Al Baida et al., 2015). Because of the technical difficulties involved, several studies chose to identify material properties on specimens machined from thick plates. For example, Gariépy et al. (2011) used material properties obtained from uniaxial tension-compression tests conducted on specimens removed from a 12.7 mm thick plates to simulate the peen forming of 1.3 mm thick sheets. However, since both plates undergo different processing routes and heat treatments, it is likely that microstructure, hence the plastic properties of the two sets of sheets differed.

Finally, rolled 2024–T3 aluminum usually has grains that have approximately the same size as the plastically deformed volume below an impact. For example, Kulkarni et al. (1981) reports average dimple diameters for typical peen forming treatment ranging from 0.20 mm for low intensity saturation treatments to 1.06 mm for high intensity forming treatments whereas Gariépy et al. (2013a) observed average grain sizes of $0.640 \times 0.115 \times 0.038$ mm in a 12.9 mm thick 2024–T351 aluminum plate. Similar average grain sizes of $706 \times 163 \times 40$ mm were reported by Seidt and Gilat (2013) for 12.7 mm thick plates of the same alloy. This challenges the relevance of continuum material models for impact simulation. In fact, several studies are starting to consider the effect of the microstructure on impact simulations; see for example Musinski and McDowell (2015) and Castro Moreno (2017).

Identifying all material parameters that are required to model the different effects listed above would require a significant experimental effort. This, however, comes with no guarantee of obtaining better results than those that would be obtained with simpler models. Indeed, most publications achieve estimates of *average* peening-induced residual stresses close to validation experiments even though they only consider von-Mises yield surfaces and Armstrong-Frederick like hardening laws. This state of affairs is usually acknowledged (see for example the introduction of Chaise et al., 2012) and most studies settle for using over-simplified models which are then carefully validated over the range of peening conditions of interest.

Inverse identification from experimental data

Eigenstrains can also be identified experimentally, thus bypassing the need for complex impact simulations. Like residual stresses, eigenstrains cannot be measured directly. Instead, they must be reconstructed from other measurements—usually elastic strains or increments of displacements as the part is being cut—by using a model that relates measured quantified to the eigenstrains.

In most circumstances, experimental conditions are such that linear elastic models can be used for the reconstruction. For instance, in specimens much thicker than the peening affected layer and assuming that peening induced eigenstrains are equibiaxial, the latter are related to elastic strains and residual stresses through

$$\sigma_{ii}(z) = -\frac{E}{1-\nu}\varepsilon_{ii}^{el}(z) = \frac{E}{1-\nu}\varepsilon_{ii}^{*}(z), \tag{2.5}$$

where $i = \{x, y\}$, E is the elastic modulus, and ν is the Poisson ratio (Korsunsky, 2005). Similar relations are available for uniformly peened thin plates and cylinders; see Ahdad and Desvignes (1996) and Korsunsky (2005).

When no analytical solutions are available, another identification strategy consists in postulating a parametric form of the eigenstrains, inputting this distribution into a model of the specimen used for the identification, and adjusting the parameters until simulations match measurements. An early instance of this strategy was proposed by Flavenot and Niku-Lari (1977) and Niku-Lari (1981) which suggested to use eigenstrains of the form

$$\varepsilon^{*}(z) = \begin{cases} \varepsilon_0^{*}\cos\left(\pi(h-z)/2d\right) & \text{if } z < d, \\ 0 & \text{otherwise,} \end{cases} \tag{2.6}$$

where ε_0^* and d are the only two adjustable parameters. The former is the magnitude of the assumed eigenstrains and the latter is the assumed depth of the plastically deformed layer. Both can be estimated from simple geometric measurements, as discussed in the articles. In most recent publications, the eigenstrains are approximated as a truncated series expansion,

$$\boldsymbol{\varepsilon}^* = \sum_{i=1}^{n} c_i \boldsymbol{\xi}_i, \tag{2.7}$$

where the $\boldsymbol{\xi}_i$ are basis functions and the c_i are adjustable parameters. Within the hypotheses of the linear theory of elasticity, minimizing the error between simulations and measurements for distributions of the form (2.7) amounts to solving the weighted least-squares problem

$$\text{minimize} \quad f(\boldsymbol{c}) = \|\boldsymbol{W}(\boldsymbol{A}\boldsymbol{c} - \boldsymbol{b})\|_2^2\,, \tag{2.8}$$

where $\boldsymbol{b}$ is a $(m \times 1)$ vector of measured quantities, $c = [c_1, c_2, \ldots, c_n]^T$, $\boldsymbol{A}$ is a $(m \times n)$ matrix where A_{ij} is the numerical equivalent of the quantity b_i computed when the j-th basis function is input into the model of the specimen, and $\boldsymbol{W}$ is a $(m \times m)$ weighting matrix used to reflect measurements uncertainty. Because least-squares problems are convex, (2.8) has a unique solution if the columns of A are linearly independent (Boyd and Vandenberghe, 2004). However, the quality of the computed solution, its ability to converge towards the 'true' solution, and its sensitivity to measurements uncertainty depend on the choice of appropriate measurement locations, basis functions, and number of terms in the series expansion, which themselves depends on a priori knowledge of the actual eigenstrain distribution and physical insight. The use of such procedures has been championed by Korsunsky and collaborators that proposed several improvements and applied them to increasingly complex components, as demonstrated in Korsunsky et al. (2004), Korsunsky (2006), Jun et al. (2011), and Salvati et al. (2017). Similar ideas had also been explored by Hill and collaborators in Hill and Nelson (1995) and Hill (1996).

The idea of characterizing eigenstrains experimentally can be traced back to a series of articles by Ueda and collaborators in Japan in the late 1970s (see Ueda et al. (1984), Ueda et al. (1985) and the literature reviews of Hill (1996) and Jun and Korsunsky (2010) for an overview of major contributions) although it appears that similar ideas had independently been developed in Germany in the late 1960s (Flavenot and Niku-Lari, 1977). The motivation behind this work as well as behind references cited in the previous paragraphs was, however, not to compute distortions, but rather to reconstruct entire residual stress fields from limited measurements. For examples, eigenstrains induced by peening or welding are confined to a small region (near the peened surface for the former; near the weld joint for the latter).

However, the residual stresses they induce extend far away into the part. By using the above approaches, it is possible to identify the eigenstrains from measurements conducted only in the region where eigenstrains are nonzero, then to input them into a model of the part to obtain residual stresses everywhere. Furthermore, since they are guaranteed to be statically admissible, the computed stresses can be used as an initial stress state for structural integrity assessments (Korsunsky, 2017).

The use of eigenstrains identified on small representative coupons to predict distortions in larger structures is comparatively marginal. Until recently, it was almost exclusively used by the welding community (Ueda et al., 1989; Luo et al., 1999; Liang et al., 2005) although it has since spread to the laser peening and additive manufacturing communities (DeWald and Hill, 2009b; Nervi et al., 2017; Setien et al., 2018).

2.3.4 Accounting for initial eigenstrains

In previous sections, we tacitly assumed that the only eigenstrain present in a part were those induced by the peening treatment. This, however, is hardly ever the case since, unless the part is carefully stress relieved, it contains eigenstrains inherited from earlier processing stages such as rolling, machining, and preliminary surface treatments. In fact, because they can cause a part to deform unpredictably during peening, unexpected or undocumented initial eigenstrains are the primary cause for peen formed parts rework, which is a labor-intensive step usually done manually with portable peening equipment (G. Levasseur[1], personal communication, June 13, 2018). Characterizing initial eigenstrains, understanding how they interact with peening treatments, and including them in numerical models of the process is therefore of paramount importance.

Origin of initial eigenstrains in heat-treatable aluminum alloys

One source of initial eigenstrains common to virtually all peen formed parts is the heat treatment undergone by the base plates in which the parts are machined. For heat treatable aluminum alloys usually used to manufacture wing skin panels, the mechanism of generation of eigenstrains can be summarized as follows (Dieter, 1961; Robinson et al., 2014). After rolling, the plates are heated to approximately 500 °C to obtain a supersaturated solid solution. This step also relieves all strain incompatibilities and residual stresses. The plates are then quenched to freeze the microstructure and aged to form precipitates. During quenching, the outer layers of the material contract. This contraction, which is resisted by the hot inte-

---

[1] CEO, Aerosphere, Pointe-Claire, QC, CA.

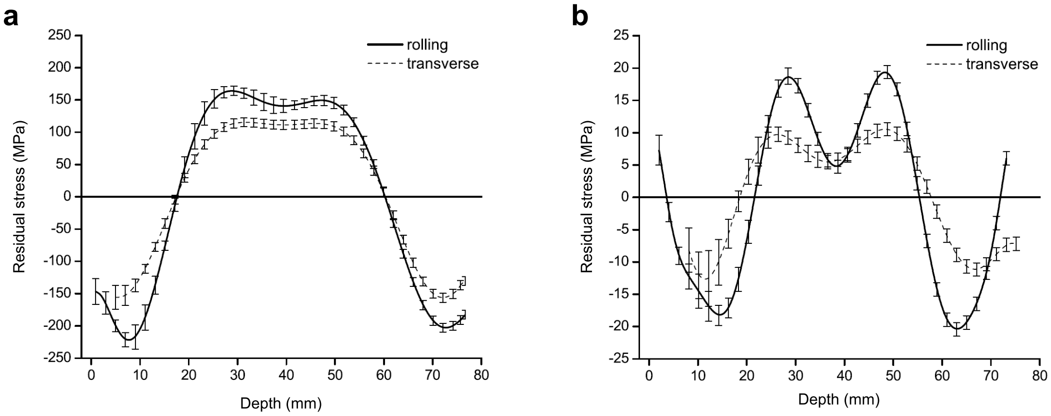

Figure 2.6 Residual stresses measured before and after the TX51 stress relief treatment in a 76 mm thick 7050–T74 aluminum plate by the slitting method. Adapted from Prime and Hill (2002) with permission from Elsevier.

rior, induces positive plastic strains on the outside (the material is stretched) and negative plastic strains in the core. As the temperature further decreases, the core contracts as well. This contraction is resisted by the outer layers that, since they cooled down, can sustain the load without yielding. This causes additional plastic strains in the core, this time positive. When the temperature homogenizes, the only remaining strain incompatibilities come from plastic strains. The latter are positive in the outer layers and negative in the core, which results in compressive residual stresses in the outer layers and tensile residual stresses in the core.

The magnitude of residual stresses depends on the through-thickness temperature gradient during quenching. For this reason, residual stresses in as-quenched thin sheets are lower than in as-quenched thick plates. For the latter, residual stresses of hundreds of megapascals are common. To mitigate initial stresses, most aluminum plates and some aluminum sheets undergo the TX51 mechanical stress relief treatment. This treatment consists in stretching the plates by a few percent immediately after quenching so that the plastic deformation that results uniformizes plastic strains, thus reducing strain incompatibilities and, consequently, residual stresses. (Thermal relief treatments are excluded as they would cause alloying elements to precipitate and the mechanical properties of the alloy to drop.) Stress relief usually reduces the magnitude of initial residual stresses to a few tens of megapascals. This is illustrated in figure 2.6 which shows residual stresses measured before and after stress relief in a 76 mm thick 7050–T74 aluminum plate. The shape of the profiles, including the slight anisotropy, is typical of that observed for other heat treatable alloys and thicknesses.

Influence of initial eigenstrains on the shape of peen formed parts

To understand how initial eigenstrains/initial stresses affect the shape of peen formed parts, it is convenient to consider what happens in the peening affected layer and in the core of the material separately.

In the peening affected layer, several studies observed that the distribution of residual stresses after peening was independent of the initial stress state. For example, Gelineau (2018) measured identical residual stresses after having shot peened (i) as-machined and (ii) polished Inconel 718 coupons, even though large initial stresses that varied between −400 and 600 MPa were present over the first 0.1 mm of the as-machined specimen and no such stresses were present in the polished specimen. (For reference, peening-induced residual stresses had a magnitude of about −200 MPa and the thickness of the plastically deformed layer was about 0.3 mm.) In another experimental study, Zeller (1993) shot peened Ck45V steel round tension test specimens that had been prestressed up to 970 MPa in tension. Figure 2.7a shows the experimental setup and figure 2.7b shows surface residual stresses measured by X-ray diffraction at different stages of the process. In this case, residual stresses immediately after peening were independent of the level of prestress. Peening-induced residual stresses that were independent of the initial stress state were also observed numerically by Gariépy et al. (2011) during impact simulation on aluminum sheets for a typical ‘as-received’ initial stress state and both numerically and experimentally by Julan (2014) on as-received on welded Inconel 600 coupons.

These results suggest that the plastic deformations induced by peening are sufficiently large to erase most initial stress states, which was partially confirmed by Mesarovic and Fleck (1999). In this numerical study of Brinell indentation, the authors showed that, over the range of parameters they investigated, uniform prestress having a magnitude of half the yield stress (whether in tension or in compression) has no effect on the size of the plastically deformed volume nor on the area, pressure, and stiffness of the contact *in the fully plastic regime*. The only noticeable effect of prestress is far away from the point of contact in regions where plastic strains and elastic strains are of the same order of magnitude.

If peening erases initial stresses in the peening affected layer, then it does not matter what initial stress states are used in local models of the process. In particular, local models that assume an initially stress-free target should yield results close to those that would be obtained if initial stresses were included in the analysis. On the other hand, initial stresses/eigenstrains present deeper into the material are not affected by the treatment. Since they also contribute to the equilibrium of the structure, they could affect the final deformed shape of the parts. Among the peen forming models reviewed in section 2.2, only Gariépy et al. (2011) and

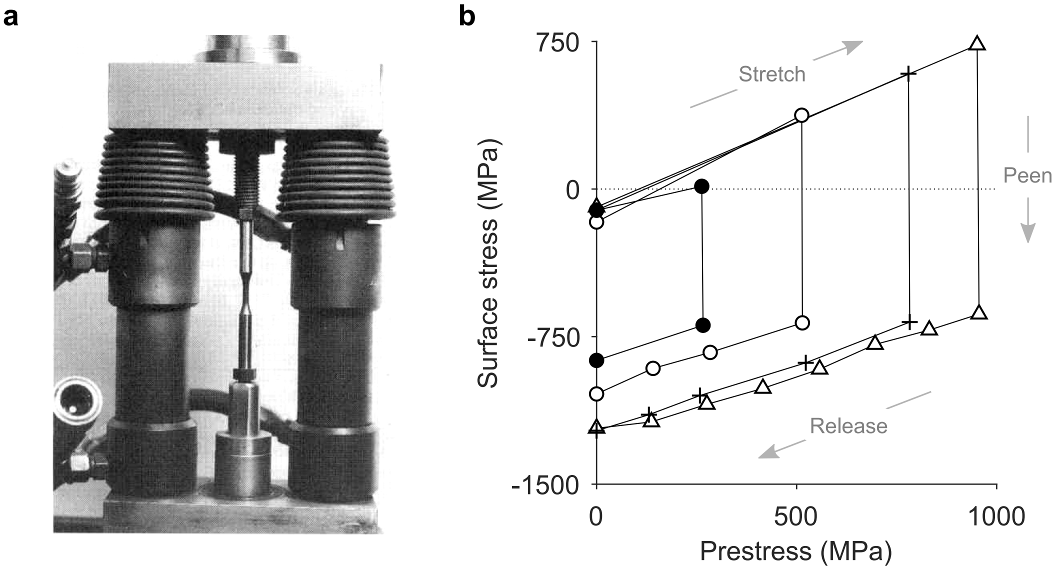

Figure 2.7 Experimental prestressing setup and residual stress measurements of Zeller (1993). (a) Round tension test specimen installed in a universal testing machine. The specimens were prestressed in tension, shot peened with the compressed air system visible in the background, then released. (b) Surface residual stresses measured by X-ray diffraction at different stages of the process. Each curve corresponds to a different (identical) specimen. Adapted from Zeller (1993).

Gariépy et al. (2013b) included initial stresses in their global model. In Gariépy et al. (2013b), as-received stresses were shown to cause variations in curvature of about 8 % in 76 × 19 × 1.6 mm aluminum coupons compared to identical simulations that did not include initial stresses.

2.4 Validating peen forming simulations

Regardless of their level of sophistication, whether they are fully numerical, or whether they are calibrated against experimental data, peen forming models must be validated in conditions representative of the intended use of the model. Table 2.1, however, shows that most models were only validated against data acquired on 76 × 19 mm strips. Furthermore, the combination of treatments and thicknesses was such that the deflection of the strips was almost always less than their thickness. In other words, validation experiments only probed the geometrically linear regime. Although this is enough for a proof of concept, such limited validation makes it impossible to assess how any of the proposed models would perform when applied to large structures; in particular thin structures that are free to deform during peening and that deflect significantly. Only VanLuchene and Cramer (1996) and Levers and

Prior (1998) hint at having used data acquired on actual wing panels, but without providing any more information.

In addition, there does not appear to exist publicly available datasets that could be used to carry out independent validations. As will be shown in chapter 5 (see tables 5.2 and 5.3), few experimental datasets even include curvature and residual stress measurements in more than one direction (which are needed to characterize the anisotropy of the response of the specimens), even fewer feature specimens that deform into the geometrically nonlinear domain, and only two report initial stress measurements. None meets all three requirements.

2.5 Addressing the inverse problem: active matter inspiration

In previous sections, we focused on the problem of predicting the final deformed shape of a peen formed parts given its initial geometry, the initial stress state, material properties, and the peening sequence. In practice, however, it is the inverse problem that process engineers are faced with, that is: determine an initial geometry and a peening sequence that will deliver a prescribed target shape. When additional constraints such as upper limits on the peening intensity, on coverage, and smoothness requirements for the peening patterns—which are required to ensure that available peening equipment can execute the computed peening sequence—are factored in, this results in a multi-constraints, possibly multi-objectives, optimization problem that must be addressed numerically.

The main contribution to this problem was presented by VanLuchene and collaborators (Homer and VanLuchene, 1991; VanLuchene et al., 1995; VanLuchene and Cramer, 1996). VanLuchene's approach is based on a finite element shell model of the part to be formed and uses the amplitude of stretching and bending loads in each element as optimization variables. Assuming that a linear model adequately describes the response of the part, its deformed shape for any combination of loads can be expressed as a linear combination of the deformed shapes obtained when unit loads are successively input in each element. This enables the optimization problem to be formulated as a linear constrained least square problem. Optimal bending and stretching loads were then related to actual process parameters through experimentally determined empirical relationships. Another strategy, proposed by Essa et al. (2015), is based on the observation that, if a model of the target shape is flattened—for example by compressing it between two rigid surfaces—then the regions of compressive stresses in the flattened configuration correspond to those that need to be stretched by peening to obtain the desired target shape. Finally, occasional press releases and patent applications show that in-house optimization procedures have been developed by most major actors in the peen forming business, although what techniques are exactly used remains unclear due to tightly enforced confidentiality policies (Harburn and Miller, 1982; Levy, 2018).

On the other hand, many robust optimization procedures have been proposed to address closely related problems encountered in other fields of engineering. For example, there are striking similarities between peen forming and shape control of thin structures with piezoelectric actuators: in both cases, a thin structure deforms in response to the incompatible expansion of its outer layers and the objective is to find an optimal placement for the actuators to achieve the desired target shape. Tools developed for actuator placement and control problems are routinely used for adaptive optics, active structures design, and vibration control (Koconis et al., 1994; Paradies and Hertwig, 1999; Irschik, 2002). Similarly, the MEMs and 4D printing communities have been developing techniques to manufacture flat composite structures that morph into prescribed three-dimensional shapes when subjected to a given stimuli (Pajot et al., 2006; Gladman et al., 2016; van Rees et al., 2017). Figure 2.8 shows one example of such a system where a patterned gold film was deposited onto a polysilicon substrate such that the differential of thermal expansion between the two layers caused the structure to deform when cooled down. In the example shown, the pattern was optimized to maximize the deflection of small cantilevered plates while maintaining the edge opposite the cantilevered edge flat (a uniform gold layer results in larger deflections but curved edges). Regardless of the scale, materials, and physical phenomena utilized for the actuation, the macroscopic response of all these systems (including peen formed parts) can be described with the same plate equations. This suggests that most of the techniques developed for shape control, MEMS design, etc., could, with minor modifications, be adapted to peen forming.

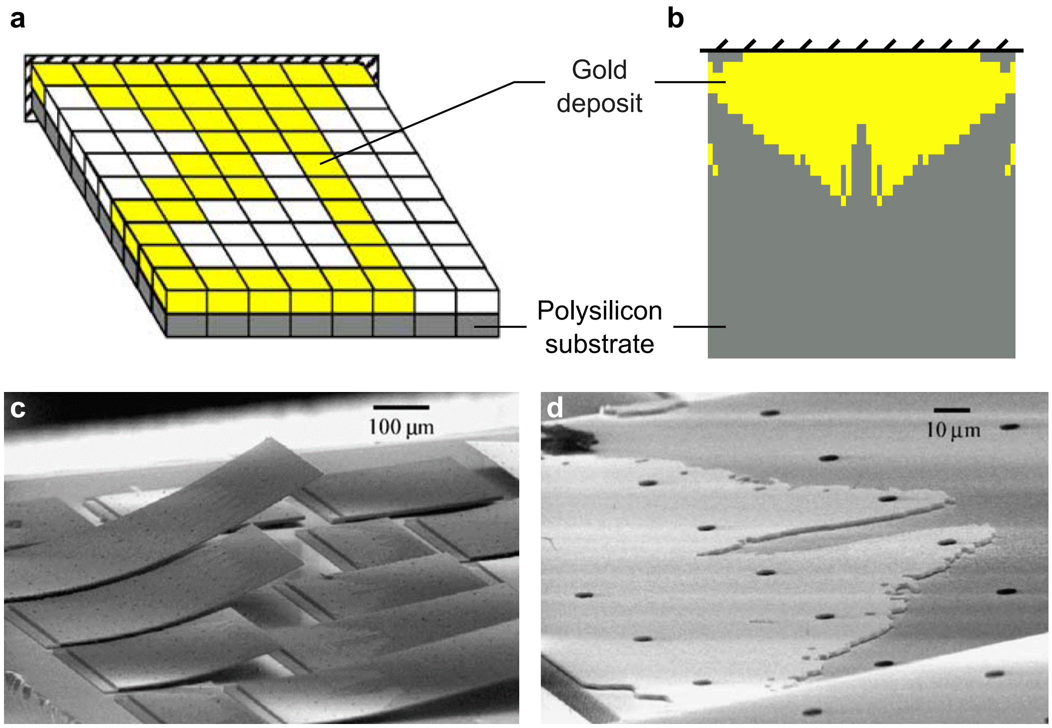

Figure 2.8 Overview of the procedure developed by Pajot et al. (2006) to design micro bilayer actuators that deform into a prescribed shape when subjected to a temperature differential. (a) The problem consists in finding a distribution of material in the upper layer that minimizes some error function—for example the error to a prescribed target shape. An iterative procedure derived from topology optimization codes was used to generate distributions of material where finite element simulations were used at each iteration to evaluate the current deformed shape of the bilayer. (b) Typical optimal distribution computed to maximize the deflection of a cantilevered plate while ensuring that the edge opposite the cantilevered edge remained straight. (c) Scanning electron micrographs of several bilayers manufactured using a polysilicon substrate and a gold deposit. (d) Zoom on the bilayer in the middle of the right row. Adapted from Pajot et al. (2006) with permission from Elsevier.

CHAPTER 3 OBJECTIVES AND RATIONALE

The main objective of this thesis is to develop numerical tools (i) to predict how thin parts deform in response to a known shot peening treatment and (ii) to assess whether a desired shape can be peen formed.

The literature review conducted in chapter 2 found a dozen studies that proposed models of the peen forming process. These models fit into three categories:

- Models where every impact is explicitly simulated;
- Models where peening induced loads are characterized numerically, with small scale impact simulations, then mapped onto a large-scale model of a part to compute distortions;
- Models where idealized loads that mimic the effect of the peening treatment are characterized experimentally, usually by calibrating small scale peen forming experiments with simulations, then mapped onto a large-scale model of a part to compute distortions.

The first two categories are fully numerical and particularly difficult to set up, primarily owing to the advanced material models required to capture the response of aluminum alloys to cyclic nonproportional loadings. The third category is still based on heuristics and lacks a sound theoretical basis. In particular, it remains unclear under what conditions loads identified on small coupons can be used to simulate the forming of large panels that are free to deform during peening and that deflect significantly. Finally, there exists no publicly available validation of the above models on parts representative of those used in production, nor does there exists publicly available experimental data that would enable to perform such a validation.

That only few studies dealt with peen forming is explained by peen forming being a niche process. However, once it is realized that peen formed parts are merely thin structures that deform in response to a strain incompatibility between their plastically deformed surface layers and the rest of the structure, the parallel between peen forming and problems encountered in other fields of engineering become clearly apparent. For instance, the theory of eigenstrains, initially developed in the field of micromechanics, provides a theoretical framework to characterize peening induced loads and to transfer loads between local and global models of the process. Other tools that have not yet been applied to peen forming include optimization strategies developed in the fields of shape control, MEMs manufacturing, and 4D printing to design and control thin actuated structures that morph from a flat configuration to a prescribed three-dimensional shape. With appropriate modifications, such strategies could provide the backbone of numerical procedure to automatically determine peening patterns and intensities.

Based on these observations, the main objective was addressed in the following three steps.

1. **Investigate the potential of eigenstrain simulations for peen forming.**
   This point is addressed in each of the following chapters. Chapter 4 details several procedures that enable to identify peening induced eigenstrains from near-surface residual stress and strain measurements. In particular, we address the issue of the uniqueness of the computed solution. Chapters 5 and 6 use these procedures to interpret the results of peen forming experiments conducted on large aluminum sheets. Finally, chapter 7 illustrates how idealized eigenstrain profiles can streamline peen forming simulations. An early version of these ideas was presented in a paper published in the Journal of Materials Processing Technology that is reproduced in appendix G.

2. **Perform conventional and stress peen forming experiments to generate data needed to validate numerical models.**
   Rectangular sheets of 2024–T3 aluminum, 4.9 mm in thickness, were selected for the experiments. All specimens were uniformly shot peened on one face with the same treatment. Aspect ratios, peening trajectories, and prestressing conditions were varied to investigate how these factors affected the final deformed shape. Most specimens were about 1 m long, which, for the treatment considered, ensured that out-of-plane deflections were sufficiently large for geometric nonlinearities to affect the observed deformed shapes. Experimental results are presented in chapter 5 and analyzed through the framework of the theory of eigenstrains in chapter 6. These results were submitted for publications in the Journal of Materials Processing Technology as a two-parts paper.

3. **Develop a numerical procedure to automatically compute peening patterns and intensities required to form metal plates into a desired target shape.**
   An optimization procedure initially intended for designing micro-actuators was adapted to peen forming. Chapter 7 presents this procedure, alongside a validation conducted on specimens that did not deform significantly during peening. These results were presented at the 13th International Conference on Shot Peening and were published in the proceedings of the conference. Additional details and results obtained on specimens that deformed into the geometrically nonlinear domain are presented in chapter 9.

CHAPTER 4 PRELIMINARIES: IDENTIFICATION OF EIGENSTRAINS IN UNIFORMLY SHOT PEENED PLATES

The literature review of chapter 2 showed that there exist several well-established procedures to identify eigenstrains experimentally. Because they are designed to be as generic as possible, these procedures seldom completely exploit the distinctive features of the problem at hand. Consequently, the inverse identification problem is ill-posed and there is little guarantee other than expertise and judgment that the computed solution is a good approximation of the reality. However, there exist simple problems for which closed form solutions relating eigenstrains, strains, and stresses are available that can be explicitly inverted, thus ensuring that the computed solution is the correct one. In this chapter, we present such relations for uniformly shot peened plates. The chapter starts by reviewing the concept of nilpotent and impotent eigenstrains that enables to address the issue of uniqueness in a much wider context. We then proceed by detailing several procedures to identify eigenstrains in uniformly shot peened plates experimentally. While most of the results presented here are not original, they have never been, to the best of our knowledge, presented in a unified fashion. Their practical importance justifies a separate chapter.

4.1 Impotent and nilpotent eigenstrains

An eigenstrain field is said to be impotent (or noneffective) if it does not induce stresses, whereas it is said to be nilpotent (or effective) if it does not induce distortions (Furuhashi and Mura, 1979; Ueda et al., 1986). For example, the uniform expansion or contraction of an unconstrained structure is impotent, as illustrated in figure 4.1a, while the symmetric axial expansion in the plate shown in figure 4.1b is nilpotent.

Within the framework of linear elasticity, Nyashin et al. (2005) proved that any eigenstrain field can be uniquely decomposed as

$$\boldsymbol{\varepsilon}^* = \boldsymbol{\varepsilon}^{*\ \text{impotent}} + \boldsymbol{\varepsilon}^{*\ \text{nilpotent}}, \tag{4.1}$$

where $\boldsymbol{\varepsilon}^{*\ \text{impotent}}$ is the impotent part and $\boldsymbol{\varepsilon}^{*\ \text{nilpotent}}$ is the nilpotent part. Nyashin et al. also showed that an eigenstrain field is impotent if and only if it is compatible, and that it is nilpotent if and only if it derives from a statically admissible stress field, i.e., if there exist a

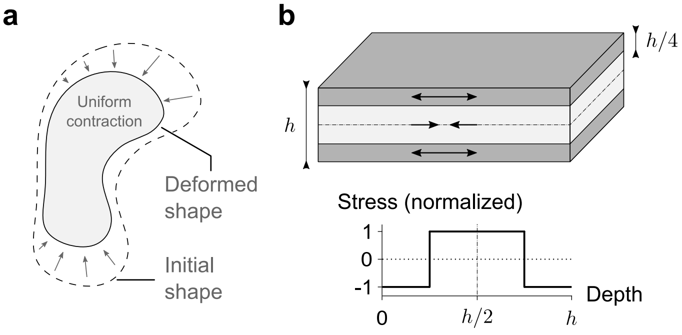

Figure 4.1 Examples of impotent and nilpotent eigenstrains. (a) The uniform contraction (or expansion) of an unconstrained structure is impotent: it induces deformations but no stresses. (b) The symmetric distribution of axial expansion in a plate shown is nilpotent: when the amplitude of the expansion in the inner layer is minus that in the outer layers, residual stresses arise but the structure does not deform—except near the edges, due to edge effects.

statically admissible stress field $\boldsymbol{\sigma}^*$ such that

$$\boldsymbol{\varepsilon}^{*\ \text{nilpotent}} = -\boldsymbol{S} : \boldsymbol{\sigma}^*, \tag{4.2}$$

where $\boldsymbol{S}$ is the compliance tensor. (Elements of the demonstration had previously been published in Furuhashi and Mura, 1979.) Because total strains are compatible and because the decomposition is unique, we conclude from the additive decomposition of strains for small strains,

$$\boldsymbol{\varepsilon} = \boldsymbol{\varepsilon}^{el} + \boldsymbol{\varepsilon}^*, \tag{4.3}$$

that

$$\boldsymbol{\varepsilon}^{*\ \text{impotent}} = \boldsymbol{\varepsilon} \tag{4.4}$$

and

$$\boldsymbol{\varepsilon}^{*\ \text{nilpotent}} = -\boldsymbol{\varepsilon}^{el}. \tag{4.5}$$

4.2 Illustrating the decomposition of eigenstrains

To illustrate this decomposition, consider the special case of a uniformly shot peened plate. It is assumed that the plate is initially eigenstrain-free, and that out-of-plane displacements are small compared to the thickness of the plates so that the theory of linear elasticity can be applied. Adopting the standard kinematic assumption that material lines perpendicular to the undeformed midsurface of a moderately thick plate remain straight during deformation, total strains are given by

$$\varepsilon_{ii} = a_i z + b_i, \qquad i = \{x, y\}. \tag{4.6}$$

Furthermore, elastic strains are related to residual stresses through Hook's law as

$$\varepsilon_{xx}^{el} = (\sigma_{xx} - \nu\sigma_{yy})/E, \qquad \varepsilon_{yy}^{el} = (\sigma_{yy} - \nu\sigma_{xx})/E. \tag{4.7}$$

Combining (4.1), (4.6), and (4.7), the eigenstrains can therefore be expressed as

$$\varepsilon_{xx}^{*} = (a_x z + b_x) - (\sigma_{xx} - \nu\sigma_{yy})/E, \qquad \varepsilon_{yy}^{*} = (a_y z + b_y) - (\sigma_{yy} - \nu\sigma_{xx})/E. \tag{4.8}$$

These equations indicate that, for a given eigenstrain profile, the impotent part is simply the line that best fits the profile. Indeed, minimizing the squared error between the eigenstrain profile and the line of slope p and y-intercept q,

$$f(p, q) = \left\| \varepsilon_{ii}^{*}(z) - (pz + q) \right\|_2^2, \tag{4.9}$$

yields

$$\begin{aligned} \frac{\partial f}{\partial p} = 0 \quad &\Longrightarrow \quad \beta_i - ph^3/3 - qh^2/2 = 0, \\ \frac{\partial f}{\partial q} = 0 \quad &\Longrightarrow \quad \alpha_i - qh^2/2 - qh = 0, \end{aligned} \tag{4.10}$$

where

$$\alpha_i = \int_0^h \varepsilon_{ii}^{*}(z)\,\mathrm{d}z, \qquad \beta_i = \int_0^h \varepsilon_{ii}^{*}(z)\,z\,\mathrm{d}z, \tag{4.11}$$

and where h is the thickness of the plate. Solving the system (4.10) for α_i and β_i, we obtain

$$p = (12\beta_i - 6\alpha_i h)/h^3, \qquad q = (4\alpha_i h - 6\beta_i)/h^2. \tag{4.12}$$

Since residual stresses satisfy forces and moment equilibrium,

$$\int_0^h \sigma_{ii}(z)\,\mathrm{d}z = 0, \qquad \int_0^h \sigma_{ii}(z)\,z\,\mathrm{d}z = 0. \tag{4.13}$$

Therefore,

$$\alpha_i = \int_0^h (a_i z + b_i)\,\mathrm{d}z = a_i h^2/2 + b_i h, \qquad \beta_i = \int_0^h (a_i z + b_i)\,z\,\mathrm{d}z = a_i h^3/3 + b_i h^2/2. \tag{4.14}$$

Finally, substituting (4.14) in (4.12) yields

$$p = a_i, \qquad q = b_i. \tag{4.15}$$

Note that, since total strains vary linearly through the thickness, finding the best fitting line through the eigenstrains amounts to projecting the eigenstrains on the subspace of nilpotent eigenstrains using the l_2-norm. Once the impotent eigenstrains have been computed, subtracting them from the eigenstrains yields the nilpotent part.

Figures 4.2a–b illustrate this decomposition for a typical distribution of equibiaxial eigenstrains in a uniformly shot peened plate. In figure 4.2b, the residual stresses were computed from the strains with

$$\sigma_{xx} = \frac{E}{1-\nu^2}\left(\varepsilon^{el}_{xx} + \nu\varepsilon^{el}_{yy}\right), \qquad \sigma_{yy} = \frac{E}{1-\nu^2}\left(\varepsilon^{el}_{yy} + \nu\varepsilon^{el}_{xx}\right), \tag{4.16}$$

the inverse of equation (4.7). To further illustrate the decomposition, figure 4.2c shows a geometric construction where a plate in which each of the eigenstrain distributions is present is cut into infinitesimally thin layers parallel to the surface of the plate. Because, in the limit of infinitesimally thin layers, eigenstrains vary linearly through the thickness, the eigenstrains in each layer are impotent. In this virtual configuration, each layer is therefore stress-free. The length of a layer located at a depth z is $(\varepsilon^*_{ii}(z) + 1)\ L_0$, where L_0 is the initial eigenstrain-free length, and its curvature is $-a_i = -d\varepsilon^*_{ii}(z)/dz$. If the strains from one layer to the next are compatible (fig. 4.2, middle), the layers can be glued back together without stretching or compressing any of them. Consequently, the structure remains stress-free. Otherwise (fig. 4.2 left and right), gluing the layers back together requires stretching some and compressing other, which induces residual stresses.

That an eigenstrain field can be uniquely decomposed into its impotent and nilpotent parts means that the source of residual stresses can be separated from that of distortions. This also means that, in the general case (see counterexamples below), both elastic strain and total strain measurements, or related quantities such as residual stress and curvature, are required to identify an eigenstrain field. Elastic strains can be measured *locally* using appropriate experimental techniques without needing to know anything about the processing history of the part. On the other hand, measuring total strains requires that a reference eigenstrain-free configuration is available and that the displacements caused by the introduction of the eigenstrains can be tracked.

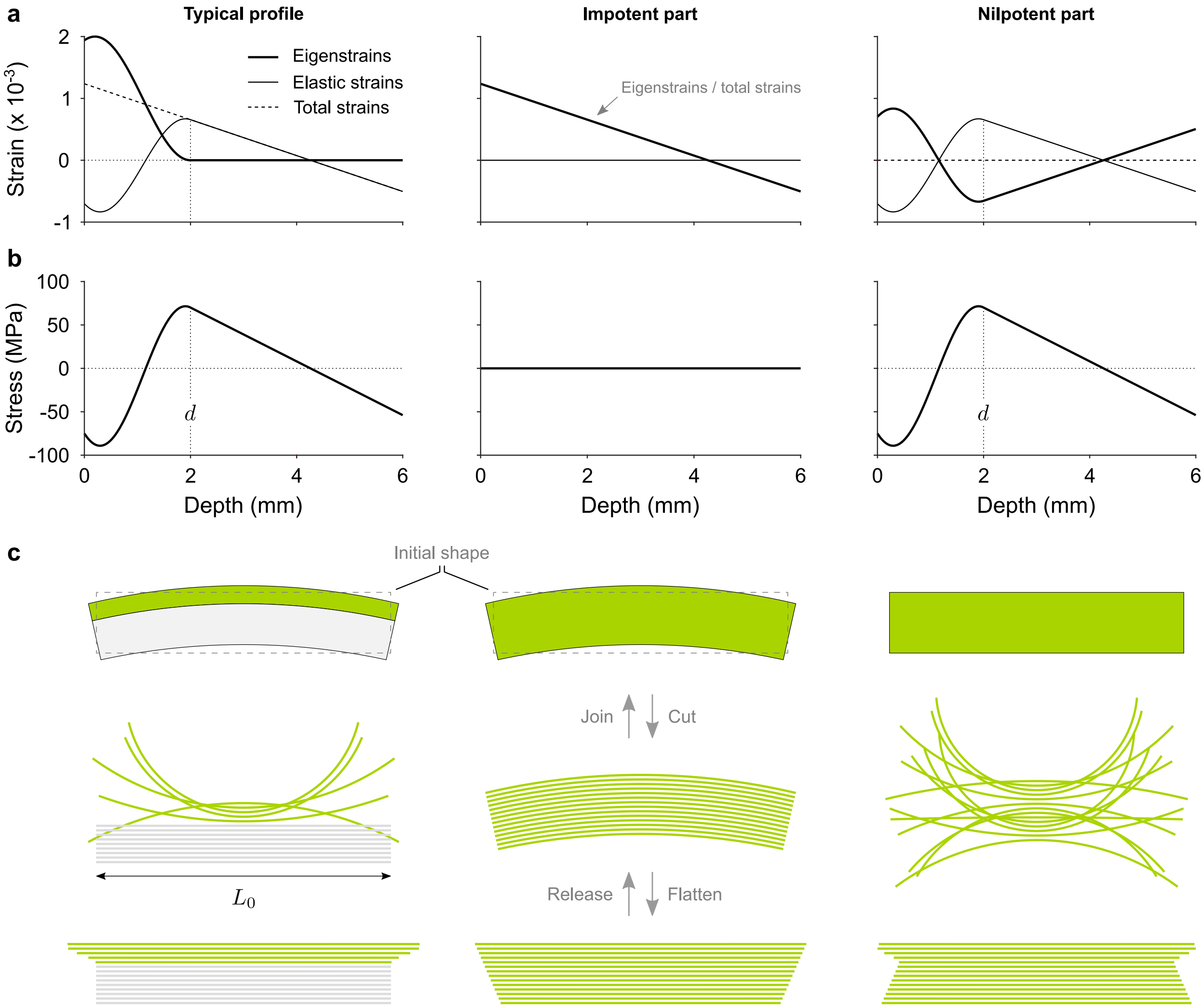

Figure 4.2 Schematic illustration of the decomposition of eigenstrains into an impotent and a nilpotent part for a uniformly shot peened plate. (a–b) In-plane strains and residual stresses in a 6 mm thick unconstrained aluminum plate (E = 71500 MPa; ν = 0.33) for a typical distribution of peening induced eigenstrains, its impotent part, and its nilpotent part. (c) If the plate were cut into infinitesimally thin layers, the deformed length of a layer located at depth z would be $(\varepsilon^*(z) + 1)\ L_0$, where ε^* is the in-plane eigenstrains and L_0 is the length of the layer where no eigenstrains are present. In this virtual configuration, all layers are stress-free. Unless the strains from one layer to next are compatible (middle), joining the layers back together requires stretching some and compressing others, which induces residual stresses. If the eigenstrains are self-equilibrated (right), the deformed configuration is the same as the initial stress-free configuration, here shown as dotted lines.

4.3 Procedures to identify peening induced eigenstrains

4.3.1 Using residual stress and strain data (exact solution)

When performing shot peening experiments, one way to characterize total strains is to attach a strain gauge to the bottom face of an unpeened plate and to measure the strains and curvatures induced by peening since

$$a_i = -\kappa_i, \quad \text{and} \quad b_i = \varepsilon_{ii}|_{z=h} + \kappa_i h, \tag{4.17}$$

where κ_i is the curvature of the peened plate in the i direction and $\varepsilon_{ii}|_{z=h}$ are total strains measured on the bottom face of the plate in the same direction. Elastic strains can then be evaluated with any appropriate technique such as hole drilling or X-ray diffraction and subtracted from the total strains to obtain the eigenstrains.

4.3.2 Using residual stress data only

In a few special cases, it is possible to identify peening induced eigenstrains from residual stress data only.

Thick specimens

First, consider the case of specimens much thicker than the depth of the peening affected layer. The thicker the specimen, the lower its curvatures an in-plane stretch. In the limiting case of a half space, curvatures and in-plane stretch are zero and equations (4.3) reduce to

$$\varepsilon^*_{ii} = -\varepsilon_{ii}. \tag{4.18}$$

In practice, this approximation is valid if the thickness of the peened part is much larger than the depth of the peening affected layer. More precisely, combining (4.12) and (4.15), it can be seen that

$$a_i = \left(12\beta_i - 6\alpha_i h\right)/h^3, \qquad b_i = \left(4\alpha_i h - 6\beta_i\right)/h^2. \tag{4.19}$$

Consequently, (4.18) is valid if

$$a_i \ll 1,\ b_i \ll 1 \quad \Longrightarrow \quad \alpha_i/h \ll 1,\ \beta_i/h^2 \ll 1. \tag{4.20}$$

Thin specimens

When conditions (4.20) do not hold—as is usually the case for thin peen formed plates—the contribution of total strains cannot be neglected. If residual stresses are measured deeper than the peening affected layer, then total strains be estimated from residual stress data only. Indeed, outside of the peening affected layer, peening induced eigenstrains are zero and equations (4.8) become

$$\varepsilon_{ii}^{el} = \varepsilon_{ii} = a_i z + b_i. \tag{4.21}$$

In practice, the depth of the plastically deformed layer can be estimated from the location of the tensile residual stress peak, as shown in figure 4.2a, and the a_i and b_i are obtained by fitting a line through the elastic strains past that point. Finally, elastic strains are substituted from the line to obtain the eigenstrains. This approach was used in Korsunsky (2006) and Zhang et al. (2008).

Similar results can be obtained by using Korsunsky's inverse identification procedure with candidate eigenstrains of the form

$$\varepsilon_{xx}^{*}(z) = \sum_{i=1}^{n} p_i \xi_i(z), \quad \varepsilon_{yy}^{*}(z) = \sum_{i=1}^{n} q_i \xi_i(z), \quad \xi_i(z) = 0 \quad \text{if } z > \hat{d}, \tag{4.22}$$

where $\hat{d}$ is an estimate the depth of the plastically deformed layer. Choosing basis functions that are zero for $z > \hat{d}$ amounts to assuming that no eigenstrains are present in the bulk, or that their magnitude is small enough so that they can be neglected. This also constrains total strains to balance out elastic strains over $z > \hat{d}$, thus setting the a_i and b_i. This approach was used in Korsunsky (2006). When dealing with shallow residual stress profiles such as those obtained by the hole drilling method, we found it be more robust than the one in the previous paragraph as it automatically fits the data, deals with experimental errors, and returns statically admissible residual stress profiles.

4.4 Accounting for initial eigenstrains

The procedures presented in section 4.3 enable to extract peening induced eigenstrains from limited elastic strain or residual stress measurements. However, for them to apply, specimens used for the identification must be initially eigenstrain-free. For most metals, initial strain incompatibilities can be relieved by annealing. For others, annealing is not an option as the temperatures required to activate relaxation mechanisms would trigger microstructural changes such as the precipitation of alloying elements in heat treatable aluminum alloys.

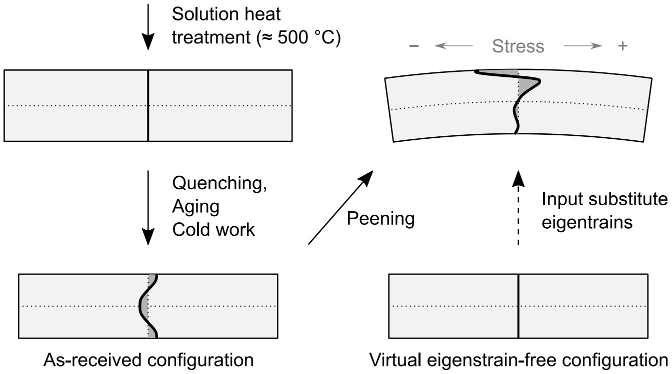

Figure 4.3 Schematic illustration of residual stresses at different stages of the manufacturing process of a heat treatable aluminum alloy plate. Starting from a solution heat treated state, the plate is quenched, aged, and cold worked, which induces symmetric residual stresses. Unless the strain incompatibilities that give rise to these stresses can be relieved—for example by annealing—the end-user has no access to an initially eigenstrain-free configuration, thus cannot use the procedures described in section 4.3. For simulation purposes, however, it is still possible to identify substitute eigenstrains that, when input into a model of the as-received plate, yield the same residual stresses and deformation as those measured from the as-received configuration.

Consider the heat treatable aluminum alloy plate shown schematically in figure 4.3. Starting from a solution heat treated state where (macroscopic) strain incompatibilities due to earlier processing stages have been released (Robinson et al., 2014), the plate is quenched, aged, and cold worked. Although cold work and stress relief treatments do partially relieve some of the strain incompatibilities induced by quenching, they do not completely erase them. Finally, the plate is peened uniformly over one face. Since no eigenstrain-free configuration is readily available to the end-user of the plate, the previously mentioned identification procedures do not apply—although they could provide close estimates of peening-induced eigenstrains. At best, only 'substitute' profiles that, when input into a model of the as-received plate, yield the same residual stresses and distortions as those measured from the as-received can be sought (fig. 4.3, right). These profiles can then be used as loads in simulations to estimate residual stresses and distortions in larger plates, even when the latter deform into the geometric nonlinear domain, provided that they are made of the *same* material and peened in the *same* conditions as the plates used for the identification.

One way to construct such substitute profiles is as follows. Suppose that a specimen was shot peened, that total strains with respect to the as-received configuration were characterized, and that elastic strains were measured up to a depth z_{max}. From these data, the procedure described in section 4.3.1 can be used to compute profiles $\check{\varepsilon}^*_{ii}(z)$, where the 'check' is used to indicate that these profiles are not the true eigenstrains. These profiles can then be extended with any function such that the resulting profiles, $\hat{\varepsilon}^*_{ii}(z)$, induce the same total strains as those that were measured. By construction, these profiles induce not only the desired deformations, but also the desired residual stresses up to $z = z_{max}$. One possible form for the substitute profiles is

$$\hat{\varepsilon}^*_{ii}(z) = \begin{cases} \check{\varepsilon}^*_{ii}(z) & \text{if } z \leq z_{max}, \\ \theta_i^{top} & \text{if } z_{max} < z \leq (z_{max} + h)/2, \\ \theta_i^{btm} & \text{if } (z_{max} + h)/2 < z \leq h, \end{cases} , \tag{4.23}$$

where the θ_i^{top} and θ_i^{btm} are adjustable constants. (Using two constants per direction enables to independently control the amount of stretching and bending induced by the profiles.) An explicit expression for the constants is (see chapter 6 for details)

$$\begin{aligned} \theta_i^{\text{top}} &= [(\alpha_i - \check{\alpha}_i)(3h + z_{max}) - 4(\beta_i - \check{\beta}_i)]/(h - z_{max})^2, \\ \theta_i^{\text{btm}} &= -[(\alpha_i - \check{\alpha}_i)(3z_{max} + h) - 4(\beta_i - \check{\beta}_i)]/(h - z_{max})^2, \end{aligned} \tag{4.24}$$

where

$$\check{\alpha}_i = \int_0^{z_{max}} \check{\varepsilon}^*_{ii}(z)\,\mathrm{d}z \qquad \text{and} \qquad \check{\beta}_i = \int_0^{z_{max}} \check{\varepsilon}^*_{ii}(z)\,z\,\mathrm{d}z. \tag{4.25}$$

In (4.24), all quantities to the right of the equal signs are known quantities. In particular, the α_i and β_i are related to measured axial strains and curvatures through (4.14) and (4.17).

The top row of figure 4.4 shows examples of substitute eigenstrains profiles computed with this procedure when z_{max} is equal to h, less than h, and zero. Data needed to construct the profiles were generated by performing a virtual experiment where known equibiaxial eigenstrains, shown as dotted lines on the figure, were induced in a model of a 6 mm thick aluminum plate. Strain and residual stress data similar to those that could have been measured experimentally were computed from the known eigenstrains using equations (4.14), (4.16), and (4.17). By construction, all substitute eigenstrain profiles induce the correct deformations. The bottom row of figure 4.4 shows the residual stresses derived from the eigenstrains. In figure 4.4a, they match the actual stresses everywhere. In figure 4.4b, they only match the actual stresses over $z \leq z_{max}$. In figure 4.4c, the substitute eigenstrains have been idealized to such an extent that the reconstructed stresses provides no information about the actual stresses. In this latter case—which is of practical interest for peen forming simulations as such simulations, while aiming to accurately predict deformations, are seldom concerned with residual stresses—equations (4.24) reduce to

$$\theta_i^{\text{top}} = (3\alpha_i h - 4\beta_i)/h^2 = a_i h/6 + b_i, \qquad \theta_i^{\text{btm}} = (4\beta_i - \alpha_i h)/h^2 = 5a_i h/6 + b_i. \tag{4.26}$$

4.5 Summary

In this chapter, we introduced the concept of nilpotent eigenstrains (that induce no deformations) and impotent eigenstrains (that induce no stress). Using the proof by Nyashin et al. (2005) that any eigenstrain field can be uniquely decomposed into a nilpotent and an impotent part, we discussed why, in general, both residual stress and total strain measurements are required to uniquely identify the eigenstrains present in a specimen. For uniformly shot peened plates, closed form solutions are available that relate eigenstrains, total strains, and residual stresses. If an initially eigenstrain-free specimen is peened and if the depth of the peening affected layer can be estimated, we showed that these relations enable to identify the eigenstrains from residual stress data only. Finally, we showed that, even when the true eigenstrains cannot be identified, it is still possible to construct substitute eigenstrains that, when input into a model of a peened part, induce at least the correct deformations. Peen forming simulations presented in the next chapters are based on these ideas.

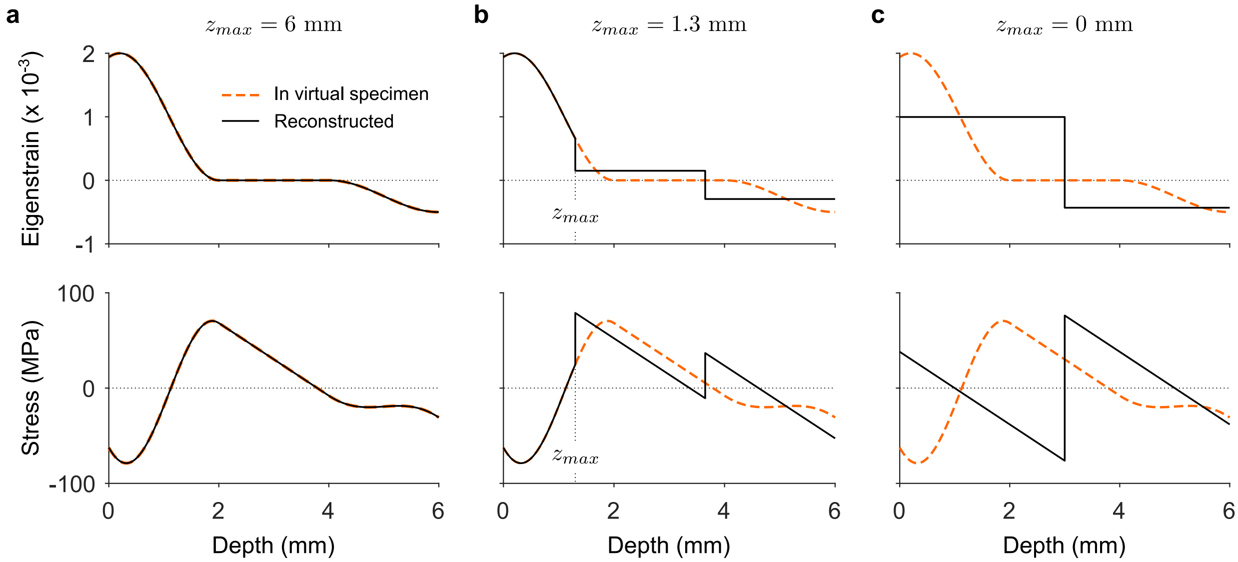

Figure 4.4 Examples of substitute eigenstrain profiles and the residual stresses they induce. A virtual experiment was conducted where the equibiaxial eigenstrains shown as dotted lines were input into a model of a 6 mm thick aluminum plate ($E = 71500$ MPa, $nu = 0.33$). Residual stress and strain data similar to those that could have been obtained experimentally were extracted from the model then used to construct the substitute profiles. All substitute profiles induce the same deformations. Whereas the profile in (a) matches the actual residual stresses everywhere, the profile in (b) only matches them over $z \leq z_{max}$, and the profile in (c) had been idealized to such an extent that it provides no information about residual stresses.

CHAPTER 5 ARTICLE 1: PEEN FORMING AND STRESS PEEN FORMING OF 2024–T3 ALUMINUM SHEETS (PART 1); 3D SCANS AND RESIDUAL STRESS MEASUREMENTS

Pierre A. Faucheux, Frédérick P. Gosselin, Martin Lévesque

Submitted to the Journal of Materials Processing Technology on November 27th 2019

Abstract

Aluminum skins on the lower wings of most commercial aircraft are shaped using shot peen forming. This process, which involves bombarding the skins with hard shot, uses local plastic flow to induce curvatures in the same way that differential expansion makes metal bilayers bend when heated. Here, we investigate experimentally how constraint conditions affect the final shape of peen formed parts. We report peen forming experiments for 4.9 mm *thick rectangular 2024–T3 aluminum sheets of different aspect ratios uniformly shot peened on one face with a low intensity saturation treatment. Some specimens were free to deform during peening while others were elastically prestressed in a four-point bending jig. For each aspect ratio and prestress condition, peening-induced residual stresses were measured in one specimen with the hole drilling method. Additional residual profiles obtained with the slitting method are also presented. Our results show that the progressive deformation of unconstrained specimens amounted to prestress. For the peening conditions investigated, this progressive deformation caused unconstrained strips to exhibit curvatures* 33 % *larger than identical strips held flat during peening. Furthermore, we found that a competition between material anisotropy and geometric effects did determine the direction along which the specimens preferentially bent.*

5.1 Introduction

Shot peen forming distinguishes itself from other metal forming treatments such as press forming, stretch forming, or creep forming by its versatility and low operating costs. It is a dieless process that consists in bombarding metal parts with hard shot to plastically deform a thin layer of material. As it flows, this layer stretches the rest of the structure, which induces curvatures and residual stresses as shown schematically in figure 5.1a and c. By tuning the peening treatment, a skilled operator can perform many operations with the same equipment, ranging from forming large wing-skin panels (Baughman, 1970; Levers, 2010) to correcting small out-of-tolerance distortions on machined parts (Skinner, 1978).

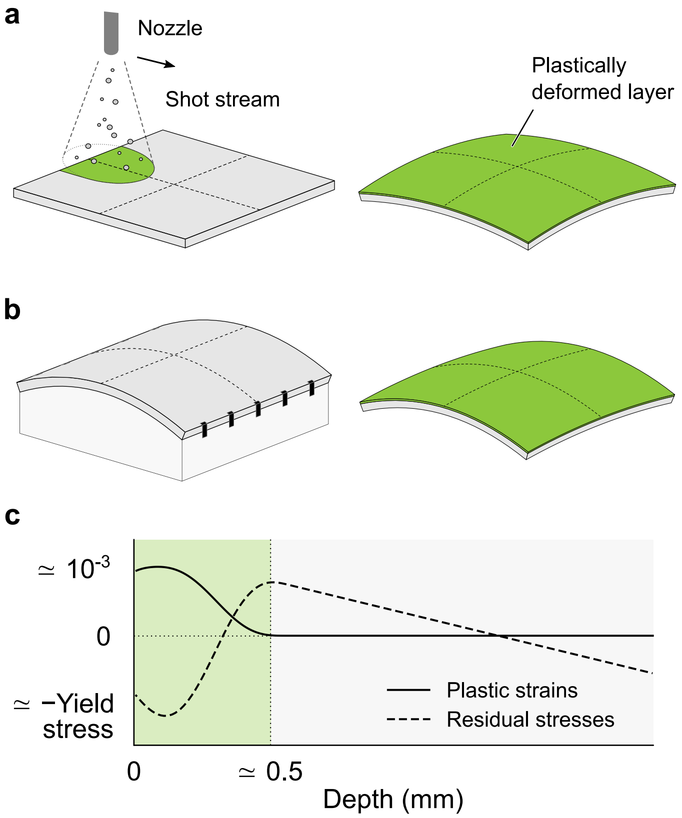

Figure 5.1 Peen forming of a metal plate. Repeated impacts plastically deform a thin layer of material which, as it stretches, causes the plate to stretch and bend. (a) Plates peened with low intensity treatments, thick plates, and plates with high aspect ratios tend to deform into spherical shapes. (b) Prebending a plate during peening results in larger curvatures along the prestress direction and smaller curvatures along the transverse direction. (c) Typical in-plane plastic strain and residual stress profiles after uniform peening. The in-plane expansion of the upper layers is resisted by the bulk, which causes compressive residual stresses near the surface. Conversely, the upper layers stretch the bulk which causes tensile stresses deeper into the material. In the bulk, stresses vary linearly owing to the stretching and bending of the specimen.

Because peening treatments stretch the material in all directions, peen formed parts tend to deform into spherical shapes, as illustrated in figure 5.1a. To break this symmetry, process engineers use jigs to hold the parts into a bent shape while they are being peened. This technique, called stress peen forming, not only induces larger curvatures along the prebending direction, but also smaller curvatures along the transverse direction, as illustrated in figure 5.1b. Theses curvatures were repeatedly observed to be proportional to the prestress curvature, with typical proportionality coefficients being listed in table 5.2.

While a large body of work dealt with residual stresses, roughness, and changes in microstructure induced by shot peening (see for example Gariépy (2012) for an overview), comparatively fewer papers considered shot peen forming in the English-speaking literature. In tables 5.2 and 5.3, we review papers featuring conventional and stress peen forming experimental results for uniformly peened rectangular plates. Most of these studies aimed at generating data to establish process parameters for a given application. These include Kulkarni et al. (1981), Miao et al. (2010), Villalva-Braga (2011), and Zhang et al. (2019), all dealing with 2024 and 7050 aluminum alloys. Other studies focused on specific aspects of the peen forming process: Johnson et al. (1981) investigated the differences in the shape of deflection versus peening time curves for aluminum, steel, and copper strips; Barrett and Todd (1984) observed how prestressing did affect the distribution of residual stresses in thick aluminum plates; Skinner (1978) demonstrated how stress peen forming could correct distortions on machined parts.

Of all the papers listed in tables 5.2 and 5.3, only three reported residual stress measurements in more than one direction, and only half reported curvature measurements in more than one direction. Rolled aluminum sheets, however, which account for most of peen formed parts, are known to exhibit anisotropic plasticity (Bron and Besson, 2004). Other sources of anisotropy that might affect the shape of peen formed parts include initial residual stresses (i.e., stresses resulting from earlier processing stages such as rolling) and prestress, whether externally applied with a jig (fig. 5.1b) or resulting from the progressive deformation of an unconstrained part (fig. 5.1a). Although these two effects were suspected to account for most of the discrepancies between previously reported numerical simulations of the process and experimental results (see Gariépy et al. (2013b) and Faucheux et al. (2018)), this could not be confirmed at the time due to lack of data.

In this paper, we investigate experimentally the effect of material anisotropy and prestress on the final deformed shape of uniformly peened aluminum sheets. We present the results of (i) conventional peen forming experiments on 4.9 mm thick and 1016 mm long 2024–T3 aluminum alloy rectangular sheets of different aspect ratios and (ii) stress peen forming experiments on 508 × 127 mm strips of the same alloy. All specimens were cut from sheets

Table 5.1 Mean static properties of 4.9 mm thick aluminum alloy 2024–T3 sheets. The reported values were averaged over three tests.

Angle w.r.t. to rolling direction (°)	Young's modulus (GPa)	Yield stress at 0.2 % (MPa)	Ultimate tensile stress (MPa)	Elongation at fracture (mm/mm)
0	71.5 ± 1.6	381 ± 0	486 ± 1	0.1836 ± 0.0070
45	71.6 ± 3.0	349 ± 1	485 ± 0	0.1920 ± 0.0145
90	71.7 ± 1.5	339 ± 1	489 ± 0	0.1946 ± 0.0058

Mean ± 95 % confidence interval

of the same lot. We probed the influence of the alignment of the specimens with respect to the rolling direction, that of their aspect ratio, and, to a lesser extent, that of the peening trajectory on curvatures and residual stresses.

5.2 Materials and methods

Material All tests were conducted on 4.9 mm thick Kaiser Stretched aluminum alloy 2024–T3 sheets purchased from Kaiser Aluminum. The sheets had been stress relieved by stretching. Metallographic specimens etched with Keller's reagent revealed large elongated grains of mean aspect ratio 7.1 : 3.6 : 1.0 along the longitudinal (L), long transverse (T), and short transverse (S) directions, respectively. Grains had an average length of 0.268 mm. The largest observed grain length was of 4.7 mm. Static properties were obtained from tensile tests performed at 0°, 45°, and 90° from the rolling direction, as per ASTM standard B557M-15 (2015). Three specimens were cut along each direction from the same sheet (the consistency of properties from one sheet to the next was not assessed). Table 5.1 lists the measured static properties along each direction. The observed elastic isotropy and mild plastic anisotropy are consistent with other experimental data from the literature (Bron and Besson, 2004; Seidt and Gilat, 2013).

Peening setup All specimens were shot peened in the Canablast compressed-air cabinet shown in figure 5.2a. The peening cell was equipped with a 6-axis robotic arm for accurate positioning of the nozzle (M–20*i*A supplied by Fanuc), with a particle velocity sensor to measure the average shot velocity (Shotmeter G3 supplied by Progressive Technologies), and with a GoPro digital camera to record the tests. Shot were recycled. Torn and broken shot were removed by separator screens (fig 5.2a 5).

Strips used for stress peen forming tests were prestressed in the four-point bending jig shown

Table 5.2 Compilation of publicly available papers and reports featuring stress peen forming experimental results for uniformly peened rectangular plates. Not included are several conference papers that were not readily available and papers written in languages that none of the authors were familiar with. This includes some possibly highly relevant studies in the German, Chinese, and Japanese-speaking literature. Brackets indicate ranges.

Reference	Material	Dimensions			Peening treatment[a]				Increment in curvature per unit increment in prestress curvature		Reported results		Notes
		Length (mm)	Width (mm)	Thickness (mm)	Media[b]	Coverage[c] (%)	Intensity[d] ($\times 10^{-3}$ in)	Prestress radius of curvature (mm)	Along prestress direction (-)	Along transverse direction (-)	Deformed shape	Residual stress[e]	
Barrett and Todd (1984)	7075–T7651 Al.	762	508	17.3	Saturation: 0.6 mm steel Forming: 3.2 mm steel	Saturation: 100 Forming: between 60 and 80	Saturation: $\simeq$ 6 A Forming: -	1700 (along short side)	-	-	-	Profiles, some in both directions (XRD)	[q]
Hu et al. (2015)	2024–T351 Al.	67	67	4	Laser peening	-	-	∞, 2000, 1000, 667	0.44	0.14	Curvature along both directions; Some 3D scans	Surface stress (XRD)	[r]
Li (1981)	LY12CZ Al.	76	76	2	$[2, 2.5]$ mm iron	100	-	∞, 5000, 1000, 500, 250	0.60[f]	-0.06[f]	Arc height	-	[p]
Miao et al. (2010), Miao et al. (2011)	2024–T3 Al.	76 76	19 76	1.6 1.6	Z425	100	5, 7.4, 8.7 A	∞, 720, 360, 240	$[0.41, 0.65]$ $[0.40, 0.65]$	- $[-0.08, -0.17]$	Arc height (in both directions for square specimens); some line scans	Profiles along prestress direction (XRD)	[r] [s]
Skinner (1978)	7075–T7651 Al.	305	44	6.35	Saturation: S230 Forming: 3/16" ball bearings	Saturation: 100 Forming: 20, 40, 60, 80	Saturation: 6 A Forming: 10, 12, 15 C	∞, 1950, 825, 625	-	-	-	Profiles along prestress direction (layer removal)	-
Villalva-Braga (2011)	7050–T7451 Al.	400	50	2, 5, 10, 15	S230, S550, 1/8"	From 60 to 200	-	1270, 850, 420, 170[g]	-	-	Curvature along prestress direction	Profiles along prestress direction (XRD)	[q]
Wang et al. (2014)	7150 Al.	300	200	8, 10, 12	3.18 mm	From $\simeq$ 50 to 100	-	810, 680, 540	-	-	Curvature along prestress direction	-	
Xiao et al. (2016)	2024–T351 Al.	100	30	5	Brinell indenter (3.175 mm diam.) 3.175 mm steel	Variable 22, 35, 46	- -	∞, 1252, 626	$[0.27, 0.46]$[h] $[0.44, 0.50]$[h]	$[-0.21, -0.12]$[h] $[-0.27, -0.23]$[h]	Curvature along both directions	-	[r]
Zhang et al. (2019)	2024–T351 Al.	120	50	1.5 2.0 2.5 3.0 3.5	Ultrasonic peening (indenter 3 mm in diam.)	-	-	∞, 1200, 1000, 800, 600, 400	0.63[i] 0.48[i] 0.38[i] 0.33[i] 0.33[i]	-0.05[i] -0.05[i] -0.05[i] -0.08[i] -0.07[i]	Curvature along both directions	-	-
Present study	2024–T3 Al.	508	127	4.9	SCCW28	100	12 A	∞, 3704, 1961, 1205, 952	$[0.22, 0.23]$	$[-0.03, -0.13]$	Curvature along both directions	Profiles in both directions (hole drilling)	[q] [s]

[a] Process parameters such as air pressure, mass flow, and exposure time are usually available when intensity or coverage are not reported.
[b] Conventional designation or diameter.
[c] As defined in SAE standard J2277 (2013), unless otherwise specified.
[d] Almen intensity, as defined in SAE standard J443 (2010), unless otherwise specified.
[e] XRD stands for X-ray diffraction.
[f] Estimated from table 1 of Li (1981). The curves deviate from linearity for prestress radii of curvature larger than 4000 mm.
[g] Computed from beam bending theory as $hE/2\sigma$, where h is the thickness of the plate, E is Young's modulus, and σ is 90 % of the yield stress.
[h] Estimated from figure 21 of Xiao et al. (2016).
[i] Estimated from figure 11 of Zhang et al. (2019).
[p] Large dispersion in results.
[q] Results on unconstrained strips also available.
[r] Features finite element impacts simulations.
[s] Half the specimens was cut with the long side aligned with the rolling direction while the other half was cut with the long side aligned with the transverse direction.

Table 5.3 Compilation of publicly available papers and reports featuring shot peen forming experimental results for uniformly peened rectangular plates. Not included are several conference papers that were not readily available and papers written in languages that none of the authors were familiar with. This includes some possibly highly relevant studies in the German, Chinese, and Japanese-speaking literature.

Reference	Material	Dimensions			Peening treatment[a]					Reported results	
		Length (mm)	Width (mm)	Thickness (mm)	Media[b]	Coverage[c] (%)	Intensity[d] ($\times 10^{-3}$ in)	Shot speed (m/s)	Specimens constrained during peening	Deformed shape	Residual stress[e]
Cao et al. (1995)	SAE 1070 steel	75	19	1.29	Similar to S110	Variable	8 A	45	Yes	Curvature in both directions; one line scan	Profiles in both directions (XRD)
Cina et al. (1990)	2024–T62 Al. 7075–T76 Al.	360	130	4.5 4.0	From S230 to S280	100	7 A, 5 C	-	No	Deflection; one line scan	-
Faucheux et al. (2018)	2024–T3(51) Al.	1000 200	1000 50	5, 10, 15 10	S230 1/8” steel S230 1/8” steel	100 80 100 80	16.8 A 22.9 C 16.8 A 22.9 C	-	No	Curvature in both directions; some line scans	Profiles on thick blocks in one direction (XRD)
Gariépy et al. (2013b)	2024–T3 Al.	76	19	1.6	Z425	Variable	-	34, 52	Yes	Arc height; curvature in both directions	Initial stress profiles in both directions (XRD)
Gelineau (2018)[f]	Inconel 718	75	19	5.0, 2.0	S130	125 200	5.1 A 9.1 A	≃ 42	Yes	3D scans, some line scans	Profiles in both directions (XRD)
Johnson et al. (1981)	HE 30 Al., mild steel, pure copper	76	25	3.2	S170, S240	Variable	-	-	Yes	Arc height	-
Kulkarni et al. (1981)	2024–T3(51) and 7050–T6(51) Al.	610	152, 305, 610[g]	1.6, 4.6, 12,7	0.6 mm steel 1.0 and 1.7 mm steel	Variable	8, 10, 16 A -	32, 53, 78	No	Curvature in both directions	Typical values (XRD)
Miao et al. (2010), Gariépy et al. (2011)	2024–T3 Al.	76	19, 76	1.6	Z425	Variable	5 A 7.4 A 8.7 A	35 54 66	Yes	Arc height; curvature in both directions for square specimens	Through thickness profiles on specimens and thick blocks along one direction (XRD)
Villalva-Braga (2011)	7050–T7451 and 7475–T7451 Al.	400	50	2 5 5 10 10 15	S230 S230 S550 S550 1/8” steel 1/8” steel	Variable	-	50, 61, 72 50, 61, 72 16, 22, 29 16, 22, 29 13, 17, 19 13, 17, 19	Some specimens	Curvature along long side	Profiles along one direction for some 7050 Al. specimens (XRD)
Present study	2024–T3 Al.	1016	254, 508, 1016	4.9	SCCW28	100	12 A	41	No	3D scans	Profiles in both directions (hole drilling, slitting)

[a] Process parameters such as air pressure, mass flow, and exposure time are usually available when intensity or coverage are not available.
[b] Conventional designation or diameter.
[c] As defined in SAE standard J2277 (2013), unless otherwise specified.
[d] Almen intensity, as defined in SAE standard J443 (2010), unless otherwise specified.
[e] XRD stands for X-ray diffraction.
[f] Also reported are microstructural characterization (including EBSD maps), some initial stress profiles, FWHM of XRD measurements, microhardness measurements, and tests on specimens of complex geometries.
[g] Limited results for specimens of other aspects ratio are available in figure 11 of Kulkarni et al. (1981).

Table 5.4 Peening parameters used to obtain a 12×10^{-3} inches A Almen intensity and 100 % coverage with SCCW28 shot.

Nozzle diameter (mm)	Air pressure (Bars)	Mass flow (kg/s)	Shot speed[†] (m/s)	Stand-off distance (cm)	Offset between strokes (mm)	Peening speed (cm/s)	Number of cycles
12.7	1.72	0.12	41	41	67	15	12

[†] Average speed at the exit of the nozzle.

in figure 5.2b. The spacing between the 4 support beams could be adjusted and several pairs of beams of different heights were used to obtain prestress curvatures ranging from 0 to $10.5 \times 10^{-4}\,\text{mm}^{-1}$ (or, equivalently, radii of curvatures ranging from infinity to 952 mm).

For conventional peen forming tests, the frame shown in figure 5.2c provided a level working surface and stops guaranteed consistent positioning from one specimen to the next. The specimens were free to deform during peening.

Peening treatment High hardness spherically conditioned cut wire steel shot SCCW28 compliant with AMS standard 2431/8B (2007) were used for all treatments. The manufacturer's specification stated a 55–62 HRC hardness and a nominal diameter of 0.71 mm.

The same treatment, representative of low intensity saturation treatments used in the industry, was applied to all specimens. The nominal peening parameters were a 12×10^{-3} inches A Almen intensity and 100 % coverage, which were obtained with the process parameters listed in table 5.4.[1] All peen forming tests were conducted as per AMS standard 2430 rev. T (2015), SAE standard J443 (2010), and SAE standard J2277 (2013). Almen tests ran at the locations indicated by downward pointing triangles in figure 5.2c gave intensities between 11.6 and 12.0×10^{-3} inches A, which substantiates that intensity was uniform over the working surface. Consistency of the process was ensured by performing additional Almen tests at the center of the specimens at the beginning and at the end of each peening day (at most two plates were peened per day). These intensities lied between 11.6 and 11.9×10^{-3} inches A.

---

[1] Alongside shot specifications, Almen intensity and coverage are the two parameters used to characterize peening treatments in the industry. Coverage is the fraction of a surface covered by dents. Intensity is primarily intended as a process control parameter. It is obtained (SAE standard J443, 2010) by (i) peening normalized SAE–1070 spring steel strips mounted on a holding fixture in the same conditions as production parts for increasing amounts of time, (ii) measuring their deflection in a standardized Almen gage, and (iii) plotting the deflection as a function of peening time. From these curves, intensity is defined as the value of the deflection which increases by 10 % when the peening time is doubled.

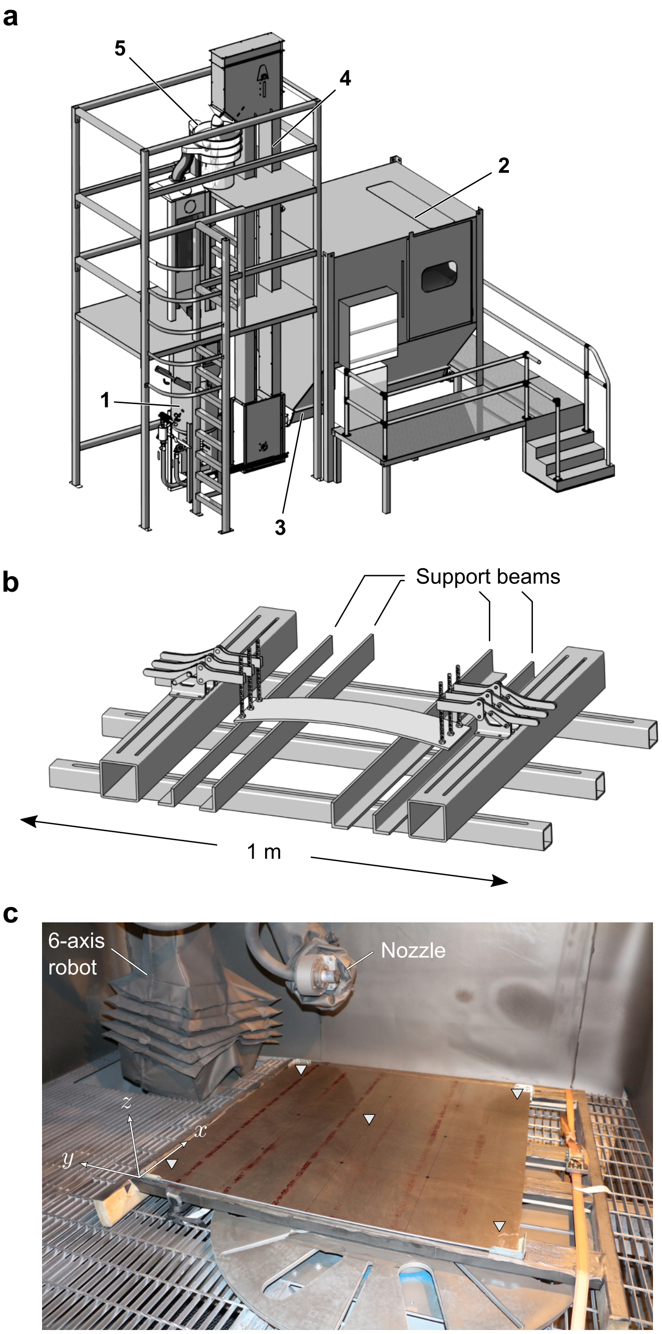

Figure 5.2 Shot peening setup. (a) Compressed air peening cabinet used for peen forming tests. Shot are propelled from a pressurized tank (1) into a closed cabinet (2) where they strike the parts. Used shot are collected at the bottom of the cabinet by an endless screw (3) followed by an elevator bucket (4). They are dropped onto a stack of separator screens (5) that removes broken shot before recycling them into the tank. (b) Four-point bending jig used for stress peen forming tests. The spacing between the 4 support beams could be adjusted. Several pairs of beams of different heights were used to obtain curvatures ranging from 0 to $10.5 \times 10^{-4}\,\mathrm{mm}^{-1}$ (associated radii of curvature: from infinity to 952 mm). (c) Interior of the peening cabinet showing the robotic arm and an unpeened 1016 × 1016 mm sheet resting on a leveled frame. During conventional peen forming tests, the sheets were free to deform. Downward pointing triangles show the locations at which Almen intensity was measured.

Distribution of impacts after one peening stroke The distribution of impacts after one peening stroke was characterized by peening a 508 × 203 mm dummy specimen with the nozzle moving at 22.5 cm/s. At that speed, the impact density was low and there was little overlap between nearby dimples. After peening, high resolution pictures of the surface were taken as the specimen was lit with softened raking lights. The pictures were then stitched together, binarized, and partitioned into bins parallel to the peening direction as shown in figure 5.3a–b. The distribution of impacts was subsequently estimated by counting the fraction of white pixels in each bin. Note that, although the shape of white spots on binarized images was markedly different from that of the dimples, their location was correct and variations in shape from one spot to the next were compensated by the many impacts considered. Figure 5.3c shows the distribution of white pixels as well as a fit of the data with

$$f(x) = A\left(1 - 4\left(\frac{x}{w}\right)^2\right)^{\beta-1},$$

where $A = 4.78$ is the amplitude in % of white pixels, $w = 205$ mm is the width, and $\beta = 6.32$ is an adjustable parameter (obtained by least-squares fitting). Superimposing several of these distributions allows to estimate the uniformity of the number of impacts per unit surface after several parallel overlapping strokes, as shown in figure 5.3d. In this case, we found that the largest spacing between parallel strokes yielding variations smaller than 1 % in the number of impacts per unit surface was 67 mm. This information was used when planning peening trajectories, as discussed below.

Peening trajectories All specimens were peened with a succession of parallel strokes, as shown in figure 5.4. To ensure that the nozzle remained approximatively normal to the peened surface as specimens deformed, the treatment was broken into 12 cycles and the trajectory for cycle $n + 1$ was computed based on the shape of the specimen at the end of cycle n. The latter was estimated by recording the position of target points drawn on the peened surface with a stylus mounted on the head of the 6-axis robot and by fitting a surface of equation

$$w(x, y) = \frac{1}{2}(ax^2 + by^2)$$

through these points, where a and b are adjustable parameters and x and y are as shown in figure 5.2. To achieve uniform coverage, the offset between two successive strokes was set to 67 mm based on the analysis of the distribution of impacts from the previous paragraph. Visual inspection confirmed that coverage was uniform. The peening speed listed in table 5.4 was set so that 100 % coverage was reached after 12 peening cycles. Coverage was

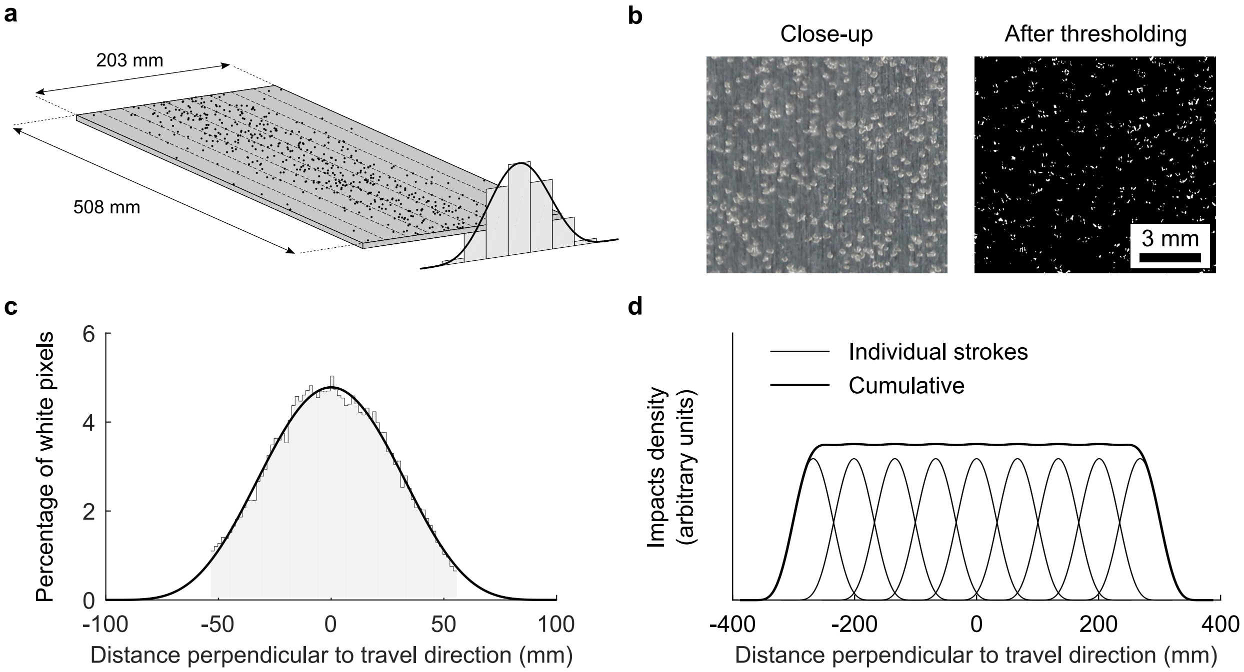

Figure 5.3 The density of impacts after a single straight peening stroke was characterized by (a) peening a dummy specimen, (b) thresholding high resolution pictures of the peened surface such that dimples appeared as white spots, and (c) counting the fraction of white pixels in bins parallel to the peening stroke. (d) The density of impacts after several parallel overlapping strokes was estimated by superimposing several of these distributions. In (d), the distributions for individual strokes are spaced 67 mm apart.

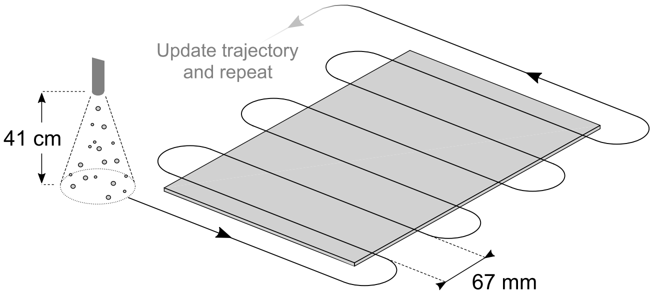

Figure 5.4 Nozzle trajectory for the first peening cycle. The trajectory was updated at the end of each cycle based on the current shape of the part so that the nozzle remained normal to, and at a constant distance from, the surface. Half of the specimens was peened with strokes parallel to the L direction while the other half was peened with strokes parallel to the T direction.

Table 5.5 Specimens used for conventional peen forming experiments.

Specimen ID	Dimensions (mm)		Peening strokes	Residual stress measurements
	Along L	Along T		
Sheet 4:1–L	1016	254	Parallel to L	Hole drilling
Sheet 2:1–L	1016	508		-
Sheet 1:1–L	1016	1016		Hole drilling
Sheet 1:2–L	508	1016		Hole drilling, Slitting
Sheet 1:4–L	254	1016		Hole drilling, (XRD)
Sheet 4:1–T	1016	254	Parallel to T	(XRD)
Sheet 2:1–T	1016	508		Hole drilling
Sheet 1:1–T	1016	1016		(XRD)
Sheet 1:2–T	508	1016		-
Sheet 1:4–T	254	1016		-

estimated as per SAE standard J2277 (2013) from magnified pictures of the peened surface; see supplementary material for details.

Specimens For comparison purposes, we chose specimens similar to those used in Kulkarni et al. (1981) for conventional peen forming tests. The specimens consisted of 10 rectangular sheets of 4:1, 2:1, 1:1, 1:2, and 1:4 aspect ratio, 1016 mm along the long side. Two sheets were peened per aspect ratio. Half of the specimens was peened with strokes parallel to the L direction while the other half was peened with strokes parallel to the T direction. Table 5.5 lists the specimens used for conventional peen forming tests.

For stress peen forming tests, we used 508×127 mm strips and prestress curvatures of 0, 2.7, 5.1, 8.3, and 10.5 × $10^{-4}\,\mathrm{mm}^{-1}$. The strip with zero prestress curvature was held flat during peening. These curvatures induce stresses of 0, 47, 90, 146, and 184 MPa on the upper face of the strips, which is well below the yield stress of the material (see table 5.1). Two strips with their long side aligned the L direction and two strips with their long side aligned with the T direction were peened for each prestress condition, except for the 8.3 × $10^{-4}\,\mathrm{mm}^{-1}$ prestress condition where three strips were used. All strips were peened with strokes parallel to their long side.

3D scans and curvature measurements After peening, all sheets used for conventional peen forming tests were scanned with a coordinate measuring machine (Mitutoyo, Crysta-Apex 163011) equipped with a REVO® 5-axis measurement system. Measurements were taken every 4 mm in continuous scanning mode along several lines parallel to the long and the short directions.

Strips used for stress peen forming tests were scanned along the lines parallel to the long and short directions passing through the center of the specimens (i) before peening while held in the prestressing jig and (ii) after peening after all constraints had been released. Measurements while on the prestressing jig were taken every 25 mm with a stylus mounted on the head of the 6-axis robot. Measurements after peening were taken every 3 mm with an electronic indicator (CDI Chicago, Logic ALG, A2720).

Coupons used for residual stress measurements (see below) were also scanned with an electronic indicator, as described above.

Curvatures were computed as $\kappa = p''/(1+p'^2)^{3/2}$, where p is an eighth-order polynomial fit to the 3D scans along the dotted lines shown in figure 5.1a and where the prime denotes differentiation with respect to the direction along which the curvature is computed. All curvatures reported in the rest of the article are average curvatures over the central 50 % of the scanning lines.

Residual stress measurements The incremental hole drilling method was used to measure residual stresses in

- 254×254 mm coupons removed from some specimens used for conventional peen forming tests (one coupon per aspect ratio; see table 5.5);
- 254 × 127 mm coupons removed from some strips used for stress peen forming tests (one coupon per prestress condition).

The coupons were removed from the center of the sheets with a lubricated jigsaw (except for sheet 1:4–L for which the coupon was removed from the end). Residual stresses were measured at the center of the coupons, far away from the edges, to minimize the effect of cutting induced plastic deformations and heating on measurement. Hill-Engineering, an external laboratory, performed all measurements as per ASTM standard E837-08 (2008). The holes were 2 mm in diameter and were drilled in 0.051 mm increments to a final depth of 1.020 mm. Uncertainty calculations—which are not part of ASTM standard E837-08 (2008)—were similar to those used for slitting measurements (see below).

Due to its higher sensitivity to low residual stress levels (Prime, 1999), the slitting method was used to characterize initial residual stresses on as-rolled sheets. Hill-Engineering performed the measurements on two 51 × 51 mm coupons (one coupon for each direction). A single strain gage located opposite to the cut on the back face of the specimens was used. The slot was incrementally cut by wire electric discharge machining by 0.051 mm to 0.254 mm increments over the first 3.43 mm. Residual stresses were computed as described in Schajer and Prime (2006), with unit pulse basis functions, Tikhonov regularization, and compliances computed from 2D plane-strain finite element simulations. The procedure used for uncertainty analysis is detailed in Prime and Hill (2006).

To validate hole drilling measurements, slitting was also used to obtain additional residual stress profiles for sheet 1:2–L. Two 15.24 × 17.78 mm coupons were removed by electric discharge machining 2.5 cm away from the edges of the coupon used for hole drilling measurements. Such small coupons were needed to ensure that the depth of the slot was approximately constant as slot cut with straight EDM wires into curved specimens are deeper at the center than they are near the edges, as illustrated in figure 5.5. The curvature of the coupons was estimated to 3×10^{-4} mm^{-1}, which gave a variation in the depth of the cut of $\delta \simeq \kappa w^2/8 \simeq 9 \times 10^{-3}$ mm when cutting along the short side, where κ and w are defined as in figure 5.5b. Such variations were a posteriori confirmed to be much smaller than the characteristic length over which residual stresses varied (see figures 5.9 and 5.10a).

X-ray diffraction measurements were attempted on several specimens (table 5.5) but the large grain size and texture of the material prevented obtaining meaningful results. See supplementary material for details.

Additional information Additional details about experimental conditions, videos of the peening treatments, 3D scans of the specimens, and tabulated residual stress profiles are provided as supplementary material.

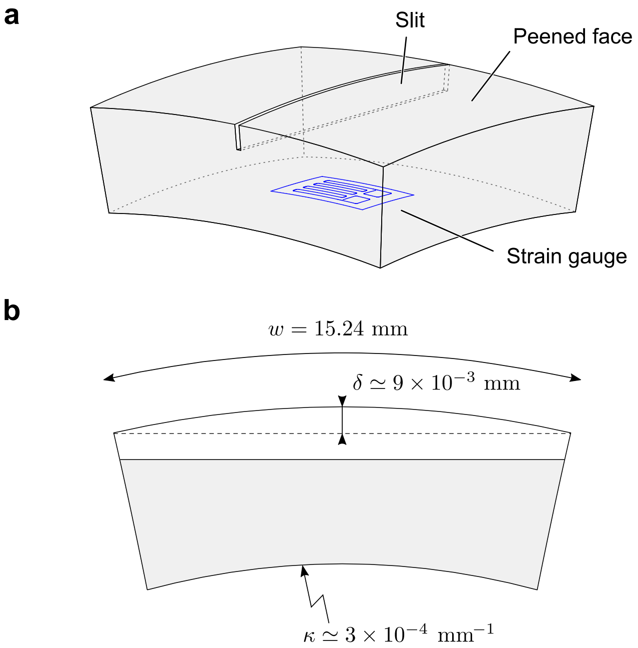

Figure 5.5 Schematic illustration of the specimens used to measure peening-induced residual stresses with the slitting method (curvature amplified for clarity). (a) Strains were measured with a single strain gauge attached to the back face of the specimens as the latter were cut with a straight EDM wire. (b) Since peened specimens are curved, the slot is deeper near the center than it is near the edges. Because slitting returns stresses averaged over the length of the slot, small 15.24×17.78 mm coupons were used so that the variation in the depth of the slot, which was estimated to $\delta \simeq 9 \times 10^{-3}$ mm from the curvature of the coupons, was small compared to the characteristic length over which residual stresses varied (see figures 5.9 and 5.10a).

5.3 Results

5.3.1 Conventional peen forming tests

Figure 5.6 shows the 3D scans of sheets used for conventional peen forming tests and table 5.6 lists their curvatures. We see that

- Sheets of 1:1 aspect ratio deformed into cylinders;
- Sheets of 1:2 and 2:1 aspect ratio assumed distinct nonzero curvature in both directions, with one of the curvatures being approximately one order of magnitude smaller than the other one;
- Sheets of 1:4 and 4:1 assumed elliptical of nearly spherical shapes, with curvatures in all directions having the same order of magnitude;
- All specimens had their largest curvature along the L direction.
- Identical specimens peened with strokes parallel to either the L or the T direction assumed almost identical shapes, with differences in curvatures of less than 7 % between the two sets of sheets;

These results are consistent with Kulkarni et al. (1981) who observed the same shapes for 4.6 mm thick and 610 mm long 2024–T3 and 7050–T6 aluminum specimens of 4:1, 2:1, 1:1, 1:2, and 1:4 aspect ratio peened with 1.7 mm steel shot propelled at 53 m/s (a more intense peening treatment than that used here). Kulkarni's 2024–T3 aluminum specimens, however, had their largest curvature along the T direction.

Figure 5.7 shows the evolution of deflection as a function of peening time for sheets peened with strokes parallel to the T direction. Similar curves were obtained for sheets peened with strokes parallel to the L direction. Most of the forming occurred during the first 2 peening cycles, with diminishing returns for each additional cycle. After 12 cycles, most sheets had reached saturation, except for 1:1 and 2:1 aspect ratio specimens, for which the positive slope suggests that they could have carried on bending.

Figure 5.8 shows initial residual stresses measured by slitting in as-received material. Data were acquired over 70 % of the thickness and the rest of the profiles was reconstructed by assuming symmetry with respect to the sheet's midplane. (Symmetric profiles are expected as both faces of a sheet experience the same sequence of operations during cold rolling; see Prime and Hill (2002) for examples of through-thickness profiles on thick aluminum plates.)

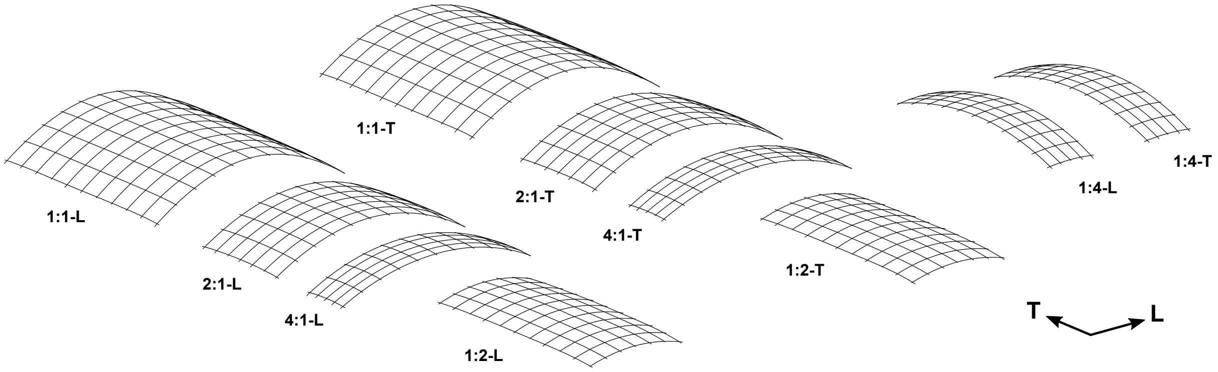

Figure 5.6 3D scans of 4.9 mm thick and 1016 mm long 2024–T3 aluminum alloy rectangular sheets peened to full coverage at a 12×10^{-3} inches A Almen intensity with SCCW28 shot. All specimens, including 1:4 aspect ratio sheets, had their largest curvature along the L direction. Out of plane displacements magnified by a factor of 4.

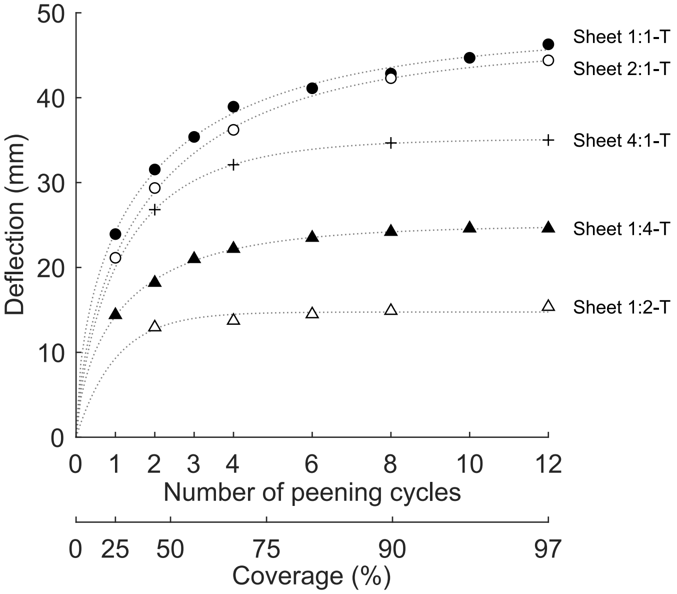

Figure 5.7 Deflection of specimens peened with strokes parallel to the T direction versus peening time. Similar curves were obtained for specimens peened with strokes parallel to the L direction. The dotted lines are a least-squares fit of $f(x) = a\,(1 - \exp(-bx^c))$, where a, b, and c are adjustable parameters.

Table 5.6 Average curvatures of peen formed sheets and of the 254×254 mm coupons removed from the center of selected sheets.

Orientation[†]	Sheets: strokes parallel to L			Sheets: strokes parallel to T			Coupons		
	Specimen	Curvature ($\times 10^{-4}$ mm^{-1})		Specimen	Curvature ($\times 10^{-4}$ mm^{-1})		Removed from	Curvature ($\times 10^{-4}$ mm^{-1})	
		Along L	Along T		Along L	Along T		Along L	Along T
	Sheet 4:1–L	2.50	2.19	Sheet 4:1–T	2.46	2.07	Sheet 4:1–L	2.66	2.14
	Sheet 2:1–L	2.93	0.17	Sheet 2:1–T	3.06	0.11	Sheet 2:1–T	3.12	1.52
	Sheet 1:1–L	3.46	-0.01	Sheet 1:1–T	3.45	$\simeq 0$	Sheet 1:1–L	2.93	1.81
	Sheet 1:2–L	3.56	0.30[‡]	Sheet 1:2–T	3.52	0.31[‡]	Sheet 1:2–L	3.03	2.08
	Sheet 1:4–L	3.00	1.81	Sheet 1:4–T	2.93	1.94	Sheet 1:4–L	3.16	1.54

[†] Horizontal lines aligned with the L direction.

[‡] The curvature was approximately constant near the center and transitioned to 1.2×10^{-4} mm^{-1} at approximately 200 mm from the edges.

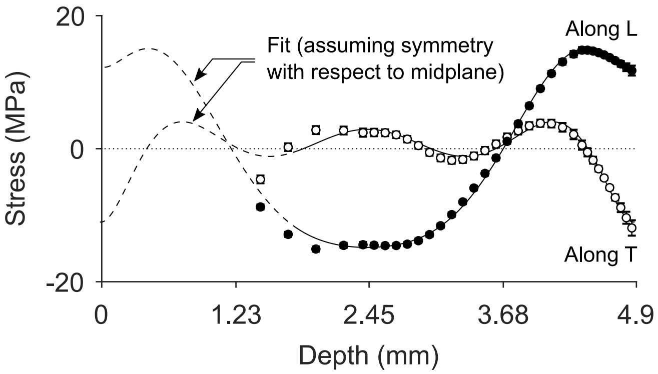

Figure 5.8 Residual stresses measured by the slitting method on two 51 × 51 mm coupons removed from an as-rolled sheet. Data were acquired up to a depth of 3.4 mm and through thickness profiles were reconstructed by assuming symmetry with respect to the midplane, fitting a smoothing spline through the cloud of points, and translating the resulting curve along the y axis to enforce forces equilibrium.

The resulting profiles were almost in equilibrium; only a slight translation of 0.15 MPa towards positive stresses was needed to equilibrate axial loads. The shape of the profiles, the low amplitude tensile stresses along the rolling direction, and the low amplitude of compressive stresses along the transverse direction are typical of quenched and stress relieved heat treatable aluminum alloys (Dieter, 1961; Prime and Hill, 2002; Robinson et al., 2014).

Figure 5.9 shows residual stresses measured by hole drilling in 254 × 254 mm coupons removed from the center of the peened sheets. All profiles display maximum compressive residual stresses of approximately −380 MPa. The depth of the plastically deformed layer, that can be inferred from the location of the tensile residual stress peak (see fig. 5.1c), is about 0.5 mm in all cases. Note that, because of rebalancing, residual stresses shown in figure 5.9 differ from those that would have been measured in the peen formed sheets prior to removal of the coupon. (Residual stresses in the original sheets are estimated in part 2.)

Figure 5.10a shows residual stresses measured by slitting in 15.24 × 17.78 mm coupons removed from sheet 1:2–L. Except for the point closest to the surface, profiles obtained by slitting and hole drilling are close and display almost equibiaxial stresses. Further investigating the differences between both sets of profiles would be hazardous as data were acquired on coupons of different geometries. Besides, hole drilling measurements are local while slitting tends to average stresses along the length of the slot and could be affected by edge effects due to the small size of the coupons. After about 0.6 mm, the slitting profiles follow a linear trend, with some oscillations that are likely due to initial stresses resulting from the manufacturing process of the sheets.

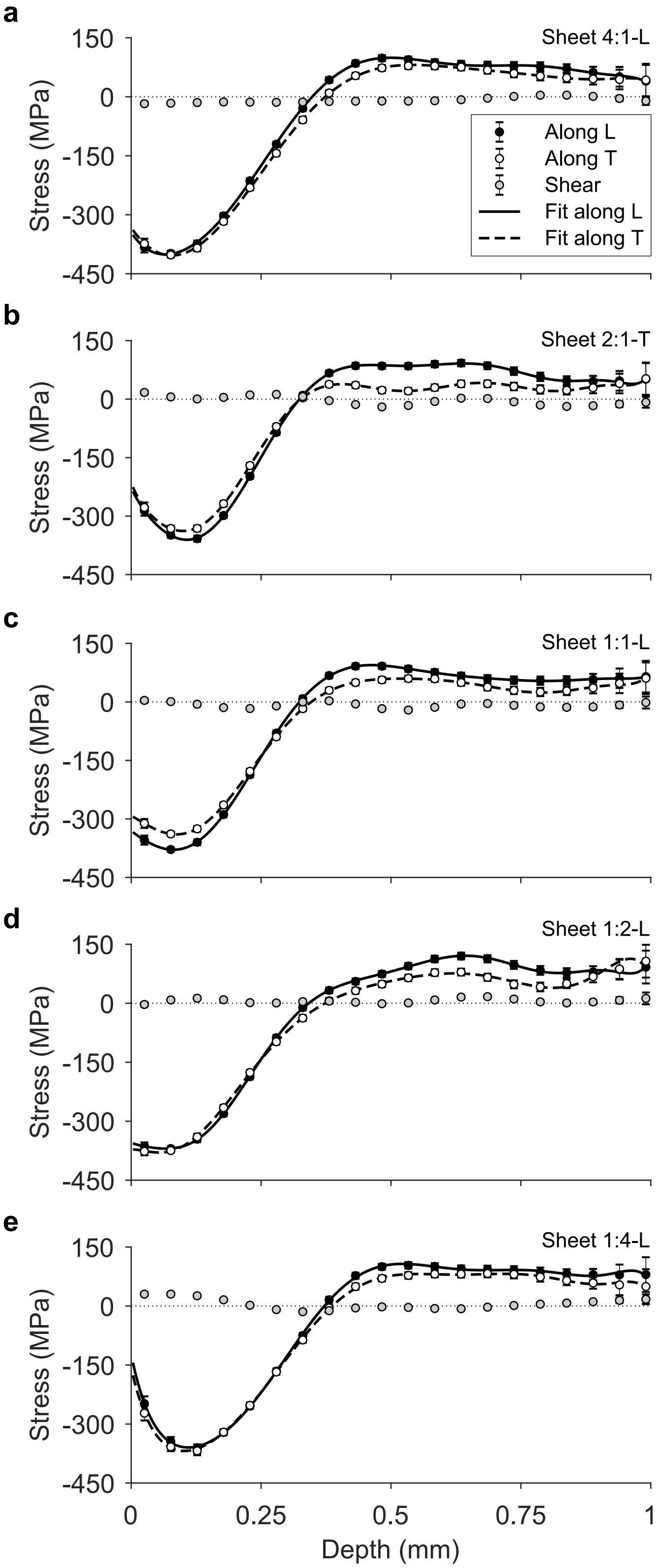

Figure 5.9 Residual stresses measured by hole drilling at the center of 254 × 254 mm coupons removed from the center of peen formed sheets. The fitting curves—shown only to guide the eye—are polynomial fits.

In figure 5.10b, we compare the oscillations in figure 5.10a—that were isolated by subtracting a linear fit over $z > 0.55$ mm (i.e., past the tensile residual stress peak) from the data—to the initial stresses from figure 5.8. Both sets of profiles have similar shape and magnitude, which is consistent with our understanding of the process: since peening only affects a thin layer of material near the surface, stresses below the plastically deformed layer are equal to the initial stresses plus a linear term due to stretching and bending of the specimens.

5.3.2 Stress peen forming tests

Figure 5.11 shows how the curvature of 508 × 127 mm strips varied as a function of prestress curvature. Curvatures along the prestress direction increased linearly with a slope of approximately 0.23, regardless of the alignment of the strips with respect to the rolling direction. Curvatures along the transverse direction decreased linearly with slope -0.03 for strips aligned with the L direction, and with slope -0.13 for strips aligned with the T direction. The magnitude of the slopes is consistent with results from the literature compiled in table 5.2. To the right of the dashed lines shown in figure 5.11—which correspond to the curvature of identical unconstrained strips peened with the same treatment; see below—the final curvature is smaller than the prestress curvature (negative springback), and vice versa.

Figure 5.12 shows residual stresses measured by hole drilling in 254 × 127 mm coupons removed from the center of strips aligned with the L direction and peened with increasing prestress curvatures. As prestress increases, near surface stresses become more compressive. The largest variations occur along the prestress direction, which causes the profiles to gradually separate. As already noted by Barrett and Todd (1984), prestress appears to have little effect on the depth of the plastically deformed layer (as inferred from the location of the tensile residual stress peak). We also observe that, whereas most profiles exhibit a local minimum approximately 0.1 mm below the surface, residual stresses in the strip that was held flat during peening do not. Whether this is due to the prestress conditions or to the variability in hole drilling measurements cannot be assessed from the single profiles reported here (see for example DeWald and Hill (2014) where replicate measurements on the same shot peened aluminum block yield both monotonically increasing and curved profiles).

Figure 5.13 shows residual stresses measured in the same conditions in a coupon removed from a strip that was free to deform during peening. The shape of the profiles is similar to that for other coupons although stresses are approximately 40 MPa higher (i.e., less compressive) over the first 0.2 mm.

Table 5.7 compares the curvatures of 508 × 127 mm strips that were held flat during peening, prestressed to $2.7 \times 10^{-4}\,\mathrm{mm}^{-1}$, and unconstrained. Curvatures along the long side of uncon-

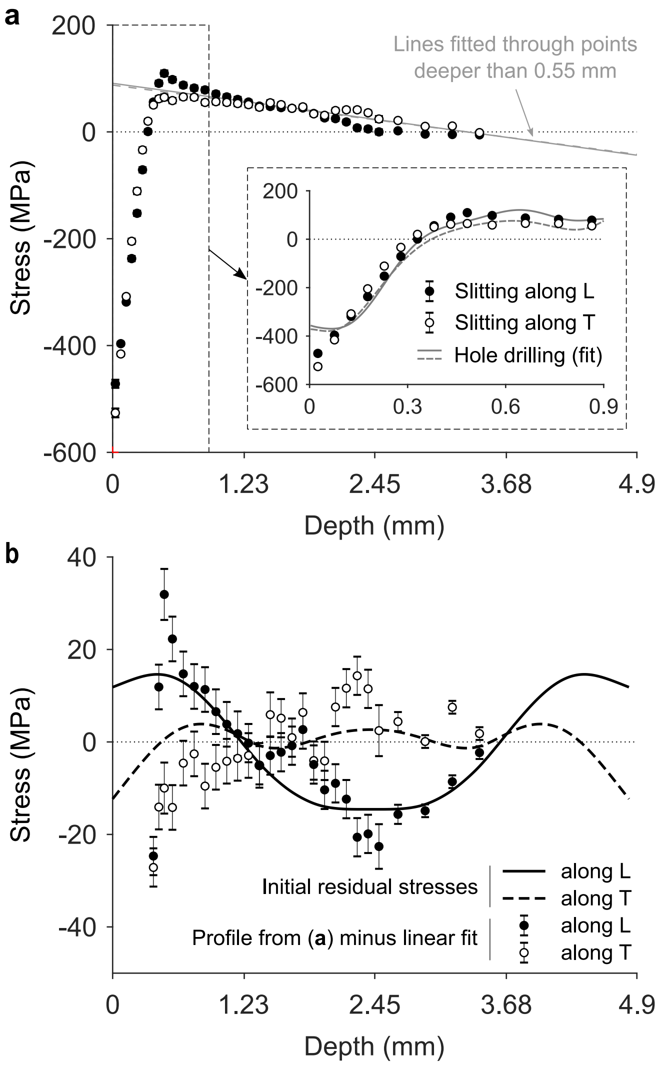

Figure 5.10 (a) Residual stresses measured by slitting in 17.78 × 15.24 mm coupons removed from sheet 1:2–L. Superimposed to the data is the fit to the residual stresses measured by hole drilling on the same sheet from figure 5.9d. (b) Same data as in (a) after having subtracted the linear portion of the profile caused by bending and stretching of the specimens following peening. The latter was obtained by fitting a line through data points deeper than 0.55 mm. The oscillations thus isolated follow the same trend as initial stresses from figure 5.8.

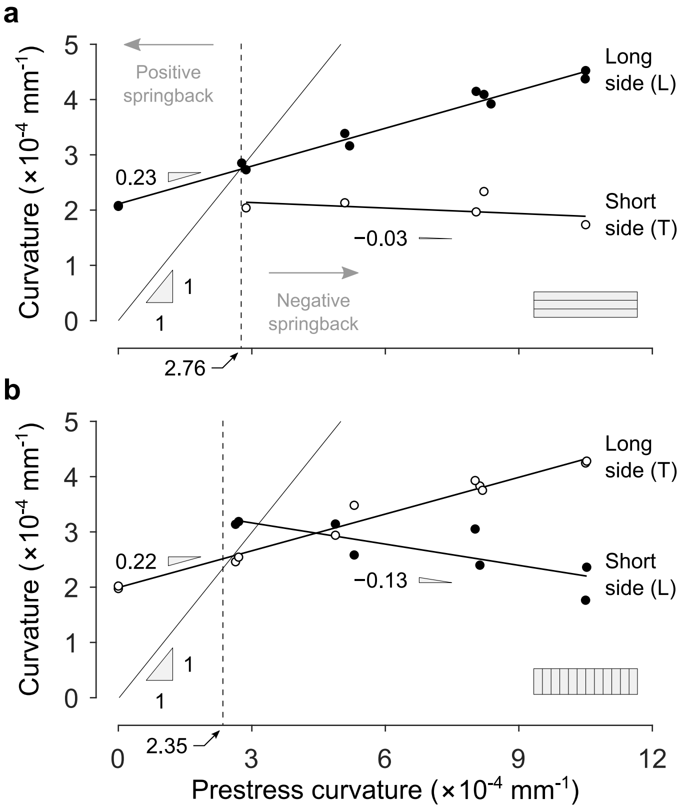

Figure 5.11 Average curvatures of 508 × 127 mm strips aligned (a) with the L direction and (b) with the T direction after all external constraints have been removed. All strips were peened with strokes parallel to their long side. Dashed lines show the curvature that unconstrained identical strips assumed when peened with the same treatment. Above this threshold, the curvatures of the strips are smaller than the prestress curvature (negative springback), and vice versa. Each point corresponds to one specimen. Eleven specimens were damaged before their curvatures along the short side could be measured.

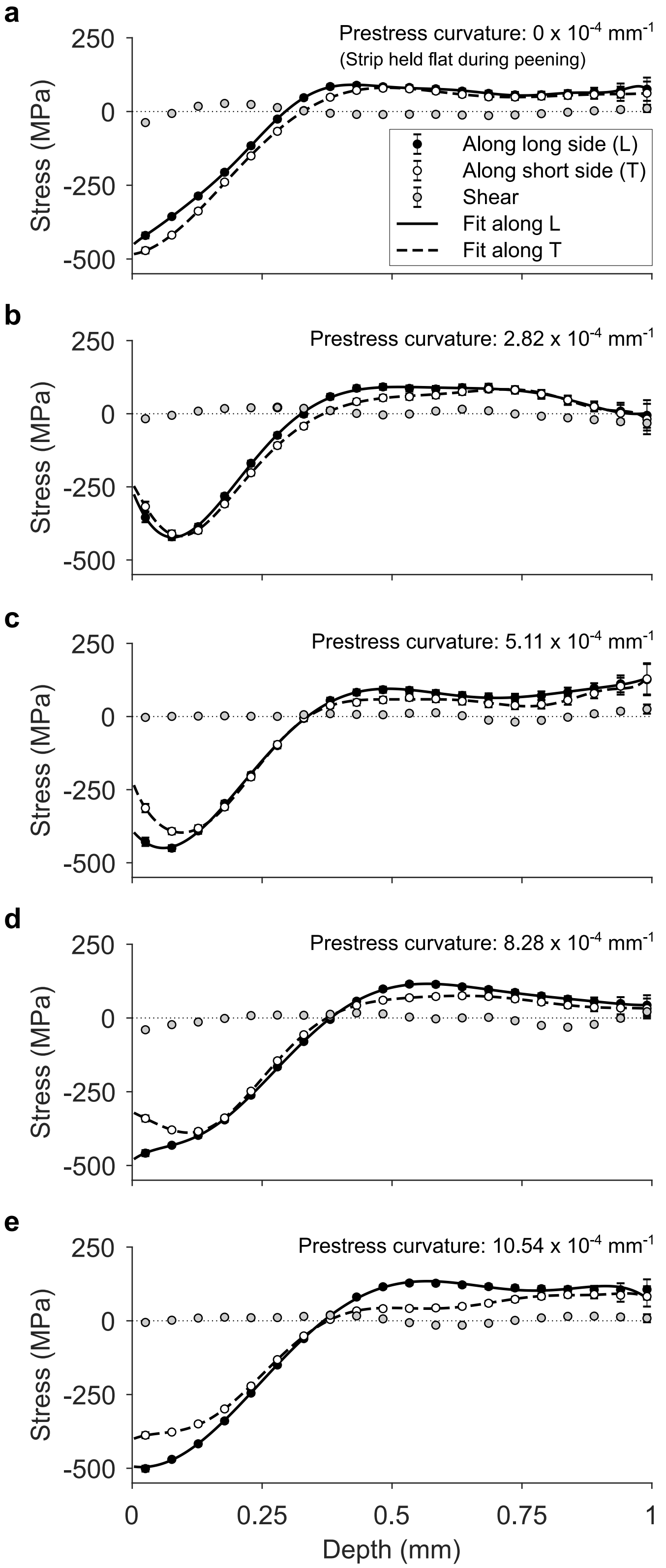

Figure 5.12 Residual stresses measured by hole drilling at the center of 254 × 127 mm coupons removed from the center of strips having their long side aligned with the L direction and peened with increasing prestress curvatures. The fitting curves—shown only to guide the eye—are polynomial fits.

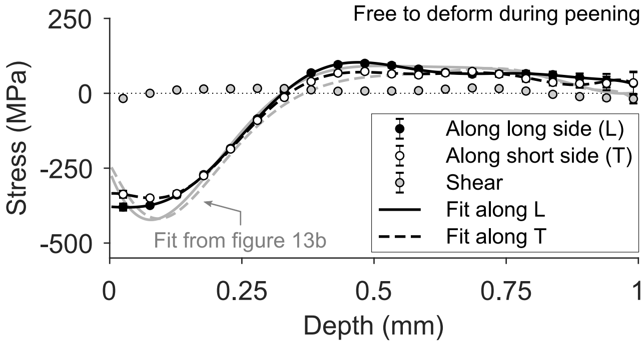

Figure 5.13 Residual stresses measured by hole drilling at the center of a 254 × 127 mm coupon removed from the center of a strip having its long side aligned with the L direction and that was free to deform during peening. The fitting curves—shown only to guide the eye—are polynomial fits. This strip assumed a curvature of $2.76 \times 10^{-4}\,\mathrm{mm}^{-1}$ along the long side. For comparison, the fit to residual stresses measured on the strip prestressed to $2.82 \times 10^{-4}\,\mathrm{mm}^{-1}$ from figure 5.12b is shown as light grey curves.

Table 5.7 Curvatures of strips that were held flat, prestressed to $2.7 \times 10^{-4}\,\mathrm{mm}^{-1}$ (nominal), and unconstrained during peening. All values $\times\, 10^{-4}\,\mathrm{mm}^{-1}$. Reported values were averaged over available results.

Long side aligned with	Held flat		Prestressed to $2.7 \times 10^{-4}\,\mathrm{mm}^{-1}$		Unconstrained	
	Along long side	Along short side	Along long side	Along short side	Along long side	Along short side
L	2.08	-	2.79	2.04	2.76	2.75
T	2.00	-	2.50	3.17	2.35	3.16

strained strips are reported as dashed lines in figure 5.11. Unconstrained strips behave as if they had been prestressed into their final shape, peened, then released: except for curvatures along the short side of strips aligned with the L direction, the curvatures of unconstrained and prestressed strips differs by less than 6 %. Their curvature is approximately 25 % larger than that of strips that were held flat during peening.

5.4 Discussion

5.4.1 Preliminaries: natural curvatures

To interpret the results of peen forming experiments, a useful tool is the concept of natural curvature. Natural curvature is defined as the curvature of a small beam cut out from a plate at a given location and along a given direction (Pezzulla et al., 2016). It is natural in the sense that it is the curvature that the beam would spontaneously adopt if it were not constrained by surrounding material. The shape of a peen formed plate can therefore be seen as a compromise between the plate reaching its natural curvatures (locally) and satisfying the geometric constraints of plate mechanics (globally). In the case of shot peen parts, natural curvatures only depend on the thickness of the part and in the distribution of peening induced plastic strains.

Now, imagine that a small coupon is carefully removed from a larger shot peened plate and that removal does not alter the distribution of plastic strains in the coupon. If the deflection of the coupon is small compared to its thickness, then its curvatures are close approximations to the natural curvatures. Indeed, the response of a plate when deflections are small is linear and its stretching and bending modes are decoupled. Therefore, the coupon can attain its natural curvature in all directions without the bending in one direction affecting the bending in other directions (Timoshenko, 1940, section 23).

This is illustrated in figure 5.14a for three geometries: that of strips used for stress peen forming experiments and that of the two types of coupons used for residual stress measurements. These curves were generated using the Abaqus finite element software by prescribing an equibiaxial thermal expansion ε^* in the upper half of a plate of thickness h and by ramping the expansion from zero. The natural curvature of this system is $3\varepsilon^*/2h$ (see Timoshenko, 1925). The plates were meshed with S4R elements and geometric nonlinearities were included in the analysis. For all three geometries, figure 5.14a shows that simulated curvatures remain close to the natural curvature, even though a small deviation is observed for 254×254 mm coupons for natural curvatures larger than $2 \times 10^{-4}\,\mathrm{mm}^{-1}$. This deviation is due to nonlinear geometric effects: when out-of-plane deflections become of the same order as the thickness, stretching and bending mode are no longer decoupled and, since the spherical shape that the coupons adopt is non-developable, some of the elastic energy must contribute to stretching the coupons, thus reducing the amount available for bending and stiffening the structure. Since the curvatures of prestressed strips (fig. 5.11) and the curvatures of coupons used for residual stress measurements (table 5.6) are all smaller than $4 \times 10^{-4}\,\mathrm{mm}^{-1}$, we conclude from figure 5.14a that these curvatures are close estimates of natural curvatures.

At this point, it is important to point out that, although the curves in figure 5.14a were generated assuming equibiaxial expansion, the expansion in the peening affected layer of the actual specimens might not be. For example, plastic anisotropy or prestress might result in larger expansion in one direction. However, the conclusion of the previous paragraph—that the curvatures of small coupons is a close approximation of natural curvatures—still holds for non-equibiaxial expansions. Indeed, since stretching and bending modes are decoupled in the

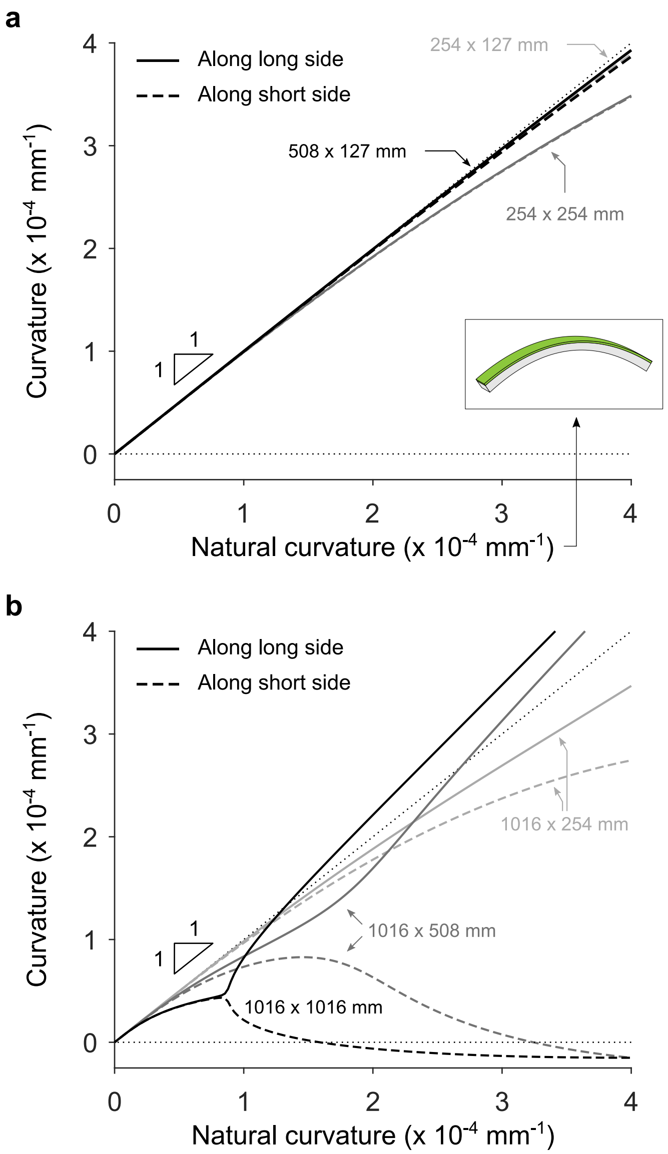

Figure 5.14 Curvature versus natural curvature for 4.9 mm thick rectangular plates of various dimensions. The curves were obtained from finite element simulations as described in Faucheux et al. (2018) assuming equibiaxial expansion in the peening affected layers. (a) For natural curvatures smaller than 3×10^{-4} mm^{-1}, the relative difference between the identity line and the curves for 254 × 254 mm plates is less than 8.5 %. It is less than 2 % for 508 × 127 mm and 254 × 127 mm plates. Therefore, curvatures measured on such specimens are close estimates of natural curvatures. (b) Larger sheets exhibit more complex behaviors. In the linear domain, say for natural curvatures smaller than 1×10^{-5} mm^{-1}, 1016×1016 mm, 1016 × 508 mm, and 1016 × 254 mm sheets deform into spherical shapes. As natural curvature increases, geometric nonlinear effects become significant and the curves bend downward. When natural curvature rises above 1×10^{-4} mm^{-1}, 1016 × 1016 mm plates transition to cylindrical shapes due to an elastic instability. For all other geometries, no such transition occurs. Instead, curvatures along the long and short side gradually diverge.

linear domain, how a plate bends in one direction does not affect how it bends in the other directions. Therefore, the same curves as in figure 5.14a would have be obtained no matter what distribution of expansion was used in the simulations (except for slight variations for the 254×254 mm coupons for natural curvatures larger than $2 \times 10^{-4}\,\mathrm{mm}^{-1}$ since geometric nonlinearities are significant in this region).

5.4.2 Explaining the shape of large sheets

We now turn our attention to the shape of large sheets used for conventional peen forming experiments. Figure 5.14b shows curvatures as a function of natural curvature for the three geometries considered here. These curves were computed using the same finite element simulations as in section 5.4.1 with equibiaxial expansion as loads. Although the expansion in the actual specimens might not be equibiaxial, this simplified model still enable to capture the main features of the response of uniformly peen formed plates.

In the linear domain, say for natural curvatures below $1 \times 10^{-5}\,\mathrm{mm}^{-1}$, all specimens deform into spherical shapes and their curvature is the same as the natural curvature. As natural curvature increases, the sheets remain spherical, but the curves depart from linearity due to stress stiffening. Because it is much easier to bend a thin plate than it is to stretch it, cylindrical shapes become energetically favorable for large natural curvatures, as discussed in Pezzulla et al. (2016). For 1016×1016 mm plates, the transition occurs suddenly at approximately $0.86 \times 10^{-4}\,\mathrm{mm}^{-1}$, whereas curvatures along the long and short direction gradually diverge for the two other geometries.

Using the values in table 5.6 as estimates for natural curvature, we found that the latter varied between 1.5 and $3.2 \times 10^{-4}\,\mathrm{mm}^{-1}$, depending on the specimen and on the direction. In this range, the curves in figure 5.14b capture the main features of the experimentally observed deformed shapes: square plates deform into cylindrical shapes, 2:1 aspect ratio plates into elliptical shapes, and 4:1 aspect ratio plates into nearly cylindrical shapes.

From figure 5.14b, we can also infer why specimens peened with strokes parallel to either the L or T direction deformed into identical shapes. For sheets of 1:1, 1:2, and 2:1 aspect ratio, this was likely because the sheets quickly ‘locked’ into cylindrical shapes, which occurred during the first half of the first peening cycle (see supplementary videos). Once in this configuration, a sheet can only continue bending in the same direction as its geometric rigidity resists other deformation modes. The precise peening trajectory is then of little importance if the specimens are peened until their deformation saturates, as was the case here (fig. 5.7). The same reasoning applies to 1:4 and 4:1 aspect ratio specimens which, although they do not ‘lock’, can only deform into nearly spherical shapes.

5.4.3 Influence of material anisotropy

Simulations in figure 5.14 predict that, when the expansion in the peening affected layers is equibiaxial, rectangular sheets spontaneously bend along the long side. This phenomenon was explained by Alben et al. (2011) which showed that highly localized regions of double curvature along the free edges of bilayer systems reduce the elastic energy of the system and make long side bending energetically favorable.

However, not all our specimens bent along the long side. Instead, all had their largest curvature along the L direction, even when the L direction was aligned with the short side. This is especially clear for 2:1 and 1:2 aspect ratio sheets which—for otherwise identical peening conditions—deformed into cylinders if their long side was aligned with L, and into flatter elliptical shapes if their long side was aligned with T (fig. 5.6). Because the only difference between these two sets of sheets was their alignment with the rolling direction, these results suggest that some form of material anisotropy resulted in larger expansion in the L direction, with the level of anisotropy being sufficiently strong to overcome the geometrical preference for the sheets to bend along their short side.

Although the 2024–T3 aluminum sheets used here had isotropic elastic properties, tensile tests revealed a mild plastic anisotropy (table 5.1). Therefore, we expect that more plastic flow would occur along some direction after each impact, resulting in larger plastic strains, hence curvatures, along this direction. However, it is not clear from the limited tensile test results available that this direction is the L one. Checking that this is the case would require compression or indentation tests.

Another possible source of material anisotropy is initial residual stresses. Their effect can be explained as follows. In as received sheets, residual stresses are symmetric with respect to the midplane of the sheets (fig. 5.8) and, therefore, do not induce curvature. This symmetry, however, is broken when peening induces large compressive residual stresses near the surface. Compared to an initially stress-free specimen, residual stresses on the back face amplify or reduce the amount of curvature that the specimen experiences, depending on their sign. Quantifying the contribution of this effect is deferred to part 2.

5.4.4 Influence of prestress

Another source of anisotropy is prestress. Here, we extend the use of the term ‘prestress’ to designate both externally applied loads (as in stress peen forming experiments) and internal loads (as in conventional peen forming experiments) that cause a sheet to assume a compound curvature. When a sheet is prestresses, initial stresses before an impact depend on the direction and cause larger plastic strains to develop in the direction in which stresses are the largest (i.e., the more tensile, or the less compressive).

This effect is most clearly seen in the curvature of strips used for stress peen forming tests which is always larger along the prestress direction (fig 5.11). It also affects the shape of unconstrained sheets that were free to deform during peening as evidenced by the fact that coupons removed from specimens used for conventional peen forming tests all had different curvatures. Indeed, recall that the curvatures of the coupons are close estimates of natural curvature, and that the latter only depend on the thickness of the coupon and on the distribution of plastic strains. Had the progressive deformation of the specimen had no effect, all coupons would have assumed the same curvatures since they were removed from specimens made from the same material and peened in the same conditions.

This effect is also apparent in figure 5.7 which shows that the deflection of sheets of different geometries saturated after different numbers of peening cycles. For example, sheet 1:2–T saturated after approximately five cycles whereas sheets 1:1–T and 2:1–T had not reached saturation after twelve cycles. Had the progressive deformation of the specimen had no effect, all curves would have saturated at the same time.

Finally, notice how residual stresses measured in coupons removed from sheets 2:1–T and 1:1–L, which deformed into cylindrical shapes, are more compressive in the bending direction (fig. 5.9b–c) whereas residual stresses in coupons removed from other sheets, which deformed into elliptical or nearly spherical shapes, are almost equibiaxial (fig. 5.9a, d, e).

5.5 Conclusion

In this paper, we presented the results of conventional and stress peen forming experiments conducted on 4.9 mm thick 2024–T3 aluminum sheets shot peened to full coverage with the same low intensity treatment. Our results highlight features of the response of thin peen formed sheets that were known to process engineers but that had been poorly documented so far. In particular, we showed that the final shape of a peen formed sheet does depend on the way the sheet deforms during peening, and that this deformation has the same effect as an externally applied prestress. We also showed that material anisotropy—in the form of plastic anisotropy or non-equibiaxial initial stresses inherited from earlier processing stages (e.g., heat treatment, rolling)—determined the direction along which our specimens bent the most. The other main observations are as follows.

1. Identical specimens peened until their deformation saturated assumed identical shapes, regardless of the peening trajectory.

2. The curvatures of prestressed strips varied linearly with the prestress curvature.
3. There exists a critical prestress curvature such that, when constraints are removed, a prestressed strip does not spring back. This curvature coincides with that which the strip would assume if it was free to deform during peening.
4. If a strip is prestressed to a curvature smaller than this critical value (for example, if it is held flat during peening), it will bend less than if it is free to deform, and vice versa.

Although similar behaviors were observed in earlier works, residual stress measurements along both direction before and after peening were seldom reported. This information is needed to understand how different sources of anisotropy—such as prestress, plastic anisotropy, and non-equibiaxial initial stresses—affect the final deformed shapes. Furthermore, such measurements enable to identify peening-induced plastic strains which provide much clearer insights into the mechanics of peen formed plates than residual stresses alone, as will be demonstrated in part 2.

Acknowledgements

The authors gratefully acknowledge financial support from Airbus, from the Rio Tinto group through a graduate scholarship, from the Canada Research Chairs program, and from the Natural Sciences and Engineering Research Council of Canada (NSERC; funding reference number 175791953). The prestressing jig used for stress peen forming tests was courtesy of Aérosphère and Centre Technologique en Aérospatiale (CTA).

CHAPTER 6 ARTICLE 2: PEEN FORMING AND STRESS PEEN FORMING OF 2024–T3 ALUMINUM SHEETS (PART 2); EIGENSTRAIN ANALYSIS

Pierre A. Faucheux, Frédérick P. Gosselin, Martin Lévesque

Submitted to the Journal of Materials Processing Technology on November 27th 2019

Abstract

In this study we use the theory of eigenstrains to investigate how different sources of anisotropy affected the results of shot peen forming experiments reported in part 1. The specimens consisted of 4.9 mm *thick 2024–T3 aluminum sheets uniformly shot peened on one face that were either free to deform or held onto a prestressing jig during peening. Potential sources of anisotropy included the plastic anisotropy of rolled aluminum, anisotropic initial stresses that redistribute when their equilibrium is disturbed by peening, the geometry of the specimens, and externally applied prestress. For the alloy and peening conditions considered, plastic anisotropy had no discernable influence on the shape of the specimens. Initial residual stresses, on the other hand, caused slightly larger bending loads in the rolling direction of the alloy. Although the magnitude of these loads was approximately 30 times smaller than peening-induced loads, it was sufficient to overcome the geometric preference for rectangular sheets to bend along their long side and cause all unconstrained specimens to bend along the rolling direction instead. Once the sheets started to deform, larger plastic strains developed in the bending direction. We show that this effect is equivalent to that used in the variant of the process called stress peen forming where parts are elastically prestressed during peening to obtain larger plastic strains in directions in which the material is stretched.*

6.1 Introduction

Lower wing skins of most commercial aircraft are shaped using shot peen forming. The process consists in bombarding thin metal parts with hard shot—usually steel spheres less than one millimeter in diameter propelled at velocities ranging from 20 to 100 m s^{-1}—to plastically deform the material over a few tenths of a millimeter. In the plastically deformed layer, the material is compressed in the direction normal to the surface and stretched in the direction parallel to the surface, which causes the part to bend and elongate, as shown schematically in figure 6.1a–b.

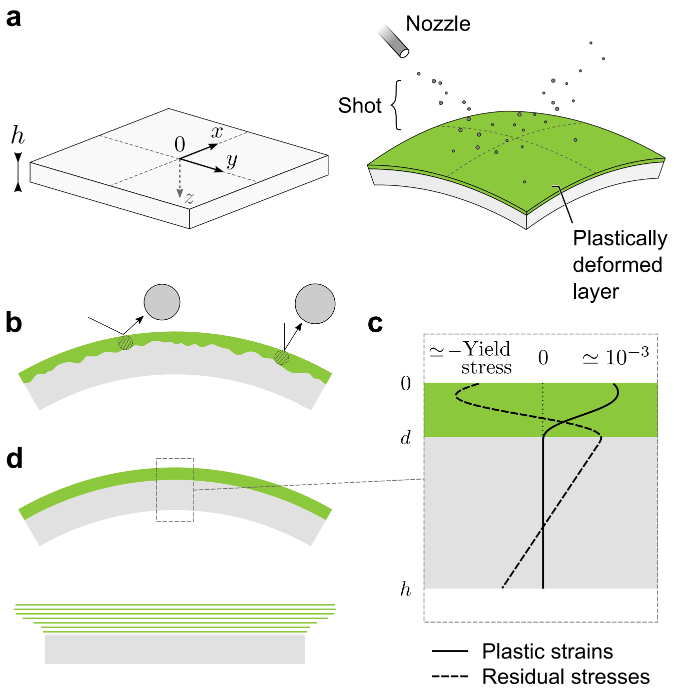

Figure 6.1 Peen forming of a metal plate. (a) Small and hard shot propelled at a metal surface at high velocity plastically deform a thin layer of material. As the material plastically flows in the direction parallel to the surface, it stretches the part and induces distortions. If controlled, this effect can be used to shape thin components. (b) At the scale of a shot, the distribution of plastic strains is highly irregular due to the stochastic nature of the process. (c) Typical in-plane plastic strain profiles after averaging in the plane of the plate. The profiles have a maximum at or near the surface and smoothly decrease to zero. Also shown is a typical in-plane residual stress profile. (d) To visualize how plastic strains cause residual stresses and distortions, it is convenient to imagine cutting the plate into infinitesimally thin layers. In this (virtual) configuration, each layer is homogeneous, unconstrained, and therefore stress-free. Gluing the layers back together requires stretching some layers and compressing others, which induces internal stresses and distortions.

Although peen forming has been used since the 1950s, the literature review conducted in part 1 (Faucheux et al., 2019) found very few experimental studies of the process. It also highlighted two major limitations of these studies. First, most publicly available data were acquired on 76 × 19 mm strips for peening conditions such that the deflection of the strips remained small compared to their thickness. Consequently, these experiments did not capture nonlinear geometric effects that become significant when forming large panels (see part 1). Secondly, residual stresses were seldom measured in more than one direction even though several phenomena could induce anisotropic residual stresses. These include plastic anisotropy of the target material and prestress—a term used to designate external loads deliberately applied to a part being peened to increase plastic flow in directions in which the material is in tension. The manufacturing process of heat treatable aluminum plates in which most peen formed parts are machined is also known to induce anisotropic initial stresses that could affect the deformed shape of the parts and should, therefore, be characterized.

In part 1, we reported the results of a peen forming experimental campaign designed to address these issues. The specimens consisted in 508 and 1016 mm long rectangular 2024–T3 aluminum sheets of different aspect ratios, sourced from the same lot, and peened with the same treatment. Some sheets were free to deform during peening while others were prestressed in a four-point bending jig. A noteworthy result was that all sheets that were free to deform bent in the rolling direction of the alloy, irrespective of their aspect ratio or of the peening trajectory. A similar phenomenon was reported in Kulkarni et al. (1981) for 2024 and 7075 aluminum although, in this case, 2024 aluminum specimens bent in the transverse direction of the alloy.

In a study about thin bilayers, Alben et al. (2011) showed that rectangular plates of uniform thickness made of an isotropically expanding active layer on top of a passive layer spontaneously bend along their long direction. This effect is purely geometric and comes from regions of double curvatures that develop near the free edges, thus reducing the elastic energy of the system and making long side bending energetically favorable. That all our specimens bent along the rolling direction instead of the long direction therefore suggests that, for the alloy and peening conditions considered, material anisotropy was sufficiently strong to overcome this effect. In this article, we aim to clarify the contribution of each source of anisotropy to explain why all plates in part 1 bent along the rolling direction.

The paper is structured as follows. After a summary of the experiments conducted in part 1, section 6.2 introduces the concept of eigenstrains on which the rest of the analysis is based. Section 6.3 presents equations needed to relate eigenstrains to residual stresses and strains in uniformly shot peened plates. Section 6.4 presents the procedures used to characterize

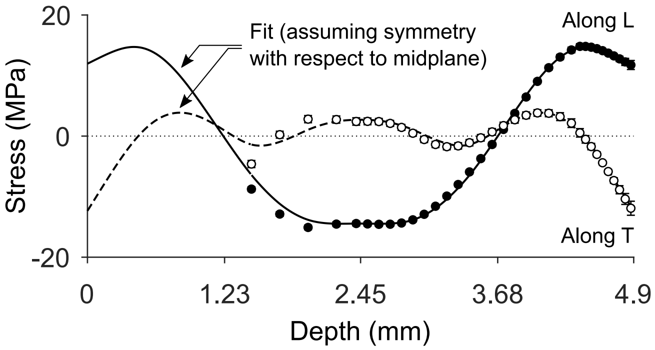

Figure 6.2 Residual stresses measured with the slitting method in 51 × 51 mm coupons removed from an as-rolled sheet.

eigenstrains present in our specimens as well as numerical models used to interpret the result. We then successively investigate the influence of prestress, plastic anisotropy, initial eigenstrains, and geometric effects on the deformed shape of the specimens in sections 6.5 and 6.6.

6.2 Background

6.2.1 Summary of peen forming experiments conducted in part 1

All peen forming experiments reported in part 1 were conducted on rectangular specimens cut from 4.9 mm thick 2024–T3 aluminum sheets from the same lot. Uniaxial tensile tests at 0, 45, and 90° from the rolling direction revealed isotropic elastic properties but a mild plastic anisotropy: the elastic modulus was 71 500 MPa and the yield stress at 0.2 % was 381 MPa along the rolling (L) direction, 349 MPa at 45° of the rolling direction, and 339 MPa along the transverse (T) direction. Residual stresses in as-received sheets were measured with the slitting method. These initial stresses were anisotropic with a magnitude of less than 20 MPa both in tension and in compression, as shown in figure 6.2.

Both conventional and stress peen forming experiments were conducted. For the former, specimens were free to deform during peening. For the latter, they were elastically prestressed on the four-point bending jig shown in figure 6.3a, shot peened, then released. Sheets of 1:4, 1:2, 1:1, 2:1, and 4:1 aspect ratio, here defined as the ratio of the dimension in the L direction to the dimension in the T direction, 1016 mm along their long side were used for conventional peen forming experiments. Smaller 508 × 127 mm strips were used for stress peen forming experiments. Prestress curvatures ranged from 0 (the strips were held flat) to $10.54 \times 10^{-4}\,\mathrm{mm}^{-1}$, which corresponds to a radius of curvature of 949 mm.

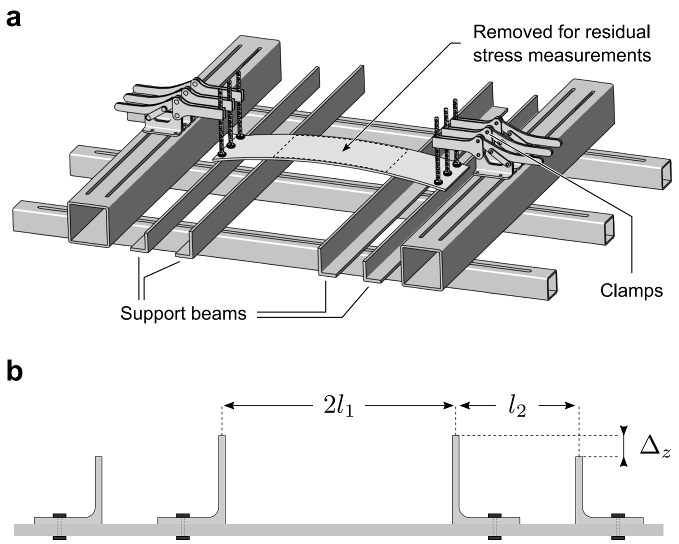

Figure 6.3 (a) Four-point bending jig used to hold 508 × 127 mm strips in a bent shape during stress peen forming experiments. The height and the spacing of the support beams could be varied to obtain different prestress curvatures. After peening, the strips were unclamped, their curvatures were measured, and a 254 × 127 mm coupon was removed from the central region for residual stress measurements. (b) Cross-sectional view of the jig. See supplementary material of part 1 for dimensions.

All sheets were peened to full coverage in an automated compressed air peening cabinet with SCCW28 steel shot, 0.71 mm in diameter. The average velocity of shot exiting the nozzle was $41\,\mathrm{m\,s^{-1}}$, which corresponds to an Almen intensity of 12×10^{-3} inches A. The treatment was applied progressively over the course of 12 peening cycles, each cycle delivering a small increment of coverage to the whole surface. For each geometry, one specimen was peened with strokes parallel to the L direction and another identical specimen was peened with strokes parallel to the T direction.

Figure 6.4 shows the final deformed shape of some of the sheets used for conventional peen forming experiments. All sheets, including those not shown, had their largest curvature along the L direction, irrespective of their aspect ratio or of the peening trajectory. While sheets of 1:1 and 2:1 aspect ratio deformed into cylindrical shapes with almost zero curvature in the T direction, other sheets assumed a compound curvature.

Because of size constraints, residual stresses could not be measured directly in as-peened specimens. Instead, smaller coupons were removed from the center of the specimens listed in table 6.1 with a jigsaw and residual stresses were measured at the center of these coupons with the hole drilling method. Residual stresses were recorded at 51 µm intervals down to a depth of 1 mm and the data were fit with a sixth order polynomial to obtain continuous

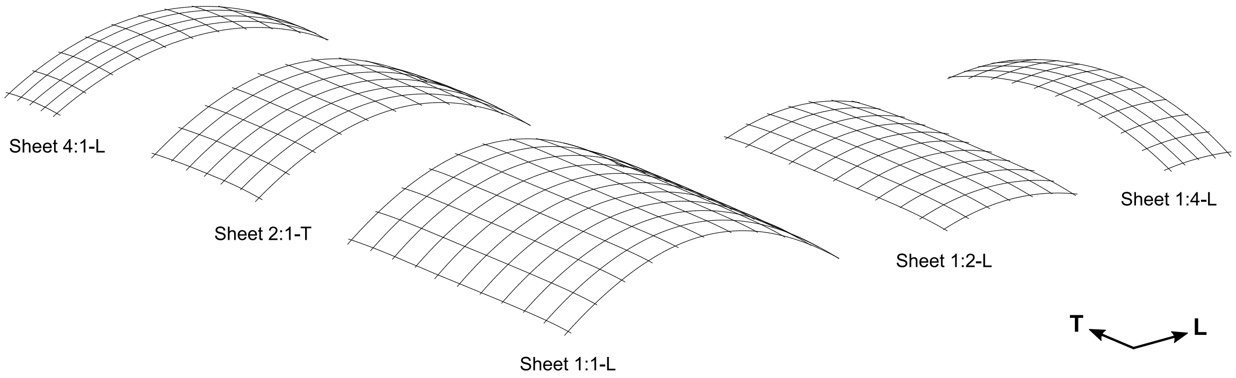

Figure 6.4 3D scans of 4.9 mm thick and 1016 mm long 2024-T3 aluminum sheets of 4:1, 2:1, 1:1, 1:2, and 1:4 aspect ratio shot peened to full coverage with SCCW28 shot at an Almen intensity of 12×10^{-3} inches A. The specimens were free to deform during peening. Deflection magnified by a factor of 4.

residual stress profiles.

The coupons, the dimensions of which were chosen as large as possible to minimize the effect of cutting induced plastic deformations and heating on measurement spots, were 254×254 mm for free-to-deform sheets and 254×127 mm for prestressed strips. Upon removal, stress rebalancing caused the coupons to deform. For example, sheet 1:1–L assumed a cylindrical shape with $3.46 \times 10^{-4}\,\mathrm{mm}^{-1}$ curvature in the L direction and almost zero curvature in the T direction while the coupon removed from it assumed an almost spherical shape with $2.93 \times 10^{-4}\,\mathrm{mm}^{-1}$ curvature in the L direction and $1.81 \times 10^{-4}\,\mathrm{mm}^{-1}$ curvature in the T direction. As a result, residual stresses measured in the coupons differed from those that would have been measured in as-peened specimens. These profiles are reproduced in the middle panels of figures 6.8 and 6.9. Their analysis constitutes the bulk of the following sections.

6.2.2 Eigenstrains

Recall that our aim is to clarify the contribution of different sources of anisotropy on the final deformed shape of aluminum sheets peen formed in part 1. This analysis must be carried out from the only experimental data available, namely residual stresses and curvatures measured on coupons removed from the specimens. Because of stress rebalancing, these stresses and curvatures differ from those in the original specimens. On the other hand, if the coupon were carefully removed and provided that no reverse yielding occurred during springback, then plastic strains were not affected by removal. Consequently, characterizing plastic strains in the coupons provides a direct mean to study the effect of the peening treatment on the

Table 6.1 List of specimens pen formed in part 1 for which residual stress measurements are available.

Specimen ID	Dimensions		Prestress curvature
	Along L (mm)	Along T (mm)	($\times 10^{-4}$ mm)
Sheet 4:1–L	1016	254	Free to deform
Sheet 2:1–T	1016	508	
Sheet 1:1–L	1016	1016	
Sheet 1:2–L	508	1016	
Sheet 1:4–L	254	1016	
Strip K0–L–A	508	127	0
Strip K1–L–A	508	127	2.82
Strip K2–L–A	508	127	5.11
Strip K3–L–A	508	127	8.28
Strip K4–L–A	508	127	10.54

original specimens.

At the scale of a shot, the distribution of plastic strains induced by shot peening treatments is highly irregular as it depends on the precise sequence of impacts and on the distribution of impact velocities. On average, however, symmetry and translational invariance require that the plastic strain field $\boldsymbol{\varepsilon}^{pl}$ only depends on the coordinate normal to the surface and that shear components be zero. In the rectangular coordinate system of figure 6.1a, this implies that

$$\boldsymbol{\varepsilon}^{pl}(z) = \begin{pmatrix} \varepsilon^{pl}_{xx}(z) & 0 & 0 \\ 0 & \varepsilon^{pl}_{yy}(z) & 0 \\ 0 & 0 & \varepsilon^{pl}_{zz}(z) \end{pmatrix}. \tag{6.1}$$

Furthermore, the fact that plastic deformations take place at constant volume requires that $\varepsilon^{pl}_{zz} = -(\varepsilon^{pl}_{xx} + \varepsilon^{pl}_{yy})$. Since peening stretches the material in the direction parallel to the surface and compresses it in the direction normal to the surface, ε_{xx} and ε_{yy} are positive while ε_{zz} is negative.

To visualize what residual stresses and distortions a peening treatment does induce, it is convenient to imagine cutting a shot peened part into infinitesimally thin layers parallel to its surface and letting the system relax, as shown schematically in figure 6.1d. In this virtual configuration, the layers are not constrained by surrounding material; the strains they undergo are equal to the plastic strains and residual stresses are zero everywhere. Since the strains from one layer to the next are incompatible, reassembling the structure requires stretching some layers and compressing others, which induces residual stresses and distortions. Figure 6.1c shows typical plastic strain and residual stress profiles in uniformly shot peened plates. Plastic strains are the largest at or near the peened surface then gradually decrease to zero. Residual stresses vary linearly in the bulk owing to the bending and stretching of the plate. They reach a maximum near the transition with the peening-affected layer, located at $z = d$, then decrease until they become compressive near the surface.

There exist a general framework to study the relationship between incompatible strains, residual stresses, and distortions called the theory of eigenstrains (Korsunsky, 2017). The term eigenstrains refers to all permanent nonelastic strains present in a structure. Thus, for small strains

$$\boldsymbol{\varepsilon} = \boldsymbol{\varepsilon}^{el} + \boldsymbol{\varepsilon}^{*}, \tag{6.2}$$

where $\boldsymbol{\varepsilon}$ are the total strains, $\boldsymbol{\varepsilon}^{el}$ are the elastic strains, and $\boldsymbol{\varepsilon}^{*}$ are the eigenstrains. Similarly, the eigenstrains can themselves be additively decomposed into thermal strains, plastic strains, and any other source of nonelastic strains. Many analytical solutions have been reported that relate specific distributions of eigenstrains to the residual stresses and distortions they induce, some of which are reviewed in Mura (1987). Conversely, several authors addressed the inverse problem of identifying eigenstrains present in a structure from limited experimental measurements; see for example Jun and Korsunsky (2010). Since plastic deformation is the only source of eigenstrains in shot peened parts, these inverse identification procedures can be used without modifications to compute peening-induced plastic strains.

In general, identifying eigenstrains is an iterative process that involves finite element simulations and optimization algorithms. For simple geometries, however, closed-form solutions that relate eigenstrains to residual stresses and total strains are available.

6.3 A model to relate eigenstrains, stresses, and strains in uniformly shot peened plates

Consider a plate of uniform thickness h, made of an isotropic material with elastic modulus E and Poisson ratio ν, and subjected to a distribution of eigenstrains of the form (6.1). Using the coordinate system of figure 6.1a, let

$$\alpha_i = \int_0^h \varepsilon^*_{ii}(z)\,\mathrm{d}z \quad \text{and} \qquad \beta_i = \int_0^h \varepsilon^*_{ii}(z)\,z\,\mathrm{d}z, \quad i = \{x, y\} \tag{6.3}$$

be the resulting eigenstrains and the first eigenstrains moment with respect to the peened surface. Within the hypotheses of the theory of linear elasticity, (residual) stresses $\boldsymbol{\sigma}$ are related to the strains through

$$\varepsilon_{xx} = a_x z + b_x, \qquad \varepsilon_{yy} = a_y z + b_y, \tag{6.4}$$

$$\varepsilon_{xx}^{el} = \varepsilon_{xx} - \varepsilon_{xx}^{*}, \qquad \varepsilon_{yy}^{el} = \varepsilon_{yy} - \varepsilon_{yy}^{*}, \tag{6.5}$$

$$\sigma_{xx} = \frac{E}{1-\nu^2}\left(\varepsilon_{xx}^{el} + \nu\varepsilon_{yy}^{el}\right), \qquad \sigma_{yy} = \frac{E}{1-\nu^2}\left(\varepsilon_{yy}^{el} + \nu\varepsilon_{xx}^{el}\right), \tag{6.6}$$

where

$$a_i = \left(12\beta_i - 6\alpha_i h\right)/h^3, \qquad b_i = \left(4\alpha_i h - 6\beta_i\right)/h^2. \tag{6.7}$$

This solution can be derived by adopting the kinematic assumption (6.4) that material lines perpendicular to the undeformed midsurface remain straight during deformation then by using the stress-strain relation (6.6) to enforce that resulting axial loads and bending moments acting on any cut through the plate must be zero, as was done in Korsunsky (2005) for equibiaxial eigenstrains. Another derivation without a priori kinematic assumptions is presented in the supplementary material.

In this simple case, the above equations can be inverted to yield the eigenstrains in terms of residual stresses and total strains. Solving (6.6) for the strains yields

$$\varepsilon_{xx}^{el} = (\sigma_{xx} - \nu\sigma_{yy})/E, \qquad \varepsilon_{yy}^{el} = (\sigma_{yy} - \nu\sigma_{xx})/E. \tag{6.8}$$

Finally, combining (6.4), (6.5), and (6.8), and noticing that

$$a_i = -\kappa_i, \tag{6.9}$$

where κ_i is the curvature of the plate in the i direction, yields

$$\begin{aligned} \varepsilon_{xx}^{*} &= \left(\varepsilon_{xx}\big|_{z=0} - \kappa_x z\right) - (\sigma_{xx} - \nu\sigma_{yy})/E, \\ \varepsilon_{yy}^{*} &= \left(\varepsilon_{yy}\big|_{z=0} - \kappa_y z\right) - (\sigma_{yy} - \nu\sigma_{xx})/E, \end{aligned} \tag{6.10}$$

where $\boldsymbol{\varepsilon}\big|_{z=0}$ are total strains measured on the upper face of the plate.

6.4 Methods

6.4.1 Near-surface eigenstrains

The near-surface eigenstrains present in our specimens were computed from residual stress and curvature measurements using equations (6.10). Here and in what follows, we used $E = 71500$ MPa and $\nu = 0.33$. Because the in-plane stretch of the coupons had not been

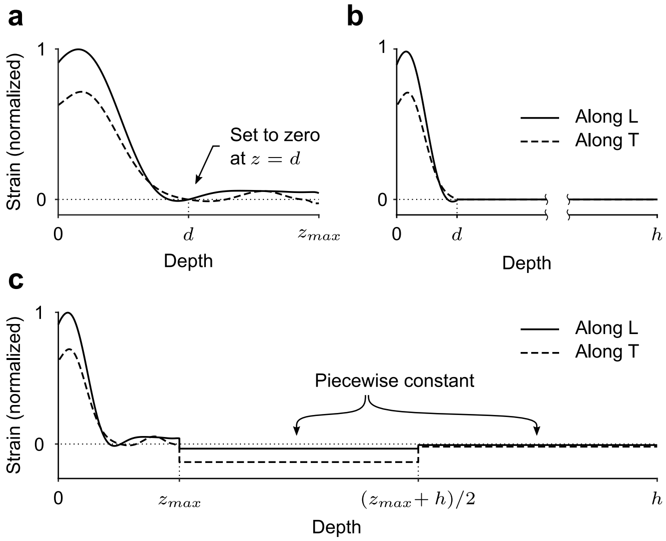

Figure 6.5 Typical eigenstrain profiles. (a) Near-surface eigenstrains computed from curvature and residual stress measurements using equation (6.10). (b) Peening-induced eigenstrains obtained by truncating the profiles in (a) at the end of the peening affected layer. (c) Through-thickness profiles obtained by extending the profiles in (a) with piecewise constant functions. The magnitude of the piecewise constant parts is chosen such that if these profiles were input in a model of a small coupon, they would induce the same axial stretch and the same curvatures as those that would be measured.

characterized, the constant terms $\varepsilon_{ii}\big|_{z=0}$ in (6.10) could not be determined directly. To enable comparing eigenstrain profiles, the missing constant was set such that the eigenstrains were equal to zero at the end of the peening-affected layer, that is, $\varepsilon^*_{ii}(d) = 0$, as shown in figure 6.5a. Since residual stress measurements showed that d varied little across specimens, we used $d = 0.5$ mm in all cases. (Recall from section 6.2.2 that the depth of the peening-affected layer can be estimated from the location of the tensile residual stress peak; also see Korsunsky, 2005.) Although it is sensitive to experimental errors and oscillations in the profiles, this approach is sufficient for the purpose of this analysis.

6.4.2 Accounting for initial eigenstrains

Equations (6.10) only return eigenstrains up to the depth at which residual stresses have been measured—in this case $z_{max} = 1$ mm. However, the shape of residual stress profiles measured in as-rolled sheets (fig. 6.2) indicates that anisotropic incompatible eigenstrains are initially present through the entire thickness of the specimens.

To estimate how eigenstrains deeper than z_{max} affected the final deformed shape of free-to-deform specimens, we first input the previously identified peening-induced eigenstrains, i.e.,

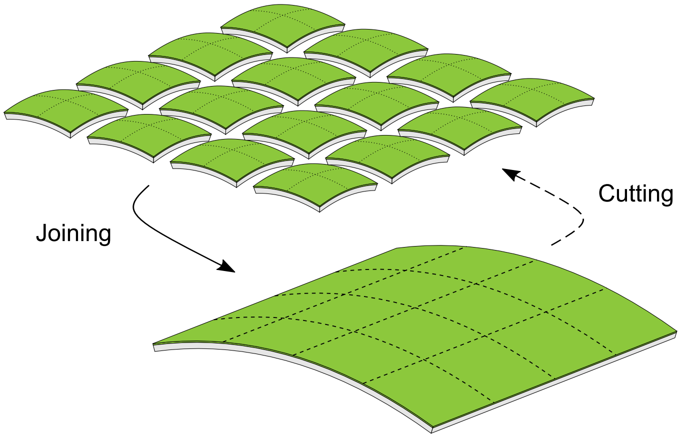

Figure 6.6 Thought experiment where a large peen formed plate is cut into many small coupons and the coupons are then joined back together. If neither cutting nor springback induce plastic deformation, then the process is reversible.

only the $z < d$ part or the profiles, into a finite element model of the specimens and solved for equilibrium. Figure 6.5b shows a typical profile used for these simulations. This provided an estimate of the shape that the specimens would have assumed if no initial eigenstrains were present. These results were then compared to a second set of simulations that included the contribution of initial eigenstrains.

A simple way to perform these simulations consists in constructing idealized eigenstrain profiles $\hat{\varepsilon}^*_{ii}(z)$ that, when input into a model of the coupons, induce the same in-plane stretch and the same curvatures as those that were experimentally measured, then to input these profiles into a model of the sheets. This process may be interpreted as reassembling a sheet by joining together several coupons, as illustrated in figure 6.6; it is the opposite of coupons removal.

Since all quantities are explicitly integrated over the thickness in conventional thin plate theories, any eigenstrain profiles having the same resulting values and first moments will yield the same deformed shape. Therefore, the only conditions that idealized profiles must satisfy to induce the desired axial stretch and curvatures is

$$\int_0^h \hat{\varepsilon}^*_{ii}(z)\,\mathrm{d}z = \alpha_i, \qquad \int_0^h \hat{\varepsilon}^*_{ii}(z)\,z\,\mathrm{d}z = \beta_i, \qquad i = \{x, y\}. \tag{6.11}$$

In what follows, we use

$$\hat{\varepsilon}^*_{ii}(z) = \begin{cases} \check{\varepsilon}^*_{ii}(z) & \text{if } z \leq z_{max}, \\ \theta_i^{top} & \text{if } z_{max} < z \leq (z_{max}+h)/2, \\ \theta_i^{btm} & \text{if } (z_{max}+h)/2 < z \leq h, \end{cases} \tag{6.12}$$

where $\check{\varepsilon}^*_{ii}$ are the eigenstrains identified in section 6.4.1 and θ_i^{top} and θ_i^{btm} are constants whose values are chosen so as to satisfy (6.11). Figure 6.5c shows a typical profile obtained in this way. The reason for choosing such profiles instead of simpler ones is that, by construction, they not only induce the correct deformations but also the correct residual stresses in the $z \leq z_{max}$ region. Consequently, they enable to estimate residual stresses present in the $z \leq z_{max}$ region of the original sheets before the coupons were removed—in other words, to correct for the stress relaxation that occurred during removal. An explicit expression for the constants can be obtained by substituting (6.12) into (6.11), integrating, and solving for the constants. This yields

$$\begin{aligned} \theta_i^{\text{top}} &= \quad [(\alpha_i - \check{\alpha}_i)(3h + z_{max}) - 4(\beta_i - \check{\beta}_i)]/(h - z_{max})^2, \\ \theta_i^{\text{btm}} &= -[(\alpha_i - \check{\alpha}_i)(3z_{max} + h) - 4(\beta_i - \check{\beta}_i)]/(h - z_{max})^2, \end{aligned} \tag{6.13}$$

where

$$\check{\alpha}_i = \int_0^{z_{max}} \check{\varepsilon}^*_{ii}(z)\,\mathrm{d}z \qquad \text{and} \qquad \check{\beta}_i = \int_0^{z_{max}} \check{\varepsilon}^*_{ii}(z)\,z\,\mathrm{d}z. \tag{6.14}$$

Finally, using the inverse of equation (6.7),

$$\alpha_i = (a_i h^2 + 2b_i h)/2, \qquad \beta_i = (2a_i h^3 + 3b_i h^2)/6, \tag{6.15}$$

and recalling that $a_i = -\tilde{\kappa}_i$ and $b_i = \tilde{\varepsilon}_{ii}|_{z=0}$, where a 'tilde' is used to indicate that a quantity is measured on a coupon, the constants can be expressed in terms of quantities that can be determined experimentally.

Again, because the in-plane stretch of the coupons had not been characterized, the value of $\tilde{\varepsilon}_{ii}|_{z=0}$ was unknown. However, for moderately curved *uniformly* shot peened plates, this term has very little influence on computed curvatures and residual stresses. Indeed, it has the same effect as a homogenous in-plane expansion which, by analogy with homogenous thermal expansion, only causes the structure to expand without inducing stresses. In fact, curvatures are independent of $b_i\,(= \tilde{\varepsilon}_{ii}|_{z=0})$ in the linear domain, that is, for very small curvatures, as shown by equation (6.9). In what follows, we arbitrarily used $\tilde{\varepsilon}_{ii}|_{z=0} = \kappa_i h/2$, which corresponds to a scenario where the midplane of the plates does not stretch. Running the simulations for any $\tilde{\varepsilon}_{ii}|_{z=0}$ in the $\pm\ 5 \times 10^{-3}\,\mathrm{mm\,mm^{-1}}$ range, where $5 \times 10^{-3}\,\mathrm{mm\,mm^{-1}}$ is the typical magnitude of peening induced eigenstrains (see later sections), yielded virtually identical results.

6.4.3 Finite element simulations

All finite element simulations were done with Abaqus 6.14. Taking advantage of symmetries, only one quarter of the geometries were meshed, as shown in figure 6.7a. Eigenstrain profiles were input as pseudo-thermal strains with the UEXPAN subroutine as described in Jun and Korsunsky (2010). The distribution of integration points through the thickness was as shown in figure 6.7c, with 99 integration points over $0 \leq z \leq z_{max}$, 3 integration points over $z_{max} \leq z \leq (z_{max} + h)/2$, and 3 integration points over $(z_{max} + h)/2 \leq z \leq h$. Geometric nonlinearities were included in all analyses. Gravity was neglected as additional simulations showed that it caused variations in curvatures of less than 5 %.

Similar simulations were used to compute residual stresses in prestressed strips while the strips were still held onto the prestressing jig. Figure 6.7b shows the 1/4th symmetry model used for these simulations. The contact between the strips, clamps, and support beams was modeled by prescribing z-displacements along the lines where the strips touched support beams.

6.5 Results

The left panels of figures 6.8 and 6.9 show near-surface eigenstrains identified in the coupons removed from free-to-deform and prestressed strips, respectively. The shape of the profiles is typical of that induced by peening treatments: eigenstrains peak at or near the peened surface then decrease gradually until they reach a plateau, approximately 0.5 mm below the surface, which corresponds to the end of the peening-affected layer. In all cases, eigenstrains are larger in the directions in which the specimens bent the most, that is, along the L direction for free-to-deform sheets, and along the prestress direction for prestressed strips.

Inputting these eigenstrains (including the piecewise constant extension not shown in the figures) into a model of the coupons yields the residual stresses shown as solid lines in the middle panels. In all cases, computed stresses match experimental data, which confirms that eigenstrains present in the coupons were correctly identified.

Estimates of residual stresses in the original specimens, prior to coupons removal, are shown in the right panels. For free-to-deform specimens, the only apparent difference between these profiles and those in the coupons is that residual stresses in the L and T directions in sheets

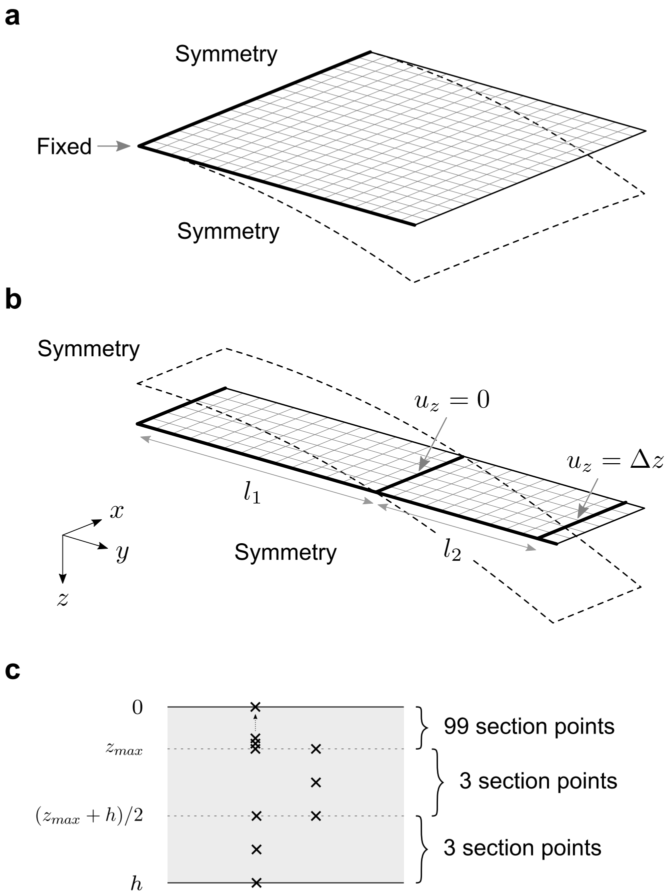

Figure 6.7 Finite element models used to simulate (a) conventional peen forming and (b) stress peen forming experiments. For the latter model, contact between prestressed strips, clamps, and support beams was modeled by prescribing z-displacements along the lines where the strips touched support beams (see figure 6.3). The mesh used for simulations was three times finer than that shown. (c) Distribution of integration points through the thickness of the shell elements.

Table 6.2 Experimental and simulated curvatures of sheets used for conventional peen forming experiments.

Specimen	Experimental curvatures ($\times 10^{-4}$ mm^{-1})		Simulated curvatures ($\times 10^{-4}$ mm^{-1})				Relative error (%)			
			Including initial eigenstrains		Neglecting initial eigenstrains		Including initial eigenstrains		Neglecting initial eigenstrains	
	Along L	Along T	Along L	Along T	Along L	Along T	Along L	Along T	Along L	Along T
Sheet 4:1–L	2.50	2.19	2.54	1.72	2.18	2.27	2	-21	-13	4
Sheet 2:1–T	3.06	0.11	3.30	0.03	2.30	0.28	8	(-73)	-25	(155)
Sheet 1:1–L	3.46	−0.01	3.25	−0.07	2.64	−0.08	-6	(600)	-24	700
Sheet 1:2–L	3.56	0.30	3.18	0.38	0.40	2.18	-11	27	-89	627
Sheet 1:4–L	3.00	1.81	3.07	1.24	2.26	2.65	2	-31	-25	46

1:1–L and 2:1–T become almost superimposed over the first 0.2 mm below the peened surface owing to the bending of the specimens. Similarly, residual stresses in the L and T direction of prestressed strips are closer to one another than residual stresses in the coupons and they exhibit almost the same minimum in both directions.

Finally, table 6.2 lists experimentally measured and simulated curvatures for free-to-deform sheets. The fact that simulations that included the contribution of initial eigenstrains do not perfectly match experiments suggests that some plastic yielding occurred during coupons removal. Indeed, experimental and simulated deformed shapes should be identical if eigenstrains in the coupons and in the sheets were the same. Nevertheless, these simulations qualitatively reproduce the response of the sheets. Putting aside directions along which the sheets are almost flat, the relative error between measured and simulated curvatures ranges between −11 and 8 % in the L direction and between −31 and 27 % in the T direction. On the other hand, simulations that neglected the contribution of initial eigenstrains display larger errors in all but one case. Errors range from −89 to −13 % in the L direction and from 4 to 627 % in the T direction. The 627 % error for sheet 1:2–L is due to simulations incorrectly predicting long side bending instead of the observed short side bending. The curvatures of prestressed strips (not shown) were identical to prestress curvatures as jig constraints prevented the strips to deform.

6.6 Discussion

6.6.1 Influence of prestress

That larger eigenstrains developed in the direction in which specimens bent the most confirms that prestress, whether it results from externally applied loads or from the progressive deformation of an unconstrained specimen, does affect the distribution of peening-induced plastic

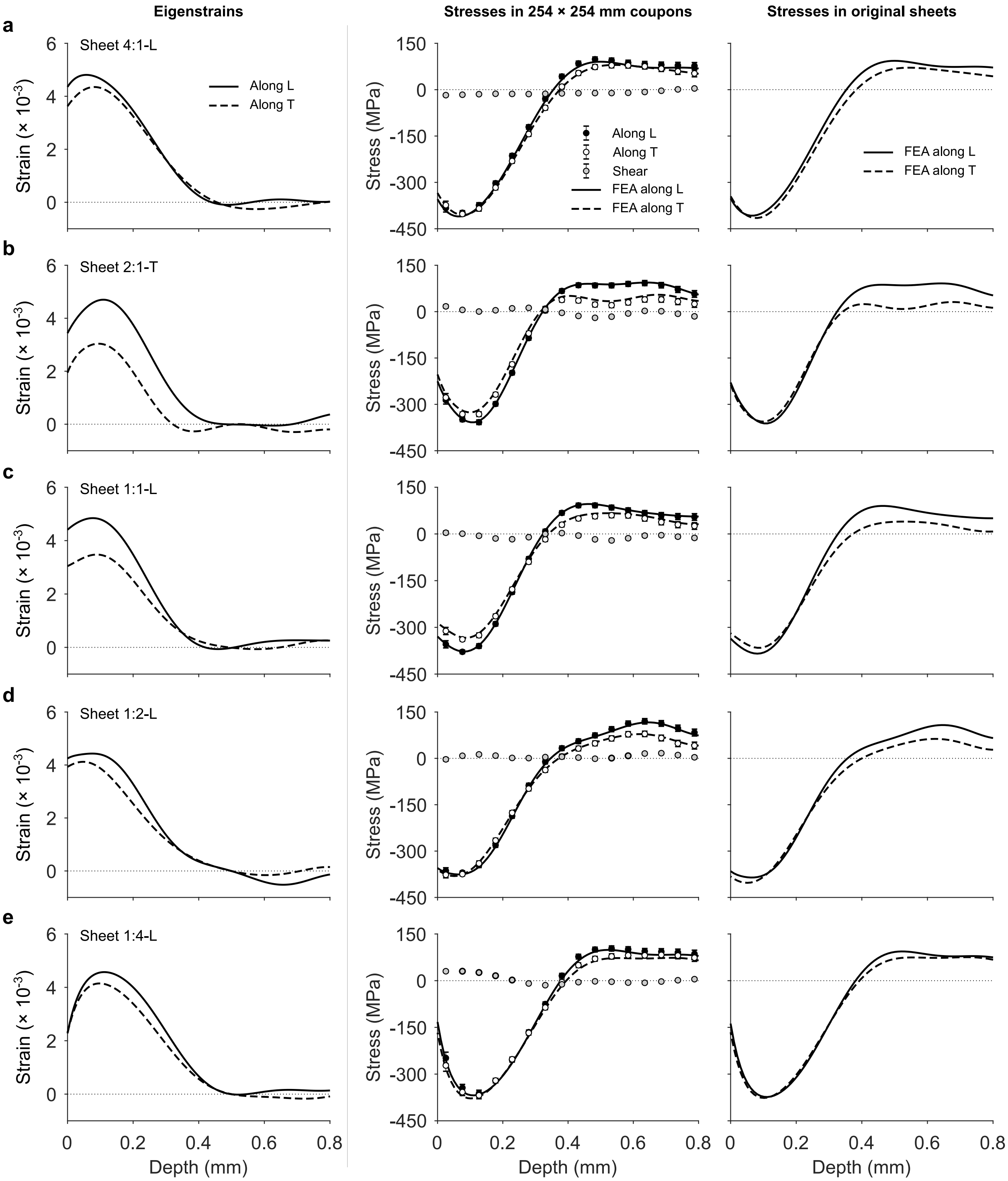

Figure 6.8 Eigenstrains and residual stresses in specimens used for conventional peen forming experiments. Left: Peening-induced eigenstrains. Middle: Residual stresses measured with the hole drilling method at the center of the coupons. Also shown are residual stresses obtained when the complete eigenstrain profiles (i.e., after they were extended to include the contribution of initial eigenstrains; see section 6.2.2) are input into a finite element model of the coupons. Right: Residual stresses in the sheets prior to removal of the coupons—estimated by inputting the same eigenstrain profiles into finite element models of the sheets.

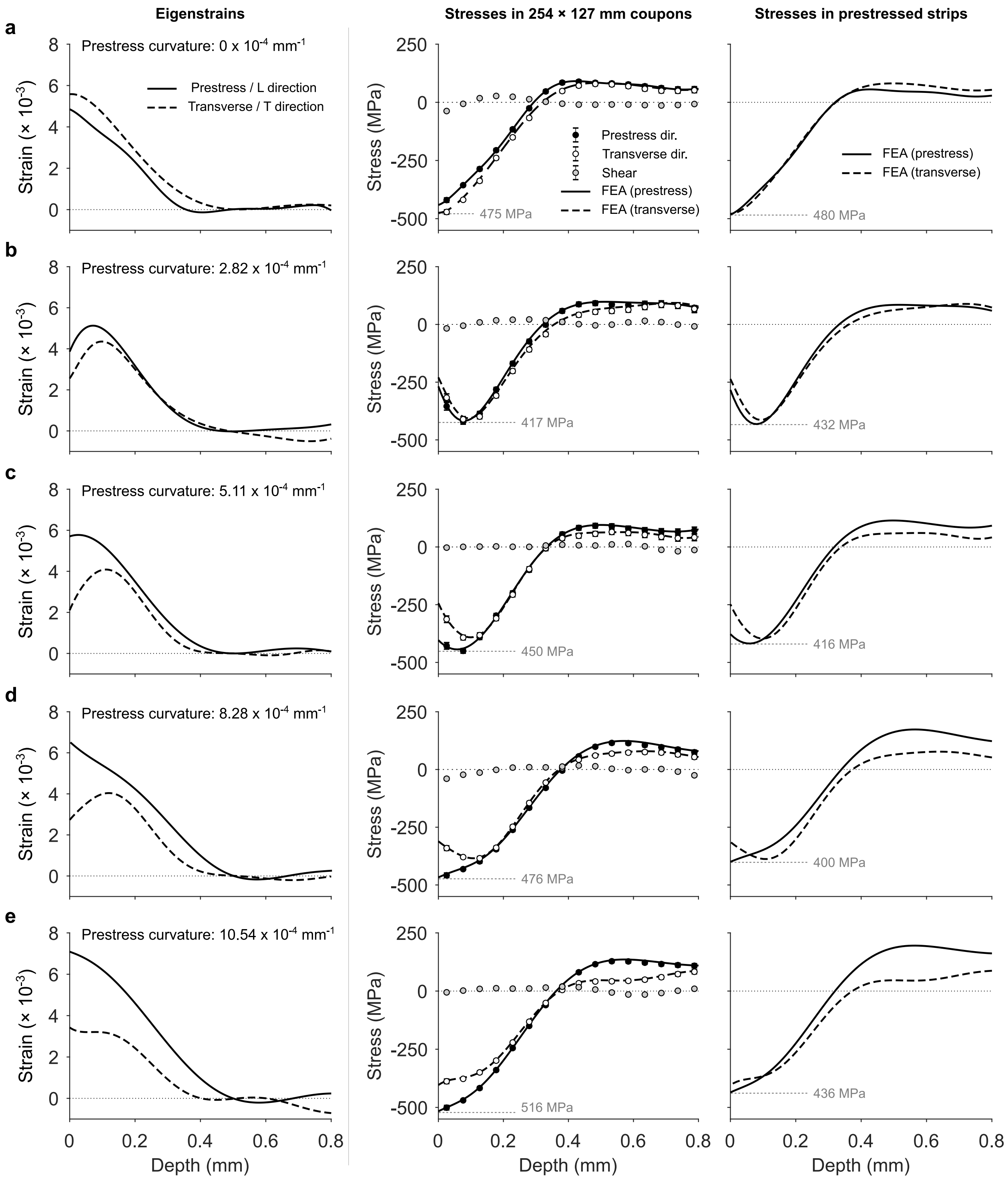

Figure 6.9 Eigenstrains and stresses in specimens used for stress peen forming experiments. Left: Peening-induced eigenstrains. Middle: Residual stresses measured with the hole drilling method at the center of the coupons and residual stresses obtained when the complete eigenstrain profiles are input into a finite element model of the coupons. Right: Stresses in the sheets prior to removal of the coupons while the sheets are still held on the prestressing jig—estimated by inputting the same eigenstrain profiles into finite element models of the strips.

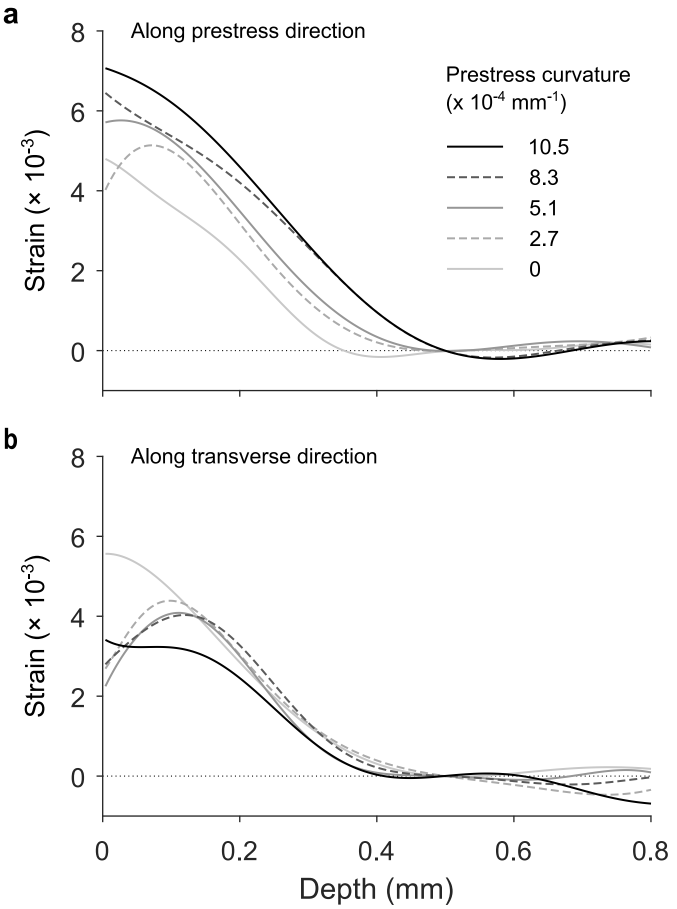

Figure 6.10 Near-surface eigenstrains in stress peen formed strips.

strains. This is further evidenced by figure 6.10 which shows the same eigenstrain profiles as in figure 6.9 but superimposed. Whereas eigenstrains along the transverse direction are almost superimposed, the magnitude of eigenstrains along the prestress direction increases with prestress curvature. Similar results were reported by Hu et al. (2015) for laser peening simulation of 2024–T3 aluminum sheets. Similarly, sheets 2:1–T and 1:1–L, which deformed into cylindrical shapes, display larger eigenstrains along the bending (L) direction whereas other unconstrained sheets, which deformed into elliptical or nearly spherical shapes, display similar eigenstrains in both directions (see fig. 6.8).

Although it can induce anisotropic eigenstrains, prestress alone, however, does not explain why all unconstrained specimens bent in the same direction. Consider for example the 1:1 aspect ratio sheet shown in figure 6.4. This sheet was peened with strokes parallel to the L direction and bent in L direction. If prestress alone did determine the bending direction, we would expect an identical sheet peened in the same conditions with strokes parallel to the T direction to bend along T. Experiments conducted in part 1 showed that this was not the case; all specimens bend along L, irrespective of the peening trajectory.

6.6.2 Influence of plastic anisotropy

One phenomenon that could explain why unconstrained specimens preferentially bent in the L direction is the known plastic anisotropy of the 2024–T3 aluminum alloy (Bron and Besson, 2004; Seidt and Gilat, 2013). Mild plastic anisotropy was observed during uniaxial tensile tests conducted in part 1. Clear evidence of how indenting a mildly plastically anisotropic material can result in a highly anisotropic response was reported in Prime (2017) where the authors measured residual stresses 40 % larger in the T direction than in the L direction at the center of a 10 mm thick 2024–T3 aluminum disk after it had been indented with two opposing cylindrical punches. This result was attributed to preferential plastic flow along the T direction as compression tests showed that stress-strain curves in the T direction were about 40 MPa below the curves in the L direction. Uniaxial compression tests reported in Seidt and Gilat (2013) for plates of the same alloy and thickness also identified the T direction as the weaker one, as did the tensile tests of part 1. These observations, however, should not be used be extrapolate the behavior of heavily shot peened specimens since laboratory tests do not capture the effect of the complex loading paths experienced by material points close to the peened surface.

Whether plastic flow occurred preferentially in the L or T direction can be assessed from eigenstrain profiles in the strip that was held flat during peening (fig. 6.9a). Indeed, for this strip, curvatures, hence the effect of prestress, were the same in all directions. Consequently, any observed anisotropy in near-surface eigenstrains would result from plastic anisotropy. Similarly, markedly anisotropic eigenstrains in free-to-deform 1:4 and 4:1 aspect ratio specimens (fig. 6.8a, e) would betray plastic anisotropy since the geometry of these specimens constrains them to deform into quasi-spherical shape, thus inducing approximately the same prestress in all directions. The profiles, however, show no clear sign of plastic anisotropy that would favor L side bending: eigenstrains are almost the same in both directions in free-to-deform specimens and they are slightly larger in the T direction for the specimen held flat during peening, which does favor T side bending.

6.6.3 Influence of initial eigenstrains

Another source of material anisotropy that could explain why free-to-deform specimens bent along the L direction is initial eigenstrains.

Figure 6.11 shows eigenstrains in an as-rolled sheet computed from the initial stress profiles

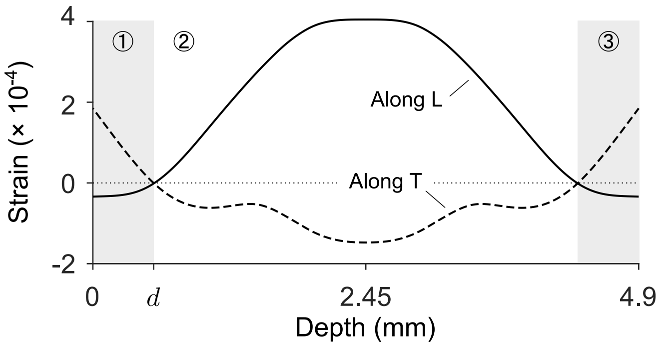

Figure 6.11 Eigenstrains in an as-received sheet computed from the residual stress profiles in figure 6.2 using equation 6.10. When a plate in which such eigenstrains are initially present is peened on the face located at $z = 0$, initial eigenstrains in the peening affected layer (region 1) are replaced by positive peening-induced eigenstrains about one order of magnitude larger than initial eigenstrains which causes the structure to bend. Eigenstrains present deeper into the material are left unaffected by the treatment.

in figure 6.2 using equation (6.10). If a specimen in which these eigenstrains are initially present is peened on the surface located at $z = 0$, large positive eigenstrains will develop in the peening affected layer and induce positive curvatures. Initial eigenstrains present deeper into the material, however, are left unaffected by the treatment. Let d be the depth the peening-affected layer. Because they are symmetric with respect to the midplane of the plate, initial eigenstrains in the $d \leq z \leq h - d$ region (region 2) induce no bending loads hence have no effect on curvatures. On the other hand, eigenstrains in the $z \geq h - d$ region (region 3) decrease curvatures if they are positive and increase curvatures if they are negative.

In this case, eigenstrains in region 3 are slightly larger in the T direction than in the L direction, thus favoring L side bending. However, their magnitude, hence the bending moment they induce, is one to two order of magnitude smaller than peening-induced eigenstrains. Although this suggests that initial eigenstrains have very little influence on the final deformed shape of the specimens, finite element simulations summarized in table 6.2 showed that this was not the case as neglecting initial eigenstrains caused simulated curvatures to vary by several tens of percent for all specimens and caused an inversion in the bending direction of the 1:2 aspect ratio sheet. Considering the low magnitude of initial eigenstrains, these results show that the response of uniformly shot peened plates, and in particular that of 1:2 aspect ratio plates, is highly sensitive to small variations in eigenstrains.

6.6.4 Competition between geometric effects and eigenstrains anisotropy

This sensitivity is surprising since, for specimens of aspect ratio smaller than one, L side bending can only occur if the eigenstrains are sufficiently anisotropic to compete against the geometric preference of rectangular sheets to bend along their long direction. This effect, which was described in Alben et al. (2011), comes from regions of double curvatures that develop near the free edges of plates loaded with biaxial eigenstrains and that lowers the elastic energy of the system, thereby making long side bending energetically favorable. In this section, we investigate the level of eigenstrain anisotropy required to overcome this effect and trigger short side bending.

To facilitate the discussion, we first introduce relevant dimensionless parameters. As discussed in Audoly and Pomeau (2010), it is usually possible to characterize the response of thin structures with very few dimensionless parameters with the same parameters being valid for both small and large deformations. Here, we propose to use

$$\bar{B} = 12(1+\nu)B_{avg}L^2/h^4, \quad \chi = (B_{long} - B_{avg})/B_{avg}, \quad \bar{\kappa} = \kappa L^2/h, \quad \nu, \tag{6.16}$$

where L is a characteristic length (here taken as the dimension along the longest side), h is the thickness, κ is any curvature measured on the plate,

$$B_{avg} = (B_{long} + B_{short})/2, \tag{6.17}$$

and B_{long} and B_{short} are the first eigenstrain moments with respect to the midplane of the plate in the long and short directions. Using the axis convention of figure 6.1a, the first eigenstrain moment with respect to the midplane of the plate along the i direction is given by

$$B_i = \int_0^h \varepsilon^*_{ii}(z)(h/2 - z)\,\mathrm{d}z. \tag{6.18}$$

The parameter $\bar{B}$ corresponds to the ratio of bending loads over bending rigidity rescaled by $(L/h)^2$, χ characterizes the anisotropy of eigenstrains, and $\bar{\kappa}$ is a dimensionless curvature. When eigenstrains are equibiaxial, these parameters coincide with those used in Faucheux et al. (2018) which, themselves, it recently came to our attention, closely resemble those used by Freund (2000) to characterize the response of thin film bilayers. In what follows, $\bar{B}$ and $\bar{\kappa}$ are referred to as the dimensionless load and the dimensionless curvature, respectively.

Figure 6.12 shows the evolution of dimensionless curvatures as a function of the dimensionless load for rectangular sheets of 1:1, 2:1, and 4:1 aspect ratio for $\chi = -6$ %, 0.1 %, and 6 %. These curves were obtained from finite element simulations using the same quarter plate model as described in section 6.4.3. Simple idealized eigenstrain profiles of the form

$$\varepsilon_{ii}^*(z) = \begin{cases} \theta_i & \text{if } z \leq h/2, \\ -\theta_i & \text{if } z > h/2, \end{cases} \tag{6.19}$$

where

$$\theta_i = \frac{\bar{B}h^3}{3(1+\nu)L^2}(1+\chi) \tag{6.20}$$

in the long direction and

$$\theta_i = \frac{\bar{B}h^3}{3(1+\nu)L^2}(1-\chi) \tag{6.21}$$

in the short direction were used to obtain the desired dimensionless loads and χ. As in section 6.4, the eigenstrains were applied uniformly. For $\chi = 0.1$ %, which corresponds to almost equibiaxial eigenstrains, simulations predict that all sheets bend preferentially along the long side, which is consistent with the analysis of Alben et al. (2011). For small dimensionless load (i.e., for small eigenstrain moments and/or thick plates), all sheets deform into spherical shapes. For larger dimensionless loads, out-of-plane deflections are no longer small compared to the thickness and geometric nonlinearities become significant: the stress stiffening that results causes the curves to bend downward. Perfect 1:1 aspect ratio sheets maintain a spherical shape far into the nonlinear domain, up to a dimensionless load of about 25, then suddenly transition to cylindrical configurations due to an elastic instability. All other geometries display a smooth transition between spherical and cylindrical shapes with curvatures in the long and short directions gradually separating. Increasing χ only causes the curves to separate faster and the elastic instability for sheets of 1:1 aspect ratio to be replaced by a smooth transition. Decreasing χ, however, causes a sudden inversion of the bending direction for sheets of 1:1 and 2:1 aspect ratio. The transition occurs at $\chi = 0$ for the former, and at about $\chi = -5$ % for the latter. In other words, for sheets of 2:1 aspect ratio, the first eigenstrain moment along the short direction must be about 10 % larger than that along the long direction for eigenstrain anisotropy to overcome the geometric preference of the sheets to bend along the long side.

The value of the dimensionless parameters for our specimens can be determined experimentally by noticing that, for a coupon small enough such that its response is not affected by geometric nonlinear effects,

$$B_i = \tilde{\kappa}_i h^3/12, \tag{6.22}$$

where $\tilde{\kappa}_i$ is the curvature of the coupon in the i direction (see appendix E for details). The third and fourth columns of table 6.3 list the values of $\bar{B}$ and χ thus computed from the

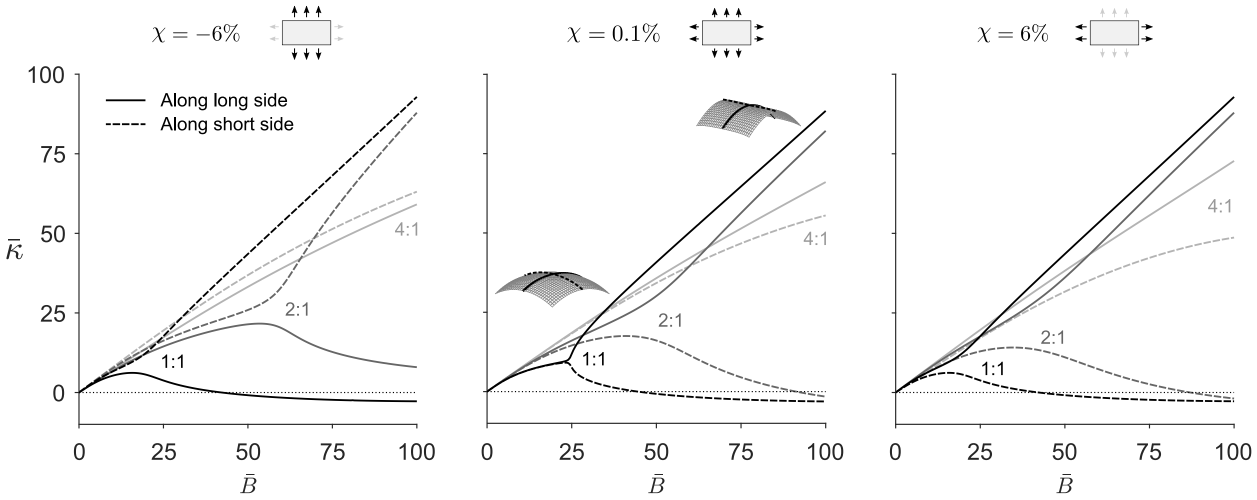

Figure 6.12 Master curves showing the relationship between dimensionless curvatures $\bar{\kappa}$ and dimensionless loads $\bar{B}$ for different levels of eigenstrain anisotropy χ for plates of 1:1, 2:1, and 4:1 aspect ratio. The curves were obtained by finite element simulations. For nearly equibiaxial eigenstrains (middle), square plates assume spherical shapes for dimensionless loads smaller than 25 then transition suddenly to an elliptical then cylindrical shapes due to an elastic instability. For all other aspect ratios and values of χ, the transition is gradual, and even more so as the strip is elongated or χ departs from 0. In the range of parameters considered here, plates always bend along the long side for $\chi > 0$ and they always bend along the short side for $\chi < -5\%$. For intermediate values of χ, the direction of largest curvature depends on the aspect ratio and on the dimensionless load.

Table 6.3 Dimensionless load $\bar{B}$ and eigenstrains anisotropy χ induced by all eigenstrains present in the specimens and by peening-induced eigenstrains only. The former were estimated from the curvature of the coupons while the latter where obtained by integrating previously identified eigenstrain profiles. Differences between the two sets of parameters are due to initial eigenstrains present below the peening-affected layer.

Specimen ID	Long side aligned with	All eigenstrains		Peening-induced eigenstrains only	
		$\bar{B}$ (-)	χ (%)	$\bar{B}$ (-)	χ (%)
Sheet 4:1–L	L	67	11.0	70.8	-4.4
Sheet 2:1–T	L	65	34.5	59.1	9.7
Sheet 1:1–L	-	66	23.7	61.5	7.6
Sheet 1:2–L	T	72	-18.6	67.0	-1.1
Sheet 1:4–L	T	66	-34.5	80.8	1.5

curvatures of coupons used for residual stress measurements. In this case, $\bar{B}$ ranges from 65 to 72, χ is positive for specimens with their long side aligned with the L direction, and it is less than $-18\,\%$ for specimens with their short side aligned with the T direction. To put these values into perspective, the last two columns of table 6.3 list the $\bar{B}$ and χ induced by peening-induced eigenstrains only—i.e., neglecting the contribution of initial eigenstrain present below the peening-affected layer. These values were obtained by integrating the previously identified near-surface eigenstrain profiles with equation (6.18) from $z = 0$ to $z = d = 0.5$ mm. Whereas $\bar{B}$ does not markedly change, χ drops by several percent, even changing signs for sheets 4:1–L and 1:4–L. This shows that χ is quite sensitive to small variations in eigenstrains and that only slightly anisotropic eigenstrains are needed to overcome the geometric preference for the sheets to bend along the long side.

The competition between geometry and eigenstrain anisotropy is further illustrated by the map in figure 6.13a which shows the direction of largest curvature as a function of the aspect ratio and χ at $\bar{B} = 70$. For perfect 1:1 aspect ratio plates, the boundary between the two regions is located at $\chi = 0$ and any small perturbation causes bending in either direction. The deformed shape on either side of the boundary are identical, but with the bending direction inverted, as illustrated in figure 6.13b. For small aspect ratios, the boundary asymptotically approaches the $\chi = 0$ line. This is because the bending along the long side and the short side of a narrow plate become decoupled. In this domain, the curvature in one direction is simply proportional to the first eigenstrain moment in this direction and there is no sharp transition when crossing the boundary: curvature in both directions are almost identical when $\chi = 0$

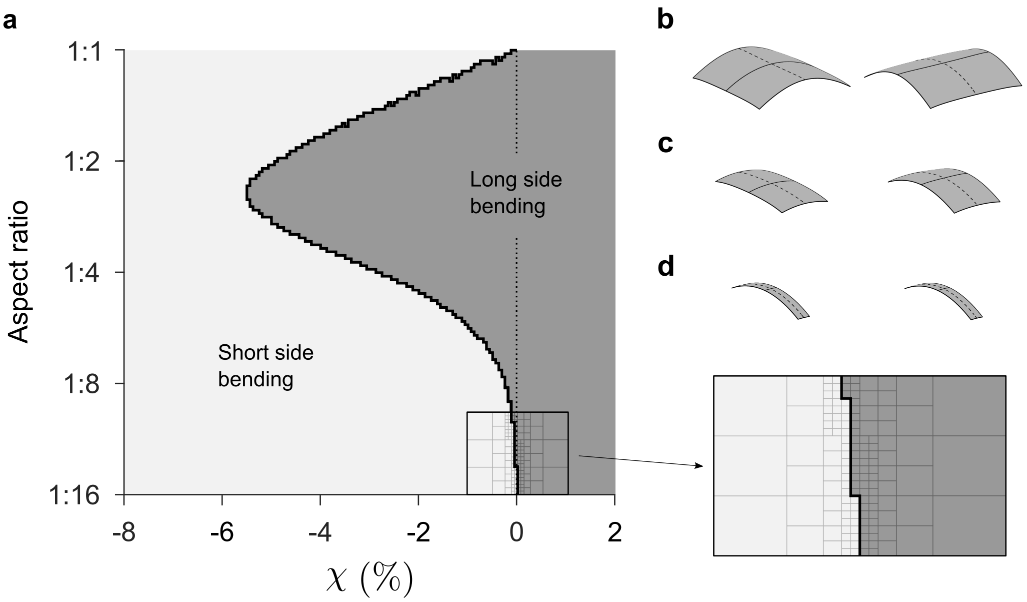

Figure 6.13 (a) Map showing the direction of largest curvature of rectangular plates of uniform thickness for $\bar{B} = 70$ and $\nu = 0.33$. The map is made of 3400 pixels, each pixel corresponding to one finite element simulation. The eigenstrains are larger along the long direction when $\chi > 0$ and vice versa. Plates of 1:1 aspect ratio and very elongated strips have their largest curvature in the direction along which the eigenstrains are the largest. For plates of intermediate ratio, there exist a domain in which the plates bend along their long side even when eigenstrains are largest along the short side. (b) Deformed shapes of plates of 1:1 aspect ratio for $\chi = \pm 1$ %, (c) of plates of 1:2 aspect ratio for $\chi = -6$ % and $\chi = -4$ %, and (d) of plates of 1:8 aspect ratio for $\chi = \pm 2$ %. Deflection magnified by a factor of 4.

and gradually separate when χ departs from zero. This is illustrated in figure 6.13d which shows the deformed shape of 1:8 aspect ratio plates for $\chi = -2$ % (left) and $\chi = 2$ % (right). For intermediate aspect ratios, the boundary between the two regions moves towards negative χ since larger eigenstrains along the short direction are required to induce short side bending. The point the furthest away from the $\chi = 0$ line is reached for an aspect ratio of (approximately) 1:2.4, which suggests that the edge effects that favor long side bending described in Alben et al. (2011) are most pronounced for this specific geometry at $\bar{B} = 70$.

6.7 Conclusion

The purpose of this paper was to clarify how different sources of anisotropy contributed to the final deformed shape of 2024–T3 aluminum rectangular sheets shot peened to full coverage with steel shot 0.71 mm in diameter and propelled at 41 m s^{-1}. In particular, we tried to explain why sheets that were free to deform during peening always bent in the rolling direction of the alloy, no matter what their aspect ratio or their alignment with respect to the rolling direction was.

Sources of anisotropy likely to explain the observed deformed shapes included the plastic anisotropy of 2024–T3 aluminum and the anisotropy of initial stresses inherited from the manufacturing process of the sheets that redistribute when their equilibrium is disturbed by peening. The analysis of plastic strain (/eigenstrain) profiles identified from residual stress and curvature measurements showed no clear sign of either mechanism prompting L side bending: peening-induced plastic strains were almost equibiaxial or slightly larger along the T direction—which would have favored T side bending—and bending moments induced by the rebalancing of initial stresses were one to two orders of magnitude smaller than those induced by the peening treatment. Further investigation revealed that the response of uniformly shot peened rectangular plates of uniform thickness is highly sensitive to small variations in internal loads and identified initial stresses as the most likely cause of L side bending. This sensitivity, however, is a feature of the simple geometries of the sheets and we believe that complex production parts such as pocketed or integrally stiffened panels should behave in a more controlled manner.

Once the sheets started to deform, significantly larger plastic strains developed in the bending direction. This effect is similar to that used in the variant of the process called stress peen forming where parts are held onto a curved jig during peening to obtain larger curvatures along the prestress direction. Whereas prestressed parts are firmly held into place during peening, the shape of unconstrained parts is continuously evolving; it depends on the precise peening sequence and on the geometry of the part. Capturing this effect in a numerical model of the process will likely require computer-intensive simulations. Alternatively, one could imagine implementing a feedback loop, possibly coupled to a learning system, to monitor the shape of a part as it is being peened and adjust the treatment accordingly. This kind of approach is well established in the industry (see for example Kittel et al., 1999; Lundquist et al., 2017) but remain largely unexplored in the literature.

Acknowledgements

The authors gratefully acknowledge financial support from Airbus, from the Rio Tinto group through a graduate scholarship, from the Canada Research Chairs program, and from the Natural Sciences and Engineering Research Council of Canada (NSERC; funding reference number 175791953). The prestressing jig used for stress peen forming tests was courtesy of Aérosphère and Centre Technologique en Aérospatiale (CTA).

CHAPTER 7 ARTICLE 3: SIMULATING PEEN FORMING AND COMPUTING PEENING PATTERNS WITH EIGENSTRAINS

Pierre A. Faucheux, Elie Sallé de Chou, Frédérick P. Gosselin, Martin Lévesque

Accepted at the 13th International Conference on Shot Peening (ICSP13), September 19–21 2017, Montréal, QC, CA

Abstract

Several procedures for the simulation of peen-forming have been reported in the literature. However, their predictive capabilities remain limited as they systematically require some form of calibration or empirical adjustments. Here, we demonstrate how simulation procedures based on the concept of eigenstrain can (i) bypass most of these limitations and (ii) provide a convenient framework to address the inverse problem of determining peening patterns that yield a desired target shape. Peen forming was modeled by mapping experimentally identified eigenstrains to finite element models of the parts to be formed. The finite element code was interfaced with an off-the-shelf optimization algorithm to compute peening patterns. For validation purposes, $305 \times 305 \times 6.5$ *mm 6061 aluminum plates were peened until saturation at* $10 \times 10^{-3}\,\text{inches A}$ *with Z425 shot. While uniformly shot peened plates deformed into a spherical shape, using appropriate peening patterns enabled to form the plates into cylindrical, 'wave', and saddle shapes. The latter are ubiquitous in wing panels manufacturing and usually require cumbersome stress peen forming operations. Here, only masking of unpeened areas was used.*

7.1 Introduction

All peening processes plastically deform a thin layer of material near the surface of the treated parts. Peening-induced plastic strains (fig. 7.1a) are incompatible; they cause residual stresses to develop inside the part and induce distortions. This latter effect can be significant when thin-walled structures are subjected to high intensity treatments. The process that makes use of peening-induced distortions to shape parts is called peen forming (fig. 7.1b). When peened uniformly with treatments of moderate intensity, plates deform into hemispherical shapes (fig. 7.1c). (Large distortions can lead to elliptical or cylindrical shapes as illustrated in Baughman (1970) and Faucheux et al. (2018); we do not consider these special cases here.) To obtain more complex geometries, it is necessary to somehow break the symmetry

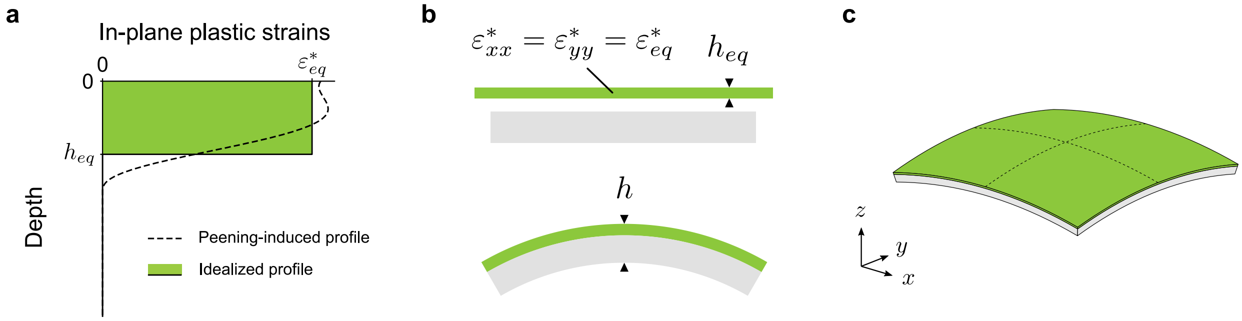

Figure 7.1 (a) Typical peening-induced plastic strain profile and equivalent 'step' profile used as loads in finite element simulations. (b) In-plane expansion of the upper layer causes the structure to bend. (c) Uniform treatments of moderate intensity make peened plates adopt a spherical deformed shape.

of peening-induced loads. Varying the intensity and/or the coverage over the surface is one way to do so. Another technique, called stress-peen forming, consists in elastically prestraining the part. This results in larger plastic strains in the direction in which the part is stretched. A combination of these techniques is usually required to form complex industrial parts (Baughman, 1970; Ramati et al., 1999).

In this paper, we focus on the computation of peening patterns. Few investigations on that topic have been reported in the shot peening literature. To the best of our knowledge, only VanLuchene and Cramer (1996) proposed a complete optimization strategy likely to yield such patterns. Nevertheless, although it was applied to form actual wing skins with "encouraging results", neither typical patterns nor experimental results were reported. The laser peening community, on the other hand, is more active on that matter, as demonstrated in Dearden and Edwardson (2003).

Interestingly, it appears that the problem at hand is similar to a variety of problems encountered in seemingly distant fields of engineering, for which successful procedures are readily available. This includes, for example, adaptive optics (Sheng, 2004), active control of plates (Koconis et al., 1994), as well as the design of passive actuators (Pajot et al., 2006; Fuchi et al., 2015). In all these examples, the common model system is a thin multilayered plate that deforms in response to the expansion of subsurface layers. Although the physical source of expansion may differ from one application to the other (plastic strains, piezoelectric effect, thermal expansion), the plate equations that govern the macroscopic response of the structures are identical. This suggest that these strategies could, for the most part, be transposed to peen forming.

In this article, we intend to demonstrate the feasibility of an automated computation of peening patterns. We first describe an optimization procedure directly inspired by Pajot et al. (2006) then present a preliminary laboratory scale validation.

7.2 Overview of numerical procedures

7.2.1 Computing deformed shapes for specified peening patterns: the direct problem

The direct problem consists in computing the deformed shape of a peened part with all peening parameters – including the peening pattern – being known. Here, we only considered geometrically linear analyses of plate-like structures. Finite element analyses were used for all simulations.

Peening induced loads were modelled as anelastic in-plane expansions of the surface of peened areas; see Faucheux et al. (2018) for details. These expansion profiles can be characterized experimentally (Korsunsky, 2009), or simulated, for example with impact simulations. When thin-shell elements are used, it is not necessary to input the full expansion profile in the model since loads are integrated over the thickness of the element: profiles having the same in-plane and bending resulting loads yield identical deformed shapes. In what follows, we used idealized ‘step’ profiles like that presented in figure 7.1a that are fully characterized by an equivalent depth h_{eq} and an equivalent in-plane expansion ε^*_{eq}.

The plates were discretized with rectangular patches (fig. 7.2a). Each patch can be meshed with one or several elements. Tri-layer laminate section properties were defined for each element, as shown in figure 7.2b. The upper and lower layers, with thicknesses of h_{eq}, could expand. The central layer did not expand. The upper and lower layers of all elements in a patch were linked to a single optimization variable $\chi_i \in [0, 1]$. The amplitude of the expansion profile input in the upper and lower layers of those elements was equal to the original expansion profile multiplied by χ_i. For idealized step profiles, it is constant through the thickness and is equal to $\varepsilon^*_{eq}\chi_i$. The case $\chi_i = 1$ corresponds to a fully peened area whereas $\chi_i = 0$ corresponds to an unpeened area. A peening pattern is fully characterized by the vector $\boldsymbol{\chi}$ that collects all optimization variables, where $\boldsymbol{\chi}^T = [\chi_1, \ldots, \chi_{2N}]$ and N is the number of patches.

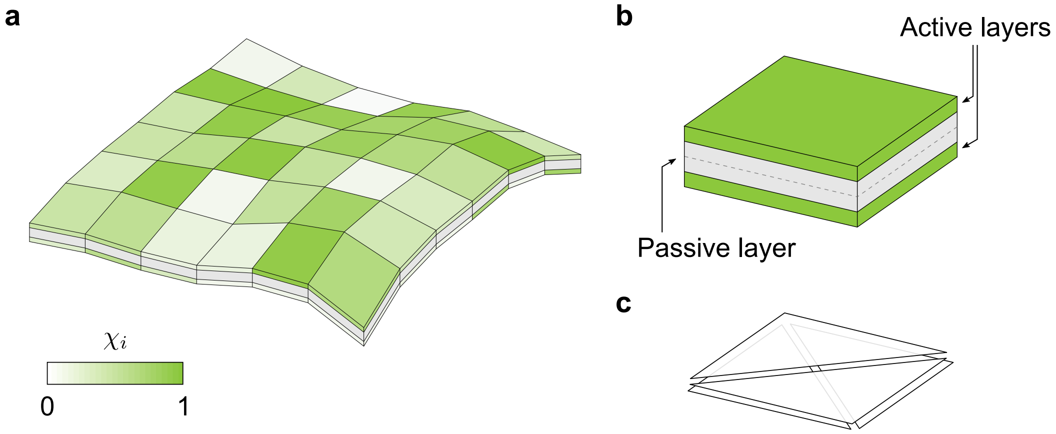

Figure 7.2 (a) Partition of a square plate into patches. One optimization variable is assigned to each face of each patch to control the amount of expansion experienced by the patch. (b) Tri-layered section properties. External layers can expand in their plane. The middle layer is passive. (c) Layout of DKT18 elements used to mesh each patch.

7.2.2 Computing peening patterns for specified target shapes: the optimization problem

The goal of the optimization procedure is to find a combination of optimization variables that best-fits a given target shape. For all the examples presented hereafter, we investigated the optimization problem

$$\begin{aligned} &\text{minimize} && \|\boldsymbol{z}(\boldsymbol{\chi}) - \boldsymbol{z}_{target}(\boldsymbol{x}_0, \boldsymbol{y}_0)\|_2^2 && \\ &\text{subject to} && 0 \leq \chi_i \leq 1, && i = 1, \ldots, n \\ & && \boldsymbol{A}^T \boldsymbol{\chi} \leq A_{max}, && \end{aligned} \tag{7.1}$$

where $\boldsymbol{z}$ is a vector of current nodal coordinates in the z direction, $\boldsymbol{x}_0$ and $\boldsymbol{y}_0$ are vectors of nodal coordinates in the x and y directions in the initial undeformed configuration, $\boldsymbol{z}_{target}(\boldsymbol{x}_0, \boldsymbol{y}_0)$ is a vector that contains coordinates of the target shape in the z direction evaluated at $(\boldsymbol{x}_0, \boldsymbol{y}_0)$, $\boldsymbol{A}$ is a vector that contains the area of the patches of elements associated with each optimization variable, and A_{max} is a user-defined upper bound on the peened area. It is implicitly understood that deformed nodal coordinates are computed with a model of the structure and that the computed solution satisfies equilibrium, compatibility, the constitutive law, and boundary conditions. The constraint $\boldsymbol{A}^T\chi \leq A_{max}$ was introduced as a remedy to checkerboard patterns that typically arise with the unconstrained formulation. Progressively decreasing the value of A_{max} forces the algorithm to eliminate inessential features in the patterns. Intermediates values of A_{max} tend to produce smooth gradients of

$\boldsymbol{\chi}$ while more stringent constraints steer the solution towards 0-1 patterns.

If the model used to compute the deformed shape is linear, the dependence of $\boldsymbol{z}$ on $\boldsymbol{\chi}$ can be made explicit by using the superposition principle. If $\boldsymbol{D}$ is a matrix whose ith column contains nodal coordinates computed for $\chi_i = 1$, $\chi_{j \neq i} = 0$, the problem can be recast in the equivalent form

$$\begin{aligned} &\text{minimize} && \|\boldsymbol{D}\boldsymbol{\chi} - \boldsymbol{z}_{target}(\boldsymbol{x}_0, \boldsymbol{y}_0)\|_2^2 \\ &\text{subject to} && 0 \leq \chi_i \leq 1, \qquad i = 1, \ldots, n \\ & && \boldsymbol{A}^T\boldsymbol{\chi} \leq A_{max}. \end{aligned} \tag{7.2}$$

This form corresponds to a norm approximation problem with constraints, which is convex (Boyd and Vandenberghe, 2004). When there are more optimization variables than nodes, $\boldsymbol{D}$ is rank-deficient and multiple optimal solutions might coexist. This problem can be dealt with constrained least square algorithms. This was the approach favored by VanLuchene and Cramer (1996). Here, we preferred to address the first form of the problem with generic gradient-based algorithms as was done in Pajot et al. (2006). This choice was primarily motivated by the flexibility permitted by this formulation. Indeed, depending on the problem at hand, it might be necessary to consider alternative expressions for the cost function. Gradient-based algorithms also exhibits fast convergence rate; in our experience, the overall shape of the pattern becomes apparent after a small number of iterations. The least square problem can also be solved very efficiently, but it requires to build the $\boldsymbol{D}$ matrix, which can be time consuming when the number of patches is large.

7.3 Materials and methods

Samples Four 305 × 305 × 6.35 mm 6061–T651 aluminum plates were peened formed for validation purposes. One plate was peened uniformly. The remaining three were peened with patterns.

Peening treatment All peening operations were performed on an automated Canablast shot peening system. Z425 ceramic shot (St-Gobain; between 0.425 and 0.6 mm in diameter) compliant with AMS 2431/7 rev. B (2013) were used. The shot were propelled at $88\,\mathrm{m\,s^{-1}}$ on average (measured with a ShotMeter G3 supplied by Progressive Technology) at a mass flow rate of 4.5 kg/ min. The Almen intensity was 10.4×10^{-3} inches A. It was chosen low enough so that out of plane displacements remained small (since we assumed geometrically linear behavior in all simulations), and that uniformly peened plates deformed into spherical shapes. All samples were peened at 250 % coverage. Unpeened areas were protected with several layers of cloth tape. The samples laid horizontally in the machine. They were secured with double sided tape during peening.

3D scans Scans of the deformed shapes were acquired on a Mitutoyo Legex 9106 three-dimensional coordinate measurement machine.

Finite element simulations Finite element simulations were done with an in-house finite element code. Each patch was meshed with four DKT18 elements (Batoz and Dhatt, 1992), as illustrated in figure 7.2c. Triangular elements were chosen for ease of implementation and in anticipation of an extension of the procedure to geometrically non-linear analysis following the procedure presented in Pajot et al. (2006). For all simulations presented hereafter, all translations and rotations were set to zero at the central node of the mesh to prevent rigid body modes. This node remained on the target shape at all time. The results were identical in all cases. A Young's modulus of 68 260 MPa and a Poisson ratio of 0.33 from the MMPDS-08 handbook were used for all simulations. Since we only intended to present a proof a concept, peening induced loads, i.e., h_{eq} and ε^*_{eq}, were not characterized experimentally. Instead, we used $h_{eq} = 0.5$ mm and $\varepsilon^*_{eq} = 10^{-3}$ which we estimated were realistic values for the peening treatment used based on our experience of the process.

Optimization Matlab's *fmincon* interior point algorithm was used for the optimization with the default termination criteria. The cost function and second constraint were scaled with $\max\left(\boldsymbol{z}_{target}\right)/100$ and A_{max}, respectively. In all the examples presented hereafter, simulations were systematically initialized from several initial guesses of $\boldsymbol{\chi}$ as multiple optimal solutions were expected. Uniform treatments, random patterns, random strips and random speckles were used as initial guesses. In all cases, the procedure converged towards the same solution.

Target shapes We selected cylindrical and saddle shapes of equation

$$z = \frac{1}{2}\left(\kappa_x x^2 + \kappa_y y^2\right), \tag{7.3}$$

as well as a 'wave' shape of equation

$$z = \begin{cases} \frac{1}{2}\kappa_y y^2 & \text{if } y > 0, \\ -\frac{1}{2}\kappa_y y^2 & \text{otherwise.} \end{cases} \tag{7.4}$$

Table 7.1 Curvature of the target shapes and upper limit on the peened area used for numerical experiments and validation.

Target shape	κ_x ($\times 10^{-5}$ mm^{-1})	κ_y ($\times 10^{-5}$ mm^{-1})	A_{max} (%)
Cylinder	-5.5	0.0	45
Saddle	-2.0	2.0	30
Wave	-	-8.0	40

Table 7.1 lists the values of κ_x, κ_y, and A_{max} used for numerical and validation experiments.

7.4 Results

7.4.1 Peening patterns

Figure 7.3 shows the optimal 0–1 peening patterns obtained for the cylinder, the saddle and the wave target shapes of table 7.1. All peening patterns exhibit the same symmetries as the target shape. It is especially clear for the saddle shape where the peening pattern consists of a repetition of the pattern obtained on 1/8th of the plate.

Similar patterns share similar features. For example, mirroring the right half of the wave pattern gives a pattern similar to that obtained for the cylinder shape (each half of the wave is a portion of a cylinder and both patterns try to achieve unidirectional curvature with straight free edges). Also note the similarity between the horizontal edges of the cylinder and the saddle shape.

In all cases, the largest discrepancies occur near the edges. This can be explained by the fact that, for all the samples considered here, it is necessary to peen large strips near the edges to approach the desired target shapes. Any attempt at minimizing the waviness near the edges, for example by using additional constraints as was done in Pajot et al. (2006), results in larger overall errors.

7.4.2 Validation

Figure 7.4 shows the patterns used for validation experiments, as well as simulated and measured deformed shapes. The patterns differ slightly from those in figure 7.3 because they were generated with an earlier version of the optimization code. The three-dimensional scans reveal that the samples exhibit the desired target shape. Here, we point out that the almost perfect match between simulations and experiments is artificial: because the actual $\{h_{eq}, \varepsilon^*_{eq}\}$

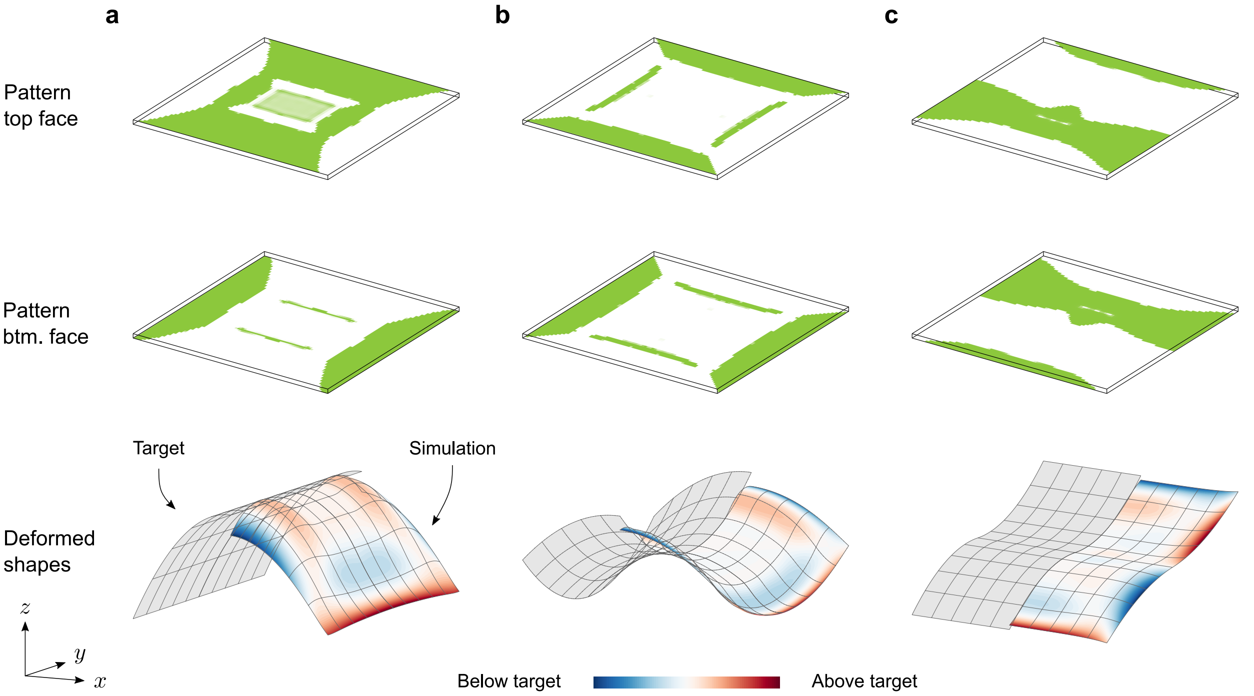

Figure 7.3 Peening patterns and simulated deformed shapes for (a) cylindrical, (b) saddle, and (c) ‘wave’ target shapes computed for the parameters listed in table 7.1. Not to scale.

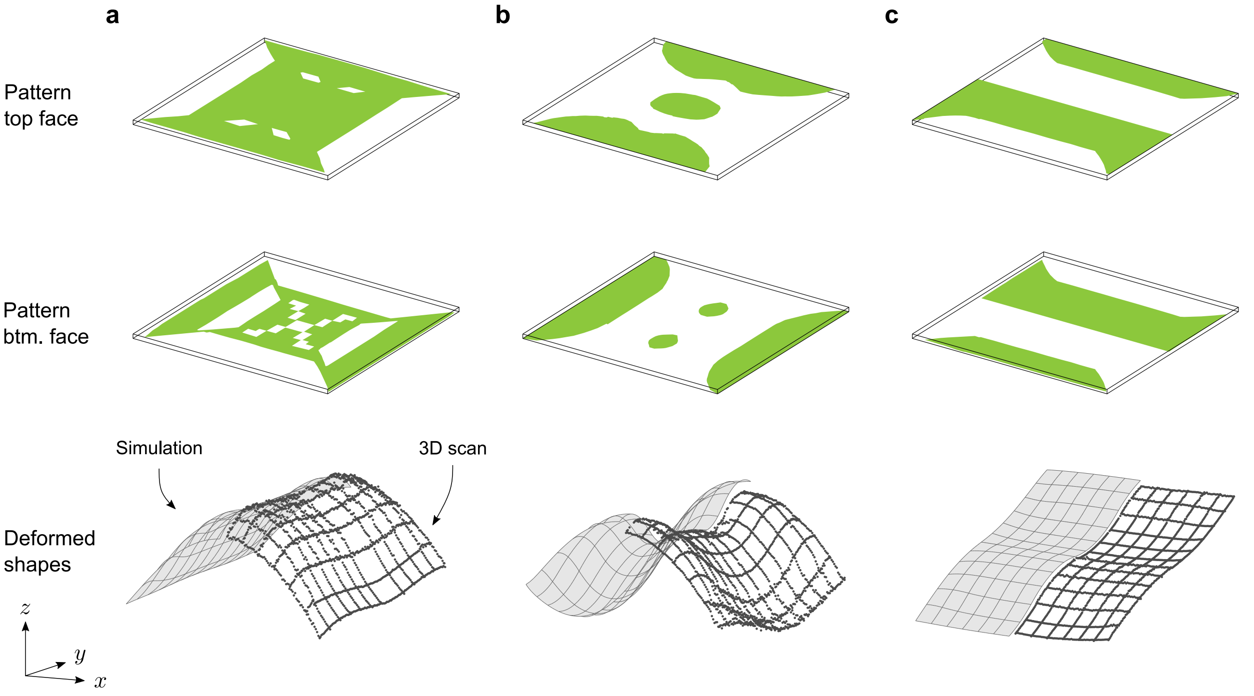

Figure 7.4 Peening patterns used for validation experiments, simulated deformed shapes, and 3D scans for (a) cylindrical, (b) saddle, and (c) ‘wave’ target shapes. Not to scale.

parameters were not characterized, computed deformed shapes were scaled by the same factor, the value of which was obtained by minimizing the squared error between simulated and measured deformed shapes. (Recall that, for the small deformations considered here, the response of the plate is linear. Therefore, scaling the deformed shape amounts to having scaled the loads and the target shape used for the optimization by the same amount.)

7.5 Conclusion

In this article, we demonstrated that it is possible to procedurally generate peening patterns for a given target shape. In particular, we managed to form a cylindrical shape, as well as a saddle shape from thick plates that deformed into a sphere when peened uniformly. Saddle shapes are usually manufactured by costly stress peen forming. Our strategy relied on (i) an idealization of peening induced loads as anelastic expansion and (ii) off-the-shelf optimization algorithms.

For demonstration purposes, we only investigated geometrically linear structural models. Extension to large displacements and rotations would be desirable for peen forming applications. A general framework for such analysis has already been presented in Pajot et al. (2006) and is currently being implemented. As an alternative to such computer intensive non-linear simulations, one could also envision using peening patterns computed with a linear code and adjust the peening intensity and/or coverage to reach the desired amplitude of deformation. Such peening patterns would not be optimal (the introduction of non-linear effects in Pajot et al. (2006) leads to different patterns that nevertheless shared striking similarities with linear patterns), but they are expected to yield results close to the optimal one. A similar argument was used by Fuchi et al. (2015) in the context of soft actuators manufacturing.

Note that the current procedure could be used for distortion correction applications, as it only involves small displacements. Additional refinements needed to tackle more complex problems can readily be implemented in the proposed framework. Obvious candidates are procedures derived from the field of topology optimization, such as appropriate filtering and penalization scheme, as well as optimization algorithms equipped to cope with large scale problems and a small number of constraints (Bendsøe and Sigmund, 2004). We recently implemented such strategies to investigate the forming of integrally stiffened panels, with encouraging results.

CHAPTER 8 ADDITIONAL RESULTS

8.1 Including geometric nonlinearities in the optimization procedure

The optimization procedure presented in chapter 7 only considered cases where the deflection of the peened formed plates remained small compared to their thickness. In this context, the response of the plates could be described with a linear model, which had two major advantages. First, evaluating the deformed shape of the structure at each iteration was fast; it only represented a fraction of the computational time, most of which was taken by the optimization algorithm. Secondly, for a cost function of the form (7.1), the optimization problem was convex. This enabled us to use efficient algorithms designed specifically for this class of problems and guaranteed that the computed solutions were global optimums. The architecture of the optimization procedure is, however, generic, and can readily be extended to large-deflection scenarios by replacing the linear plate model with one that includes geometric nonlinear effects—at the expense of evaluation speed and convexity.

To illustrate this, figure 8.1 shows peening patterns computed for the same specimen, the same peening treatment, and the same target shape using both a linear and a nonlinear plate model. Also shown are simulated and measured deformed shapes. The specimens were 762 × 762 × 4.9 mm 2024–T3 aluminum sheets from the same lot as those used for the experimental campaign of chapter 5 and peened with the same treatment. The target shape was a saddle of equation (7.3) with $\kappa_x = -\kappa_y = -10^{-4}$ mm^{-1}. For these parameters, the lateral deflection of the target is about 14.5 mm which, because it is only about three times the thickness, corresponds to the very beginning of the nonlinear regime. The depth h_{eq} and the amplitude ε^*_{eq} of the equivalent eigenstrain profiles used for simulations were obtained by requiring that the equivalent profiles yielded the same resulting eigenstrains α and the same first eigenstrain moment β as profiles that had previously been identified during the experimental campaign. This condition can be written as

$$h_{eq} = 2\beta/\alpha, \qquad \varepsilon^*_{eq} = \alpha^2/2\beta. \tag{8.1}$$

Here, we used $h_{eq} = 0.31$ mm et $\varepsilon^*_{eq} = 4.1 \times 10^{-3}$ in both directions, which were obtained by taking the average of the same parameters computed in the L and T directions from the eigenstrain profiles for coupon 4:1–L (fig. 6.8a). To account for in-plane deformations, the optimization problem was reformulated as

$$\begin{aligned} &\text{minimize} && \|\boldsymbol{z}(\boldsymbol{\chi}) - \boldsymbol{z}_{target}(\boldsymbol{x}, \boldsymbol{y})\|_2^2 && \\ &\text{subject to} && 0 \leq \chi_i \leq 1, && i = 1, \ldots, n \\ & && \boldsymbol{A}^T \boldsymbol{\chi} \leq A_{max}, && \end{aligned} \tag{8.2}$$

where the target shape is now evaluated from the current nodal coordinates—and not from the initial nodal coordinates as was the case in (7.1). Because of this modification, the optimization problem is no longer convex. As a result, there could be several local optima toward which the optimization algorithm could have converged, irrespective of whether a linear or the nonlinear finite element code was used. For linear simulations, the same finite element code as in chapter 7 was used. For nonlinear simulations, we implemented the small strain corotational formulation presented in Caselli and Bisegna (2013) using the same DKT18 element as in chapter 7 as a core element. Corotational formulations are appealing for the problem at hand because they make the computation of gradients with respect to the magnitude of follower loads (which are the optimization variables used here) much easier than would be the case with total or updated Lagrangian formulations (Pajot and Maute, 2006).

The left panels of figure 8.1 show the results obtained with the nonlinear code. The optimal pattern features an outer ring peened on both faces surrounding an unpeened region and exploits an elastic instability similar to that illustrated in figure 8.2 to achieve the desired saddle shape. Because it cannot capture this instability, the linear code returns a markedly different pattern shown in the right panels of figure 8.1. However, since out-of-plane deflections are moderate, the deformed shape obtained with this pattern stays close to the target shape, except near the rim of the plate where it causes the edges to curl. The largest error on z-displacements between the target shape and simulations is ± 1.97 mm for the linear pattern and ± 0.55 mm for the nonlinear pattern. The same error between the target shape and experiments is 2.53 mm for the linear pattern and 2.56 mm for the nonlinear pattern.

8.2 Automating the identification of peening patterns and process parameters

In all optimization examples presented so far, the peening treatment was selected beforehand and target shapes were chosen such that they could be closely approached with this treatment. This was done iteratively by increasing the curvatures of the target shapes until the optimal shape could not keep pace with the target. In practice, however, it is the opposite problem that needs to be solved: the target shape is a requirement and the objective is (i) to determine

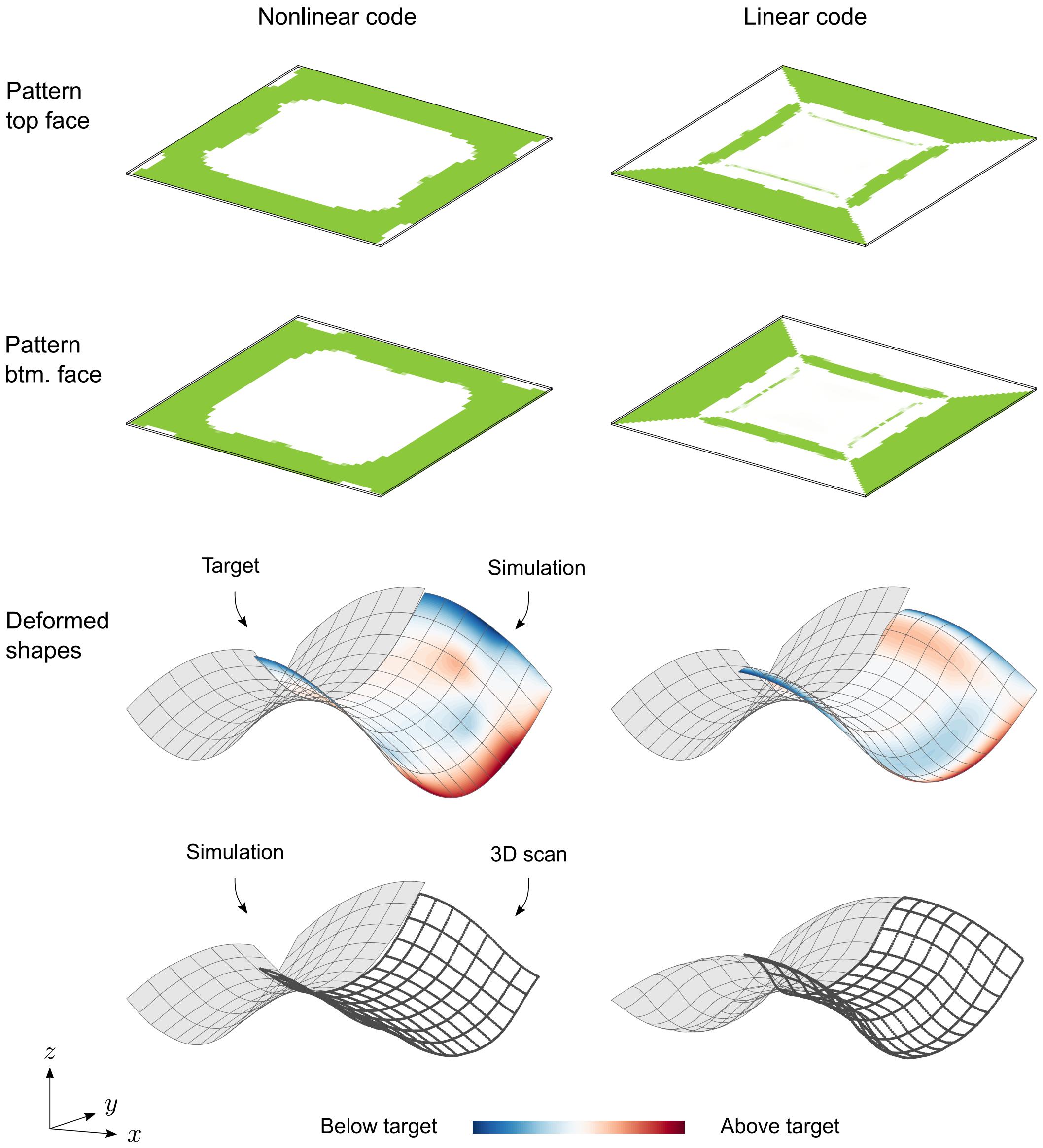

Figure 8.1 Optimal peening patterns computed with the linear and nonlinear optimization codes for 762 × 762 × 4.9 mm 2024–T3 sheets peened to full coverage with SCCW28 shot at an Almen intensity of 12×10^{-3} inches A and a target shape of equation $z = \left(\kappa_x x^2 + \kappa_y y^2\right)/2$ whith $\kappa_x = -\kappa_y = -10^{-4}$. Also shown are simulated deformed shape and 3D scans of sheets used for validation experiments. The largest error on z-displacements between the target shape and simulations is ± 1.97 mm for the linear pattern and ± 0.55 mm for the nonlinear pattern. The same error between the target shape and experiments is 2.53 mm for the linear pattern and 2.56 mm for the nonlinear pattern.

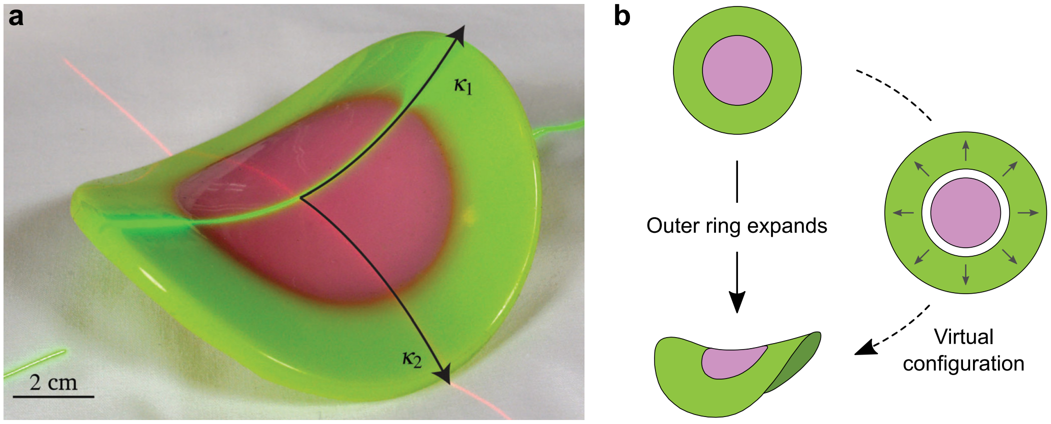

Figure 8.2 Illustration of the elastic instability causing an initially flat plate to deform into a saddle shape when an outer ring of material undergoes uniform in-plane expansion. (a) Composite structure made of a ring of polyvinylsiloxane surrounding an annulus of the same material but with a different initial concentration in free polymer chains. The system was initially flat. The diffusion of free polymer chains caused the outer ring to swell and triggered the instability. (b) Schematic illustration of the process. Adapted from Pezzulla et al. (2015) with permission from The Royal Society of Chemistry.

whether the prescribed shape can be peen formed and, when this is the case, (ii) to find a peening pattern and process parameters that yield the desired shape within acceptable tolerances. In addition, the treatment must be compatible with production requirements. The latter usually include using as few different shot types as possible, [1] ensuring that the maximum allowed intensity and coverage are not exceeded, and maximizing the smoothness of the patterns—as intricate patterns with many details and sudden variations of intensity or coverage are harder to manufacture than smoother, simpler patterns. To achieve this, we propose the following four-step procedure.

1. Run the optimization procedure presented in previous sections without any constraint apart from the upper and lower bound on $\boldsymbol{\chi}$ and with a very large value for the amplitude of the expansion in the active layer. For example, use the $\{h_{eq}, \varepsilon^*_{eq}\}$ computed with equations (8.1) for the most intense treatment that the available peening equipment can deliver. If, at the end of this analysis, the optimal shape does match the target shape within tolerances, proceed to step 2. Otherwise, the target shape can likely not be peen formed.

---

[1] Usually one or two, and ideally the same as those already used in production, since switching to a different media in large peening cabinets requires an in-depth cleaning followed by conformity tests. This process can takes up to several hours and interrupts production.

2. Re-run the analysis by progressively decreasing the intensity of the treatment until the error between the optimal shape and the target shape becomes unacceptable—using the same metrics as those used to accept or reject a part to define ‘acceptable’. This gives a lower bound on the intensity of the peening treatment.

3. Identify process parameters that (i) deliver an intensity within the upper bound of step 1 and the lower bound of step 2 and (ii) that are compatible with production requirements. For example, only a finite number of shot type might be available, and certain combinations of intensity and shot size might be proscribed if they result in a poor surface finish.

4. For this treatment, re-run the analysis by progressively adding or tightening constrains to steer the optimal solution towards a peening pattern that can be easily manufactured.

   For example, decreasing the upper limit on the area that is allowed to be peened tends to force the algorithm towards 0–1 designs that can be manufactured by masking the part with a ‘negative’ of the peening pattern and indiscriminately blasting the entire surface. Similar 0–1 designs can be obtained with appropriate penalty schemes, as described in Bendsøe and Sigmund (2004) and Pajot et al. (2006). When automated peening equipment is available that can continuously adjust process parameters, less severe constraints that allow for smooth transitions between peened and unpeened areas can be used, such as those listed in VanLuchene and Cramer (1996). Note that, although they can improve the manufacturability of a pattern, constraints inevitably degrade the agreement between the optimal solution and the desired shape.

   If, at the end of this step, the optimal shape does match the target shape within tolerances, return to step 3 and select a different treatment.

To illustrate the third step, suppose that a perfect 0–1 pattern has been computed, that is, that all components of the optimal $\boldsymbol{\chi}$ are either zero or equal to the same value, χ. We now wish to find a treatment that induce the same axial loads and bending moments as a step of depth h_{eq} and of magnitude $\chi\,\varepsilon^*_{eq}$. Unless fast and accurate impact models are available, this must be done experimentally. To narrow down the search, a preliminary step would be to build databases of $\{h_{eq}, \varepsilon^*_{eq}\}$ versus process parameters using available experimental data sets. Most companies and research team involved with peening processes already have databases of residual stress profiles at their disposals from which it is possible to extract eigenstrain profiles using the procedures listed in chapter 4 then $\{h_{eq}, \varepsilon^*_{eq}\}$ using equations (8.1).

8.3 A fast experimental procedure to identify peening induced loads

Identifying peening induced loads from residual stress measurements is costly and time consuming, even when only a few candidate treatments have to be characterized. Alternatively, these loads can be obtained directly from curvature and extension measurements performed on small representative coupons. Indeed, combining equations (8.1), (6.4), (6.9), and (6.15) yields

$$h_{eq} = \frac{2}{3}\left[\frac{3h\,\tilde{\varepsilon}\big|_{z=0} - 2\tilde{\kappa}h^2}{2\,\tilde{\varepsilon}\big|_{z=0} - \tilde{\kappa}h}\right], \qquad \varepsilon^*_{eq} = \frac{3}{4}\left[\frac{\left(2\,\tilde{\varepsilon}\big|_{z=0} - \tilde{\kappa}h\right)^2}{3\,\tilde{\varepsilon}\big|_{z=0} - 2\tilde{\kappa}h}\right], \tag{8.3}$$

where, it is recalled, $\tilde{\kappa}$ is the curvature of a small coupons of the same thickness, made of the same material, and peened in the same conditions as the actual part, and $\tilde{\varepsilon}\big|_{z=0}$ is the in-plane strain on the upper face of the coupon measured with respect to an unpeened configuration.

Rereading Harburn and Miller (1982) in light of the results presented here reveals that the idea of characterizing peening induced loads by measuring the curvature and extension of small coupons has been used by Boeing since at least the 1980s. Additional details on how the company has been building databases of curvature and extension for materials, thicknesses, and peening treatments used in production to generate data to feed their own optimization procedures can be found in VanLuchene et al. (1995).

Despite its simplicity, this approach is hampered by the fact that peening induced in-plane strains are small. For example, based on the experimentally determined eigenstrain profiles of figures 6.8 and 6.9 and on equations (6.3), (6.4), and (6.7), in-plane strains in the 4.9 mm thick coupons used for the experimental campaign can be estimated to about $10^{-3}\,\mathrm{mm\,mm^{-1}}$ on the upper face, and to about half this value on the bottom face. Although such strains can readily be measured with appropriate equipment, for example strain gauges, this requires special care and instrumentation that is not always compatible with production requirements.

Now suppose that several coupons of different thicknesses were machined in the same base plate and that all were peened in the exact same conditions. Further suppose that the coupons were initially stress-free. Because they result from highly localized interactions between shot and the peened surface, peening induced plastic strains should be almost identical in all the coupons—provided that their thickness is large compared to the thickness of the peening affected layer such that geometry does not affect the outcome of the impacts. When this is the case, the resulting eigenstrains and the first eigenstrains moment in all coupons are identical and are equal to

$$\alpha = \int_0^d \varepsilon^*(z)\,\mathrm{d}z, \qquad \beta = \int_0^d \varepsilon^*(z)\,z\,\mathrm{d}z,$$

where d is the depth of the peening affected layer. Finally, combining equations (E.1) and (E.2) yields

$$\tilde{\kappa}^{(i)} {h^{(i)}}^3/12 = \alpha h^{(i)}/2 - \beta, \tag{8.4}$$

where superscripts are used to denote quantities referring to the ith coupon. Writing this equation for each coupon results in a linear system that can be solved for α and β. With this method, the only quantity that needs to be measured is the curvature of the coupons, which can for example be done using Almen gauges already used in production. Note that, although two measurements suffice to determine α and β, performing more measurements and seeking the least-squares solution to (8.4) should prove less sensitive to dispersion in the results and experimental errors. A similar method had previously been proposed by Roth et al. (1984) and Bernasconi and Roth (1987), although the author's aim was not to identify loads for peen forming, but rather to quickly estimate the depth of the peening affected layer and the magnitude of peening induced residual stresses for fatigue applications.

To illustrate this method, figure 8.3 shows a plot of $\tilde{\kappa}h^3/12$ versus h for 174–PH steel and 2024–T3 aluminum strips peened with the same treatment as that used in the experimental campaign of chapter 5 and with a lower intensity treatment using the same shot but half the Almen intensity. The 174–PH steel was chosen based on the experimental results of Zhang et al. (2008) which showed that, for this material, peening induced eigenstrains were independent of the thickness of the strips for Almen intensities close to those considered here. The strips were removed by water jet cutting from as-rolled sheets of different thickness. Their in-plane dimension was 76×19 mm with the longest side being aligned with the rolling direction of the sheets. During peening, the strips were held flat with the holder shown in figure 8.4. Their final curvature was measured with a conventional Almen gauge. Also shown on the upper right graph are experimental points obtained in chapter 5 for 2024–T3 strips aligned with the L direction that were held flat during peening. The values obtained with both sets of strips are close, even though the strips were cut from different plates.

As predicted by equation (8.4), $\tilde{\kappa}h^3/12$ appears to vary linearly with the thickness. A discrepancy with the theory, however, is that y-intercepts for aluminum strips peened with the higher intensity treatment are positive. This implies that β is negative, which cannot be the case if the hypotheses listed above are valid since peening induces positive eigenstrains, thus positive β. Similar curves with positive y intercept were obtained for this alloy over a wide range of intensities. Possible explanations for this behavior include initial residual stresses being present in the strips and stress peen forming taking place as a result of the holder constraining the in-plane expansion of the strips which, in both cases, results in different eigenstrains in each strip. Additional tests with different constraining conditions would be

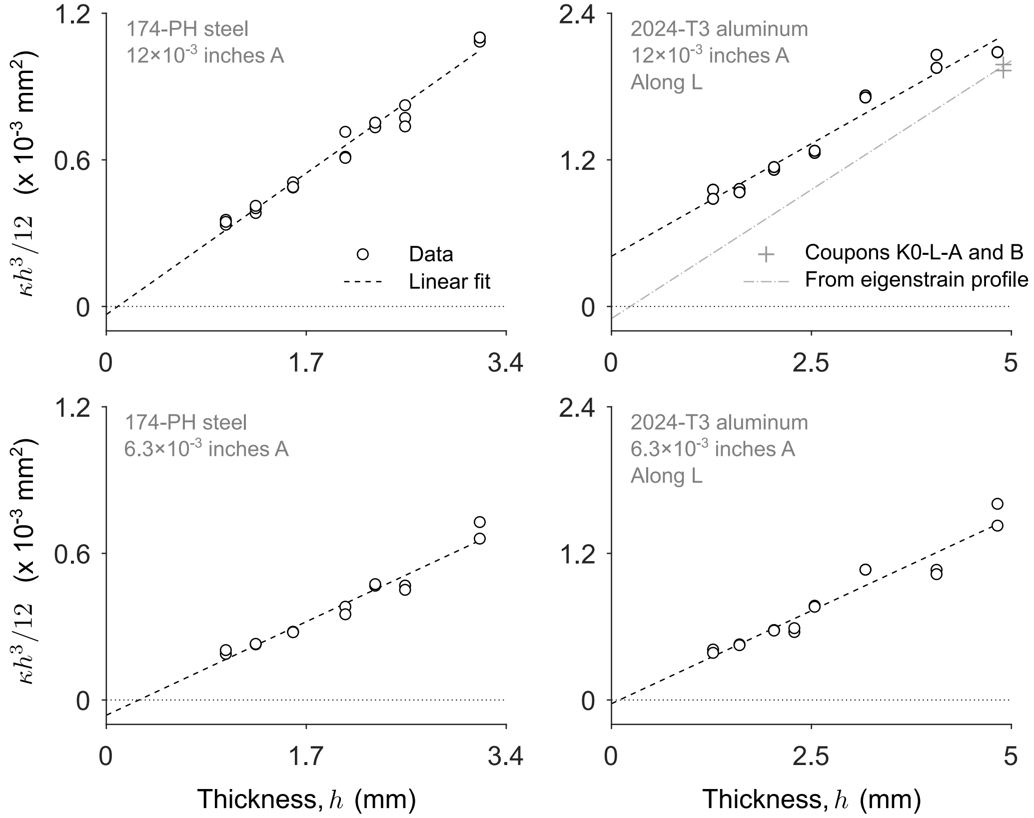

Figure 8.3 Evolution of $\kappa h^3/12$ versus h for 76 × 19 mm 174–PH and 2024–T3 strips shot peened with two different treatments. Specimens on the top row were peened with SCCW28 at an Almen intensity of 12×10^{-3} inches A as in the experimental campaign of chapter 5. Specimens on the bottom row were peened with the same shot at a lower intensity of 6.3×10^{-3} inches A. All specimens were held flat in the holder shown in figure 8.4 during peening. Also shown on the upper right graph are data points for strips K0–L–A and B from chapter 5 and the line of equation $y = \alpha/2 - \beta$ for the α and β obtained by integrating the eigenstrain profile identified experimentally for coupon K0–L–A (see fig. 6.9a).

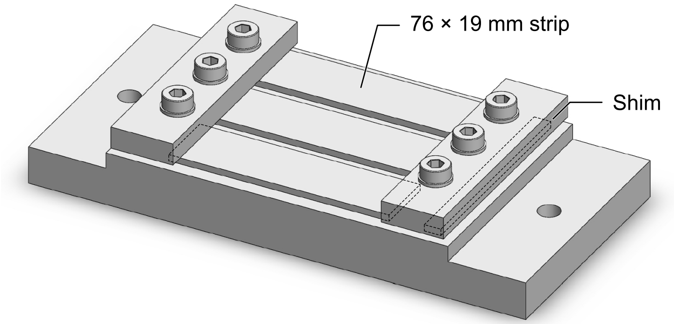

Figure 8.4 Holder used to prevent strips used for the fast identification procedure to deform during peening. Up to three 76 × 19 mm strips were peened at the same time.

required to assess whether these mechanisms do explain the observed results. Despite this shortcoming, the slope of the experimental curve yields a value of α close to that of the eigenstrain profile in the L direction of figure 6.9a, which suggests that α is correctly identified. This is illustrated by the dash-dotted line whose slope and y-intercept were obtained by integrating the profile of figure 6.9a.

CHAPTER 9 GENERAL DISCUSSION

9.1 Eigenstrains as a unifying framework for peen forming simulations

In the literature review that opened this manuscript (chapter 2), we saw that existing peen forming models used many different kinds of loads to simulate the effect of the peening treatment. Some models used unbalanced residual stress profiles; others used plastic strain profiles; others still used thermal strains; and one used distributed axial loads and bending moments. In some of these models, loads were idealized while in others, authors insisted that using detailed through-thickness profiles was a prerequisite to obtaining accurate results. When the sole objective of a simulation is to compute how thin structures deform in response to a peening treatment, all these strategies are, in fact, equivalent.

First, we saw that plastic strains and thermal strains are but two equivalent sources of eigenstrains. Performing a static analysis using either as loads thus yield the same deformed shape. Secondly, we recalled in section 4.3.2 that so-called unbalanced, non-equilibrated, or induced residual stresses—that is, stresses that would exist in an infinitely thick or in a perfectly constrained specimen—were directly proportional to the eigenstrains. Using unbalanced residual stresses as an initial state is thus equivalent to inputting the associated eigenstrain distribution. In fact, initial residual stresses and eigenstrain play a similar role in equilibrium equations where they both contribute to an internal loads term. For this reason, they are usually dealt in the same way by finite element codes (Bathe, 2014). The main reason to prefer eigenstrains over unbalanced stresses is conceptual as eigenstrains do not require the abstraction effort of introducing a virtual intermediate configuration in which unbalanced residual stresses are present. Finally, directly inputting resulting loads and bending moments to the nodes of a finite element model amounts to performing manually the integration of distributed loads over each element and is, therefore, equivalent to the previous loading schemes. Note that, when using this approach for geometrically nonlinear analyses, care must be taken to define the loads as follower loads.

Concerning the difference between idealized loads and accurate through-thickness profiles, it has to be realized that, when working with thin shell formulations, all quantities are at some point integrated through the thickness of the elements. The deformed shape of the structure therefore depends on *resulting* loads and bending moments; not on their through-thickness distribution. In other words, any two eigenstrain or unbalanced stress distributions that induce the same resulting loads and bending moments yield the same deformed shape. There are two situations in which it is necessary to input detailed through thickness profiles: (i) whenever residual stresses in the part must be evaluated and (ii) whenever reverse yielding is likely to occur—for example, when performing springback simulation on prestressed parts. Otherwise, idealized profiles provide a convenient way to simplify input files and reduce the number of through-thickness integration points required to accurately compute peening induced loads.

Idealized profiles were used several times in previous chapters as well as in Homer (1989) and Nervi et al. (2017), among others. The simplest idealized profile is the piecewise constant profile

$$\varepsilon^*_{ii}(z) = \begin{cases} \theta_i^{\text{top}} & \text{if } 0 \leq z < h/2, \\ \theta_i^{\text{btm}} & \text{if } h/2 \leq z \leq h, \end{cases}$$

already introduced in chapter 4 where $i = \{x, y\}$ and θ_i^{top} and θ_i^{btm} are adjustable constants. Another option is the 'step' profile

$$\varepsilon^*_{ii}(z) = \begin{cases} \varepsilon^*_{eq\,i} & \text{if } 0 \leq z \leq h_{eq\,i}, \\ 0 & \text{otherwise}, \end{cases}$$

used for optimization simulations in chapters 7 and 8. The former can induce any combination of axial loads and bending moments while the later, despite being easier to interpret, cannot induce pure bending loads. Note that in the above examples, only two parameters per direction are needed to characterize the loads. Possible pairs of parameters include θ_i^{top} and θ_i^{btm}, $h_{eq\,i}$ and $\varepsilon^*_{eq\,i}$, but also axial loads and bending moments, and natural stretch and curvature, among others. Relations between several such pairs of parameters are listed in appendix F. Because they contain all the information about the amount of stretching and bending induced by a given treatment in a given material for given constraining conditions, these parameters provide a convenient way to compare treatment. When combined with other indicators such as resulting surface roughness, durability of the shot, and operating costs, they enable to quickly select the best treatment for a given application.

9.2 Summary of findings

This thesis aimed at developing tools to predict how thin structures deform in response to shot peening treatments and to assess whether a given target shape can (or cannot) be peen formed.

The proposed approach consists in modeling peening induced loads as a thin layer of material parallel to the peened surface in which incompatible nonelastic strains (the eigenstrains) are present. While these eigenstrains can be estimated numerically, this requires advanced impact models and lengthy computations. Here, we preferred to identify them experimentally from limited measurements performed on small representative coupons. These eigenstrains were then mapped to thin shell models to predict the final deformed shapes of larger plates. Finally, we demonstrated how coupling such eigenstrain simulations to standard optimization procedures enabled to automatically identify peening patterns and process parameters required to form initially flat plates into desired target shapes.

In chapter 4, we summarized procedures to experimentally identify eigenstrains in uniformly shot peened plates and provided missing justifications to existing procedures. In particular, we used the concept of impotent and nilpotent eigenstrains to explain why both residual stresses and total strains must be measured to ensure that the computed solution is unique. We also explained why, in most circumstances, curvature and axial stretch measurements conducted on small representative coupons provide all the necessary information to predict how larger parts treated in the same conditions will deform.

In chapter 5, we reported the results of a peen forming experimental campaign conducted on 4.9 mm thick 2024–T3 aluminum sheets. The specimens, which were cut from the same base plate and peened with the same treatment, consisted in ten 1016 mm long sheets of various aspect ratio that were free to deform during peening and in twenty-six 508 × 127 mm strips subjected to increasing levels of prestress in a four-point bending jig. Unlike previous studies which, with only a few exceptions, measured residual stresses in at most one direction, we used the hole drilling and the slitting method to characterize all three in-plane components of the residual stresses for each geometry and peening condition. The obtained results were consistent with those reported in the literature. In particular, they confirmed that a transition between spherical and cylindrical deformed shapes was caused by an elastic instability. One original observation was that the progressive deformation of unconstrained specimens has the same effect as an externally applied prestress and causes unconstrained specimens to curve more than if they had been held flat during peening (by up to 33 % for the peening conditions investigated). We also observed that all specimens bent along the rolling direction of the alloy, irrespective of their aspect ratio and of the peening trajectory, which was attributed to material anisotropy.

In chapter 6, we used eigenstrain simulations to investigate whether plastic anisotropy or anisotropic initial eigenstrains caused all specimens to bend along the same direction. Our main contribution was to show that the response of rectangular sheets uniformly shot peened on one face was highly sensitive to small variations of eigenstrains and to quantify this sensitivity. A consequence of this is that, despite the geometry of the sheets favoring long side bending, only slightly anisotropic eigenstrains are required to trigger short side bending. Because of the small level of anisotropy involved, we could not determine with certainty whether plastic anisotropy or initial eigenstrains were responsible for the observed deformed shapes, although available evidence points towards the latter.

In chapters 7 and 8, we presented the first validated procedure to automatically compute peening patterns required to form flat plates into desired target shapes. The proposed procedure included geometric nonlinearities that had been neglected in earlier work. Finally, we outlined several strategies to relate the output of the optimization procedure to actual process parameters, one of which, because it only requires curvature measurements on small representative coupons, is compatible with a production environment.

While most of the ideas presented in this manuscript were directly inspired from work conducted in other fields of engineering—in particular from actuators design, 4D printing, and biomechanics—their relevance to peen forming was seldom obvious. In that sense, the main contribution of this work was to make these connections explicit, thus considerably expanding the range of tools available to model the process.

9.3 Recommendations for future work

In this work, we only considered rectangular sheets of uniform thickness. In practice, however, peen formed parts feature complex geometries with continuous variations in thickness, pockets, and sometimes integral stiffeners, as illustrated in figure 9.1. Furthermore, because they are machined from thick aluminum plates, these parts contain initial stresses likely to have a higher magnitude than those encountered in previous chapters. Finally, the largest parts are usually free to deform during peening and, therefore, undergo stress peen forming as they progressively deform. Before models are developed that can simulate realistic peening operations on such parts, several questions remain to be addressed, three of which are discussed next.

Transferability of eigenstrains

Eigenstrain simulations adopted in this work rely on experimentally identifying peening induced eigenstrains on small representative coupons, mapping these eigenstrains to a large-scale model of a structure, and solving for equilibrium. The physical argument that underpins this approach is that, because peening induced plastic strains result from highly localized interactions between shot and the surface of the target, their distribution must be independent of the geometry of the target far away from the point of impact. Consequently,

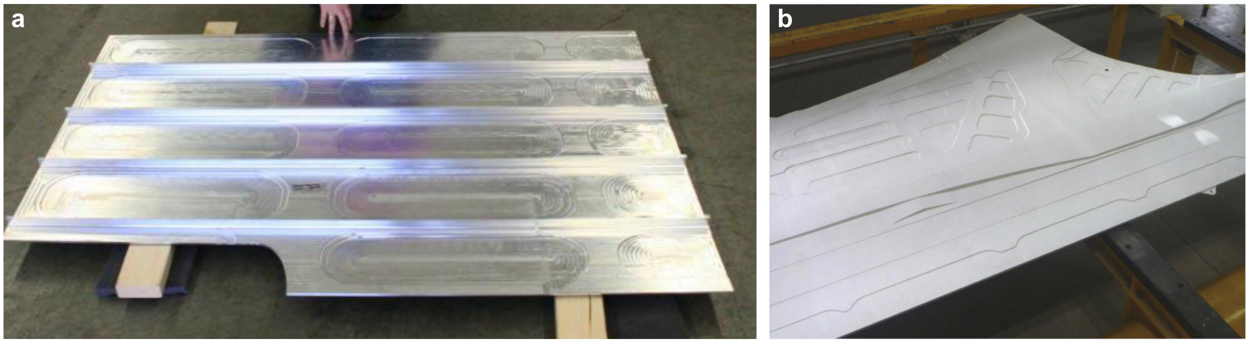

Figure 9.1 Typical wing panels before peen forming. (a) Integrally stiffened panels with pockets and thickness variations. Source: Rankin et al. (2013). (b) Wing skin panels with stepped pockets. Source: Gariépy et al. (2014).

peening plastic strains far away from the edges of the coupon must be identical to those in the larger structure, hence the mapping strategy. This property is sometimes referred to as the "principle of transferability of eigenstrains" (Jun et al., 2011).

Because the mapping operates between identical geometries (for example, from a flat coupon to a flat surface, or from a rounded edge to the same rounded edge), this approach cannot realistically be applied to complex geometries with many geometric features due to the large number of experiments it would involve. To alleviate the experimental effort, several studies considered mapping eigenstrain profiles identified on flat coupon directly onto complex geometries (DeWald and Hill, 2009b; Coratella et al., 2015; Salvati and Korsunsky, 2018). This was done by performing the following sequence of operations. For each integration point of the model of a peened part:

1. Find the nearest point located on a peened surface.
2. At this point, construct a local frame having with its z axis pointing towards the integration point. Assuming that the peening treatment induces equibiaxial eigenstrains, the orientation of the two other axes can be chosen arbitrarily.
3. Compute the distance from the point on the surface to the integration point.
4. Read the eigenstrains measured at that depth.
5. Transform the coordinates to align the frame in which the eigenstrains were measured with the new local frame.
6. Input the transformed eigenstrains at the integration point.

While this approximation seems reasonable when the radii of curvature of the surface are much larger than both the radius of the shot and the depth of the plastically deformed layer, it clearly does not apply when theses quantities are of the same order, or for sharp corners. This was confirmed experimentally by DeWald and Hill (2009b), Coratella et al. (2015), and Gelineau (2018) which implemented this strategy to estimate residual stresses in massive peened parts. In all cases, the agreement between simulations and residual stress measurements was decent for convex geometries with large radii of curvature but quickly deteriorated for small radii of curvature or concave geometries. The conditions for which this approximation is valid remain to be clarified.

Impacts on prestressed targets

Another open question concerns the effect of initial stresses on the post-peening state. Such initial stresses could result from earlier processing stages or from externally applied loads, as is the case for stress peen forming. Although many studies considered impacts on an initially stress-free target, only a handful investigated the effect of prestress.

In particular, it would be desirable to clarify the physical mechanisms whereby residual stresses induced by peening treatments appear to be independent of the level of prestress. This phenomenon, which was discussed in section 2.3.4, is exemplified by the experimental results of Zeller (1993) which measured identical compressive residual stresses on the surface of tensile test specimens that were prestressed in tension, shot peened, and held in tension for measurements. Although it underpins several stress peening models mentioned in Schulze (2002), as well as the peen forming models of Cao et al. (1995), Gariépy et al. (2011), and Gariépy et al. (2013c), it has not, to the best of our knowledge, been the subject of any in-depth investigation. Clarifying under what conditions can peening induced stresses be considered independent of the initial stress states is needed both to clarify the domain of validity of these models and to guide the development of a next generation of efficient peen and stress peen forming models.

Accounting for variability

Even when the process is tightly controlled, peen forming retains a certain degree of unpredictability. Putting aside the dispersion of impact velocities inherent to the process—which, based on our experience and exchanges with peen forming professionals, has very little effect on the consistency of the process if adequate peening practices are followed—the main source of variability is initial residual stresses that differ from one part to the next. In chapters 5 and 6, we showed that initial residual stresses did affect the final deformed shape of our specimens. This effect is likely to be more pronounced for parts machined in thick aluminum plates as the latter usually feature larger initial stresses than thinner sheets (although this depends on what stress relief treatment is used). Furthermore, the distribution of initial stresses is more complex as it depends on (i) the location in the base plate where a part has been machined, (ii) residual stresses induced during machining, and (iii) how these stresses redistributed.

Including initial stresses in simulations requires characterizing them first. Because of the experimental effort involved, this cannot be done on a part-by-part basis. Therefore, unless the manufacturing chain produces consistent parts, accounting for varying initial stresses requires feedback systems which monitor the shape of the parts as they are being peened and adjust process parameters accordingly. The need for automated feedback systems has been recognized by the industry for many years as is made clear by Blackwell et al. (2004) in a synthesis of Airbus UK's research efforts on peen forming. Such systems are already in use in production (Kittel et al., 1999; Friese et al., 2002) and other are currently being developed for laser peen forming, needle peen forming, and distortion correction (Lundquist et al., 2017; Bovid, 2019).

Note that, because peen forming is a niche process with low production rate, collecting enough data to implement statistical corrections is difficult. In this context, expanding existing experimental data sets with numerical results obtained from simulations of the process such as those developed in this work could provide a way to teach robots to peen form parts semi-autonomously (Bousmalis and Levine, 2017).

CHAPTER 10 CONCLUSION

In this work, we established a framework based on the concept of eigenstrains to study, simulate, and optimize the shot peen forming process. Within this framework, we clarified the mechanics of peen formed plates, showed how eigenstrain simulations could be coupled with off-the-shelf optimization algorithms to automatically determine peening patterns required to form initially flat plates into desired target shapes, and provided procedures to identify peening induced loads from limited measurements. Although our attention was limited to the forming thin aluminum sheets, most of the tools presented here could be adapted to other materials, geometries, and peening treatments—including laser and needle peening.

These results are, however, only one more step towards the simulation of peen forming operations on realistic aircraft parts. Such parts are usually machined from thick rolled aluminum plates and present complex geometries with continuous variations in thickness, pockets, and stiffeners. Extending eigenstrain simulations to complex geometries will thus require investigating how geometric features affect the underlying distribution of eigenstrains. Another challenge is the variability of initial residual stresses from one part to the next. Such stresses result from the manufacturing process of the base plates and complicate peen forming operations by causing the parts to deform unpredictably when their equilibrium is disturbed. Until advances in process control enable to obtain consistent initial stress distributions, or until experimental techniques become available to measure initial stresses in each part, this puts a limitation on the accuracy of peen forming simulations.

While this issue could be addressed with feedback systems where peening strategies are automatically adjusted to correct for deviations from the target shape, teaching peening robots requires large experimental datasets that only a handful of companies have access to. In this context, simulations could provide a virtual environment in which to do most of the teaching. Such tools could in turn help new entrants in the peen forming business to develop their own processing strategies. In particular, there is potential for developing peen forming in fields other than aerospace engineering, among which shipbuilding and architecture are prime candidates (Lee and Kim, 2012; Hackel et al., 2017). Automating distortion correction of machined parts is another avenue that is just starting to be investigated. Although these applications have been anticipated since shot peen forming was first introduced in production in the 1950s, they never quite materialized. For this, we share the belief of Grasty and Andrew (1996) that “the process would almost certainly find wider application if it were better known and understood” and hope that the results presented here contributed to this understanding.

APPENDIX A ADDITIONAL INFORMATION ABOUT PEEN FORMING EXPERIMENTS

A.1 Specimens

Tables A.1 to A.3 list specimens used for peen forming tests and residual stress measurements and figure A.1 shows the cutting plan.

Table A.1 Specimens used for conventional peen forming tests. These specimens were sheared from larger sheets to their final dimensions.

Specimen ID	Dimensions (mm)		Peening strokes
	Along L	Along T	
Sheet 4:1–L	1016	254	Parallel to L
Sheet 2:1–L	1016	508	
Sheet 1:1–L	1016	1016	
Sheet 1:2–L	508	1016	
Sheet 1:4–L	254	1016	
Sheet 4:1–T	1016	254	Parallel to T
Sheet 2:1–T	1016	508	
Sheet 1:1–T	1016	1016	
Sheet 1:2–T	508	1016	
Sheet 1:4–T	254	1016	

Table A.2 Specimens used for stress peen forming tests. These specimens were sheared from larger sheets to their final dimensions. All were peened with strokes parallel to their long side.

Specimen ID	Dimensions (mm)		Prestress curvature ($\times 10^{-4}$ mm^{-1})		Final curvatures [a] ($\times 10^{-4}$ mm^{-1})	
	Along L	Along T	Nominal	Actual	Along long side	Along short side
Strip K0–L–A	508	127	0.0	$\simeq 0$	2.07	–
Strip K0–L–B	508	127	0.0	$\simeq 0$	2.08	–
Strip K0–T–A	127	508	0.0	$\simeq 0$	1.97	–
Strip K0–T–B	127	508	0.0	$\simeq 0$	2.02	–
Strip K1–L–A	508	127	2.7	2.77	2.85	–
Strip K1–L–B	508	127	2.7	2.87	2.73	2.04
Strip K1–T–A	127	508	2.7	2.63	2.46	3.14
Strip K1–T–B	127	508	2.7	2.70	2.54	3.19
Strip K2–L–A	508	127	5.1	5.20	3.16	–
Strip K2–L–B	508	127	5.1	5.09	3.39	2.13
Strip K2–T–A	127	508	5.1	4.88	2.94	3.14
Strip K2–T–B	127	508	5.1	5.30	3.48	2.58
Strip K3–L–A	508	127	8.3	8.38	3.92	–
Strip K3–L–B [b]	508	127	8.3	8.04	4.15	1.97
Strip K3–L–C [b]	508	127	8.3	8.22	4.09	2.33
Strip K3–T–A	127	508	8.3	8.19	3.75	–
Strip K3–T–B [b]	127	508	8.3	8.13	3.83	2.40
Strip K3–T–C [b]	127	508	8.3	8.02	3.93	3.05
Strip K4–L–A	508	127	10.5	10.49	4.37	–
Strip K4–L–B	508	127	10.5	10.50	4.52	1.74
Strip K4–T–A	127	508	10.5	10.50	4.25	1.76
Strip K4–T–B	127	508	10.5	10.52	4.28	2.36
Strip U–L–A	508	127	Free to deform		2.86	–
Strip U–L–B	508	127			2.65	2.75
Strip U–T–A	127	508			2.39	3.16
Strip U–T–B	127	508			2.30	–

[a] Once peened and released from the jig.

[b] Peened for twice as long as the other strips due to an input error.

Table A.3 Specimens used for residual stress measurements.

Specimen ID	Dimensions (mm)		Removed from	Cutting method	Measurement technique	Notes
	Along L	Along T				
Coupon 10	254	254	–	Shearing	Hole drilling	[a]
Coupon 11	254	254	–	Shearing		[b]
Coupon 4:1–L	254	254	Sheet 4:1–L	Jigsaw		
Coupon 2:1–T	254	254	Sheet 2:1–T	Jigsaw		
Coupon 1:1–L	254	254	Sheet 1:1–L	Jigsaw		
Coupon 1:2–L–A	254	254	Sheet 1:2–L	Jigsaw		
Coupon 1:4–L–A	254	254	Sheet 1:4–L	Jigsaw		
Coupon K0–L–A	254	127	Strip K0–L–A	Jigsaw		
Coupon K1–L–A	254	127	Strip K1–L–A	Jigsaw		
Coupon K2–L–A	254	127	Strip K2–L–A	Jigsaw		
Coupon K3–L–A	254	127	Strip K3–L–A	Jigsaw		
Coupon K4–L–A	254	127	Strip K4–L–A	Jigsaw		
Coupon U–L–A	254	127	Strip U–L–A	Jigsaw		
Coupon 13	50.80	50.80	–	EDM	Slitting	[a, c]
Coupon 14	50.80	50.80	–	EDM		[a, d]
Coupon 1:2–L–B	15.24	17.78	Coupon 1:2–L–A	EDM		[c]
Coupon 1:2–L–C	17.78	15.24	Coupon 1:2–L–A	EDM		[d]
Coupon 12	254	254	–	Shearing	X-ray diffraction	[a]
Coupon 1:4–L–B	254	254	Sheet 1:4–L	Jigsaw		
Coupon 1:1–T	254	254	Sheet 1:1–T	Jigsaw		
Coupon 4:1–T	254	254	Sheet 4:1–T	Jigsaw		

[a] From top face.
[b] From bottom face.
[c] Along T.
[d] Along L.

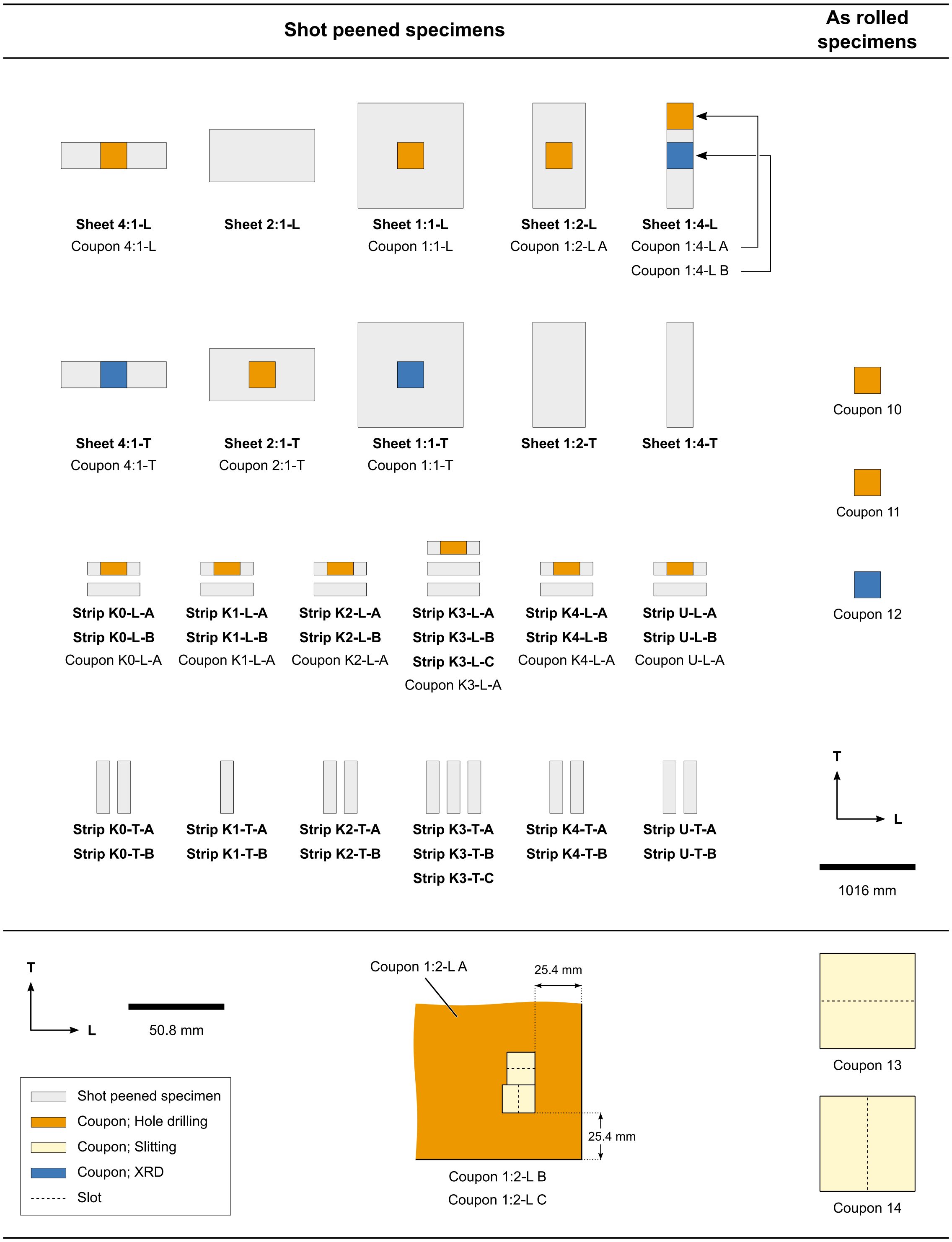

Figure A.1 Cutting plan for specimens used for peen forming tests and residual stress measurements.

A.2 Material

A.2.1 Certification sheets

Material certification sheets are given in appendix B.

A.2.2 Microstructure

Figure A.2 shows metallographic sections in the TS, LS, and LT planes obtained from three $8 \times 8 \times 4.9$ mm coupons removed with a Struers Discotom–100 cut-off machine from sheet 1:4–L. The coupons were polished on a Struers Tegramin–25 automatic polishing machine as described in table A.4. Following polishing, the coupons were immersed in Keller's reagent for twenty seconds to reveal the microstructure, then immediately rinsed in warm water.

Grain size was computed with the intercept methods (ASTM E112-12 standard, 2012) using grids of five by five test lines aligned with the principal directions of the specimens, 10.7 mm apart from each other. Mean intercept lengths are reported in table A.5. Also reported are the largest observed grain dimensions along each direction. The latter were obtained by visual inspection and are given for information purposes only.

A.2.3 Tensile tests

Rectangular tension test specimens compliant with ASTM standard B557M-15 (2015) were removed by water jet cutting from a randomly selected sheet. Figure A.3 shows the geometry of the specimens. Three specimens were cut aligned with the rolling direction, three specimens were cut at 45° of the rolling direction, and three specimens were cut at 90° of the rolling direction.

Prior testing, lateral faces were gently polished with sandpaper to obtain a smooth surface finish. The area of the cross section within the gage length was measured with a caliper at five different locations and the smallest value was retained. All tests were conducted as per ASTM standard B557M-15 (2015). The speed of testing, controlled by the rate of separation of the two heads of the testing machine, was set to $0.7\,\mathrm{mm\,min^{-1}}$. Figure A.4 shows all stress-strain curves and table A.6 lists static properties extracted from these curves.

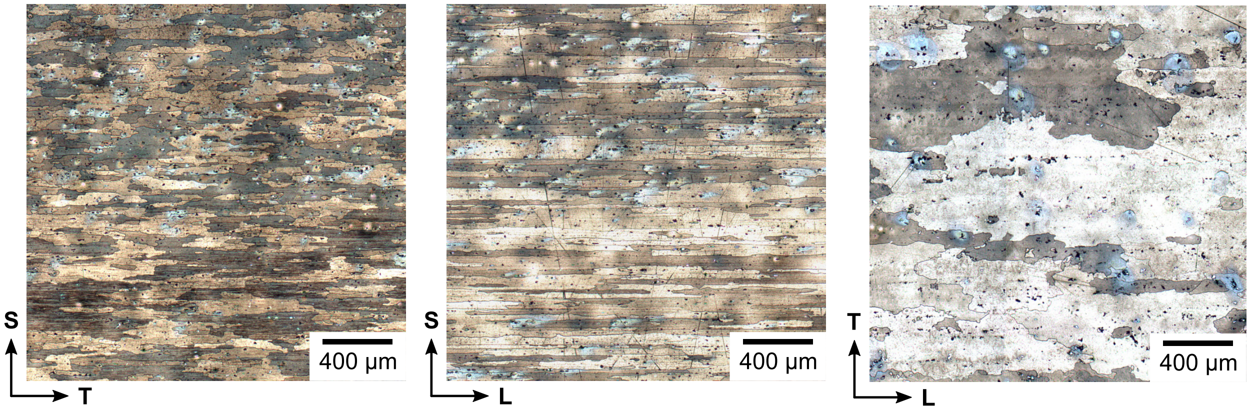

Figure A.2 Typical metallographic sections in the ST, SL, and TL planes of the 4.9 mm thick 2024–T3 aluminum alloy sheets.

Table A.4 Polishing method for micrographs.

Step #	Surface	Abrasive	Grit / Grain size	Lubricant	Rotational speed (rpm)	Force (N)	Time (s)
1	SiC foil	SiC	# 324	Water	150	180	70
2	Largo paper 9	Diaduo-2 9	9 µm	–	150	210	360
3	Final finish cloth	Diamond solution	9 µm	Water base extender	150	150	210
4	Final finish cloth	Diamond solution	1 µm	Water base extender	150	150	210

Table A.5 Grain dimensions for 4.9 mm thick Kaiser Stretched aluminum alloy 2024–T3 sheets: mean intercept length and largest dimension. All dimensions in mm.

Along L		Along T		Along S		Overall mean aspect ratio
Mean	Max	Mean	Max	Mean	Max	
0.268	4.62	0.137	2.80	0.038	0.64	7.1 : 3.6 : 1.0

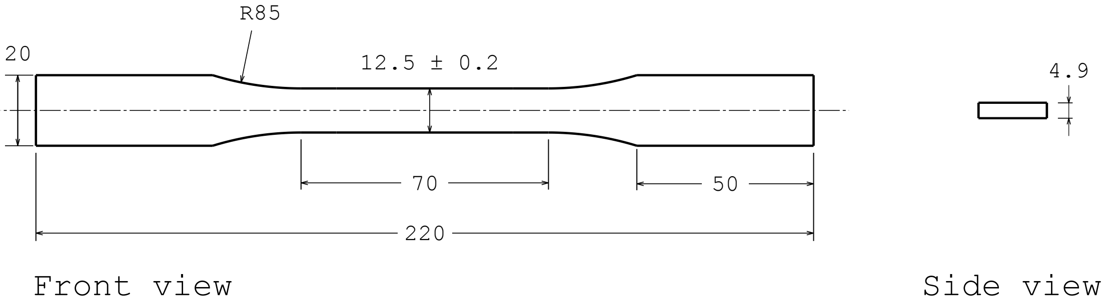

Figure A.3 Schematic of tension test specimen. All dimensions in mm.

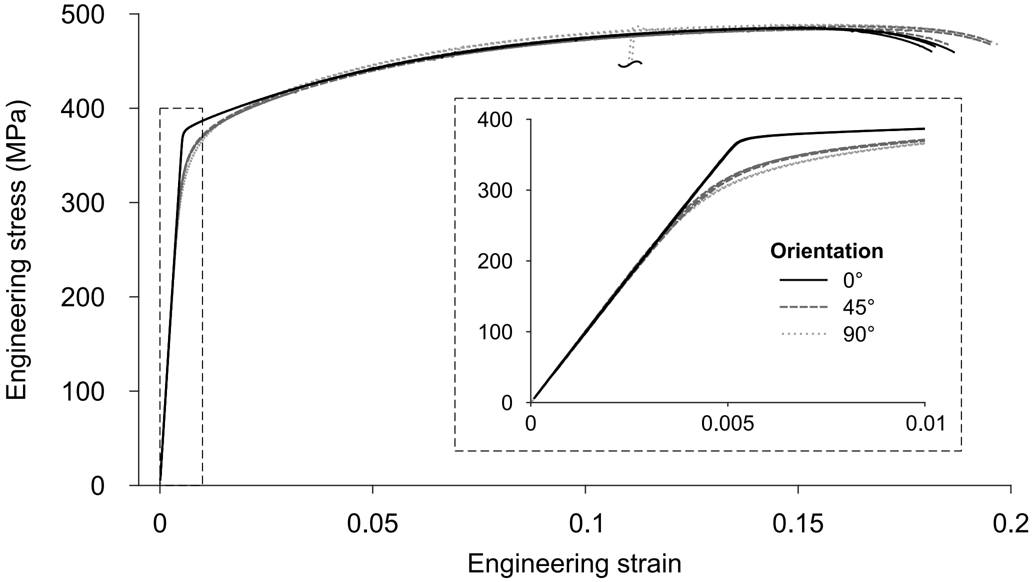

Figure A.4 Stress-strain curves at 0°, 45°, and 90° from the rolling direction. Three curves were obtained for each direction. The drop at approximately 0.1 mm mm^{-1} is due to an input error in a displacement limit which caused one test to halt prematurely. This test was then resumed until break.

Table A.6 Static properties extracted from the stress-strain curves shown in figure A.4.

Angle w.r. to rolling direction (°)	Young's modulus (GPa)	Yield stress at 0.2 % (MPa)	Ultimate tensile stress (MPa)	Elongation at fracture (mm/mm)
0	72.1	381	486	0.1824
0	70.8	381	486	0.1815
0	71.6	381	485	0.1868
45	70.3	349	484	0.1954
45	72.7	349	484	0.1853
45	71.8	350	487	0.1853
90	71.2	337	489	0.1923
90	71.6	338	489	0.1970
90	72.4	338	489	0.1944

A.3 Peening treatment

A.3.1 Media

Media inspection Media was inspected as per AMS standard 2430 rev. T (2015) and AMS standard 2431/8B (2007). Media size was controlled with a stack of 18 and 30 U.S. sieves mounted on a Rotap eccentric sieve shaker. For each 100 g sample of shot tested, no shot were retained in the coarser sieve, and less than three shot passed through the finer sieve. Media geometry was checked by visual inspection using an optical microscope. No unacceptable shapes were observed. After inspection, the media was loaded into the peening cabinet which was run until the media went through two recycling loops.

Distribution of shot diameters The distribution of shot diameters was assessed by image analysis of six shot pictures similar to that shown in figure A.5a using ImageJ's (Rueden et al. (2017), Schindelin et al. (2012)) UCB Hough circle transform plugin. The workflow was like that described in ImageJ's documentation. Figure A.5b shows the outcome of this process when applied to figure A.5a, and figure A.6 shows the final diameters distribution. The results were fitted with a gaussian distribution, yielding a mean diameter of 0.74 mm and a 0.03 mm standard deviation. Supplier's specifications stated a 0.71 mm nominal diameter.

A.3.2 Intensity

Almen intensity measurements and Almen intensity controls were done following AMS standard 2430 rev. T (2015) and SAE standard J443 (2010) with Almen A strips and a TSP–3 #2 Almen gage (EI Electronics Inc). Saturation curves were obtained by fitting equation

$$y(x) = a_1\left(1 - \exp(-a_2 x)\right) \tag{A.1}$$

to the data points, where a_1 and a_2 are adjustable parameters.

A.3.3 Coverage

Coverage was determined manually by coloring magnified pictures of a dummy aluminum alloy 2024–T351 specimen peened for an increasing number of cycles. Two pictures of 12 × 9 mm randomly selected areas were used for each estimation of coverage. Figure A.7 shows representative pictures of the surface of the specimens and figure A.8 shows the evolution of coverage as a function of peening time for a 15 cm/s peening speed. At that speed, full coverage was reached after 12 cycles.

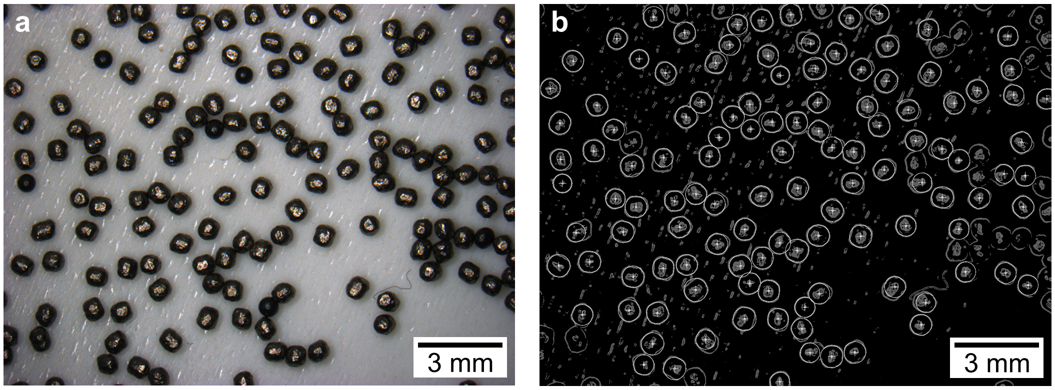

Figure A.5 (a) Magnified picture of the high hardness special conditioned cut wire steel shot SCCW28. (b) Outcome of the automated procedure used to determine the distribution of shot diameters when applied to the picture in (a). ImageJ's Hough circle transform was used to best-fit circles to the shot. Some shot whose boundary was not clearly delimited were excluded from the count. See for example the bottom right corner of (b).

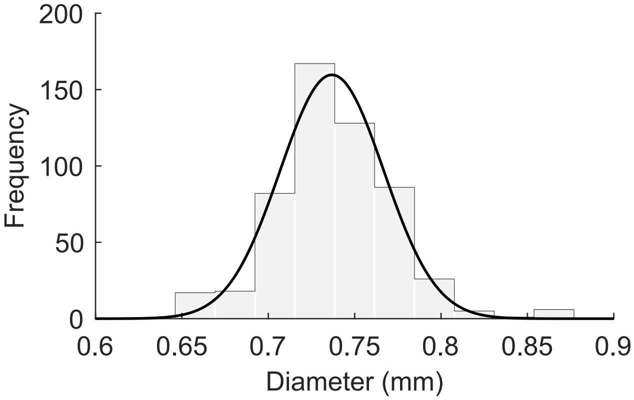

Figure A.6 Distribution of shot diameters obtained by applying Hough circle transform to magnified pictures of the shot (911 shot characterized). The solid line is a best fit of the normal distribution probability density function to the histogram with mean 0.74 mm and standard deviation 0.03 mm.

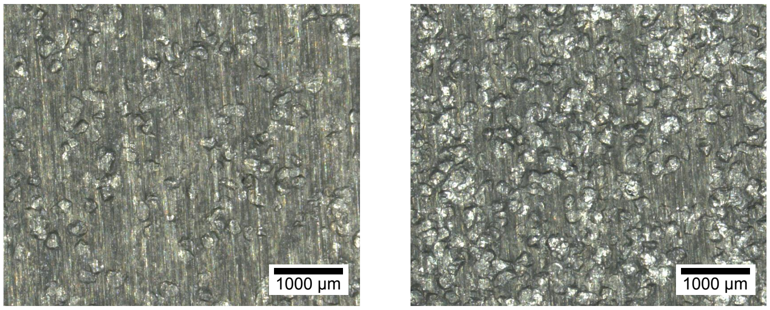

1 cycle; coverage ≈ 25 %

3 cycles; coverage ≈ 56 %

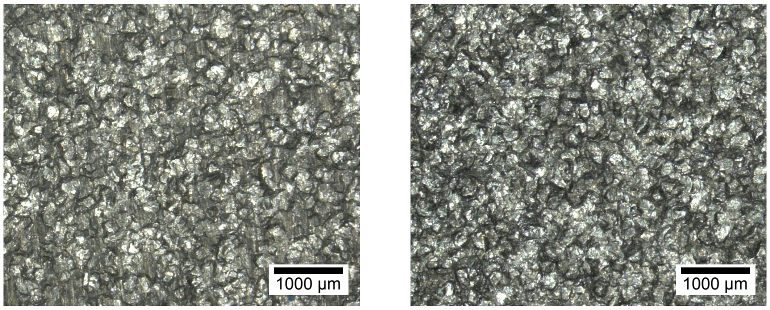

6 cycles; coverage ≈ 82 %

12 cycles; coverage ≈ 97 %

Figure A.7 Magnified pictures of the surface of a dummy specimen peened for increasing numbers of cycles. The reported coverage was estimated from larger pictures, as described in section A.3.3.

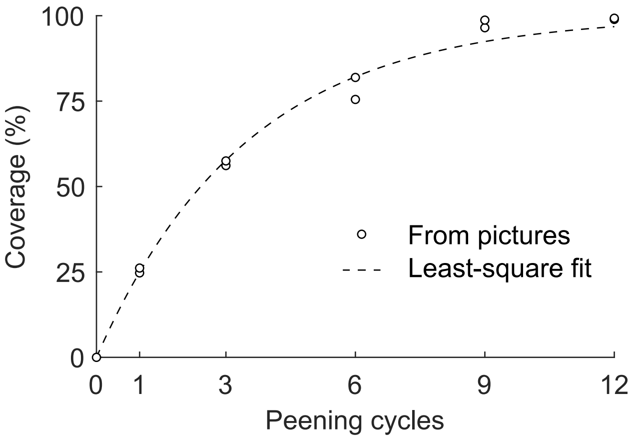

Figure A.8 Coverage versus peening cycles for a peening speed of 15 cm/s. Dots correspond to the values obtained by manually post-processing pictures of the peened surface and the dashed line if a least-square fit of equation $f(x) = 100\,(1-(1-a)^x)$, with a an adjustable parameter whose value was estimated to $a \simeq 0.25$.

A.4 Stress peen forming setup

Figure A.9 shows a side-view of the the four-point bending jig used for stress peen forming experiments and table A.7 lists the spacing and height difference between the support beams of the jig for each prestress conditions.

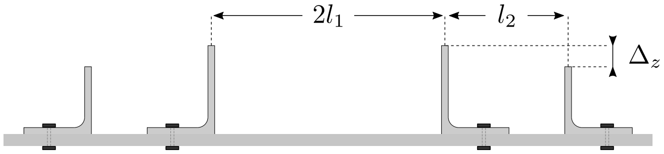

Figure A.9 Front view of the four-point bending jig used for stress peen forming tests with dimensions.

Table A.7 Spacing and height difference between the support beams of the four-point bending jig for each prestress condition. Refer to figure A.9 for the keys.

Prestress curvature ($\times 10^{-4}$ mm^{-1})	l_1 (mm)	l_2 (mm)	Δ_z (mm)
0	195	52	0
2.82	149	100	5
5.11	158	90	9
8.28	144	98	14
10.54	164	80	15

A.5 Peen forming tests

Supplementary videos 1 to 10 show the first three peening cycles of specimens used for conventional peen forming tests. Due to an input error, the peening strokes for cycles 2 and 4 of sheet 2:1–L were aligned with T instead of L. The snapping of sheet 1:1–L from a quasi-spherical to a cylindrical shape is clearly visible at 00:17:50 of supplementary video 3.

Figure A.10 summarizes how these specimens were positioned inside the peening cabinet. The start of the peening trajectory was always to the bottom left of the schematics shown in figure A.10b, and the direction of the peening strokes was as shown by the dotted lines.

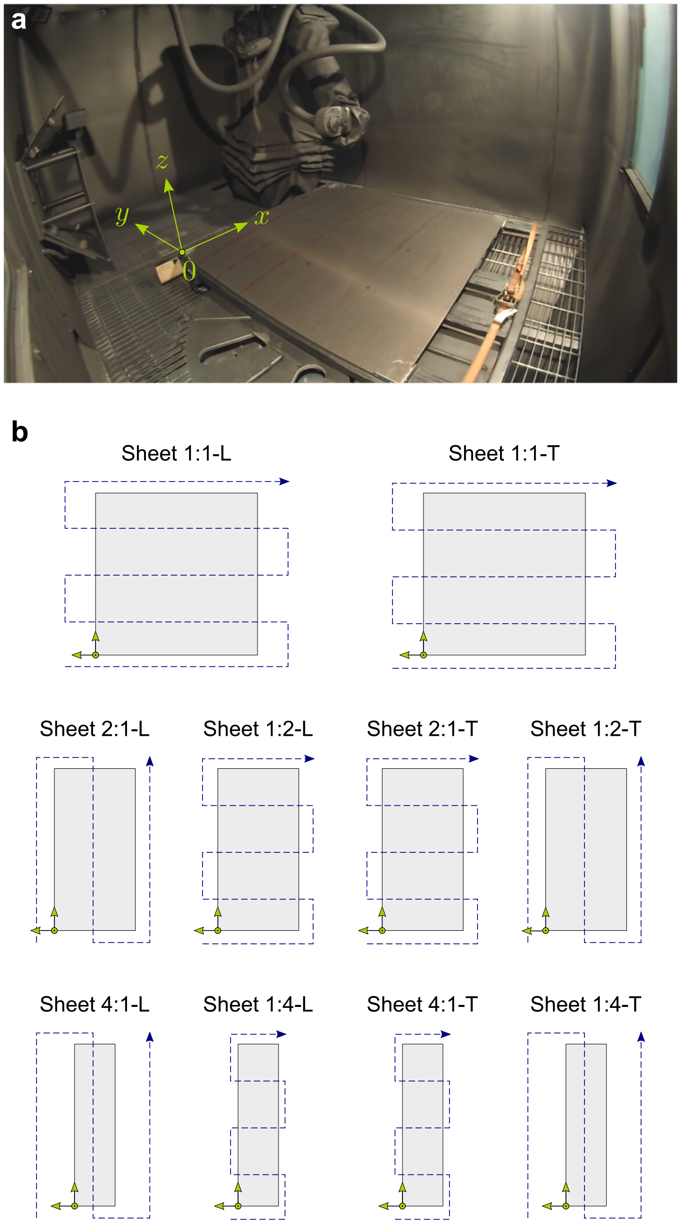

Figure A.10 (a) Coordinate system. (b) Orientation of the sheets used for conventional peen forming tests, and direction of the peening strokes. The start of the peening trajectory was always to the bottom left of the schematics. Arrows correspond to the x and y axes shown in (a).

A.6 3D scans

Three-dimensional CMM scans of sheets used for conventional peen forming tests are available in the attached ‘supplementary data’ folder. The x, y, and z coordinates are as shown in figure A.10. Figure A.11 shows the lines of CMM scans passing through the center of the specimens, which were used to compute curvatures.

The uncertainty of the coordinate measuring machine was estimated to 0.14 µm from 25 measurements on a reference sphere as per ISO 10360-5:2010 standard (2010). The head of the scanning probe was a sphere 6 mm in diameter.

Table A.8 lists the curvature of coupons used for hole drilling measurements.

Table A.8 Curvatures ($\times\ 10^{-4}\,\mathrm{mm}^{-1}$) of coupons used for residual stress measurements.

Specimen ID	Along L	Along T
Coupon 4:1–L	2.66	2.14
Coupon 2:1–T	3.12	1.52
Coupon 1:1–L	2.93	1.81
Coupon 1:2–L–A	3.03	2.08
Coupon 1:4–L–A	3.16	1.54
Coupon K0–L–A	2.05	2.97
Coupon K1–L–A	3.00	2.48
Coupon K2–L–A	3.27	2.36
Coupon K3–L–A	4.03	2.08
Coupon K4–L–A	4.93	1.87
Coupon U–L–A	3.01	2.61

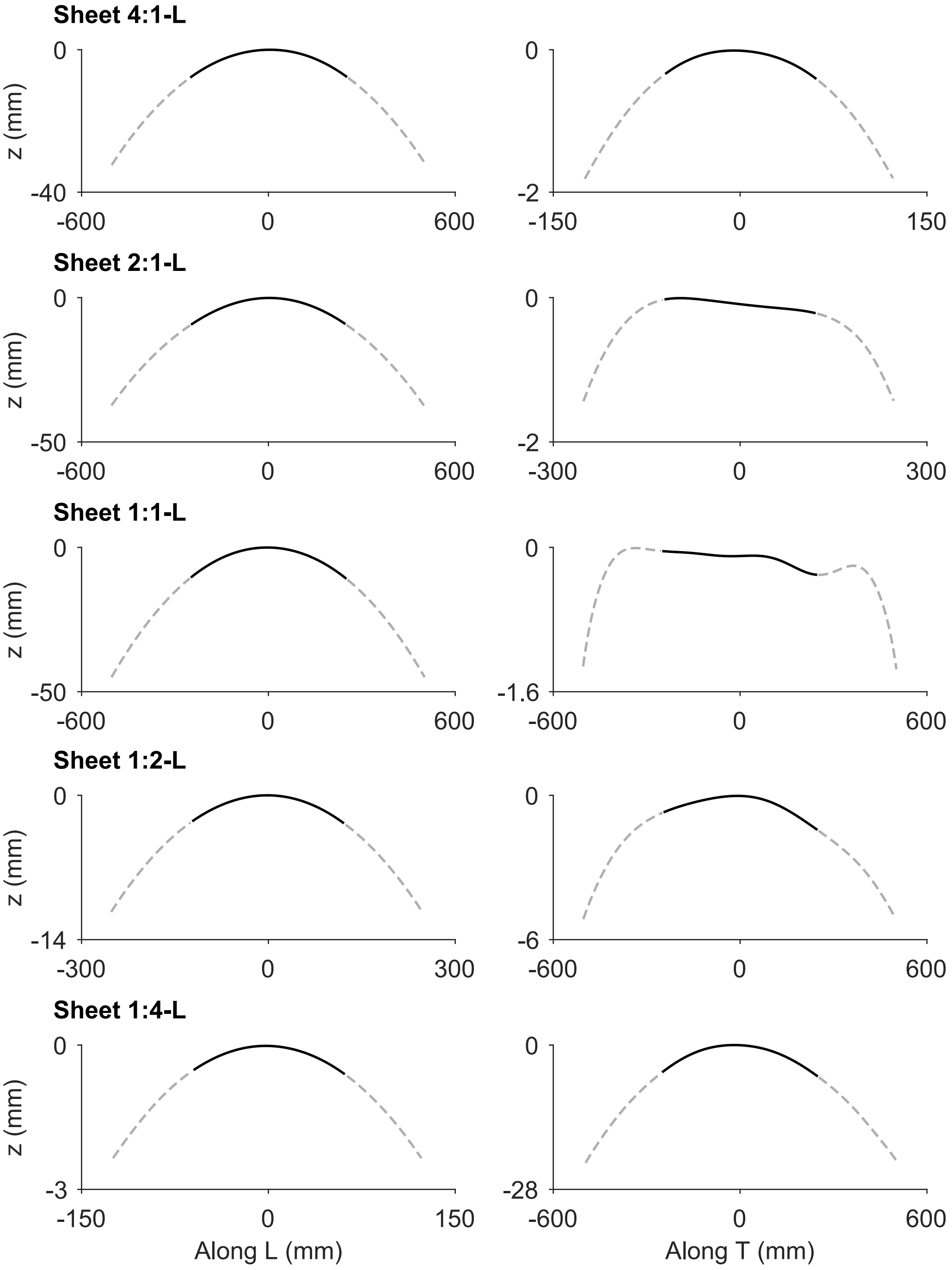

Figure A.11 Line of CMM scans passing through the center of the specimen. Curvatures reported in the main article were averaged over the section shown in solid lines.

A.7 Residual stress measurements

A.7.1 Experimental setups

Figure A.12 shows a typical specimen used for hole drilling measurements with the strain gage still attached. Figure A.13 shows close-ups of the slitting setup.

A.7.2 Tabulated residual stress profiles

Tabulated residual stress profiles are available in appendix C. Also included are X-ray diffraction profiles. X-ray diffraction results are given for information purposes only as the large grain size and the texture of the material prevented to obtain meaningful results (Stresstech, 2018):

> All samples outside the deformed regions from peening showed extreme texture / large gain size ($I_{max}/I_{min} > 3$ and asymmetrical peaks [1]). Extra tilts and oscillation in both the tilt and rotation directions were utilized to collect the most reliable data possible while maintaining directional sensitivity. Some tilts were omitted from the calculation due to lack of diffracted data. In addition, smoothing and a parabolic fit were used to best "average out" the calculation effects of the multiple and asymmetrical peaks [...].

Figure A.14 lists experimental parameters used for X-ray diffraction measurements. The uncertainty for X-ray diffraction measurement reported in appendix C describes the quality of the fit of the d versus $\sin^2\psi$ data. This is only one part of the total uncertainty. Other factors, such as measurement repeatability and the adequacy of the material parameters, were not taken into account.

---

[1] I_{max}/I_{min} is the ratio of the largest to the smallest intensity measured for different positions of the diffractometer. It tends to 1 for isotropic materials and larger values indicate the presence of a crystallographic texture.

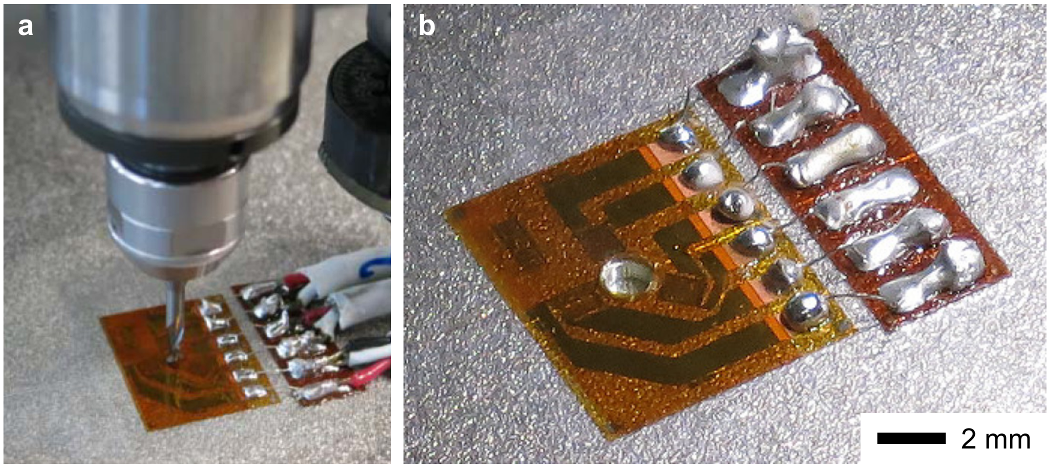

Figure A.12 Typical specimen used for hole drilling measurements. A strain gage was installed on the peened surface to monitor relaxation of the part as a 2 mm hole was drilled in its center.

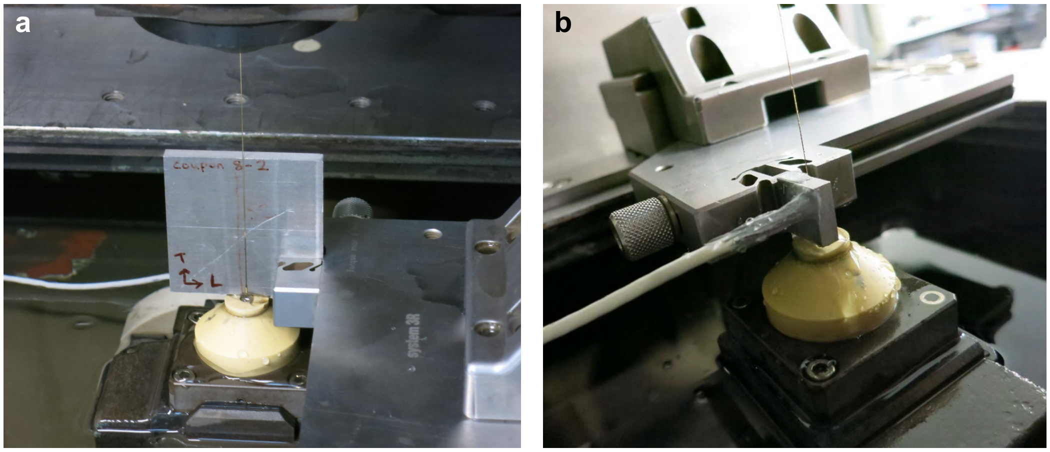

Figure A.13 EDM setup used for slitting measurements. (a) Coupon 14. (b) Coupon 1:2–L B. Visible is the wiring to the strain gage and the protective coating used to isolate the strain gage from the bath.

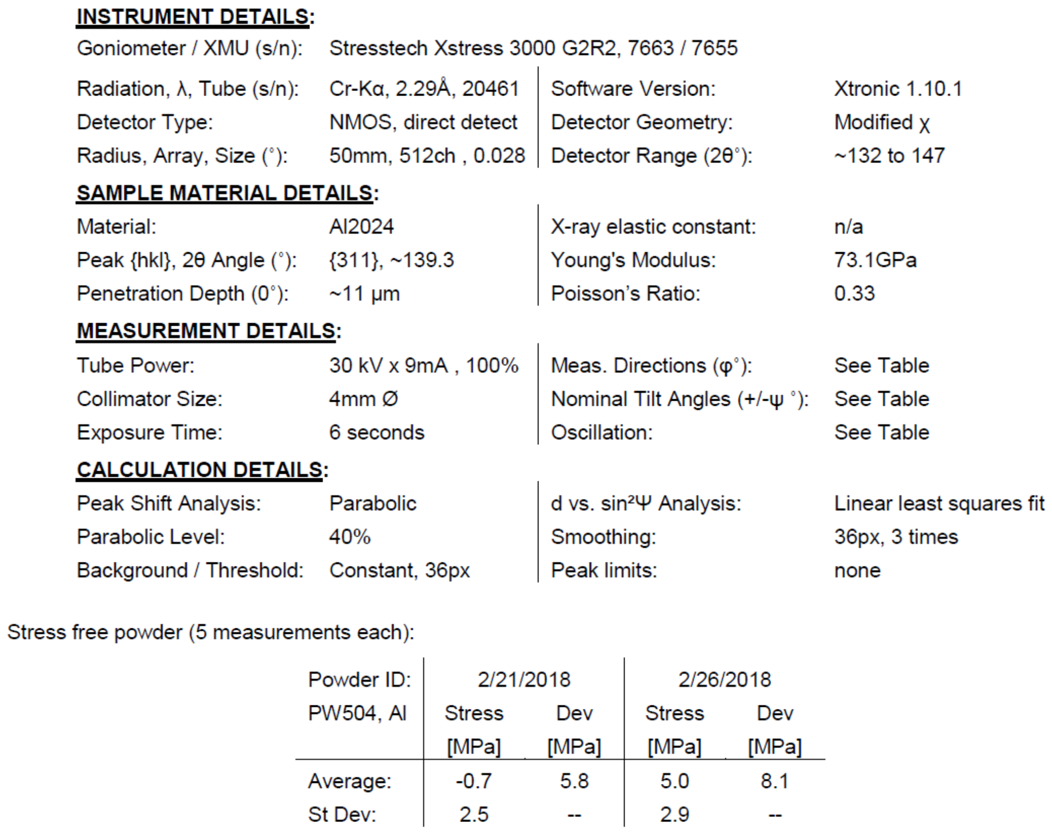

INSTRUMENT DETAILS:

Goniometer / XMU (s/n):	Stresstech Xstress 3000 G2R2, 7663 / 7655		
Radiation, λ, Tube (s/n):	Cr-Kα, 2.29Å, 20461	Software Version:	Xtronic 1.10.1
Detector Type:	NMOS, direct detect	Detector Geometry:	Modified χ
Radius, Array, Size (°):	50mm, 512ch , 0.028	Detector Range (2θ°):	~132 to 147

SAMPLE MATERIAL DETAILS:

Material:	Al2024	X-ray elastic constant:	n/a
Peak {hkl}, 2θ Angle (°):	{311}, ~139.3	Young's Modulus:	73.1GPa
Penetration Depth (0°):	~11 μm	Poisson's Ratio:	0.33

MEASUREMENT DETAILS:

Tube Power:	30 kV x 9mA , 100%	Meas. Directions (φ°):	See Table
Collimator Size:	4mm Ø	Nominal Tilt Angles (+/-ψ °):	See Table
Exposure Time:	6 seconds	Oscillation:	See Table

CALCULATION DETAILS:

Peak Shift Analysis:	Parabolic	d vs. sin²Ψ Analysis:	Linear least squares fit
Parabolic Level:	40%	Smoothing:	36px, 3 times
Background / Threshold:	Constant, 36px	Peak limits:	none

Stress free powder (5 measurements each):

Powder ID: PW504, Al	2/21/2018		2/26/2018	
	Stress [MPa]	Dev [MPa]	Stress [MPa]	Dev [MPa]
Average:	-0.7	5.8	5.0	8.1
St Dev:	2.5	--	2.9	--

Figure A.14 Experimental parameters for X-ray diffraction measurements. Source: Stresstech (2018).

APPENDIX B MATERIAL CERTIFICATION SHEETS

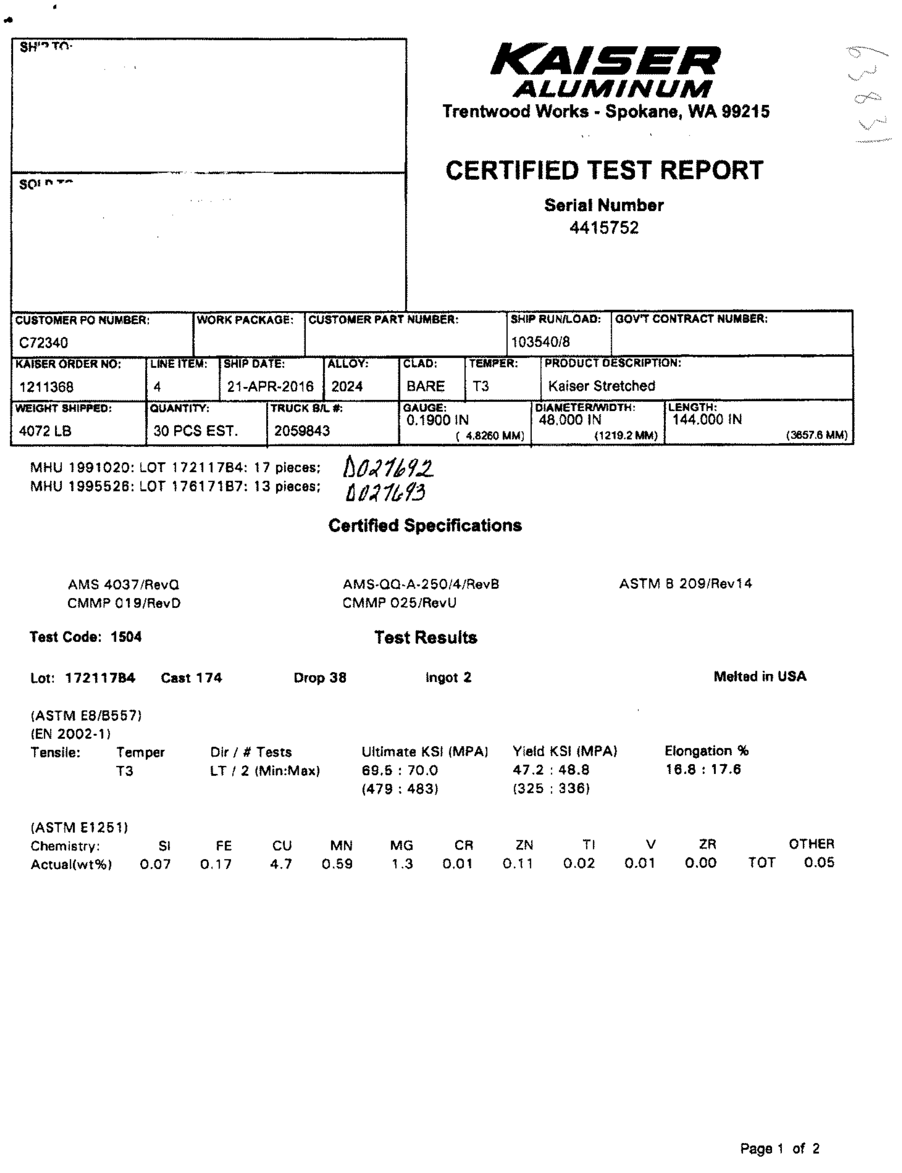

SHIP TO:	
SOLD TO:	

KAISER ALUMINUM
Trentwood Works - Spokane, WA 99215

CERTIFIED TEST REPORT

Serial Number
4415752

CUSTOMER PO NUMBER: C72340	WORK PACKAGE:	CUSTOMER PART NUMBER:	SHIP RUN/LOAD: 103540/8	GOV'T CONTRACT NUMBER:

KAISER ORDER NO: 1211368	LINE ITEM: 4	SHIP DATE: 21-APR-2016	ALLOY: 2024	CLAD: BARE	TEMPER: T3	PRODUCT DESCRIPTION: Kaiser Stretched

WEIGHT SHIPPED: 4072 LB	QUANTITY: 30 PCS EST.	TRUCK B/L #: 2059843	GAUGE: 0.1900 IN (4.8260 MM)	DIAMETER/WIDTH: 48.000 IN (1219.2 MM)	LENGTH: 144.000 IN (3657.6 MM)

MHU 1991020: LOT 172117B4: 17 pieces; D027692
MHU 1995526: LOT 176171B7: 13 pieces; D027693

Certified Specifications

AMS 4037/RevQ	AMS-QQ-A-250/4/RevB	ASTM B 209/Rev14
CMMP 019/RevD	CMMP 025/RevU	

Test Code: 1504

Test Results

Lot: 172117B4 **Cast 174** **Drop 38** **Ingot 2** **Melted in USA**

(ASTM E8/B557)
(EN 2002-1)

Tensile:	Temper	Dir / # Tests	Ultimate KSI (MPA)	Yield KSI (MPA)	Elongation %
	T3	LT / 2 (Min:Max)	69.5 : 70.0 (479 : 483)	47.2 : 48.8 (325 : 336)	16.8 : 17.6

(ASTM E1251)

Chemistry:	SI	FE	CU	MN	MG	CR	ZN	TI	V	ZR		OTHER
Actual(wt%)	0.07	0.17	4.7	0.59	1.3	0.01	0.11	0.02	0.01	0.00	TOT	0.05

Page 1 of 2

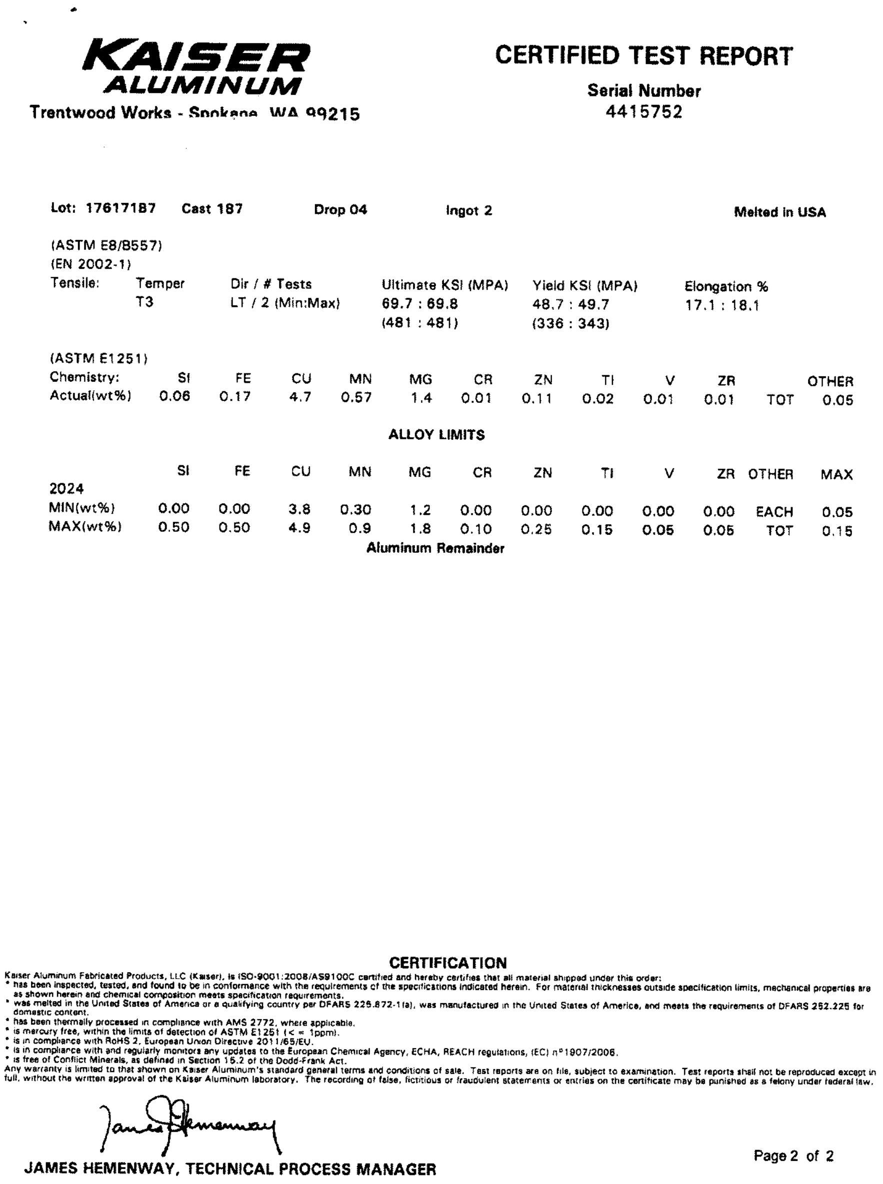

KAISER ALUMINUM
Trentwood Works - Spokane WA 99215

CERTIFIED TEST REPORT

Serial Number
4415752

Lot: 176171B7 **Cast 187** **Drop 04** **Ingot 2** **Melted in USA**

(ASTM E8/B557)
(EN 2002-1)

Tensile:	Temper	Dir / # Tests	Ultimate KSI (MPA)	Yield KSI (MPA)	Elongation %
	T3	LT / 2 (Min:Max)	69.7 : 69.8 (481 : 481)	48.7 : 49.7 (336 : 343)	17.1 : 18.1

(ASTM E1251)

Chemistry:	SI	FE	CU	MN	MG	CR	ZN	TI	V	ZR		OTHER
Actual(wt%)	0.06	0.17	4.7	0.57	1.4	0.01	0.11	0.02	0.01	0.01	TOT	0.05

ALLOY LIMITS

2024	SI	FE	CU	MN	MG	CR	ZN	TI	V	ZR	OTHER	MAX
MIN(wt%)	0.00	0.00	3.8	0.30	1.2	0.00	0.00	0.00	0.00	0.00	EACH	0.05
MAX(wt%)	0.50	0.50	4.9	0.9	1.8	0.10	0.25	0.15	0.05	0.05	TOT	0.15

Aluminum Remainder

CERTIFICATION

Kaiser Aluminum Fabricated Products, LLC (Kaiser), is ISO-9001:2008/AS9100C certified and hereby certifies that all material shipped under this order:
* has been inspected, tested, and found to be in conformance with the requirements of the specifications indicated herein. For material thicknesses outside specification limits, mechanical properties are as shown herein and chemical composition meets specification requirements.
* was melted in the United States of America or a qualifying country per DFARS 225.872-1(a), was manufactured in the United States of America, and meets the requirements of DFARS 252.225 for domestic content.
* has been thermally processed in compliance with AMS 2772, where applicable.
* is mercury free, within the limits of detection of ASTM E1251 (< = 1ppm).
* is in compliance with RoHS 2, European Union Directive 2011/65/EU.
* is in compliance with and regularly monitors any updates to the European Chemical Agency, ECHA, REACH regulations, (EC) n°1907/2006.
* is free of Conflict Minerals, as defined in Section 15.2 of the Dodd-Frank Act.

Any warranty is limited to that shown on Kaiser Aluminum's standard general terms and conditions of sale. Test reports are on file, subject to examination. Test reports shall not be reproduced except in full, without the written approval of the Kaiser Aluminum laboratory. The recording of false, fictitious or fraudulent statements or entries on the certificate may be punished as a felony under federal law.

James Hemenway

JAMES HEMENWAY, TECHNICAL PROCESS MANAGER

Page 2 of 2

APPENDIX C TABULATED RESIDUAL STRESS DATA

C.1 Hole drilling

Table C.1 Residual stresses measured by hole drilling in coupon 2:1–T.

Depth	Along L		Along T		Shear		Depth	Along L		Along T		Shear	
(mm)	Stress (MPa)	Uncertainty (MPa)	Stress (MPa)	Uncertainty (MPa)	Stress (MPa)	Uncertainty (MPa)	(mm)	Stress (MPa)	Uncertainty (MPa)	Stress (MPa)	Uncertainty (MPa)	Stress (MPa)	Uncertainty (MPa)
0.025	-286.1	12.8	-277.9	12.8	17.1	5.1	0.533	84.8	7.6	20.7	7.6	-16.3	3.6
0.076	-348.9	6.7	-331.6	6.7	5.7	2.4	0.584	89.6	7.9	29.6	7.9	-6.0	3.7
0.127	-357.9	7.5	-331.6	7.5	0.3	3.8	0.635	92.4	8.3	39.3	8.3	2.4	3.9
0.178	-298.6	6.7	-268.2	6.7	4.4	3.6	0.686	85.5	8.7	39.3	8.7	1.4	4.0
0.229	-197.9	6.6	-170.3	6.6	10.7	3.3	0.737	71.7	9.7	32.4	9.7	-6.9	4.1
0.279	-85.5	6.7	-70.3	6.7	12.3	3.4	0.787	57.2	10.8	24.8	10.8	-15.3	4.5
0.330	9.7	6.7	3.4	6.7	6.5	3.4	0.838	47.6	11.0	22.8	11.0	-18.7	4.9
0.381	66.9	6.9	37.9	6.9	-3.9	3.4	0.889	45.5	14.0	29.0	14.0	-17.0	4.9
0.432	85.5	7.1	35.9	7.1	-13.9	3.5	0.940	46.9	25.2	40.0	25.2	-12.9	7.5
0.483	84.8	7.3	22.8	7.3	-20.0	3.6	0.991	51.0	41.3	52.4	41.3	-8.2	13.9

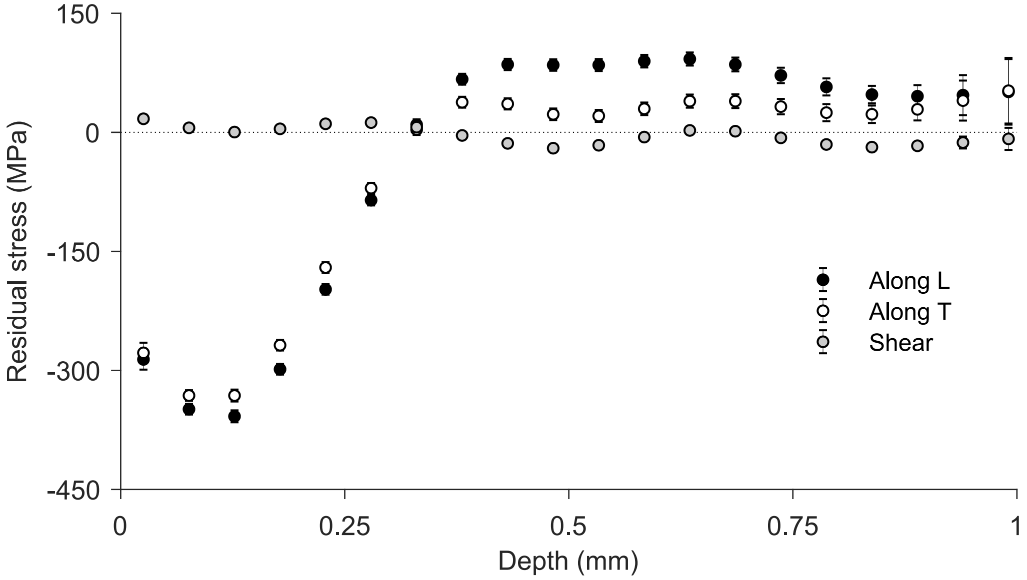

Table C.2 Residual stresses measured by hole drilling in coupon 1:1–L.

Depth	Along L		Along T		Shear		Depth	Along L		Along T		Shear	
(mm)	Stress (MPa)	Uncertainty (MPa)	Stress (MPa)	Uncertainty (MPa)	Stress (MPa)	Uncertainty (MPa)	(mm)	Stress (MPa)	Uncertainty (MPa)	Stress (MPa)	Uncertainty (MPa)	Stress (MPa)	Uncertainty (MPa)
0.025	-354.4	11.5	-311.6	11.5	3.9	5.6	0.533	84.8	7.5	60.0	7.5	-20.8	4.2
0.076	-378.5	5.6	-338.5	5.6	0.8	3.0	0.584	75.8	7.8	59.3	7.8	-13.8	4.3
0.127	-359.9	7.2	-325.4	7.2	-6.0	4.4	0.635	66.9	8.2	49.6	8.2	-5.4	4.4
0.178	-288.9	6.7	-264.1	6.7	-14.5	4.0	0.686	60.0	8.6	37.9	8.6	-4.1	4.5
0.229	-186.8	6.5	-177.9	6.5	-16.9	3.8	0.737	55.8	9.6	29.6	9.6	-8.7	4.7
0.279	-80.0	6.6	-89.6	6.6	-10.4	3.9	0.787	54.5	10.6	25.5	10.6	-12.7	5.0
0.330	8.3	6.7	-17.2	6.7	-0.0	3.9	0.838	55.2	10.8	28.3	10.8	-13.8	5.5
0.381	67.6	6.8	29.6	6.8	2.8	3.9	0.889	57.9	14.0	35.9	14.0	-12.7	5.5
0.432	91.7	7.0	49.6	7.0	-5.2	4.0	0.940	60.7	24.9	47.6	24.9	-8.0	7.8
0.483	91.7	7.2	56.5	7.2	-17.3	4.1	0.991	64.8	40.6	60.7	40.6	-1.6	15.3

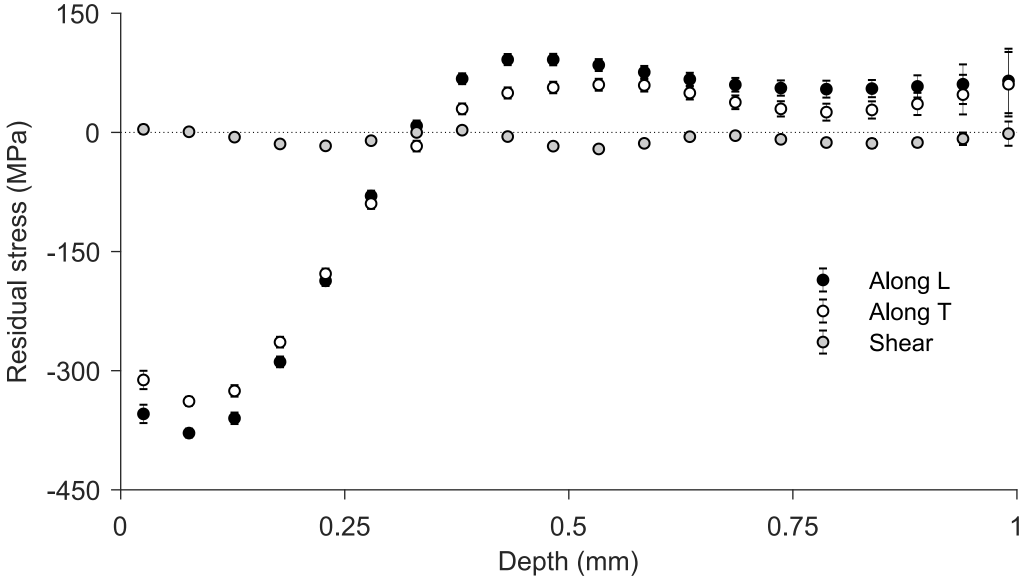

Table C.3 Residual stresses measured by hole drilling in coupon 1:2–L–A.

Depth	Along L		Along T		Shear		Depth	Along L		Along T		Shear	
(mm)	Stress (MPa)	Uncertainty (MPa)	Stress (MPa)	Uncertainty (MPa)	Stress (MPa)	Uncertainty (MPa)	(mm)	Stress (MPa)	Uncertainty (MPa)	Stress (MPa)	Uncertainty (MPa)	Stress (MPa)	Uncertainty (MPa)
0.025	-363.7	9.8	-376.8	9.8	-3.2	5.5	0.533	94.4	8.0	64.5	8.0	0.9	4.0
0.076	-369.6	5.4	-374.5	5.4	8.4	2.8	0.584	112.5	8.3	78.0	8.3	8.4	4.1
0.127	-345.5	7.9	-339.9	7.9	12.8	4.2	0.635	120.0	8.7	79.2	8.7	15.7	4.3
0.178	-280.6	7.2	-265.6	7.2	8.9	3.9	0.686	113.0	9.1	65.9	9.1	16.8	4.4
0.229	-186.6	7.0	-176.1	7.0	1.5	3.7	0.737	97.5	10.1	48.1	10.1	10.7	4.5
0.279	-87.7	7.1	-97.9	7.1	0.8	3.8	0.787	83.5	11.1	41.4	11.1	3.5	4.9
0.330	-10.8	7.2	-37.7	7.2	4.2	3.8	0.838	77.7	11.5	50.0	11.5	0.8	5.4
0.381	32.8	7.3	6.1	7.3	5.3	3.8	0.889	79.7	14.5	67.6	14.5	3.2	5.3
0.432	55.5	7.5	31.9	7.5	2.5	3.9	0.940	85.5	25.4	87.3	25.4	7.7	7.8
0.483	74.4	7.7	48.5	7.7	-1.1	4.0	0.991	92.0	41.7	106.9	41.7	12.4	15.0

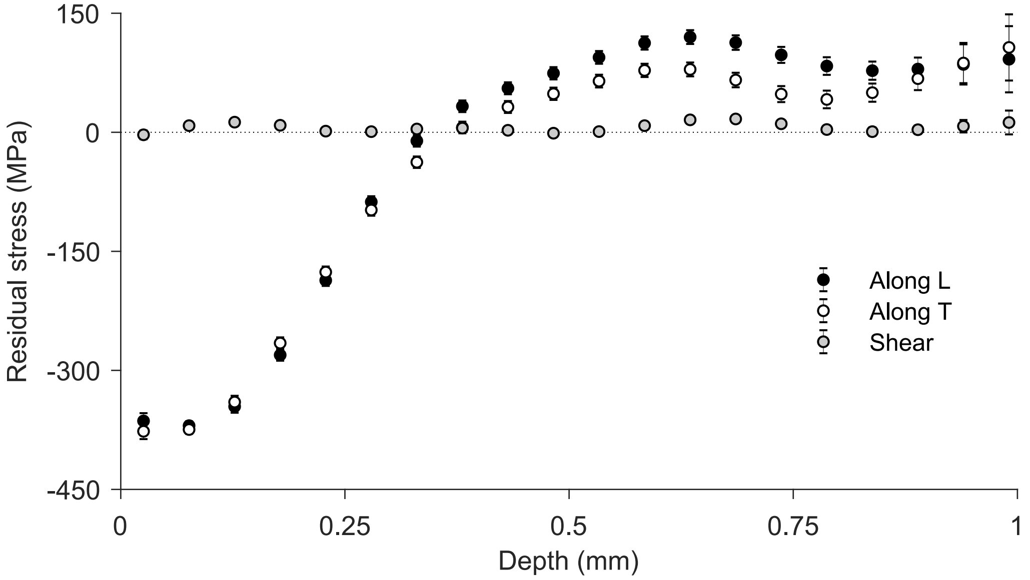

Table C.4 Residual stresses measured by hole drilling in coupon 4:1–L.

Depth	Along L		Along T		Shear		Depth	Along L		Along T		Shear	
(mm)	Stress (MPa)	Uncertainty (MPa)	Stress (MPa)	Uncertainty (MPa)	Stress (MPa)	Uncertainty (MPa)	(mm)	Stress (MPa)	Uncertainty (MPa)	Stress (MPa)	Uncertainty (MPa)	Stress (MPa)	Uncertainty (MPa)
0.025	-383.3	12.6	-373.4	12.6	-17.7	3.9	0.533	94.5	7.9	78.7	7.9	-10.9	2.5
0.076	-398.3	6.7	-402.2	6.7	-16.3	1.5	0.584	87.2	8.2	78.4	8.2	-10.1	2.6
0.127	-373.9	8.1	-384.6	8.1	-14.5	2.2	0.635	82.9	8.6	75.5	8.6	-7.5	2.6
0.178	-302.7	7.0	-317.0	7.0	-13.2	2.6	0.686	80.3	9.0	68.0	9.0	-3.5	2.8
0.229	-213.7	6.9	-230.9	6.9	-13.6	2.4	0.737	78.6	9.9	59.3	9.9	0.9	3.0
0.279	-120.8	7.0	-143.6	7.0	-14.1	2.3	0.787	76.8	11.0	52.6	11.0	4.0	3.2
0.330	-29.3	7.1	-58.7	7.1	-13.2	2.3	0.838	71.6	11.3	48.2	11.3	4.2	3.2
0.381	42.8	7.2	9.8	7.2	-12.0	2.4	0.889	62.1	14.2	45.5	14.2	1.1	3.9
0.432	85.0	7.4	53.7	7.4	-11.2	2.4	0.940	50.9	25.0	44.0	25.0	-4.2	6.5
0.483	98.3	7.6	73.5	7.6	-11.0	2.4	0.991	39.8	41.2	42.6	41.2	-10.5	10.4

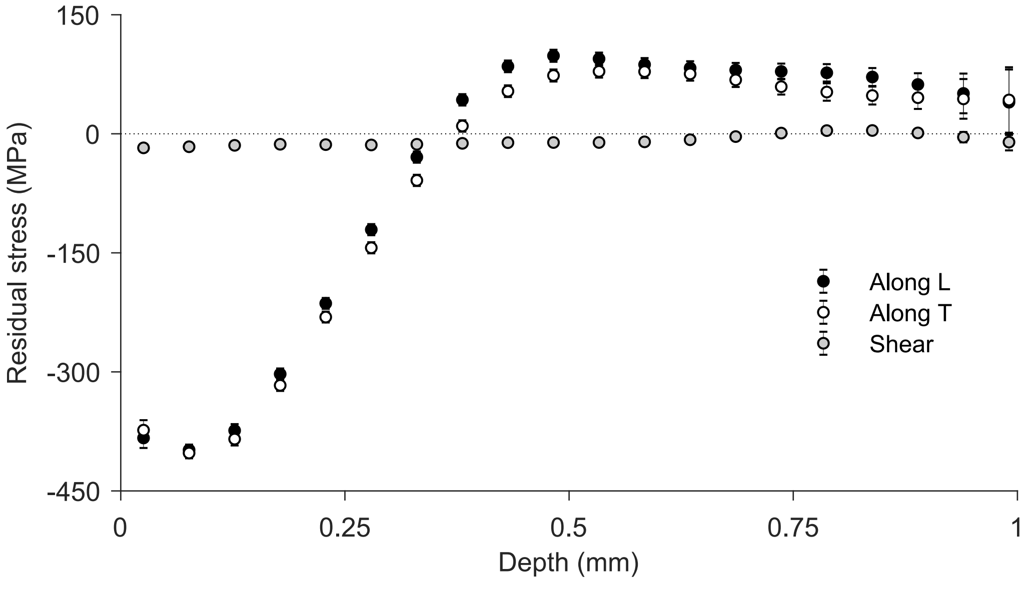

Table C.5 Residual stresses measured by hole drilling in coupon 1:4–L–A.

Depth	Along L		Along T		Shear	
(mm)	Stress (MPa)	Uncertainty (MPa)	Stress (MPa)	Uncertainty (MPa)	Stress (MPa)	Uncertainty (MPa)
0.025	-248.2	18.6	-272.4	18.6	30.3	4.1
0.076	-344.1	11.0	-357.9	11.0	30.3	2.1
0.127	-362.7	11.0	-368.2	11.0	26.2	2.8
0.178	-321.3	6.9	-320.6	6.9	15.9	2.8
0.229	-254.4	6.9	-252.4	6.9	2.1	2.8
0.279	-165.5	6.9	-167.6	6.9	-9.0	2.8
0.330	-75.2	6.9	-86.2	6.9	-14.5	2.8
0.381	15.9	7.6	-4.8	7.6	-11.7	2.8
0.432	77.2	7.6	49.6	7.6	-4.8	2.8
0.483	100.0	7.6	70.3	7.6	-2.1	2.8
0.533	103.4	8.3	77.9	8.3	-3.4	2.8
0.584	100.7	8.3	81.4	8.3	-6.2	2.8
0.635	94.5	9.0	81.4	9.0	-6.9	3.4
0.686	93.1	9.7	82.7	9.7	-2.8	3.4
0.737	91.0	10.3	80.7	10.3	1.4	3.4
0.787	86.2	11.7	73.8	11.7	4.8	4.1
0.838	82.0	11.7	64.8	11.7	7.6	4.1
0.889	80.0	14.5	58.6	14.5	11.0	4.1
0.940	79.3	26.2	53.8	26.2	14.5	6.9
0.991	80.0	44.1	49.6	44.1	17.2	12.4

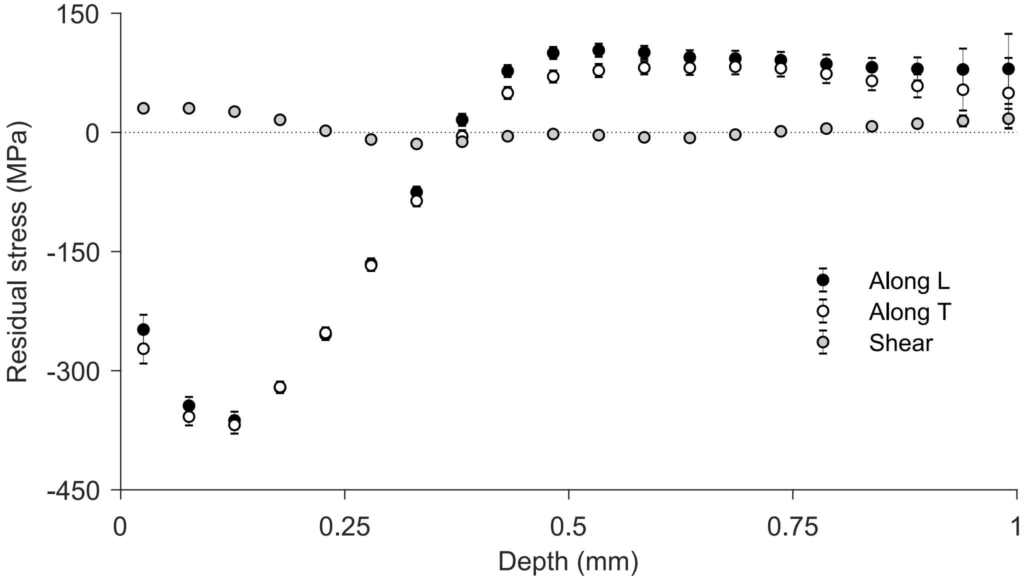

Table C.6 Residual stresses measured by hole drilling in coupon K0–L–A.

Depth	Along L		Along T		Shear		Depth	Along L		Along T		Shear	
(mm)	Stress (MPa)	Uncertainty (MPa)	Stress (MPa)	Uncertainty (MPa)	Stress (MPa)	Uncertainty (MPa)	(mm)	Stress (MPa)	Uncertainty (MPa)	Stress (MPa)	Uncertainty (MPa)	Stress (MPa)	Uncertainty (MPa)
0.025	-420.1	9.7	-471.3	9.7	-37.4	4.5	0.533	81.6	7.9	76.9	7.9	-9.3	3.1
0.076	-356.0	5.4	-418.9	5.4	-6.5	1.9	0.584	77.0	8.2	69.4	8.2	-9.6	3.2
0.127	-286.4	7.8	-337.5	7.8	17.9	3.0	0.635	69.2	8.5	58.1	8.5	-11.9	3.3
0.178	-205.9	7.1	-239.2	7.1	27.4	3.1	0.686	61.5	9.0	49.7	9.0	-13.6	3.3
0.229	-115.9	6.9	-150.5	6.9	24.0	2.8	0.737	56.5	9.8	49.2	9.8	-11.6	3.6
0.279	-25.6	7.0	-67.0	7.0	13.5	2.8	0.787	56.9	10.6	51.9	10.6	-7.3	3.9
0.330	46.8	7.1	3.3	7.1	2.3	2.9	0.838	61.3	11.1	54.5	11.1	-2.3	4.0
0.381	84.7	7.2	48.6	7.2	-5.9	2.9	0.889	66.2	14.3	57.5	14.3	2.4	4.3
0.432	88.9	7.4	71.7	7.4	-9.8	2.9	0.940	70.9	24.1	60.2	24.1	6.6	7.1
0.483	84.0	7.6	79.0	7.6	-10.1	3.0	0.991	75.7	39.4	62.2	39.4	10.5	12.3

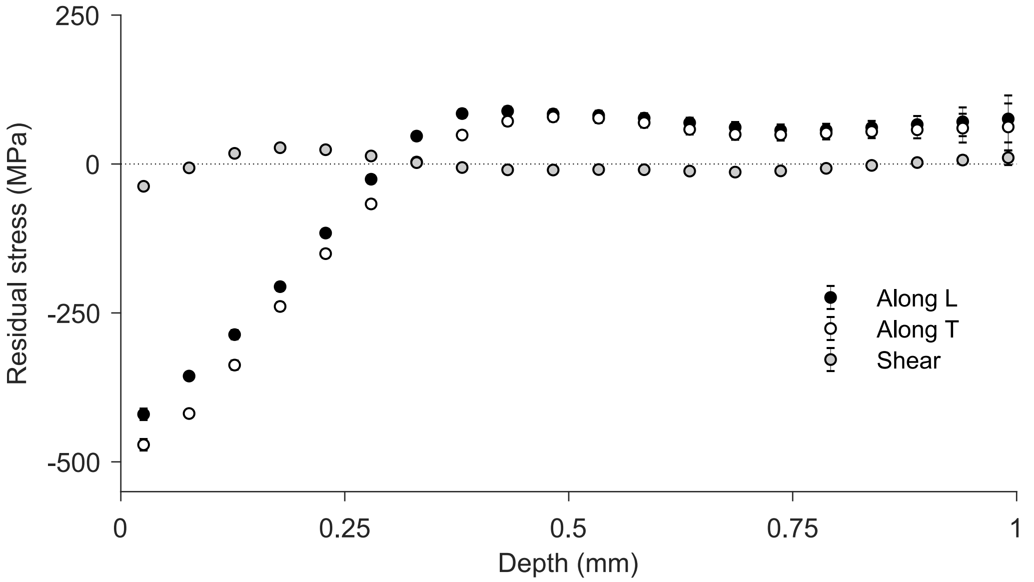

Table C.7 Residual stresses measured by hole drilling in coupon K1–L–A.

Depth	Along L		Along T		Shear		Depth	Along L		Along T		Shear	
	Stress	Uncertainty	Stress	Uncertainty	Stress	Uncertainty		Stress	Uncertainty	Stress	Uncertainty	Stress	Uncertainty
(mm)	(MPa)	(MPa)	(MPa)	(MPa)	(MPa)	(MPa)	(mm)	(MPa)	(MPa)	(MPa)	(MPa)	(MPa)	(MPa)
0.025	-354.5	16.5	-317.2	16.5	-17.2	5.8	0.533	86.5	10.2	58.2	10.2	-1.0	4.4
0.076	-420.6	11.5	-410.7	11.5	-5.4	3.2	0.584	84.3	10.6	63.5	10.6	9.0	4.5
0.127	-386.3	9.5	-399.1	9.5	8.8	4.6	0.635	89.3	11.1	75.6	11.1	15.6	4.6
0.178	-281.6	8.9	-308.4	8.9	17.7	4.1	0.686	90.8	11.6	85.1	11.6	10.2	4.7
0.229	-169.3	8.9	-201.9	8.9	20.4	4.0	0.737	81.4	12.3	81.5	12.3	-0.7	4.9
0.279	-73.6	9.0	-108.7	9.0	21.5	4.1	0.787	65.0	13.9	67.4	13.9	-8.5	5.2
0.330	-1.3	9.1	-42.6	9.1	18.4	4.1	0.838	45.2	15.1	47.0	15.1	-14.1	5.8
0.381	58.4	9.3	10.9	9.3	10.8	4.1	0.889	26.0	16.1	24.0	16.1	-20.4	5.7
0.432	87.2	9.5	41.5	9.5	1.2	4.2	0.940	9.0	28.5	1.7	28.5	-27.2	7.9
0.483	91.8	9.8	54.4	9.8	-4.1	4.3	0.991	-5.5	51.9	-18.1	51.9	-32.1	15.7

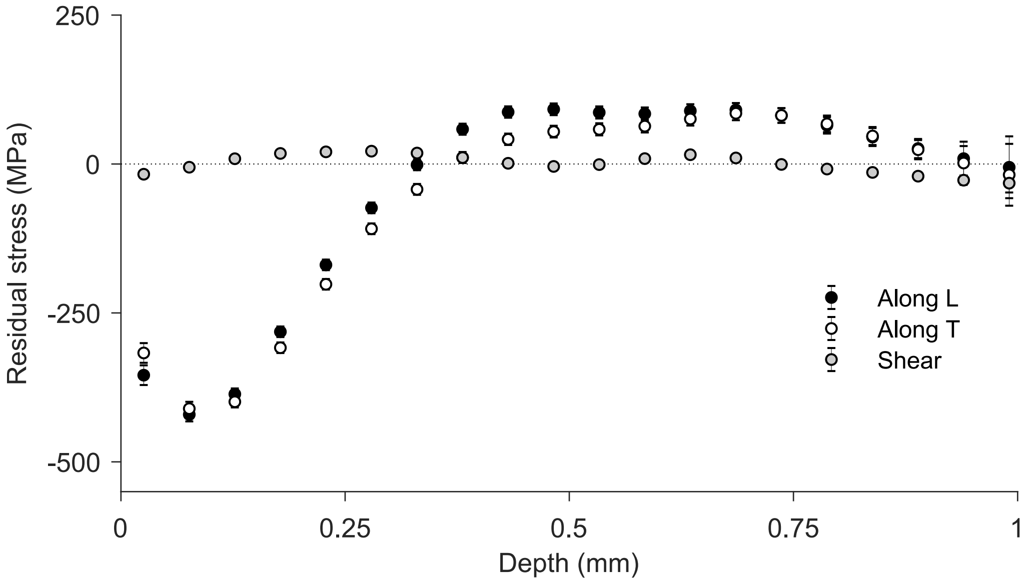

Table C.8 Residual stresses measured by hole drilling in coupon K2–L–A.

Depth	Along L		Along T		Shear		Depth	Along L		Along T		Shear	
(mm)	Stress (MPa)	Uncertainty (MPa)	Stress (MPa)	Uncertainty (MPa)	Stress (MPa)	Uncertainty (MPa)	(mm)	Stress (MPa)	Uncertainty (MPa)	Stress (MPa)	Uncertainty (MPa)	Stress (MPa)	Uncertainty (MPa)
0.025	-428.3	14.3	-313.0	14.3	-2.9	5.8	0.533	89.5	10.6	65.0	10.6	11.1	4.4
0.076	-450.0	10.1	-392.3	10.1	0.5	3.3	0.584	79.3	11.1	60.5	11.1	13.0	4.5
0.127	-390.8	9.9	-381.9	9.9	1.5	4.6	0.635	72.1	11.6	52.4	11.6	2.8	4.6
0.178	-297.2	9.3	-309.2	9.3	2.4	4.2	0.686	67.1	12.1	44.0	12.1	-12.4	4.8
0.229	-199.9	9.3	-206.6	9.3	0.8	4.1	0.737	65.1	12.8	38.0	12.8	-18.7	4.9
0.279	-99.4	9.4	-95.6	9.4	0.5	4.1	0.787	71.5	14.4	41.5	14.4	-13.2	5.3
0.330	-6.4	9.5	-4.9	9.5	6.2	4.1	0.838	83.1	15.8	56.1	15.8	-2.3	5.8
0.381	54.8	9.7	38.2	9.7	9.7	4.2	0.889	97.4	16.6	78.9	16.6	9.4	5.8
0.432	82.6	10.0	48.4	10.0	7.2	4.2	0.940	111.9	28.8	103.8	28.8	18.3	7.9
0.483	91.7	10.3	56.9	10.3	6.1	4.3	0.991	126.0	53.4	128.8	53.4	25.5	15.8

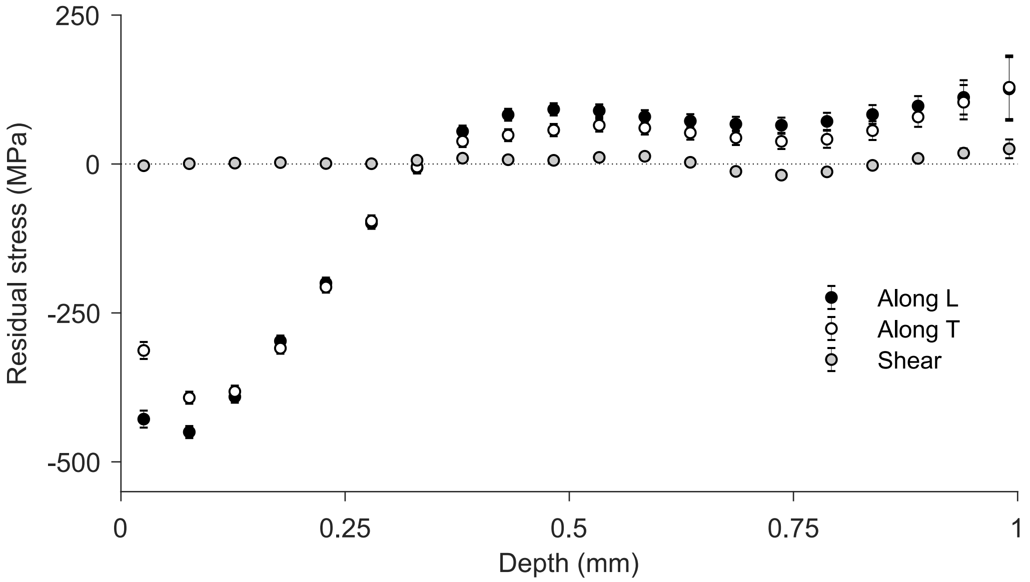

Table C.9 Residual stresses measured by hole drilling in coupon K3–L–A.

Depth	Along L		Along T		Shear		Depth	Along L		Along T		Shear	
(mm)	Stress (MPa)	Uncertainty (MPa)	Stress (MPa)	Uncertainty (MPa)	Stress (MPa)	Uncertainty (MPa)	(mm)	Stress (MPa)	Uncertainty (MPa)	Stress (MPa)	Uncertainty (MPa)	Stress (MPa)	Uncertainty (MPa)
0.025	-458.2	10.1	-340.5	10.1	-39.9	6.2	0.533	115.0	6.9	68.6	6.9	3.1	4.9
0.076	-431.5	5.4	-379.4	5.4	-22.6	3.9	0.584	114.0	7.1	73.0	7.1	-2.9	5.0
0.127	-397.9	7.8	-384.4	7.8	-13.6	5.1	0.635	105.7	7.5	75.4	7.5	0.3	5.1
0.178	-345.5	6.8	-338.8	6.8	-1.5	4.6	0.686	96.5	8.0	73.1	8.0	2.1	5.3
0.229	-261.6	6.9	-248.1	6.9	8.2	4.5	0.737	86.6	8.6	64.8	8.6	-9.4	5.5
0.279	-165.8	7.0	-145.1	7.0	9.9	4.6	0.787	74.7	9.0	54.1	9.0	-25.2	5.7
0.330	-79.7	6.3	-56.8	6.3	9.2	4.6	0.838	63.9	10.0	43.7	10.0	-31.3	6.4
0.381	-4.8	6.4	6.2	6.4	12.6	4.6	0.889	55.9	13.6	36.6	13.6	-21.6	6.5
0.432	57.0	6.5	42.6	6.5	17.1	4.7	0.940	49.1	21.5	33.8	21.5	-0.9	8.2
0.483	98.3	6.7	60.3	6.7	14.1	4.8	0.991	43.4	33.8	32.2	33.8	21.4	16.9

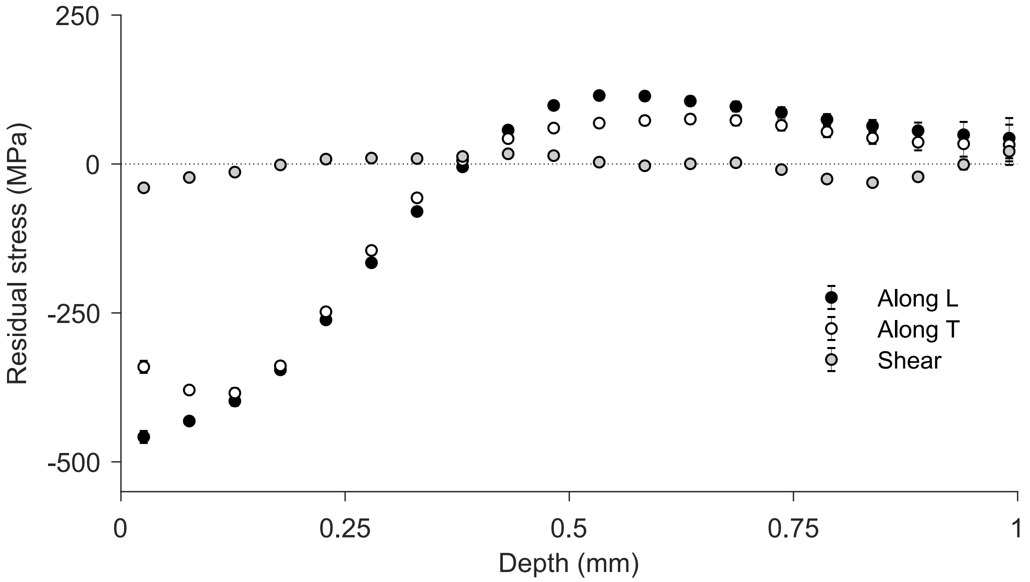

Table C.10 Residual stresses measured by hole drilling in coupon K4–L–A.

Depth	Along L		Along T		Shear		Depth	Along L		Along T		Shear	
(mm)	Stress (MPa)	Uncertainty (MPa)	Stress (MPa)	Uncertainty (MPa)	Stress (MPa)	Uncertainty (MPa)	(mm)	Stress (MPa)	Uncertainty (MPa)	Stress (MPa)	Uncertainty (MPa)	Stress (MPa)	Uncertainty (MPa)
0.025	-501.2	9.8	-387.9	9.8	-5.5	5.0	0.533	128.1	6.6	41.9	6.6	-6.3	3.5
0.076	-469.8	4.0	-377.2	4.0	2.0	2.3	0.584	127.3	6.8	43.8	6.8	-14.9	3.6
0.127	-417.1	6.6	-349.6	6.6	9.3	3.6	0.635	121.9	7.1	49.0	7.1	-15.0	3.7
0.178	-339.5	6.1	-298.9	6.1	12.2	3.5	0.686	116.0	7.7	59.5	7.7	-8.5	3.8
0.229	-245.2	5.7	-221.2	5.7	10.4	3.2	0.737	111.5	8.4	72.9	8.4	1.3	4.0
0.279	-149.8	5.9	-131.7	5.9	11.0	3.3	0.787	108.7	8.9	83.0	8.9	9.9	4.4
0.330	-60.4	5.9	-51.3	5.9	15.0	3.3	0.838	106.5	9.5	88.5	9.5	15.1	4.7
0.381	19.6	6.0	4.7	6.0	18.7	3.3	0.889	105.1	13.2	89.3	13.2	15.8	4.7
0.432	80.7	6.1	33.5	6.1	16.6	3.4	0.940	105.1	22.1	86.7	22.1	12.9	7.4
0.483	115.3	6.3	41.1	6.3	6.5	3.4	0.991	106.1	34.4	82.7	34.4	8.6	13.5

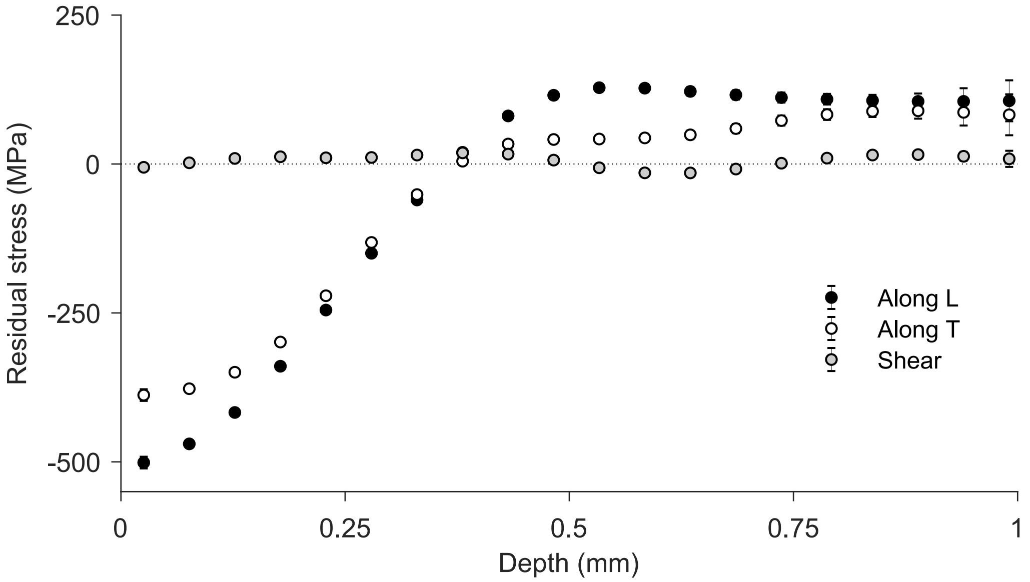

Table C.11 Residual stresses measured by hole drilling in coupon U–L–A.

Depth	Along L		Along T		Shear	
(mm)	Stress (MPa)	Uncertainty (MPa)	Stress (MPa)	Uncertainty (MPa)	Stress (MPa)	Uncertainty (MPa)
0.025	-379.9	11.7	-337.2	11.7	-17.2	5.5
0.076	-374.4	5.5	-349.6	5.5	0.0	2.8
0.127	-339.2	8.3	-335.1	8.3	11.0	4.1
0.178	-271.7	6.9	-275.1	6.9	14.5	4.1
0.229	-184.1	6.2	-186.2	6.2	15.2	4.1
0.279	-85.5	6.9	-90.3	6.9	16.5	4.1
0.330	6.2	6.9	-13.8	6.9	15.9	4.1
0.381	68.3	6.9	39.3	6.9	11.7	4.1
0.432	95.8	6.9	67.6	6.9	6.9	4.1
0.483	100.0	6.9	73.1	6.9	7.6	4.1
0.533	93.1	7.6	64.8	7.6	7.6	4.1
0.584	80.7	7.6	61.4	7.6	9.0	4.1
0.635	69.6	8.3	68.3	8.3	13.8	4.1
0.686	64.1	8.3	73.1	8.3	17.9	4.8
0.737	64.8	9.0	64.1	9.0	15.9	4.8
0.787	65.5	9.7	49.0	9.7	7.6	4.8
0.838	62.1	10.3	36.5	10.3	-3.4	5.5
0.889	52.4	13.8	32.4	13.8	-11.0	5.5
0.940	42.1	22.8	33.1	22.8	-15.2	7.6
0.991	33.1	37.2	35.2	37.2	-18.6	15.2

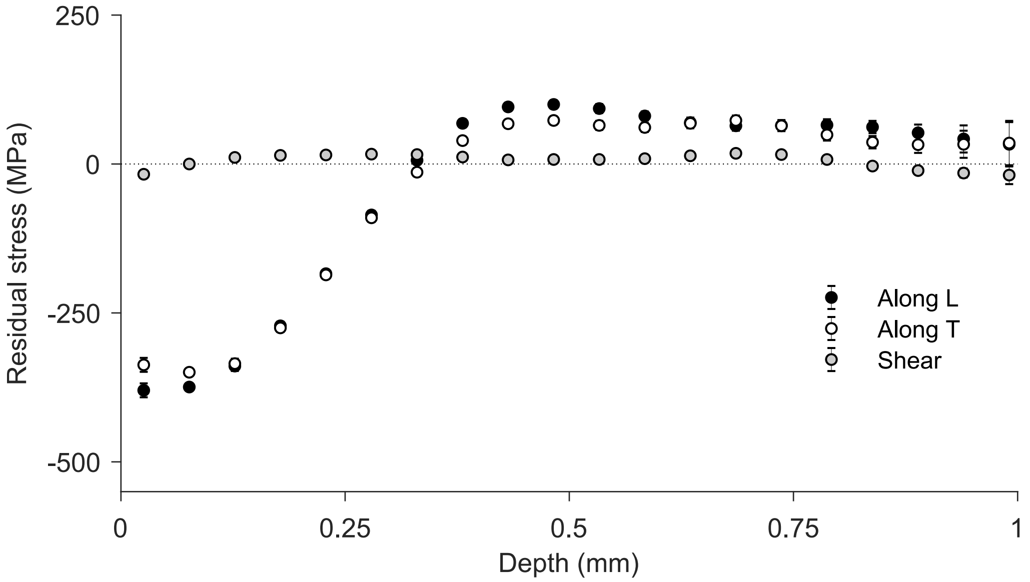

Table C.12 Residual stresses measured by hole drilling in coupons 10 (left/top) and 11 (right/bottom).

Depth	Along L		Along T		Shear		Depth	Along L		Along T		Shear	
(mm)	Stress (MPa)	Uncertainty (MPa)	Stress (MPa)	Uncertainty (MPa)	Stress (MPa)	Uncertainty (MPa)	(mm)	Stress (MPa)	Uncertainty (MPa)	Stress (MPa)	Uncertainty (MPa)	Stress (MPa)	Uncertainty (MPa)
0.025	8.1	10.2	7.8	10.2	-15.4	5.3	0.533	11.7	8.7	-3.0	8.7	9.1	3.9
0.076	12.3	6.3	-2.9	6.3	-20.8	2.7	0.584	17.8	9.1	8.7	9.1	9.7	4.0
0.127	10.8	8.5	-26.0	8.5	-23.3	4.0	0.635	15.1	9.5	15.5	9.5	4.9	4.1
0.178	14.5	7.7	-33.3	7.7	-15.9	3.7	0.686	7.4	9.9	12.6	9.9	-4.4	4.2
0.229	24.0	7.6	-14.1	7.6	-1.8	3.6	0.737	1.3	10.7	1.7	10.7	-12.1	4.4
0.279	23.4	7.8	-0.1	7.8	6.9	3.6	0.787	-0.9	12.0	-10.0	12.0	-14.9	4.8
0.330	10.1	7.8	-4.8	7.8	9.0	3.6	0.838	1.8	12.5	-15.6	12.5	-12.3	5.2
0.381	1.2	8.0	-13.7	8.0	9.6	3.7	0.889	6.9	14.8	-11.4	14.8	-5.2	5.1
0.432	2.0	8.2	-16.7	8.2	9.5	3.7	0.940	10.8	26.1	2.8	26.1	5.2	7.6
0.483	5.0	8.4	-14.1	8.4	8.4	3.8	0.991	12.6	44.5	21.9	44.5	16.6	14.5

Depth	Along L		Along T		Shear		Depth	Along L		Along T		Shear	
(mm)	Stress (MPa)	Uncertainty (MPa)	Stress (MPa)	Uncertainty (MPa)	Stress (MPa)	Uncertainty (MPa)	(mm)	Stress (MPa)	Uncertainty (MPa)	Stress (MPa)	Uncertainty (MPa)	Stress (MPa)	Uncertainty (MPa)
4.875	8.0	7.1	9.6	7.1	12.7	5.6	4.367	21.9	5.1	-9.1	5.1	-1.4	4.2
4.824	19.4	2.8	10.0	2.8	9.6	3.0	4.316	16.1	5.3	-12.7	5.3	-9.1	4.3
4.773	29.0	4.6	8.7	4.6	3.1	4.4	4.265	7.6	5.7	-14.8	5.7	-13.8	4.4
4.722	34.0	5.0	7.2	5.0	0.9	4.0	4.214	-0.9	6.2	-13.9	6.2	-11.8	4.5
4.671	33.2	4.6	5.8	4.6	9.6	3.8	4.163	-6.9	6.7	-9.6	6.7	-8.0	4.7
4.621	28.2	4.5	3.7	4.5	14.6	3.9	4.113	-9.7	6.9	-3.6	6.9	-4.5	5.0
4.570	24.0	4.6	0.1	4.6	2.7	3.9	4.062	-9.8	8.0	2.5	8.0	0.2	5.5
4.519	22.7	4.7	-2.2	4.7	-8.3	3.9	4.011	-8.2	12.0	7.8	12.0	4.9	5.5
4.468	23.0	4.8	-3.5	4.8	-6.4	4.0	3.960	-5.9	19.0	12.9	19.0	7.9	7.7
4.417	23.7	5.0	-5.5	5.0	0.3	4.1	3.909	-3.4	27.8	17.9	27.8	9.1	15.1

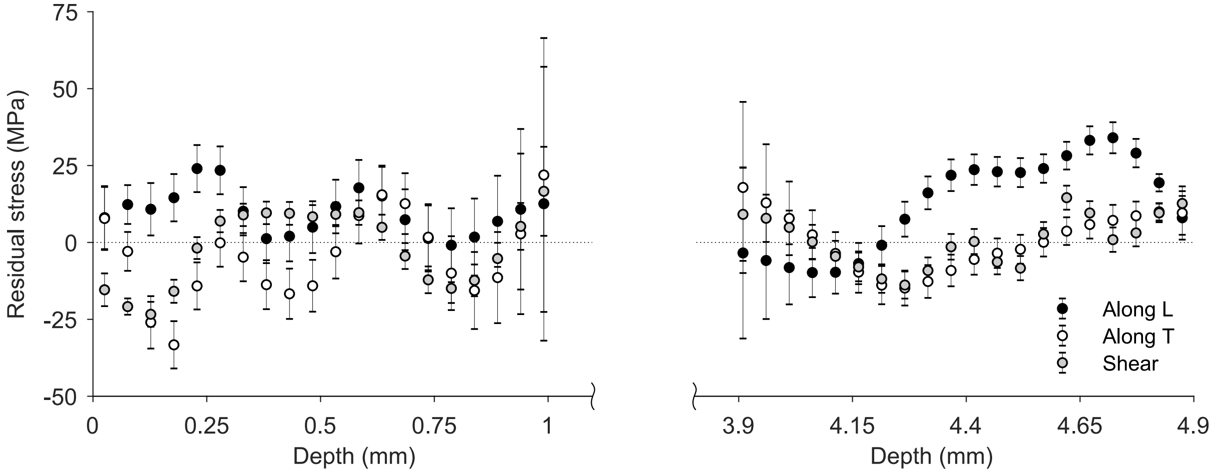

C.2 Slitting

Table C.13 Residual stresses measured by slitting in coupons 1:2–L–B and 1:2–L–C.

Depth	Along L		Along T		Depth	Along L		Along T	
(mm)	Stress (MPa)	Uncertainty (MPa)	Stress (MPa)	Uncertainty (MPa)	(mm)	Stress (MPa)	Uncertainty (MPa)	Stress (MPa)	Uncertainty (MPa)
0.025	-471.6	7.6	-526.1	8.3	1.270	55.8	4.1	51.0	4.8
0.076	-396.5	3.4	-415.8	3.4	1.372	48.3	4.1	46.2	4.8
0.127	-318.6	2.8	-308.2	3.4	1.473	47.6	4.1	54.5	4.8
0.178	-237.2	4.8	-204.8	4.8	1.575	45.5	4.1	51.0	4.1
0.229	-152.4	4.8	-111.0	5.5	1.676	44.1	4.1	44.1	4.1
0.279	-71.0	4.8	-33.8	4.8	1.778	44.8	4.1	46.9	4.1
0.330	0.7	4.1	20.0	4.1	1.880	34.5	4.1	33.8	4.1
0.381	55.8	4.1	50.3	4.1	1.981	26.2	4.1	31.0	4.1
0.432	91.0	4.8	62.1	4.8	2.083	24.8	4.1	40.0	4.1
0.483	109.6	5.5	64.8	5.5	2.184	18.6	4.1	41.4	4.1
0.559	97.9	4.8	58.6	4.8	2.286	7.6	4.1	41.4	4.1
0.660	87.6	4.8	65.5	4.8	2.388	5.5	4.1	35.9	4.1
0.762	82.0	4.8	64.8	4.8	2.489	0.0	4.8	24.1	5.5
0.864	78.6	4.8	55.2	4.8	2.667	2.1	2.1	21.4	2.1
0.965	71.0	4.8	56.5	4.8	2.921	-4.1	1.4	10.3	1.4
1.067	65.5	4.8	55.2	4.8	3.175	-4.8	1.4	11.0	1.4
1.168	60.7	4.8	53.1	4.8	3.429	-5.5	1.4	-1.4	1.4

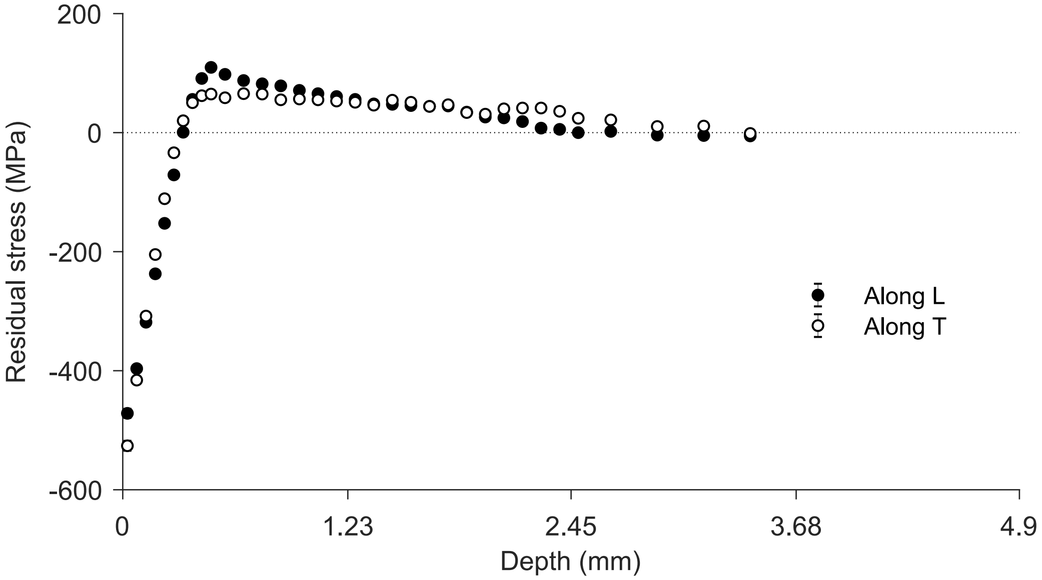

Table C.14 Residual stresses measured by slitting in coupons 13 and 14.

Depth	Along L		Along T		Depth	Along L		Along T	
(mm)	Stress (MPa)	Uncertainty (MPa)	Stress (MPa)	Uncertainty (MPa)	(mm)	Stress (MPa)	Uncertainty (MPa)	Stress (MPa)	Uncertainty (MPa)
0.025	11.7	0.7	-11.9	1.2	1.270	-1.4	0.4	0.7	0.6
0.076	12.3	0.6	-10.4	0.9	1.372	-3.7	0.3	-0.3	0.5
0.127	12.8	0.4	-8.9	0.7	1.473	-5.9	0.3	-1.1	0.5
0.178	13.2	0.3	-7.3	0.5	1.575	-8.0	0.3	-1.6	0.5
0.229	13.7	0.2	-5.9	0.3	1.676	-9.9	0.3	-1.8	0.5
0.279	14.1	0.2	-4.4	0.3	1.778	-11.6	0.3	-1.4	0.5
0.330	14.4	0.3	-3.0	0.4	1.880	-12.9	0.3	-0.6	0.5
0.381	14.7	0.3	-1.7	0.5	1.981	-13.8	0.3	0.5	0.5
0.432	14.8	0.4	-0.5	0.6	2.083	-14.4	0.3	1.4	0.5
0.483	14.8	0.4	0.5	0.7	2.184	-14.6	0.3	2.1	0.5
0.559	14.2	0.5	2.1	0.7	2.286	-14.6	0.3	2.4	0.5
0.660	13.1	0.4	3.2	0.6	2.388	-14.5	0.4	2.4	0.6
0.762	11.3	0.4	3.8	0.6	2.489	-14.4	0.4	2.4	0.6
0.864	9.0	0.3	3.8	0.5	2.667	-14.5	0.4	2.7	0.6
0.965	6.5	0.4	3.4	0.5	2.921	-15.1	0.4	2.8	0.6
1.067	3.8	0.4	2.7	0.6	3.175	-12.9	0.4	0.2	0.6
1.168	1.1	0.4	1.7	0.6	3.429	-8.8	0.4	-4.6	0.6

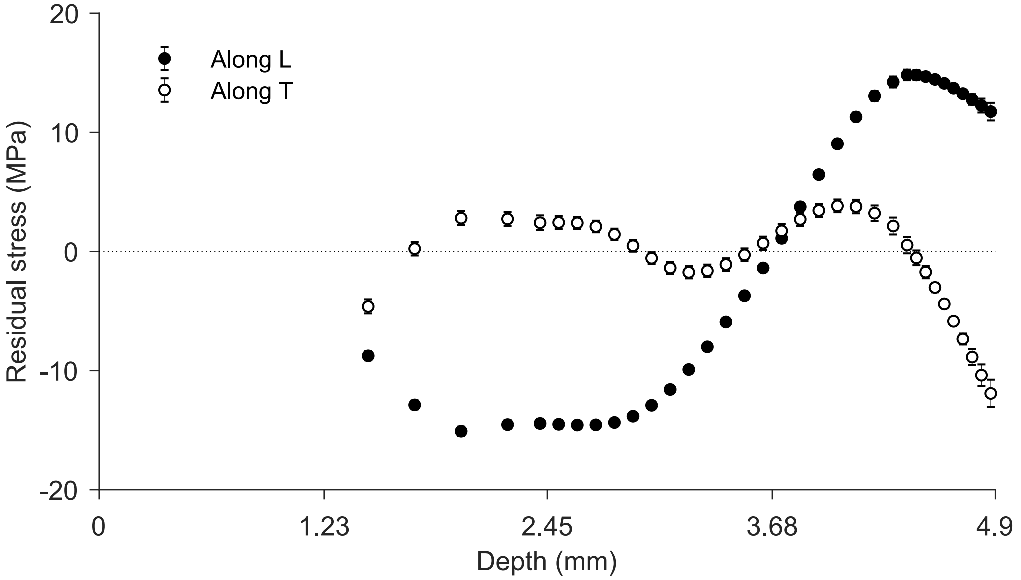

C.3 X-ray diffraction

Table C.15 Residual stresses measured by X-ray diffraction in coupon 1:1–T.

Depth	Along L			Along T		
(mm)	Stress (MPa)	Uncertainty (MPa)	FWHM (°)	Stress (MPa)	Uncertainty (MPa)	FWHM (°)
0.000	-142	10	3.16	-130	3	3.14
0.024	-267	13	3.09	-200	7	3.09
0.076	-304	30	2.93	-334	15	2.81
0.138	-242	38	2.79	-322	36	2.66
0.182	-80	48	2.67	-468	41	2.51
0.231	-567	72	2.75	-188	35	2.38
0.336	-268	134	2.18	33	37	2.28
0.435	80	102	2.60	-27	30	2.20
0.615	16	-	2.29	190	-	2.29

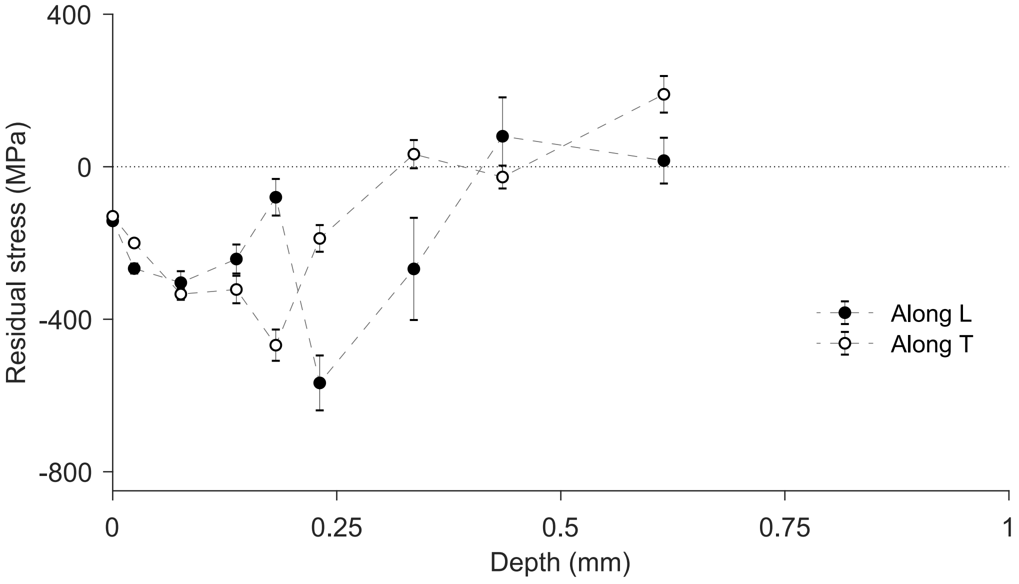

Table C.16 Residual stresses measured by X-ray diffraction in coupon 4:1–T.

Depth	Along L		
(mm)	Stress (MPa)	Uncertainty (MPa)	FWHM (°)
0.000	-161	6	3.16
0.024	-275	15	3.06
0.077	-335	13	2.89
0.127	-445	21	2.73
0.182	-474	-	2.29
0.225	-332	44	2.18
0.374	-639	169	2.04
0.454	60	71	2.18
0.606	27	80	2.03

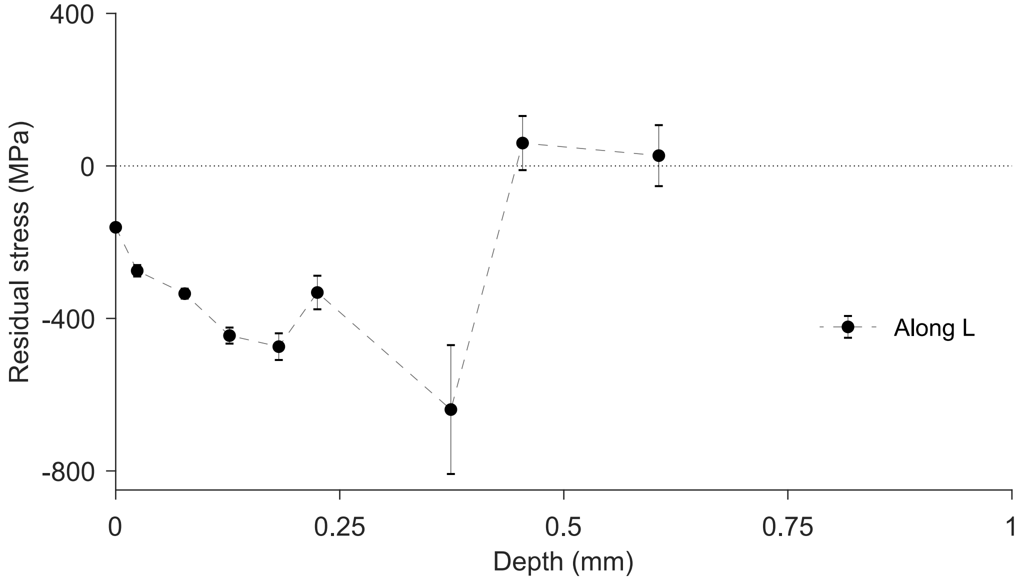

Table C.17 Residual stresses measured by X-ray diffraction in coupon 1:4–L–B.

Depth	Along T		
(mm)	Stress (MPa)	Uncertainty (MPa)	FWHM (°)
0.000	-196	6	3.16
0.025	-199	18	3.07
0.072	-432	40	2.90
0.120	-358	49	2.72
0.178	-376	-	2.60
0.350	-144	127	2.29
0.449	178	39	2.21
0.615	20	69	2.23

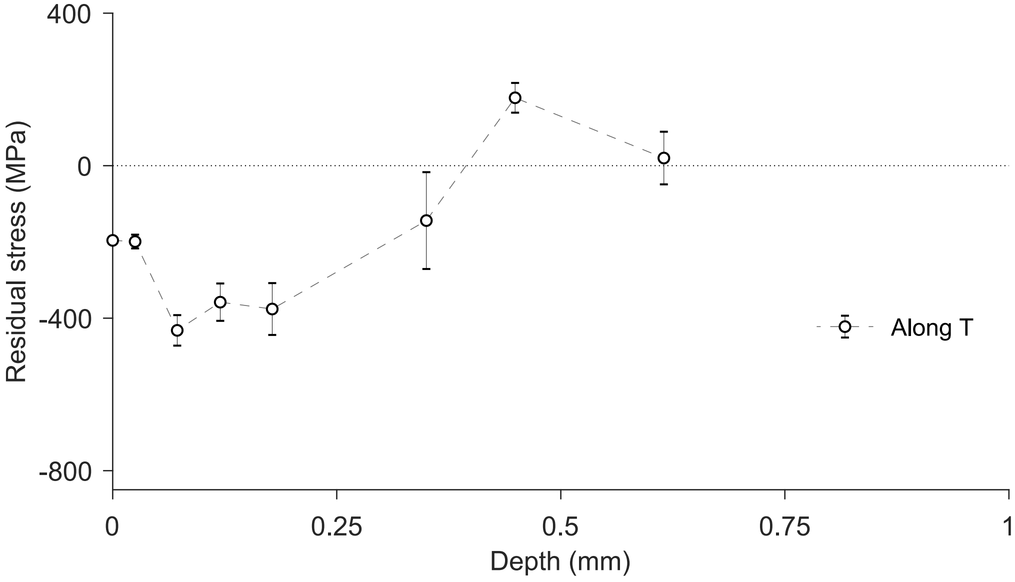

Table C.18 Residual stresses measured by X-ray diffraction in coupon 12.

Depth	Along L			Along T		
(mm)	Stress (MPa)	Uncertainty (MPa)	FWHM (°)	Stress (MPa)	Uncertainty (MPa)	FWHM (°)
0.000	-174	33	2.41	38	34	2.48
0.028	-165	92	2.26	-115	57	2.32
0.334	-288	74	2.29	39	76	2.22
0.698	-83	55	2.43	83	40	2.31
1.025	220	66	2.40	61	57	2.30
1.273	-198	45	2.40	-17	39	2.15
1.522	49	40	2.16	84	33	2.32
1.787	-79	49	2.41	172	35	2.22
2.009	-2	-	2.31	51	-	2.34

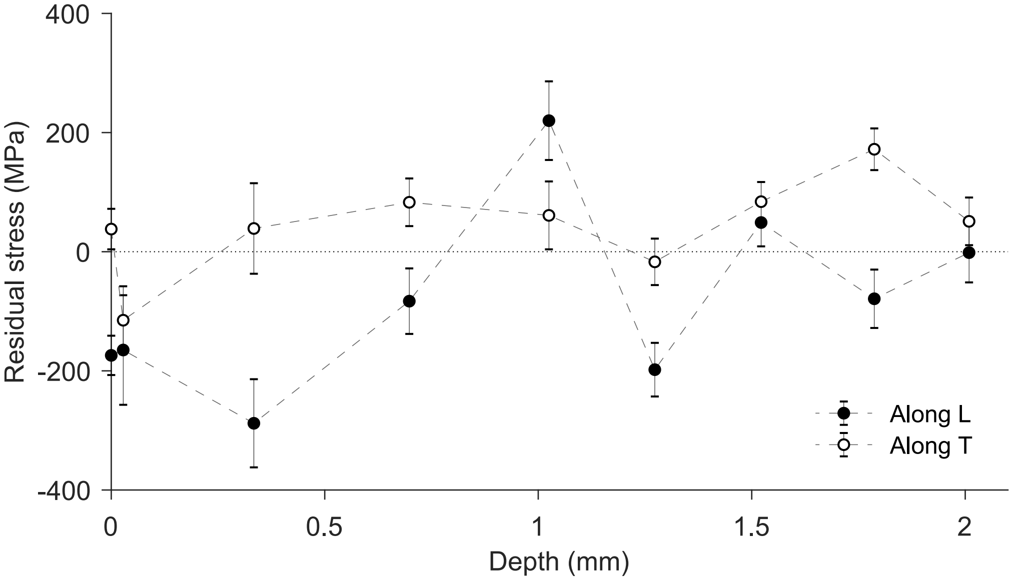

APPENDIX D A MODEL TO RELATE BIAXIAL EIGENSTRAINS TO STRESSES AND STRAINS IN PLATES OF UNIFORM THICKNESS

Consider an unconstrained plate of any shape but of uniform thickness h, made of an isotropic material, and loaded with some distribution of eigenstrains. We adopt a rectangular coordinate system with its origin at a point on the upper surface, far away from the edges. The axes of this coordinate system, $\{\boldsymbol{e}_x, \boldsymbol{e}_y, \boldsymbol{e}_z\}$, are oriented so that $\boldsymbol{e}_z$ is normal to the surface, as shown in figure D.1. Furthermore, we assume that all components of displacement gradient are small compared to unity so that the linear theory of elasticity can be applied.

The solutions are sought by the stress method—which consists in assuming a plausible form of the stress field, working backward through the equations to construct the other mechanical fields, and determining all integration constants by applying boundary conditions. Derivations closely follow section 12.2 of Forest and Amestoy (2017). The same results can be obtained using a strength-of-materials approach as described in Korsunsky (2005).

D.1 Eigenstrains in one direction only

Consider distributions of eigenstrains of the form

$$\varepsilon^*_{xx}(z), \tag{D.1}$$

with all other eigenstrain components being zero. We choose a candidate stress field of the form

$$\boldsymbol{\sigma} = \sigma_{xx}(z)\, \boldsymbol{e}_x \otimes \boldsymbol{e}_x + \sigma_{yy}(z)\, \boldsymbol{e}_y \otimes \boldsymbol{e}_y \tag{D.2}$$

based on the following observations:

- Because of the traction-free conditions on the upper and lower surfaces, σ_{zz} is zero;
- By translational invariance, the stress field should neither depend on x nor on y.

As required by equilibrium, this stress field has zero divergence. Stresses are related to elastic strains $\boldsymbol{\varepsilon}^{el}$ through

$$\boldsymbol{\varepsilon}^{el} = \frac{1+\nu}{E}\boldsymbol{\sigma} - \frac{\nu}{E}\mathrm{tr}\,(\boldsymbol{\sigma})\,\boldsymbol{I}, \tag{D.3}$$

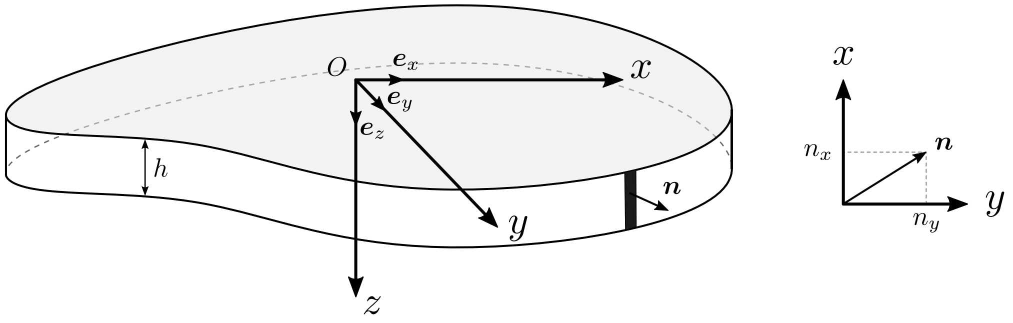

Figure D.1 Undeformed configuration of a generic plate, axes convention, and notations. The plate is loaded with a distribution of eigenstrains that induces distortions.

or, in indicial form,

$$\varepsilon_{xx}^{el} = \frac{1}{E}\left(\sigma_{xx} - \nu\sigma_{yy}\right), \qquad \varepsilon_{yy}^{el} = \frac{1}{E}\left(\sigma_{yy} - \nu\sigma_{xx}\right) \qquad \varepsilon_{zz}^{el} = -\frac{\nu}{E}\left(\sigma_{xx} + \sigma_{yy}\right), \tag{D.4}$$

where E is Young's modulus, ν is the Poisson ratio, $\mathrm{tr}(\square)$ is the trace, and $\boldsymbol{I}$ is the identity tensor. From the additive decomposition of total strains between elastic strains and eigenstrains, $\boldsymbol{\varepsilon} = \boldsymbol{\varepsilon}^{el} + \boldsymbol{\varepsilon}^{*}$, we obtain

$$\varepsilon_{xx} = \frac{1}{E}\left(\sigma_{xx} - \nu\sigma_{yy}\right) + \varepsilon_{xx}^{*}, \qquad \varepsilon_{yy} = \frac{1}{E}\left(\sigma_{yy} - \nu\sigma_{xx}\right), \qquad \varepsilon_{zz}^{el} = -\frac{\nu}{E}\left(\sigma_{xx} + \sigma_{yy}\right). \tag{D.5}$$

Compatibility ($\varepsilon_{ik,jl} + \varepsilon_{jl,ik} = \varepsilon_{il,jk} + \varepsilon_{jk,il}$) requires that

$$\varepsilon_{xx,zz} = 0, \qquad \varepsilon_{yy,zz} = 0, \tag{D.6}$$

which implies that

$$\varepsilon_{xx} = az + b, \qquad \varepsilon_{yy} = cz + d, \tag{D.7}$$

where a, b, c, and d are integration constants. Finally, substituting (D.7) in (D.5) yields

$$\begin{aligned} \sigma_{xx} &= \frac{E}{1-\nu^2}\left[(az+b) + \nu(cz+d) - \varepsilon_{xx}^{*}\right], \\ \sigma_{yy} &= \frac{E}{1-\nu^2}\left[(cz+d) + \nu(az+b) - \nu\varepsilon_{xx}^{*}\right]. \end{aligned} \tag{D.8}$$

The integration constants can be obtained by enforcing traction-free boundary conditions on the lateral surfaces (the traction-free boundary condition on the upper and lower surfaces are already satisfied as the candidate stress field has no stress component in the z direction.) However, since a complex stress field is expected to develop near the edges due to edge effects, the since the simple linear stress field in (D.8) cannot be expected to meet traction-free conditions everywhere. Instead, we settle for imposing the less severe requirement that *resulting* loads on lateral faces must be zero.

Resulting forces $\boldsymbol{R}$ and resulting moments $\boldsymbol{M}$ per unit length (computed with respect to the origin) acting on an elementary surface element of the lateral face are equal to

$$\boldsymbol{R} = \int_0^h \begin{bmatrix} \sigma_{xx} n_x \\ \sigma_{yy} n_y \\ 0 \end{bmatrix} \mathrm{d}z = \begin{bmatrix} I_x n_x \\ I_y n_y \\ 0 \end{bmatrix} \tag{D.9}$$

$$\boldsymbol{M} = \int_0^h \begin{bmatrix} -z\sigma_{yy} n_y \\ z\sigma_{xx} n_x \\ x\sigma_{yy} n_y - y\sigma_{xx} n_x \end{bmatrix} \mathrm{d}z = \begin{bmatrix} -J_y n_y \\ J_x n_x \\ xI_y n_y - yI_x n_x \end{bmatrix}, \tag{D.10}$$

where $\boldsymbol{n}$ is a unit vector normal to the lateral faces,

$$\begin{aligned} I_x &= \int_0^h \sigma_{xx}\,\mathrm{d}z &&= \frac{E}{1-\nu^2}\left[(a+\nu c)\frac{h^2}{2} + (b+\nu d)h - \alpha\right], \\ I_y &= \int_0^h \sigma_{yy}\,\mathrm{d}z &&= \frac{E}{1-\nu^2}\left[(\nu a+c)\frac{h^2}{2} + (\nu b+d)h - \nu\alpha\right], \\ J_x &= \int_0^h \sigma_{xx}\,z\,\mathrm{d}z &&= \frac{E}{1-\nu^2}\left[(a+\nu c)\frac{h^3}{3} + (b+\nu d)\frac{h^2}{2} - \beta\right], \\ J_y &= \int_0^h \sigma_{yy}\,z\,\mathrm{d}z &&= \frac{E}{1-\nu^2}\left[(\nu a+c)\frac{h^3}{3} + (\nu b+d)\frac{h^2}{2} - \nu\beta\right], \end{aligned} \tag{D.11}$$

and

$$\alpha = \int_0^h \varepsilon^*_{xx}(z)\,\mathrm{d}z, \qquad \beta = \int_0^h \varepsilon^*_{xx}(z)\,z\,\mathrm{d}z. \tag{D.12}$$

The requirement that both $\boldsymbol{R}$ and $\boldsymbol{M}$ vanish yields $I_x = I_y = J_x = J_y = 0$, i.e.,

$$\begin{aligned} a\,\frac{h^2}{2} \quad + b\,h \quad + c\,\frac{h^2}{2}\nu + d\,h\nu \quad &= \alpha \\ a\,\frac{h^2}{2}\nu + b\,h\nu \quad + c\,\frac{h^2}{2} \quad + d\,h \quad &= \alpha\nu \\ a\,\frac{h^3}{3} \quad + b\,\frac{h^2}{2} \quad + c\,\frac{h^3}{3}\nu + d\,\frac{h^2}{2}\nu &= \beta \\ a\,\frac{h^3}{3}\nu + b\,\frac{h^2}{2}\nu + c\,\frac{h^3}{3} \quad + d\,\frac{h^2}{2} \quad &= \beta\nu. \end{aligned} \tag{D.13}$$

which is a linear system of equations of solution

$$a = \left(-6\alpha h + 12\beta\right)/h^3, \qquad b = \left(4\alpha h - 6\beta\right)/h^2, \qquad c = d = 0. \tag{D.14}$$

Stresses and strains are thus given by

$$\varepsilon_{xx} = az + b, \qquad \varepsilon_{yy} = 0 \tag{D.15}$$
$$\varepsilon^{el}_{xx} = \varepsilon_{xx} - \varepsilon^{*}_{xx}, \qquad \varepsilon^{el}_{yy} = 0 \tag{D.16}$$
$$\sigma_{xx} = \frac{E}{1-\nu^2}\,\varepsilon^{el}_{xx}, \qquad \sigma_{yy} = \nu\sigma_{xx}. \tag{D.17}$$

Integrating the strains to reconstruct the displacements [1] yields

$$\begin{aligned} u_x &= \quad bx + gy + ez + axz + i, \\ u_y &= -gx + fz + j, \\ u_z &= -ex - fy - \frac{a}{2}x^2 - \frac{\nu}{1-\nu}\left(bz + \frac{a}{2}z^2\right) + k, \end{aligned} \tag{D.18}$$

where e, f, g, i, j, and k are integration constants. Since the system is unconstrained, displacements boundary conditions only amount to those needed to remove rigid body motions. By setting $u_x = u_y = u_z = 0$ at the origin, $u_x = u_y = 0$ at $(0, 0, h)$, and $u_y = 0$ at any point along the $\boldsymbol{e}_x$ axis, we obtain $e = f = g = i = j = k = 0$. The displacement field then becomes

$$\begin{aligned} u_x &= axz + bx, \\ u_y &= 0, \\ u_z &= -\frac{a}{2}x^2 - \frac{\nu}{1-\nu}\left(bz + \frac{a}{2}z^2\right). \end{aligned} \tag{D.19}$$

Finally, curvatures along the $\boldsymbol{e}_z$ and $\boldsymbol{e}_y$ axes are (using the small slope approximation)

$$\kappa_x = -a, \qquad \kappa_y = 0. \tag{D.20}$$

Since they satisfy all field equations and boundary conditions, the above stress, strain, and displacement fields are solution to the problem. This solution is valid several h away from the lateral edges—so that edge effects can be neglected.

---

[1] See Forest and Amestoy (2017) for a systematic integration procedure.

D.2 Same eigenstrains in both directions

Consider an equibiaxial distribution of eigenstrains of the form $\varepsilon^*_{xx}(z) = \varepsilon^*_{yy}(z) = \varepsilon^*(z)$, with all other eigenstrain components being zero. Applying the superposition principle to the results in (D.15)–(D.17) and (D.20) yields

$$\varepsilon_{xx} = az + b, \qquad \varepsilon_{yy} = \varepsilon_{xx} \tag{D.21}$$

$$\varepsilon^{el}_{xx} = \varepsilon_{xx} - \varepsilon^*, \qquad \varepsilon^{el}_{yy} = \varepsilon^{el}_{yy} \tag{D.22}$$

$$\sigma_{xx} = \frac{E}{1-\nu}\,\varepsilon^{el}_{xx}, \qquad \sigma_{yy} = \sigma_{xx}, \tag{D.23}$$

$$\kappa_x = -a, \qquad \kappa_y = -a, \tag{D.24}$$

with the same a and b as in (D.14).

D.3 Different eigenstrains in each direction

Consider a biaxial distribution of eigenstrains of the form $\varepsilon^*_{xx}(z), \varepsilon^*_{yy}(z)$, with all other eigenstrain components being zero. Applying the superposition principle to the results in (D.15)–(D.17) and (D.20) yields

$$\varepsilon_{xx} = a_x z + b_x, \qquad \varepsilon_{yy} = a_y z + b_y \tag{D.25}$$

$$\varepsilon^{el}_{xx} = \varepsilon_{xx} - \varepsilon^*_{xx}, \qquad \varepsilon^{el}_{yy} = \varepsilon_{yy} - \varepsilon^*_{yy} \tag{D.26}$$

$$\sigma_{xx} = \frac{E}{1-\nu^2}\left[\varepsilon^{el}_{xx} + \nu\varepsilon^{el}_{yy}\right], \qquad \sigma_{yy} = \frac{E}{1-\nu^2}\left[\varepsilon^{el}_{yy} + \nu\varepsilon^{el}_{xx}\right], \tag{D.27}$$

$$\kappa_z = -a_x, \qquad \kappa_y = -a_y, \tag{D.28}$$

where

$$a_i = \left(-6\alpha_i h + 12\beta_i\right)/h^3, \qquad b_i = \left(4\alpha_i h - 6\beta_i\right)/h^2, \tag{D.29}$$

and

$$\alpha_i = \int_0^h \varepsilon^*_{ii}(z)\,\mathrm{d}z, \qquad \beta_i = \int_0^h \varepsilon^*_{ii}(z)\,z\,\mathrm{d}z. \tag{D.30}$$

Inverting equations (D.27) yields

$$\varepsilon^{*\ \text{nilpotent}}_{xx} = -\frac{1}{E}(\sigma_{xx} - \nu\sigma_{yy}), \qquad \varepsilon^{*\ \text{nilpotent}}_{yy} = -\frac{1}{E}(\sigma_{yy} - \nu\sigma_{xx}), \tag{D.31}$$

with

$$\varepsilon^{*\ \text{nilpotent}}_{ii} = \varepsilon^*_{ii} - \varepsilon_{ii}. \tag{D.32}$$

APPENDIX E ESTIMATING FIRST EIGENSTRAIN MOMENTS FROM CURVATURE MEASUREMENTS

Consider a uniformly shot peened plate with an (average) distribution of eigenstrains of the form (6.1). The first eigenstrain moments with respect to the *midplate* of the plate introduced in equation (6.18), B_i, is related to the resulting eigenstrains, α_i, and the first eigenstrain moments with respect to the *surface* of the plate, β_i, through

$$B_i = \alpha_i h/2 - \beta_i. \tag{E.1}$$

Now, assume that a coupon is removed from the shot peened plate and that removal does not alter the distribution of eigenstrains. For example, imagine removing a 254 × 254 × 4.9 mm coupon from a 1016 × 1016× mm plate peen formed to a dimensionless load $\bar{B} = 70$. For $\bar{B} = 70$, the response of the plate is well into the nonlinear regime, as shown in figure 6.12. However, since $\bar{B}$ scales with L^2 (eq. 6.16), $\bar{B}$ drops to approximately 4.4 for the coupon, which is very nearly in the linear domain. In other words, removing a small coupon from a larger plate is a way to do away with geometric nonlinearities.

In the linear domain, the analytical solution presented in section 6.3 applies. The latter can be used to express the α_i and β_i in terms of measurable quantities. For example, substituting (6.9) and (6.15) in (E.1) yields

$$B_i = \tilde{\kappa}_i h^3/12, \tag{E.2}$$

where a tilde is used to indicate that curvatures are measured on the coupon.

APPENDIX F RELATIONS BETWEEN PAIRS OF PARAMETERS USED TO DESCRIBE EIGENSTRAIN DISTRIBUTIONS IN SHOT PEENED PLATES

Consider a plate of thickness h and a rectangular x, y, z coordinate system with its origin on the upper face of the plate and its z axis in the direction normal to the surface pointing downward. Now assume that a distribution of eigenstrains of the form $\varepsilon^*_{xx}(z)$, $\varepsilon^*_{yy}(z)$ is present in the plate (all other components being zero). We define the following pairs of parameters.

- The resulting eigenstrains and first eigenstrains moments with respect to the upper surface in direction i,
$$\alpha_i = \int_0^h \varepsilon^*_{ii}(z)\,\mathrm{d}z, \qquad \beta_i = \int_0^h \varepsilon^*_{ii}(z)\,z\,\mathrm{d}z.$$
- The resulting eigenstrains and first eigenstrains moments with respect to the midplane of the plate in direction i,
$$A_i = \int_0^h \varepsilon^*_{ii}(z)\,\mathrm{d}z, \qquad B_i = \int_0^h \varepsilon^*_{ii}(z)(h/2 - z)\,\mathrm{d}z.$$
- The natural curvature $\kappa_{0\,i}$ and natural stretch $\varepsilon_{0\,i}$ in direction i, as defined in section 5.4.1.
- The curvature $\tilde{\kappa}_i$ and the axial strain $\tilde{\varepsilon}_{ii}\big|_{z=0}$ that would be measured on the *upper* face of a small beam aligned with the i direction removed from the plate. Alternativelly, the same quantities measured on a small beam made of the same material and peened in the exact same conditions as the plate.
- The depth $h_{eq\,i}$ and magnitude $\varepsilon^*_{eq\,i}$ of a equivalent 'step' distribution of eigenstrains (that would induce the same curvature and axial stretch as the actual distribution).
- The magnitudes θ_i^{top} and θ_i^{btm} of an equivalent piecewise constant distribution of eigenstrains of the form
$$\varepsilon^*_{ii}(z) = \begin{cases} \theta_i^{\mathrm{top}} & \text{if } z \leq h/2, \\ \theta_i^{\mathrm{btm}} & \text{if } z > h/2. \end{cases} \tag{F.1}$$

These pairs of parameters are related through the relations listed in table F.1.

Table F.1 Relations between $\{\alpha, \beta\}$, $\{A, B\}$, $\{\kappa_0, \varepsilon_0\}$, $\{\tilde{\kappa}, \tilde{\varepsilon}|_{z=0}\}$, $\{h_{eq}, \varepsilon^*_{eq}\}$, and $\{\theta^{\text{top}}, \theta^{\text{btm}}\}$. Subscripts have been dropped for clarity; each relation is implicity written for the i direction.

… function of …	$\{\alpha, \beta\}$	$\{A, B\}$	$\{\kappa_0, \varepsilon_0\}$	$\{\tilde{\kappa}, \tilde{\varepsilon}\|_{z=0}\}$	$\{h_{eq}, \varepsilon^*_{eq}\}$	$\{\theta^{\text{top}}, \theta^{\text{btm}}\}$
$\{\alpha, \beta\}$	–	$A = \alpha$ $B = \alpha h/2 - \beta$	$\kappa_0 = (6\alpha h - 12\beta)/h^3$ $\varepsilon_0 = \alpha/h$	$\tilde{\kappa} = (6\alpha h - 12\beta)/h^3$ $\tilde{\varepsilon}\|_{z=0} = (4\alpha h - 6\beta)/h^2$	$h_{eq} = 2\beta/\alpha$ $\varepsilon^*_{eq} = \alpha^2/2\beta$	$\theta^{\text{top}} = (3\alpha h - 4\beta)/h^2$ $\theta^{\text{btm}} = (4\beta - \alpha h)/h^2$
$\{A, B\}$	$\alpha = A$ $\beta = Ah/2 - B$	–	$\kappa_0 = 12B/h^3$ $\varepsilon_0 = A/h$	$\tilde{\kappa} = 12B/h^3$ $\tilde{\varepsilon}\|_{z=0} = (Ah + 6B)/h^2$	$h_{eq} = h - 2B/A$ $\varepsilon^*_{eq} = A^2/(Ah - 2B)$	$\theta^{\text{top}} = (Ah + 4B)/h^2$ $\theta^{\text{btm}} = (Ah - 4B)/h^2$
$\{\kappa_0, \varepsilon_0\}$	$\alpha = \varepsilon_0 h$ $\beta = \left(6\varepsilon_0 h^2 - \kappa_0 h^3\right)/12$	$A = \varepsilon_0 h$ $B = \kappa_0 h^3/12$	–	$\tilde{\kappa} = \kappa_0$ $\tilde{\varepsilon}\|_{z=0} = \varepsilon_0 + \kappa_0 h/2$	$h_{eq} = h\left(1 - \kappa_0 h/6\varepsilon_0\right)$ $\varepsilon^*_{eq} = \varepsilon_0/\left(1 - \kappa_0 h/6\varepsilon_0\right)$	$\theta^{\text{top}} = \varepsilon_0 + \kappa_0 h/3$ $\theta^{\text{btm}} = \varepsilon_0 - \kappa_0 h/3$
$\{\tilde{\kappa}, \tilde{\varepsilon}\|_{z=0}\}$	$\alpha = \left(2h\,\tilde{\varepsilon}\|_{z=0} - \tilde{\kappa}h^2\right)/2$ $\beta = \left(3h^2\,\tilde{\varepsilon}\|_{z=0} - 2\tilde{\kappa}h^3\right)/6$	$A = \tilde{\varepsilon}\|_{z=0}\,h - \tilde{\kappa}h^2/2$ $B = \tilde{\kappa}h^3/12$	$\kappa_0 = \tilde{\kappa}$ $\varepsilon_0 = \tilde{\varepsilon}\|_{z=0} - \tilde{\kappa}h/2$	–	$h_{eq} = \dfrac{6h\,\tilde{\varepsilon}\|_{z=0} - 4\tilde{\kappa}h^2}{6\,\tilde{\varepsilon}\|_{z=0} - 3\tilde{\kappa}h}$ $\varepsilon^*_{eq} = \dfrac{3}{4}\dfrac{\left(2\,\tilde{\varepsilon}\|_{z=0} - \tilde{\kappa}h\right)^2}{3\,\tilde{\varepsilon}\|_{z=0} - 2\tilde{\kappa}h}$	$\theta^{\text{top}} = (6\tilde{\varepsilon} + \tilde{\kappa}h)/9$ $\theta^{\text{btm}} = (6\tilde{\varepsilon} - 5\tilde{\kappa}h)/9$
$\{h_{eq}, \varepsilon^*_{eq}\}$	$\alpha = h_{eq}\varepsilon^*_{eq}$ $\beta = h^2_{eq}\varepsilon^*_{eq}/2$	$A = h_{eq}\varepsilon^*_{eq}$ $B = h_{eq}\varepsilon^*_{eq}\left(h - h_{eq}\right)/2$	$\kappa_0 = 6h_{eq}\varepsilon^*_{eq}\left(h - h_{eq}\right)/h^3$ $\varepsilon_0 = h_{eq}\varepsilon^*_{eq}/h$	$\tilde{\kappa} = 6h_{eq}\varepsilon^*_{eq}(h - h_{eq})/h^3$ $\tilde{\varepsilon}\|_{z=0} = h_{eq}\varepsilon^*_{eq}(4h - 3h_{eq})/h^2$	–	$\theta^{\text{top}} = h_{eq}\varepsilon^*_{eq}(3h - 2h_{eq})/h^2$ $\theta^{\text{btm}} = h_{eq}\varepsilon^*_{eq}(2h_{eq} - h)/h^2$
$\{\theta^{\text{top}}, \theta^{\text{btm}}\}$	$\alpha = (\theta^{\text{top}} + \theta^{\text{btm}})h/2$ $\beta = (\theta^{\text{top}} + 3\theta^{\text{btm}})h^2/8$	$A = (\theta^{\text{top}} + \theta^{\text{btm}})h/2$ $B = (\theta^{\text{top}} - \theta^{\text{btm}})h^2/8$	$\kappa_0 = 3(\theta^{\text{top}} - \theta^{\text{btm}})/2h$ $\varepsilon_0 = (\theta^{\text{top}} + \theta^{\text{btm}})/2$	$\tilde{\kappa} = 3\left(\theta^{\text{top}} - \theta^{\text{btm}}\right)/2h$ $\tilde{\varepsilon}\|_{z=0} = \left(5\theta^{\text{top}} + \theta^{\text{btm}}\right)/4$	$h_{eq} = \dfrac{\theta^{\text{top}} + 3\theta^{\text{btm}}}{\theta^{\text{top}} + \theta^{\text{btm}}}\dfrac{h}{2}$ $\varepsilon^*_{eq} = \dfrac{\left(\theta^{\text{top}} + \theta^{\text{btm}}\right)^2}{\theta^{\text{top}} + 3\theta^{\text{btm}}}$	–

APPENDIX G ARTICLE 4: SIMULATING SHOT PEEN FORMING WITH EIGENSTRAINS

Pierre A. Faucheux, Frédérick P. Gosselin, Martin Lévesque

Published in the Journal of Materials Processing Technology on April 1st 2018

Notations and the coordinate system in figure G.2 have been edited from the published version of this article for consistency.

Abstract

Shot peen forming is a cold work process used to shape thin metallic components by bombarding them with small shots at high velocities. Several simulation procedures have been reported in the literature for this process, but their predictive capabilities remain limited as they systematically require some form of calibration or empirical adjustments. We intend to show how procedures based on the concept of eigenstrains, which were initially developed for applications in other fields of residual stress engineering, can be adapted to peen forming and stress-peen forming. These tools prove to be able to reproduce experimental results when the plastic strain field that develop inside a part is known with sufficient accuracy. They are, however, not mature enough to address the forming of panels that are free to deform during peening. For validation purposes, we peen formed several 1 by 1 meter 2024–T3 aluminum alloy panels. These experiments revealed a transition from spherical to cylindrical shapes as the panel thickness is decreased for a given treatment, that we show results from an elastic instability.

G.1 Introduction

Peen forming is a cold work process predominantly used by aircraft manufacturers to shape wing skins Baughman (1970). The process consists of bombarding thin metallic parts with small shots in order to plastically deform a thin surface layer of material. As a result of strain incompatibility between the surface and the core—left unaffected by the treatment—the whole structure deforms and compressive residual stresses develop near the surface. Figure G.1 shows schematically the process application on a wing skin, as well as typical peening-induced plastic strain and residual stress fields. Although the range of accessible curvatures is limited, it is possible to peen form a wide variety of shapes once appropriate

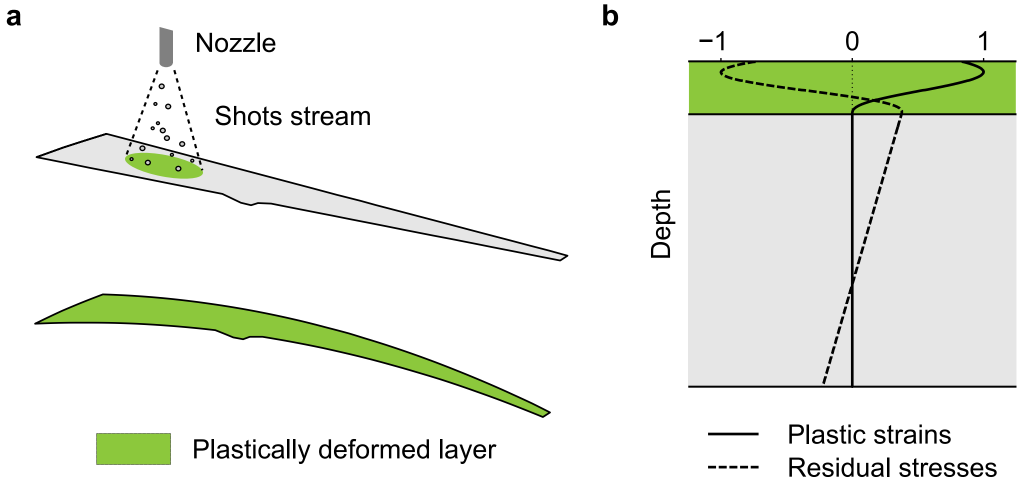

Figure G.1 Schematic illustration of the peen forming process. (a) Peen forming of a wing panel. In-plane expansion of the plastically deformed layer causes the part to bend and elongate. (b) Typical (normalized) in plane residual stress and plastic strain profiles after uniform peening. The linear part in the residual stress profile is due to bending.

parameters are set. Larger curvatures can be achieved by elastically prestraining the parts before peening to increase the effect of the treatment in a given direction (Ramati et al., 1999). This variant of the process is called stress peen forming.

Simulating the whole process explicitly (i.e., simulating *every* shot hitting the target) is currently beyond reach. For that reason, most available publications on the topic relied on a two-step local-global approach. The local step aims at characterizing the effect of a given treatment on a given material, usually in terms of residual stresses and plastic strains. It is performed either experimentally (Levers and Prior, 1998) or numerically as in the work of Chaise (2011) on ultrasonic shot peening. Mylonas and Labeas (2011) provide an overview of recent research on local peening simulations in a non peen forming-specific context. Stresses or strains induced by the peening treatment are then post-processed to extract loads that are input in structural models of parts to compute equilibrium configurations. The local step involves contact, plasticity, and large deformations that are characteristics of a forming analysis. The global step, on the other hand, can be seen as a springback analysis, as it was demonstrated in Chen et al. (2014) that the re-balancing of the part usually involves only elastic transformations.

Several types of (idealized) loads used in global simulations were reported in the literature: Levers and Prior (1998) and Wang et al. (2006) reproduced the expansion of subsurface layers where Gariépy et al. (2011) used peening-induced non-equilibrated residual stress profiles. The main shortcoming of these approaches is that, although the choice of the loading is guided by some a priori knowledge of the post-peening state, several parameters systematically have to be adjusted by comparing simulated deformed shapes with their experimental counterparts. The workload is significant, and simulations are limited to the vicinity of the process parameters for which the calibration has been performed.

We aimed to show that procedures based on the concept of eigenstrain, which are commonly used in other fields of residual stress engineering, can be adapted to simulate peen forming. These tools have the potential to bypass the calibration step and to simulate peening conditions out of reach of existing procedures. To illustrate this point, we investigate the nature of a transition between spherical and cylindrical deformations observed on panels of varying thickness peen formed under identical conditions. The reason behind this transition has not been explained in peening literature yet, to the best of our knowledge.

The paper is structured as follows. Section G.2 summarizes key results and simulation strategies from the eigenstrain literature and reviews two of the main previously published peen forming experimental campaigns. Section G.3 presents experimental methods. Section G.4 introduces the proposed simulation strategy. The latter is put to the test against experimental results from the literature as well as from results generated for the purpose of this study in section G.5. Both conventional and stress peen forming are considered. The main findings are discussed in section G.6.

G.2 Background

G.2.1 Eigenstrains

The term eigenstrain was coined by Mura to designate anelastic deformations present inside a structure, regardless of the physical phenomenon they originate from (Mura, 1987). Stress-free strains and inherent strains are equivalent designations sometimes encountered in the literature. The concept of stress-sources (initial unbalanced residual stresses) used in Niku-Lari (1981) for fast experimental estimation of peening induced residual stresses is also intimately related to eigenstrains as both quantities are proportional, as discussed in Terasaki et al. (1999). Thermal strains, plastic strains, and volumetric expansion caused by phase transitions or solvent absorption are some examples of eigenstrains. In shot peened parts, only plastic strains usually contribute to the eigenstrains $\boldsymbol{\varepsilon}^*$.

In any structure free of external loads, residual stresses and distortions can always be attributed to an incompatible eigenstrain field. If the latter is known, or if it can be estimated with sufficient accuracy, then the computation of stresses and distortions—the direct problem—can be dealt with as an inclusion problem (Mura, 1987). This approach has been successfully applied to many engineering problems as illustrated by Deng et al. (2007), Hu et al. (2015), and Depouhon et al. (2015) which investigated residual stresses and distortions induced by welding, laser peening and thermo-mechanical treatments. In these studies, the authors made use of a two-step procedure involving a local analysis to compute eigenstrains followed by a global springback analysis to obtain the final deformed shape. In all cases, the mapping of eigenstrains to large scale models was done following the procedure described in Hill (1996): thermal expansion coefficients $\boldsymbol{\alpha}$ equal to the eigenstrains were defined over the whole domain, that is, $\alpha_{ij} = \varepsilon^*_{ij}$, and a unit increment of temperature was applied. The validity of this procedure stems from the fact that two identical eigenstrain fields yield the same residual stresses and distortions, no matter what physical phenomena cause them.

It is commonly accepted that eigenstrains induced by surface treatments are insensitive to the topography of the surface, provided that curvatures vary gradually and that the target is exempt of sharp geometric features (Ahdad and Desvignes, 1996). This was confirmed experimentally in Coratella et al. (2015) on laser peened 7050 aluminum samples. Zhang et al. (2008) also demonstrated that, for the conditions of the study, eigenstrains in shot peened 17–4 PH steel strips were independent of the thickness of the strips. They suggested that this result might hold for a variety of materials and peening conditions. Similar observations by Achintha and Nowell (2011) on laser peened Ti–6Al–4V support Zhang and collaborators' hypothesis. These results further suggest that the effect of a given treatment could conveniently be characterized—either numerically or experimentally—in terms of eigenstrains on small representative volumes of the target material. For example, peening a small strip could enable estimating the post-peening state of a massive part subjected to the same sequence of operations, as was already suggested in Niku-Lari (1981).

Since eigenstrains cannot be measured directly, they have to be reconstructed from various experimental data such as elastic strains or residual stresses. In the general 3D case, this is a complex inverse problem (Jun et al., 2011). However, several robust reconstruction procedures have been developed for specific configurations. These include closed form relations between residual stresses and eigenstrains such as those reported in Ahdad and Desvignes (1996) and Korsunsky (2005), as well as more generic numerical procedures. For example, Korsunsky (2006) started by postulating a form of the eigenstrain field as a sum of trial basis functions,

$$\boldsymbol{\varepsilon}^* = \sum_{i=1}^{n} c_i \boldsymbol{\xi}_i,$$

where the $\boldsymbol{\xi}_i$ are basis functions and the c_i are adjustable coefficients. The choice of basis functions was guided by some a priori knowledge of the eigenstrain field shape, and the objective of the procedure was to find coefficients that minimized the squared difference between measured and simulated residual elastic strains. The latter were obtained by successively inputting each basis function in a linearly elastic model of the structure of interest. For a linearly elastic model, the solution to this least-square problem is unique.

G.2.2 Coverage and Almen intensity

The post-peening state of a shot peened part depends on numerous parameters, such as: the characteristics of the part itself (material, geometry), properties of the shots (material, size and shape), and process parameters (type of peening machine, type of fixtures used to secure the part, velocity of the shots, angle of impingement, stand-off distance, mass flow rate, peening time and trajectories). As a consequence of the random nature of the process, many of these parameters have to be described by appropriate statistical distributions.

In the industry, only two parameters are usually used to characterize peening treatments, namely, coverage and Almen intensity. Coverage is defined as the fraction of a peened surface covered by dimples if it is smaller than 98 %, and as a multiple of the time necessary to reach full coverage otherwise. For example, 200 % coverage is obtained by peening a sample twice the time necessary to reach full coverage. Almen intensity is an indirect measurement of the energy conveyed by the shot stream. It is obtained by peening normalized SAE 1070 steel strips in the same conditions as the part for increasing peening times and is defined as the deflection of the strips (in unit of length) read at the peening time for which doubling the peening time would cause the deflection to increase by 10 %.

G.2.3 Experimental peen forming results from the literature

To the best of our knowledge, only Kulkarni et al. (1981) (supported by Boeing) and Villalva-Braga (2011) (supported by Embraer) reported extensive peen forming results in the open literature. Other studies, such as the work of Miao et al. (2010), investigated comparatively fewer peening conditions and were limited to small specimens—predominantly 76 × 19 mm Almen strip-like geometries.

Kulkarni et al. (1981) peen formed both 2024–T3 and 7075–T6 aluminum rectangular plates. Most specimens were 610 mm long with varying length to width ratios and thicknesses. The influence of shot speed, shot size, coverage, the geometry of the samples and their orientation with respect to the rolling direction were investigated. Kulkarni's results highlight the complex dependence of the final curvature of a specimen on peening conditions. In particular, they revealed that a transition from spherical shapes (identical curvatures in all directions) to cylindrical shapes (curvature almost zero in one direction) occurred as either the shot speed

Table G.1 Peen forming treatments used in Villalva-Braga (2011) for 10 and 15 mm thick plates.

Treatment ID	Media[†]	Coverage (%)	Prestress[‡]	Shots velocity (m/s)
1, 2, 3	S550	200	No	16.2, 22.4, 28.6
4, 5, 6	S550	200	Yes	16.2, 22.4, 28.6
7, 8, 9	1/8” (steel)	200	No	12.5, 16.9, 18.5
10, 11, 12	1/8” (steel)	200 %	Yes	12.5, 16.9, 18.5

[†] S550 and 1/8” shots are 1.4 and 3.2 mm in diameter, respectively.
[‡] The prestress curvature depended on the thickness of the specimens.

increased or as the length to width ratio approached unity. However, the fact that residual stress measurements were not reported hinders further analysis of the data.

Villalva-Braga (2011) peened formed 7050–T7451 and 7475–T7351 aluminum strips with dimensions 400 × 50 mm and with thicknesses ranging from 2 to 15 mm. Half the samples were prestressed in uniaxial bending while the other half were free to deform during peening. About one hundred and forty combinations of material, thickness, shot type, intensity, coverage, and prestress were investigated. Peening conditions for which residual stress measurements are available, , namely 7050–T7451 aluminum strips peened with the treatments listed in table G.1, are further discussed in the following sections where they serve as a benchmark for our simulations. Only peening conditions for which residual stress measurements were available were retained, namely 7050–T7451 aluminum strips peened with the treatments listed in table G.1. Residual stresses were measured for each peening condition in the longitudinal direction (private communication) by X-ray diffraction on 50 × 50 mm strips cut from one sample.

G.3 Experimental methods

G.3.1 Peening conditions

All peen forming experiments were conducted by Korea Aerospace Industries, an industrial partner. Two peen forming treatments representative of industrial practices were selected, namely, a saturation treatment and a more intense forming treatment. Table G.2 lists the media type, coverage, and Almen intensity for each peening condition. The treatments were applied by the same operator with a portable peening hose. The parts were free to deform during peening.

Table G.2 Peen forming treatments used for the experimental campaign.

Treatment	Media[†]	Coverage (%)	Almen intensity ($\times 10^{-3}$ inches)	Stand-off distance (mm)
Saturation	S230	100	16.8 *A*	760
Forming	1/8” (steel)	80	22.9 *C*	45

[†] S230 and 1/8” shots are 0.6 and 3.2 mm in diameter, respectively.

G.3.2 Samples

Three kind of samples were peened:

- 1000 × 1000 mm 2024–T3 aluminum plates 5, 10 and 15 mm thick were used for large scale forming experiments. One plate of each thickness was formed with each treatment—for a total of 6 plates.
- 200 × 50 × 10 mm strips were used to assess the variability of the process. These strips were peened in the same conditions as the plates at 40, 60, 80, and 100 % coverage. Three strips were peened for each condition—for a total of 24 strips.
- 250 × 250 × 15 mm blocks were used for residual stress measurements. For each treatment, one block was peened in the same conditions as the plates—for a total of 2 blocks.

The 5, 10, and 15 mm thick samples were machined from the same 9.53, 12.7, and 19.05 mm thick plates, respectively. During machining, the same amount of material was removed from both sides of the original plates.

G.3.3 Residual stress measurements

Residual stresses were measured by X-ray diffraction at the center of the 250 × 250 × 15 mm blocks by Proto Manufacturing Ltd., an external laboratory, on a Proto-LXRD machine equipped with a copper X-ray tube. Diffracting planes {311} and a radiocristallographic constant of 52.94 GPa were selected. A single profile corrected for material removal and stress gradients was generated for each treatment.

G.3.4 Deformed shapes measurements

Three dimensional scans performed in a coordinate-measuring machine were used to obtain the final deformed shapes of the specimens. The latter were gently held into place with clips during scanning. A grid of 11 by 11 points was used for large plates. Small strips were scanned on their unpeened face along two perpendicular lines passing through the middle of the strips with the position of the probe being recorded every 35 µm.

The orientation the specimens relative to the rolling direction was not recorded. In particular, we had no available information regarding the direction in which residual stresses were measured.

G.4 Simulation strategy

G.4.1 Overview

To simulate peen forming, we adopted a conventional local-global approach where eigenstrain profiles reconstructed from residual stress measurements on small coupons were mapped onto thin-shell finite element models of the peen formed parts to compute their final deformed shapes.

To obtain eigenstrrain profiles, an experimental approach was preferred to local impact simulations as identifying a suitable material model for rolled aluminum sheets subjected to complex, possibly nonproportional loads, represented a significant challenge. In both the reconstruction procedure and global simulations, it was assumed that strains remained small and that the additive decomposition of the total strain $\boldsymbol{\varepsilon}$ between an elastic part $\boldsymbol{\varepsilon}^{el}$ and eigenstrains $\boldsymbol{\varepsilon}^{*}$,

$$\boldsymbol{\varepsilon} = \boldsymbol{\varepsilon}^{el} + \boldsymbol{\varepsilon}^{*},$$

held true. Note that since the only source of eigenstrains in shot peened parts is plastic strains, $\boldsymbol{\varepsilon}^{*}$ actually corresponds to the plastic part of the strain tensor.

In what follows, (x, y, z) cartesian coordinates are adopted with the origin on the peened surface of the plate, the z direction perpendicular to the surface, and the x direction aligned with the long side of the plate, as shown in figure G.2. The thickness is denoted by h.

G.4.2 Local analysis: reconstructing eigenstrain profiles

The eigenstrain fields were reconstructed from limited local residual stress measurements following the inverse procedure described in Korsunsky (2006). We assumed eigenstrain profiles of the form

$$\varepsilon^{*}_{xx}(z) = \varepsilon^{*}_{yy}(z) = \sum_{i=1}^{n} c_i \xi_i(z),$$

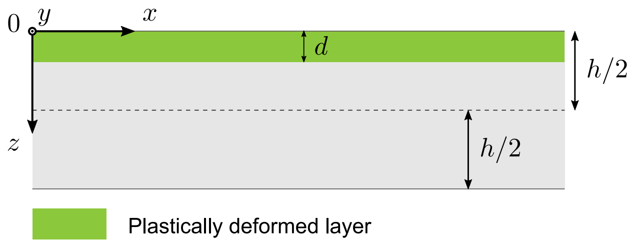

Figure G.2 Axis convention.

with $\varepsilon^*_{zz} = -2\varepsilon^*_{xx}$ (due to plastic incompressibility) and all other components being zero. This is the form we expect when the target has negligible plastic anisotropy and the coverage is sufficiently high. The ξ_i are basis functions and the c_i are free unknown parameters. Korsunsky's procedure returns the c_i that minimize the error between experimental residual stresses and residual stresses derived from the assumed eigenstrain field. The same basis functions as Korsunsky (2006) were used, namely,

$$\xi_i(z) = \begin{cases} (z-d)^{i+2} & \text{if } z \leq d, \\ 0 & \text{otherwise,} \end{cases} \tag{G.1}$$

where d is the thickness of the plastically deformed layer. Since the problem is non-linear in d, Korsunsky (2006) suggested to run the reconstruction procedure several times, each time with a different value for d, and to retain only the 'best' match. In our implementation, this was done by supplementing the reconstruction procedure by an outer optimization loop over d performed with Matlab's default *fminsearch* function. The number n of terms in the approximation was set at the beginning of the identification process. It was always taken significantly smaller than the number of experimental points.

Computing the residual stresses induced by a given eigenstrain profile—the direct problem—requires a model of the structure. Because of the optimization loop, the direct problem had to be solved numerous times. To speed up the process, we used the same analytical strength of materials thin plate model as in Korsunsky (2005). Once a satisfactory value of d was found, the final evaluation of the c_i coefficients was carried out on a 3D finite element model of the samples. This additional step was deemed necessary in order to relax the thin-shell assumption of the analytical plate model used in preliminary runs, as some residual stress measurements were performed on thick samples. All finite element simulations were done with Abaqus 6.14. Meshes of C3D20R brick elements with at least 10 elements over d were used. It should be noted that, in all the cases investigated, the c_i coefficients obtained from the analytical model and from the 3D finite element simulations were almost identical.

G.4.3 Global analysis: computing deformed shapes

Finite element simulations

Since peen forming usually involves large deflections, models used to compute the deformed shape of peen formed parts must include geometric nonlinearities. Here, we used off-the-shelf finite element models with large deflection capabilities.

All finite element simulations were done with Abaqus 6.14. The structural models were discretized with regular meshes of multipurpose S4R shell elements checked for convergence. The three translations and the three rotations were set to zero at the central node of the model to prevent rigid body modes. Eigenstrain profiles were input in the finite element models according to the thermal analogy discussed in section G.2.1. We used the USDFLD and UEXPAN subroutines to specify the appropriate through-thickness expansion coefficients at each section point. The expansion coefficient values were computed using USDFLD, which can access section point data, then passed as arguments to UEXPAN. Between 10 and 20 section point in the $0 \leq z \leq d$ interval were used to accurately approximate the eigenstrain profiles. To ensure that no additional plastic deformation occurred during springback, through-thickness von Mises equivalent stresses were compared to the yield stress of the material at the end of each analysis. Geometric nonlinearities were included in all simulations.

Loads idealization

Since all quantities are integrated through the thickness in conventional thin shell formulations, inputting (i) an idealized eigenstrain profiles that induces the same *resulting* axial forces and bending moments as the actual profile or (ii) the actual profile itself yields the same deformed shape. For illustration purposes, consider a profile of the form

$$\varepsilon^*_{xx}(z) = \varepsilon^*_{yy}(z) = \gamma(z), \qquad \varepsilon^*_{zz}(z) = -2\gamma(z),$$

all other components being zero. Let

$$A = \int_0^h \gamma(z)\,\mathrm{d}z,$$

be the resulting eigenstrain and

$$B = \int_0^h \gamma(z)(h/2 - z)\,\mathrm{d}z$$

be the first eigenstrain moment with respect to the midplane of the plate. These quantities are respectively proportional to the axial force and bending moment per unit length. The simplest idealized profile, which is also the most convenient to input, is a step of amplitude ε^*_{eq} and depth h_{eq}. For the idealized step profile to yield the same resulting axial forces and bending moments as the original one, equilibrium requires that

$$A = h_{eq}\varepsilon^*_{eq} \qquad \text{and} \qquad B = h_{eq}\varepsilon^*_{eq}\left(h - h_{eq}\right)/2,$$

or, equivalently, that

$$h_{eq} = h - 2B/A \qquad \text{and} \qquad \varepsilon^*_{eq} = A^2/\left(Ah - 2B\right).$$

Figure G.3 shows a typical peening-induced eigenstrain profile and its idealized counterpart. The latter can conveniently be input in any numerical thin plate model by defining bi-layer laminate section properties consisting of an 'active' layer of thickness h_{eq} with in-plane expansion ε^*_{eq} and a 'passive' layer of thickness $h - h_{eq}$. Note that the same approach also applies to non-equibiaxial eigenstrains. In this case, writing the equilibrium of forces and moments in both the x and y directions yields two pair of parameters and the idealized profile can be input by defining a tri-layer stacking sequence with the appropriate expansion in each direction (bi-layer if both directions share the same h_{eq}). Note that, although using an idealized eigenstrain profile yields the same deformed shape as the complete profile, residual stresses will differ. These simplifications are relevant in a peen forming context were the primary concern is to get the shape of the part right and residual stresses are seen merely as a positive side effect.

Dimensional analysis

The deformed shape of peen formed plates depends on the thickness of the plate h, a characteristic length L, the Poisson ratio ν, and (assuming equibiaxial expansion in the upper layer) the resulting eigenstrains A and first eigenstrains moment B. It does not depend on Young's modulus E since the modulus is the only quantity that has the dimension of a pressure and that cannot, therefore, be used to form any dimensionless group. This is a consequence of the loads being fully characterized in terms of eigenstrains. Physically, inputting a given eigenstrain profile into a stiff material induces large residual stresses that are counter-balanced by the rigidity of the plate (both quantities scale with the modulus), and vice versa for flexible materials. Let κ_i be the curvature at the center of the plate in the i direction. Using curvatures to characterize deformed shapes, dimensional analysis requires

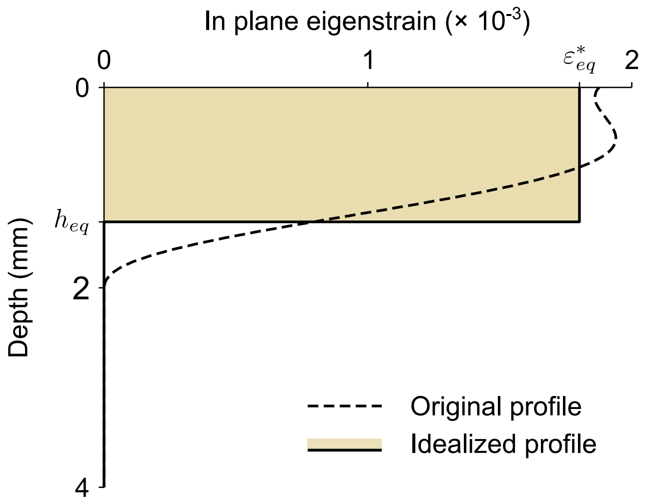

Figure G.3 Typical peening induced eigenstrains profile and equivalent step profile having the same resulting eigenstrain and first eigenstrain moment. The original profile is of the form $\gamma(z) = \sum_{i=1}^{4} c_i \xi_i(z)$, with $c_1 = -5.65 \times 10^{-3}$, $c_2 = -6.38 \times 10^{-3}$, $c_3 = -2.48 \times 10^{-3}$ and $c_4 = -3.22 \times 10^{-4}$, with $z_0 = 2.05$ mm, and the same ξ_i as in equation (G.1). The idealized profile is a step of amplitude $\varepsilon^*_{eq} = 1.80 \times 10^{-3}$ over a depth of $h_{eq} = 1.35$ mm. Both profiles yield the same deformed shapes when input in a thin shell model.

that the problem be fully characterized by 5 dimensionless groups.

We now introduce Γ_A and Γ_B, defined respectively as the ratio of in-plane loads over in-plane rigidity, and as the ratio of bending moments over bending rigidity [1]. These parameters account for the combined effect of the treatment and the geometry. The former governs in-plane behavior and the latter the bending response. For beams (section G.5.1),

$$\Gamma_A = A/h, \qquad \Gamma_B = 12B/h^2, \tag{G.2}$$

whereas for thin plates (section G.5.2),

$$\Gamma_A = (1+\nu)A/h, \qquad \Gamma_B = 12(1+\nu)B/h^2. \tag{G.3}$$

For the other dimensionless groups, we chose $\kappa_i h$, ν, and L/h.

In what follows, all peen forming results are presented by plotting $\kappa_x h$ and $\kappa_y h$ as a function

---

[1] The biaxial modulus of a plate is given by $E/(1-\nu)$ and its bending rigidity by $Eh^3/12\left(1-\nu^2\right)$. The axial modulus of a beam is E and its bending modulus $Eh^3/12$. The only loads applied to the system are caused by the eigenstrains. For thin plates, the upper layers of which expand equibiaxialy, $\sigma_{xx}(z) = \sigma_{yy}(z) = \gamma(z)E/(1+\nu)$, and in-plane loads and bending moments per unit length—obtained after integration over the thickness—are given by $AE/(1-\nu)$ and $BE/(1-\nu)$, respectively. Similar expressions are obtained for beams by replacing $E/(1-\nu)$ with E.

of Γ_B after both quantities were rescaled by $(L/h)^2$. This scaling, which was obtained by inspection, forces data obtained for different L/h ratios to collapse onto a single master curve. We call

$$\bar{\kappa}_i = \kappa_i L^2/h, \qquad \text{and} \qquad \bar{B} = 12(1+\nu)BL^2/h^4 \tag{G.4}$$

the dimensionless curvature in the i direction and the dimensionless load, respectively.

G.5 Applications and results

The simulation strategy presented above was put to the test against experimental results from Villalva-Braga (2011), and against experimental results generated for the purpose of this study. Incomplete data compelled us to make several additional hypotheses for both data sets. These hypotheses are listed before each result section.

G.5.1 Validation against experimental results from Villalva-Braga (2011)

Working hypotheses

Forming simulations were done according to the procedure presented in section G.4. A Young's modulus of 71 GPa and a Poisson's coefficient of 0.33 from the MMPDS-08 handbook (MMPDS-08, 2013) were used for all simulations.

In the experiments of Villalva-Braga (2011), prestrain in the form of a uniaxial bending about the y axis was applied to half of the samples. For prestrained plates, as well as for plates that bend significantly, it is expected for ε^*_{yy} to be smaller than ε^*_{xx} (Hu et al., 2015). Consequently, it was necessary to reconstruct both in-plane components of the eigenstrain field, as both enter the computation of residual stresses (simulated residual stress profiles that the reconstruction procedure attempted to match with measurements depend on the whole eigenstrain field). Since residual stresses measurements in the transverse direction were not available, we assumed an eigenstrain distribution of the form

$$\varepsilon^*_{yy}(z) = \alpha\, \varepsilon^*_{xx}(z), \qquad 0 \le \alpha \le 1.$$

This approximation was expected to yield results close to those observed on slightly bent plates for $\alpha = 1$ whereas taking $\alpha = 0$ yielded an upper bound for ε^*_{xx}.

As Korsunsky's reconstruction procedure relies on a linearly elastic model of the structure to compute residual stresses, eigenstrain profiles were not extracted from mm thick as well as from some 5 mm thick samples for which the maximum out of plane displacement Δz was not

Table G.3 Parameters used for reconstructing eigenstrain profiles in 10 mm thick plates and equivalent step profiles.

Treatment ID	n†	$d^\dagger$(mm)	h_{eq} (mm)	ε^*_{eq} ($\times 10^{-3}$)	
				$\alpha = 1$	$\alpha = 0$
1	4	0.76	0.44	2.60	3.46
2	3	0.80	0.54	2.65	3.52
3	4	1.09	0.63	3.29	4.37
4‡	-	-	-	-	-
5	4	1.39	0.76	4.05	5.39
6	5	1.42	0.90	4.09	5.44
7	3	0.95	0.66	3.01	4.00
8	6	1.44	1.09	3.57	4.75
9	6	1.65	1.35	3.91	5.19
10	4	1.50	0.80	4.02	5.34
11	5	2.20	1.23	5.09	6.76
12	7	2.35	1.27	5.03	6.69

† For a given set of basis functions and a given set of experimental data, parameters n and d uniquely define the profile.

‡ Satisfactory reconstruction was not achieved.

small when compared to the thickness h ($\Delta z > h/10$), and for which geometric nonlinearities might have had to be taken into account.

Results

Table G.3 summarizes parameters used to extract eigenstrain profiles on 10 mm thick plates, as well as the characteristics of the idealized profiles used as loads in finite element simulations. The table shows that the depth of the plastically deformed layer d, the depth of the idealized profile h_{eq}, and its amplitude ε^*_{eq} rise as the intensity of the treatment increases. It can also be seen that d et h_{eq} are independent of the choice of α.

Figure G.4 displays eigenstrain profiles extracted for treatments 7 to 9 on 10 and 15 mm thick free-to-deform plates. Contrary to the observations of Zhang et al. (2008), it appears that eigenstrains depend on the thickness of the plates. Nevertheless, it can be seen that the profiles have a similar shape and an almost identical d from one thickness to the next.

Figure G.5 compares simulated and experimental curvatures for 10 and 15 mm thick plates. Although peen forming was automated, the results exhibit significant scatter. For thin samples peened with smaller shots, most experimental points lie within the bounds delimited by simulations. The agreement between simulations and experimental results deteriorates as

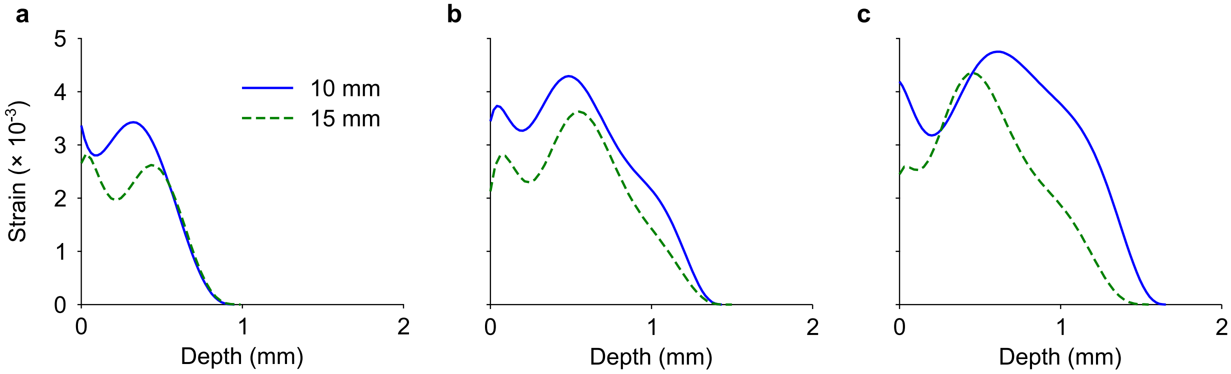

Figure G.4 Eigenstrain profiles reconstructed from residual stress measurements reported in Villalva-Braga (2011) for 10 and 15 mm thick plates that were free to deform during peening. The reconstruction assumes that $\varepsilon^*_{xx} = \varepsilon^*_{yy}$ ($\alpha = 1$). Treatment number: (a) 7; (b) 8; (c) 9.

the treatment intensity increases. For 5 mm thick plates (results not shown here), simulation consistently underestimated experimental curvatures with relative errors ranging from 20 to 75 %, even though a seemingly satisfactory reconstruction of the eigenstrain profiles was achieved. The specific reasons for this behavior are yet to be understood.

Figure G.6 shows the same results (for $\alpha = 1$ only) cast into dimensionless form and superimposed to the results of several hundred finite element simulations for which L, h, h_{eq}, and ε^*_{eq} were randomly selected from a range a realistic values (ν was kept constant at 0.33). All numerical results collapse onto a single master curve. Experimental points follow the same trend, except for the outliers identified in figure G.5.

G.5.2 Peen forming of large 2024–T3 panels

Working hypotheses

Forming simulations were done according to the procedure described in section G.4. A Young's modulus of 73.5 GPa and a Poisson ratio of 0.33 from the MMPDS-08 handbook were used for all simulations.

Since residual stress measurements were not available for the 1000 × 1000 mm plates, eigenstrain profiles extracted from the 250 × 250 × 15 mm blocks were used as input for all forming simulations. This choice was motivated by the results of Zhang et al. (2008) and Achintha and Nowell (2011) which suggest that peening induced eigenstrain profiles are independent of the thickness of the part.

A small imperfection was introduced in the global model to break its symmetry and trigger

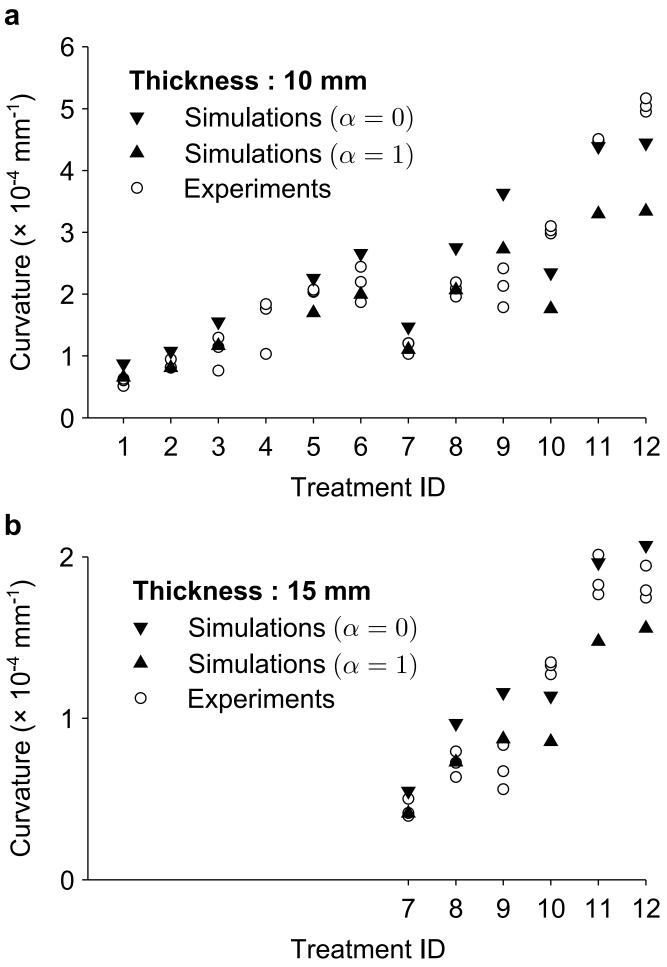

Figure G.5 Experimental curvatures reported in Villalva-Braga (2011) for (a) 10 mm and (b) 15 mm thick samples, alongside simulated curvatures. Experimental conditions are listed in table G.1. The intensity of the peening treatment increases with the treatment ID.

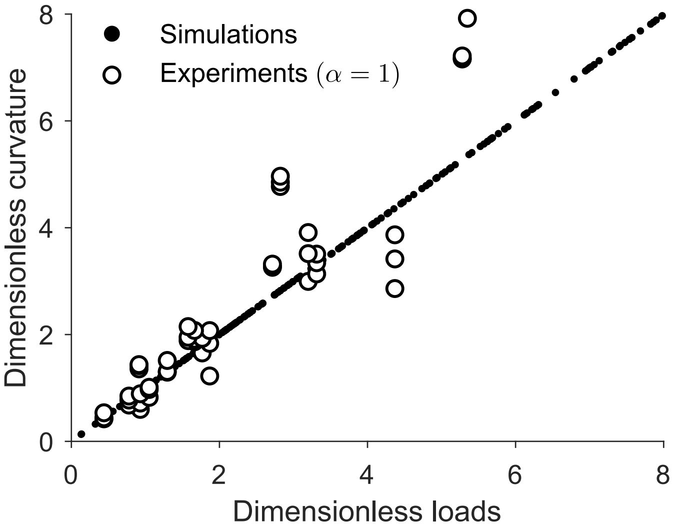

Figure G.6 Dimensionless curvature versus dimensionless loads for strips of 1:8 aspect ratio. All parameters for finite element simulations were randomly selected from a range of realistic values, except for ν that was kept constant at 0.33. Experimental points for $\alpha = 0$ are not shown to avoid clutter. They are slightly offset to the right.

potential elastic instabilities. These imperfections took the form of a $1\,\%$ difference between the amplitude of the expansion input in the model in the x direction (resp. $-1\,\%$ in the y direction) and ε^*_{eq}. (For actual peen formed parts, such imperfections would be a consequence of material anisotropy, geometric imperfections, boundary conditions and process variability.)

Simulations presented hereafter do not include gravity as running the same simulations considering gravity resulted in variations of curvatures of less than $3\,\%$ in all cases.

Results

Figure G.7 displays measured residual stress profiles, along with residual stress and plastic strain profiles reconstructed using the procedure of section G.4.2, for the $250 \times 250 \times 15$ mm blocks. Figure G.7a shows that differences between experimental data and reconstructed residual stress profiles mostly lie within experimental errors, the most significant discrepancy being of 25 MPa. Figure G.7b shows that the plastically deformed layer of the forming treatment is about twice as deep as that for the saturation treatment. Although the magnitude of both profiles is similar, residual stresses near the surface are lower for the forming treatment due to the bending of the samples. Table G.4 lists the parameters used to extract eigenstrain profiles, as well as characteristics of the idealized profiles used as loads in finite element simulations.

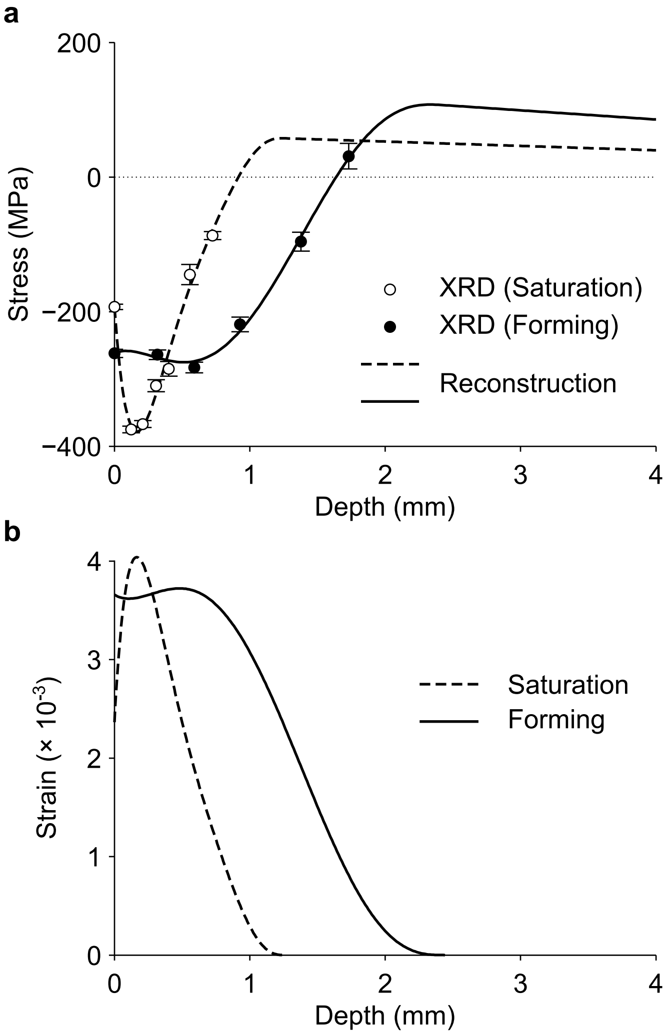

Figure G.7 Residual stress and eigenstrain profiles for the saturation and the forming treatment. (a) Residual stresses measured by X-ray diffraction in 250 × 250 × 15 mm blocks of 2024–T3 aluminum. Also shown are the residual stresses obtained when the eigenstrain profiles shown in (b) are input in a model of the blocks. (b) Eigenstrain profiles reconstructed with the procedure described in Korsunsky (2006). Parameters used for the reconstruction are listed in table G.4.

Table G.4 Parameters used for reconstructing eigenstrain profiles in the 250 × 250 × 15 mm blocks and equivalent step profiles.

Treatment	n	d (mm)	h_{eq} (mm)	ε^*_{eq} ($\times 10^{-3}$)
Saturation	4	1.26	0.72	3.22
Forming	3	2.44	1.51	3.42

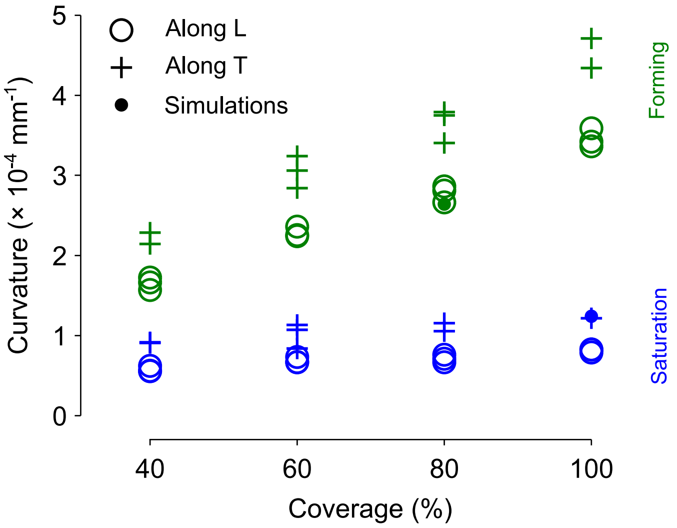

Figure G.8 Curvatures versus coverage for 200 × 50 × 10 mm strips peened with the saturation and the forming treatment. Also shown are simulated curvatures obtained by inputting the eigenstrain profiles from figure G.7 in a 3D finite element model of the strips. For the simulations, curvatures in both directions are equals.

Three dimensional scans of the 200 × 50 × 10 mm strips revealed that curvatures in the transverse direction were always larger than curvatures in the longitudinal direction for this specific geometry, as shown in figure G.8. This could be attributed to the known plastic anisotropy of the 2024–T3 aluminum alloy (Bron and Besson, 2004). Indeed, the elastic response of this alloy is almost perfectly isotropic, and the curvatures of thick blocks should be identical in both directions if their upper layers expand equibiaxially.

Three dimensional scans of the 1000 × 1000 mm plates revealed that thick shot-peened plates consistently adopted a hemi-spherical shape while thinner plates deformed cylindrically. This behavior is illustrated in figure G.9 for the forming treatment. The magnitude of out-of-plane deflection varied significantly between those two configurations, as shown in figure G.10. Curvatures at the center of the plate along the x and y axes are given in table G.5. The latter were approximately constant over the scanning lines, except for local variations near free edges.

Table G.5 compares simulated curvatures against validation experiments. Although simulations successfully captured the overall deformed shapes (i.e., spherical or cylindrical) of the plates, quantitative agreement is only satisfactory for the 15 mm thick plate submitted to the forming treatment (note that the eigenstrain profile was extracted from a sample of the same thickness). Curvatures were significantly underestimated for thinner plates subjected to the forming treatment. They were overestimated in all cases for plates subjected to the

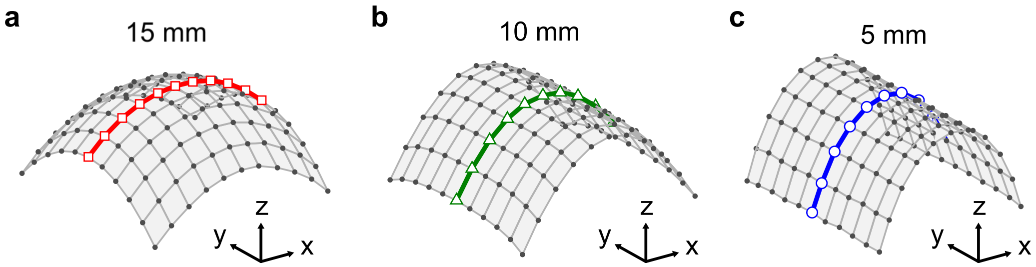

Figure G.9 Measured deformed shapes (not to scale) of 1 × 1 m 2024–T3 aluminum plates of thickness (a) 15 mm, (b) 10 mm, and (c) 5 mm subjected to the forming treatment. The plates were free to deform during peening. Interpolation of the surface between experimental points is here only to guide the eye. Similar shapes were observed for the saturation treatment.

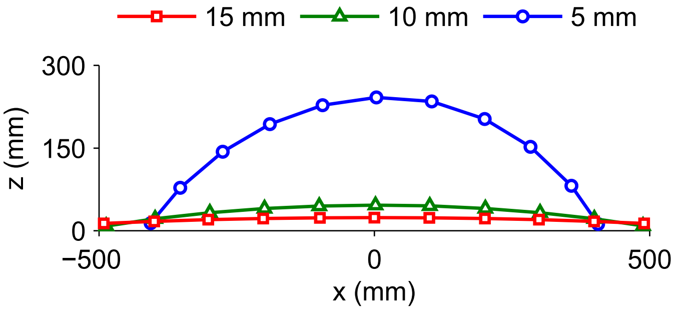

Figure G.10 Cross sectional views of the CMM scans of figure G.9 in the (xz) plane passing through the center of the plates.

Table G.5 Experimentally measured and simulated curvatures for 1000 × 1000 mm 2024–T3 aluminum plates.

Treatment	Thickness (mm)	Curvatures ($\times 10^{-4}$ mm^{-1})				Relative error (%)	
		Experiments		Simulations			
		Along x	Along y	Along x	Along y	Along x	Along y
Saturation	5	4.25	$\simeq 0$	5.82	$\simeq 0$	37	-
	10	0.59	0.56	0.87	0.71	49	28
	15	0.32	0.28	0.55	0.53	76	85
Forming	5	21.70	$\simeq 0$	11.00	$\simeq 0$	-49	-
	10	3.08	$\simeq 0$	2.63	$\simeq 0$	-15	-
	15	0.99	0.79	0.97	0.89	-2	13

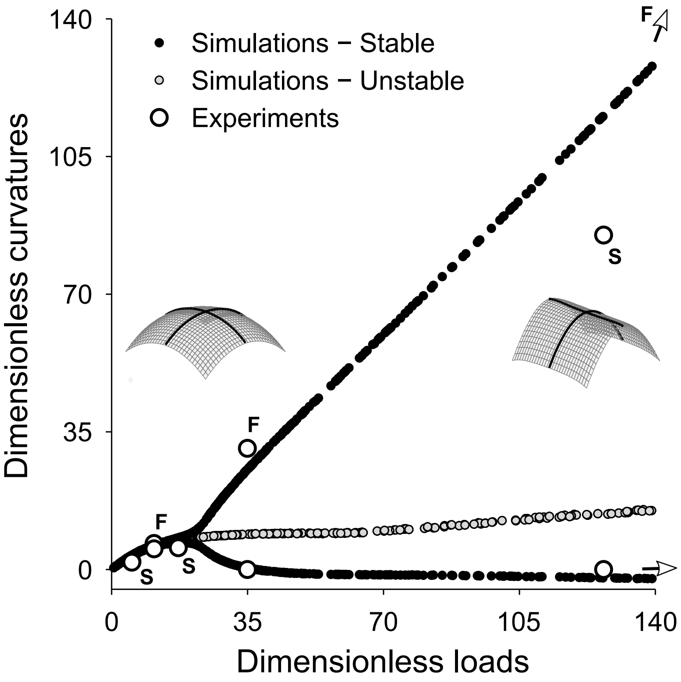

Figure G.11 Dimensionless curvatures versus dimensionless loads for square panels. Labels **F** and **S** refer to the forming and to the saturation treatments, respectively. Results for the 5 mm plate subjected to the forming treatment lie outside the graph at $(230, 0)$ and $(230, 434)$. All parameters for finite element simulations were randomly selected from a range of realistic values, except for ν that was kept constant at 0.33. For dimensionless loads smaller than $\simeq 22$, there is a single spherical equilibrium shape. For larger values of this parameter, two cylindrical configurations (bending along x or bending along y) and one instable spherical configuration coexist. A small imperfection was input in the model to trigger the transition from the unstable spherical to a stable cylindrical shape.

saturation treatment.

Figure G.11 presents the results of table G.5 cast into dimensionless form. They are superimposed to the results of several hundred finite element simulations whose parameters (except ν, which was kept constant) were randomly selected from a range a realistic values. Finite element simulations reveal that, for small dimensionless loads, curvatures are identical in both principal directions, yielding a spherical shape. As dimensionless loads increase, one of the curvatures drops to zero while the other increases steadily, yielding a cylindrical shape. Between those two extremes, simulations predict a narrow region where curvatures assume distinct but nonzero values. Such elliptic shapes can indeed be observed in figure G.9.b.

G.6 Discussion

The procedure presented in this article differs from existing peen forming simulations in that the link between the loads used in global simulations and the post-peening state is now explicit, thus bypassing the need for lengthy calibration phases. This was made possible by determining the plastic strain field for each combination of material, treatment and prestrain. The procedure is otherwise similar to those reported by Levers and Prior (1998) and Wang et al. (2006), and is almost identical to the procedure reported in Gariépy et al. (2011). Indeed, induced stresses used as loads by Gariépy et al.—defined as "unbalanced residual stresses [. . .] encountered in a fully constrained component that does not allow stretching or bending"—are directly proportional to eigenstrains (Korsunsky, 2005).

The results of section G.5.1 revealed that the proposed procedure yielded excellent agreement between simulated and experimental curvatures for moderate intensity treatments, both for free-to-deform and stress peen formed (i.e. prestrained) parts, provided that the post peening state was accurately known. For large shots, experimental results lay outside the bounds delimited by simulations. Recall that those bounds were obtained for limiting cases (namely uniaxial and equi-biaxial plastic strains). Identifying the reason behind these discrepancies is yet to be done. Obtaining more experimental data could provide more insight. In particular, some characterization of the response in the transverse direction would have been desirable.

In section G.5.2, the same procedure was applied to predict the deformed shape of free-to-deform plates based on residual stress measurements performed on thick blocks of material. Recall that these simulations were carried out under the assumption that shot-peening-induced plastic strains were independent of the thickness of the part. This approach significantly underestimated the curvature of free-to-deform thin panels subjected to the forming treatment. The eigenstrain profiles reported in figure G.4 suggest that this difference could be attributed to the stress peen forming that takes place as the plates deform: thinner plates exhibit larger curvatures, larger prestrains and hence larger subsurface expansion than those measured on thicker plates. Unlike the stress-peen forming experiments of Villalva-Braga (2011), the prestrain was a consequence of the continuous re-balancing of the part. Not only was it complex and continuously evolving as the treatment progressed, it was also path dependent. For this kind of simulations, the local and global models would have to be coupled, as was already concluded by Cao et al. (1995) and Gariépy et al. (2011). The coupling was not accounted for in this article. The main obstacle to simulating free-to-deform panels is the availability of models able to produce fast estimates of the post-peening state, possibly for partial coverages, for each increment of the simulation. Identifying a suitable material model for the aluminum alloys that are used to manufacture the vast majority of peen formed parts is another (plastic anisotropy, cyclic non-proportional loading and experimental identification on thin sheets). We recognize that simplified procedures could be developed for special cases as was done by Cao et al. (1995) for parts treated until saturation (i.e. for which an increase in peening time does not result in additional deflection).

These elements do not explain why the curvatures induced by the saturation treatment were overestimated. One possible explanation is that the simulations did not account for the plastic anisotropy of the 2024–T3 aluminum alloy. This plastic anisotropy could lead to direction-dependent plastic strains. If the only residual stress profile available for the saturation treatment—which was then used to feed the forming simulations—was measured in the direction along which the magnitude of plastic deformations was the largest, it is likely that simulated curvatures were over-estimated. This supposes that the contribution of continuous re-balancing (if there is one) was small compared to the contribution of plastic anisotropy, which is possible since plates peened with the saturation treatment were only slightly bent (the out-of-plane deflection of the 5 mm thick plate formed with the saturation treatment was 63 mm). Additional residual stress measurements would be necessary to confirm this hypothesis. Variability in the process could also play a role. Indeed, the process is intrinsically random and some dispersion is unavoidable, as illustrated in figures G.5 and G.8 (note that every sample was peened under the same conditions and that the results of Villalva-Braga (2011) were generated on an automated peening setup). Here, we tacitly assumed that the only residual stress profiles available were representative of the average post-peening state. It is to be expected that the effect of this dispersion would be less pronounced for thicker plates, as finite element simulations of figure G.11 predict that variations in subsurface expansion do not affect curvatures as significantly as they do for thinner plates (the sensibility of curvature with respect to the 'intensity' of the treatment for a given geometry, which corresponds to the slope of the curve, is approximately twice as low before the bifurcation than it is after).

Although it failed at making quantitative predictions in a number a situations, the proposed model captured the main features of the response of peened formed plates, in particular the transition from spherical to cylindrical shapes evidenced in figures G.9, G.11, and by Kulkarni et al. (1981). Neglected by the peening community, similar phenomenon (i.e. the shape transition of a thin plate whose upper layers expand/contract) have been extensively studied in the context of composites (Hyer, 1981) and MEMS manufacturing (Freund and Suresh, 2004). Even though the physical sources of eigenstrains may differ, the model system used in those publications is identical to that presented here (a thin multilayer plate with prescribed strain mismatch). By thinking in terms of eigenstrains, it is possible to transpose the conclusion that the transition results from an elastic instability to our specific problem. Insight into the physics of the transition can be gained by considering the following argument (see Pezzulla et al. (2016) and Freund and Suresh (2004) for a more in depth analysis): for a thin plate, the elastic energy of a cylindrical shape (pure bending without extension of the neutral axis) varies with h^3 whereas the elastic energy of a spherical shape (purely in extension as spheres are non-developable surfaces) varies with h. Since the plate seeks to adopt the shape with minimal energy, the sphere is favored for large thicknesses and vice-versa. The bifurcation occurs when the two energies are comparable. Past the bifurcation point, the spherical shape remains an equilibrium configuration, but it is unstable (fig. G.11). Note that in figure G.11, the progressive nature of the transition is a consequence of the small imperfections input in the model.

Figure G.11 also demonstrated that with a proper choice of dimensionless parameters, the results of all simulations, as well as most experiments, collapsed onto a single master curve. Similar curves can readily be obtained for random geometries, as illustrated in figure G.6 for rectangular strips of aspect ratio 1:8. They enable fast appreciation of the influence of the treatment, thickness and scale, and could prove most useful to support fast engineering decisions in developing peen forming strategies. One could also envision adjusting peening parameters and peening patterns on scale models of complex parts before scaling up to production. This would be of particular interest to industrials as discussed in Kulkarni et al. (1981). Scaling relations derived from the results of section G.4.3 are given in appendix H.

G.7 Conclusion

In this article, we demonstrated that a decoupled local-global simulation procedure based on the concept of eigenstrains can predict, without calibration, the deformed shape of peen formed plates, provided that the post-peening state of the material is known, or that it can be predicted with sufficient accuracy. The same procedure was used to predict the shape of large free-to-deform thin panels based on eigenstrain profiles obtained on small thick samples. This approach proved to be inadequate when the parts bent significantly during the peening treatment, i.e. when the local and global scales were strongly coupled.

A selection of peen forming experiments on large 2024–T3 aluminum plates was also presented. These results highlighted a transition from spherical to cylindrical deformed shapes as the thickness of the panels decreased for a given treatment. By reasoning in terms of eigenstrains, it was possible to reuse existing results from studies in the fields of MEMS and composite manufacturing to show that this transition was caused by an elastic instability. This information could enable industrials to develop new forming strategies making use of instabilities instead of trying to avoid them (Baughman, 1970).

We believe that this kind of approach (i.e. reduction to previously solved problems) has the potential to quickly widen the range of tools available for the simulation of peen forming. Such tools are essentials for peen forming to get rid of its black-art reputation.

G.8 Acknowledgements

The authors gratefully acknowledge financial support from Airbus, from the Rio Tinto group through a graduate scholarship, and from the Canada Research Chairs program.

APPENDIX H SCALING RELATIONS FOR GEOMETRICALLY SIMILAR PEEN FORMED PLATES

Consider two geometrically similar structures: (i) a large plate of any shape and (ii) a scale model of the plate, the dimensions of which have been scaled by a factor c.

If both plates are loaded with equibiaxial in-plane eigenstrains—such as those that could be induced by shot peening—their response is entirely characterized by the dimensionless parameters

$$\Gamma_A^{(i)}, \quad \Gamma_B^{(i)}, \quad \nu^{(i)}, \quad L^{(i)}/h^{(i)},$$

where superscripts $i = 1, 2$ refer to the original plate and to the scale model, respectively. Therefore, the deformed shapes are geometrically similar if both plates share the same dimensionless parameters. Because one is a scale model of the other, this is already the case for the L/h ratio. If both plates are made of the same material, hence have the same ν, the similarity condition reduces to

$$\Gamma_A^{(1)} = \Gamma_A^{(2)}, \quad \Gamma_B^{(1)} = \Gamma_B^{(2)}. \tag{H.1}$$

Using (G.3), (H.1) can be rewritten as

$$A^{(2)} = cA^{(1)}, \quad B^{(2)} = c^2 B^{(1)}, \tag{H.2}$$

or, equivalently,

$$h_{eq}^{(2)} = ch_{eq}^{(1)}, \quad \varepsilon_{eq}^{*\,(2)} = \varepsilon_{eq}^{*\,(1)}. \tag{H.3}$$

REFERENCES

Abaqus 6.14 (2014). *Analysis user's guide; Volume V: prescribed conditions, constraints & interactions*. Dassault Systèmes, Simulia Corp., Providence, RI, USA.

Achintha, M. and Nowell, D. (2011). Eigenstrain modelling of residual stresses generated by laser shock peening. *Journal of Materials Processing Technology*, 211(6):1091–1101.

Ahdad, F. and Desvignes, M. (1996). Contraintes résiduelles et déformations plastiques. Leurs relations mutuelles pour des pièces de géométries simples. *Matériaux et techniques*, 84(5-6):46–50.

Al Baida, H., Langlade, C., Kermouche, G., and Ambriz, R. R. (2015). Identifying the stress–strain curve of materials by microimpact testing. Application on pure copper, pure iron, and aluminum alloy 6061-T651. *Journal of Materials Research*, 30(14):2222–2230.

Alben, S., Balakrisnan, B., and Smela, E. (2011). Edge effects determine the direction of bilayer bending. *Nano Letters*, 11(6):2280–2285.

Almen, J. O. (1944). Shot blasting test. U.S. Patent No. 2,350,440.

AMS 2431/7 rev. B (2013). Peening media; ceramic shot. Standard, SAE Aerospace.

AMS standard 2430 rev. T (2015). Shot peening, automatic. Standard, SAE International.

AMS standard 2431/8B (2007). Peening media (AWCH) conditioned carbon steel cut wire shot, high hardness (55 to 62 HRC). Standard, SAE International.

ASTM E112-12 standard (2012). Test methods for determining average grain size. Standard, ASTM International.

ASTM standard B557M-15 (2015). Standard test methods for tension testing wrought and cast aluminum- and magnesium-alloy products (metric). Standard, ASTM International, West Conshohocken, PA.

ASTM standard E837-08 (2008). Standard test method for determining residual stresses by the hole-drilling strain-gage method. Standard, ASTM International, West Conshohocken, PA.

Audoly, B. and Pomeau, Y. (2010). *Elasticity and geometry: from hair curls to the non-linear response of shells*. Oxford University Press, Oxford ; New York.

Badreddine, J., Remy, S., Micoulaut, M., Rouhaud, E., Desfontaine, V., and Renaud, P. (2014). CAD based model of ultrasonic shot peening for complex industrial parts. *Advances in Engineering Software*, 76:31–42.

Ballard, P. (1991). *Contraintes résiduelles induites par impact rapide. Application au choc laser*. PhD thesis, École Polytechnique X.

Barrett, C. F. and Todd, R. (1984). Investigation of the effects of elastic pre-stressing technique on magnitude of compressive residual stress induced by shot peen forming in thick aluminum plates. In *Proceedings of the Second International Conference on Shot Peening*, pages 15–21, Chicago.

Bathe, K.-J. (2014). *Finite element procedures*. Prentice-Hall, Englewood Cliffs, N.J, 2nd ed edition.

Batoz, J.-L. and Dhatt, G. (1992). *Modélisation des structures par éléments finis. Volume 3, coques*. Presses de l'Université Laval, Sainte-Foy.

Baughman, D. L. (1970). Peen forming. *Machine design*, 42(27):156–160.

Benallal, A., Le Gallo, P., and Marquis, D. (1989). An experimental investigation of cyclic hardening of 316 stainless steel and 2024 aluminium alloy under multiaxial loadings. *Nuclear Engineering and Design*, 114(3):345–353.

Bendsøe, M. P. and Sigmund, O. (2004). *Topology optimization*. Springer Berlin Heidelberg, Berlin, Heidelberg.

Bernasconi, J. and Roth, M. (1987). The Niku-Lari method and the stress source method: application to residual stress distribution of shot peened plates. *Advances in surface treatments tech.*, 4:221–250.

Blackwell, P., Griffiths, M., Ward, T., and Gardiner, S. (2004). A computer modelling capability for shot peen forming. *Metal Finishing News*, 5(March issue).

Bousmalis, K. and Levine, S. (2017). Closing the simulation-to-reality gap for deep robotic learning. Google AI blog. `https://ai.googleblog.com/2017/10/closing-simulation-to-reality-gap-for.html`.

Bovid, S. (2019). Laser peen forming. Webinar: technology and applications. LSP Technoligies, Inc.

Boyd, S. P. and Vandenberghe, L. (2004). *Convex optimization.* Cambridge University Press, Cambridge, UK ; New York.

Bron, F. and Besson, J. (2004). A yield function for anisotropic materials Application to aluminum alloys. *International Journal of Plasticity*, 20(4-5):937–963.

Cao, J., Lee, W., Cheng, H. S., Seniw, M., Wang, H.-P., and Chung, K. (2009). Experimental and numerical investigation of combined isotropic-kinematic hardening behavior of sheet metals. *International Journal of Plasticity*, 25(5):942–972.

Cao, W., Fathallah, R., and Castex, L. (1995). Correlation of Almen arc height with residual stresses in shot peening process. *Materials science and Technology*, 11(9):967–973.

Caselli, F. and Bisegna, P. (2013). Polar decomposition based corotational framework for triangular shell elements with distributed loads. *International Journal for Numerical Methods in Engineering*, 95(6):499–528.

Castro Moreno, A. (2017). Shot peening FEM simulation: a novel approach based on crystal plasticity. In *Proceedings of the 13th international conference on shot peening*, pages 360–365, Montréal, QC, CA.

Chaise, T. (2011). *Mechanical simulation using a semi analytical method: from elasto-plastic rolling contact to multiple impacts.* PhD thesis, INSA de Lyon.

Chaise, T., Li, J., Nélias, D., Kubler, R., Taheri, S., Douchet, G., Robin, V., and Gilles, P. (2012). Modelling of multiple impacts for the prediction of distortions and residual stresses induced by ultrasonic shot peening (USP). *Journal of Materials Processing Technology*, 212(10):2080–2090.

Chen, Z., Yang, F., and Meguid, S. A. (2014). Realistic finite element simulations of arc-height development in shot-peened almen strips. *Journal of Engineering Materials and Technology*, 136(4):041002.

Cina, B., Kaatz, T., and Eldror, I. (1990). The effect of heating shot peened sheets and thin plates of aluminium alloys. *Journal of materials science*, 25(9):4101–4105.

Clauer, A. H. (2019). Laser shock peening, the path to production. *Metals*, 9(6):626.

Coratella, S., Sticchi, M., Toparli, M., Fitzpatrick, M., and Kashaev, N. (2015). Application of the eigenstrain approach to predict the residual stress distribution in laser shock peened AA7050-T7451 samples. *Surface and Coatings Technology*, 273:39–49.

Dane, C. B. and Hackel, L. A. (1997). Laser peening of metals – Enabling laser technology. In *Proceedings of the 1997 Materials Research Society Fall Meting*, pages 73–85, Boston, MA.

Dearden, G. and Edwardson, S. P. (2003). Some recent developments in two-and three-dimensional laser forming for ‘macro’ and ‘micro’ applications. *Journal of Optics A: Pure and Applied Optics*, 5(4):S8.

Deng, D., Murakawa, H., and Liang, W. (2007). Numerical simulation of welding distortion in large structures. *Computer Methods in Applied Mechanics and Engineering*, 196(45-48):4613–4627.

Depouhon, P., Sprauel, J., and Mermoz, E. (2015). Prediction of residual stresses and distortions induced by nitriding of complex 3d industrial parts. *CIRP Annals - Manufacturing Technology*, 64(1):553–556.

DeWald, A. T. and Hill, M. R. (2009a). Eigenstrain-based model for prediction of laser peening residual stresses in arbitrary three-dimensional bodies. Part 1: model description. *The Journal of Strain Analysis for Engineering Design*, 44(1):1–11.

DeWald, A. T. and Hill, M. R. (2009b). Eigenstrain-based model for prediction of laser peening residual stresses in arbitrary three-dimensional bodies. Part 2: model verification. *The Journal of Strain Analysis for Engineering Design*, 44(1):13–27.

DeWald, A. T. and Hill, M. R. (2014). Repeatability of incremental hole drilling and slitting method residual stress measurements. In Rossi, M., Sasso, M., Connesson, N., Singh, R., DeWald, A., Backman, D., and Gloeckner, P., editors, *Residual Stress, Thermomechanics & Infrared Imaging, Hybrid Techniques and Inverse Problems, Volume 8*, pages 113–118. Springer International Publishing.

Dieter, G. E. (1961). *Mechanical metallurgy.* Metallurgy and Metallurgical Engineering Series. McGraw-Hill, New York.

Essa, Y., Laspalas, M., Garcia, E., Escolán, A., Hernández-Gascón, B., and Martin de la Escalera, F. (2015). Numerical analysis to optimize peen-forming process parameters. pages 1–10, Berlin, Germany.

Faucheux, P. A., Gosselin, F. P., and Lévesque, M. (2019). Peen forming and stress peen forming of 2024–T3 aluminum sheets: Part 1: experimental results. Manuscript submitted for publication to Journal of Materials Processing Technology.

Faucheux, P. A., Gosselin, F. P., and Lévesque, M. (2018). Simulating shot peen forming with eigenstrains. *Journal of Materials Processing Technology*, 254:135–144.

Flavenot, J. F. and Niku-Lari, A. (1977). La mesure des contraintes résiduelles. Méthode de la flèche. Méthode de la source des contraintes. Application au grenaillage de précontrainte et à d'autres traitements superficiels. Technical Report 31, CETIM, Senlis, France.

Forest, S. and Amestoy, M. (2017). Mécanique des milieux continus. Course notes. École des Mines de Paris. Available at `http://mms2.mines-paristech.fr`.

François, M. (2001). A plasticity model with yield surface distortion for non proportional loading. *International Journal of Plasticity*, 17(5):703–717.

Freund, L. B. (2000). Substrate curvature due to thin film mismatch strain in the nonlinear deformation range. *Journal of the Mechanics and Physics of Solids*, 48:1159–1174.

Freund, L. B. and Suresh, S. (2004). *Thin film materials: stress, defect formation and surface evolution*. Cambridge University Press.

Friese, A., Lohmar, J., and Wüstefeld, F. (2002). Current applications of advanced peen forming implementation. In *Proceedings of the 8th international conference on shot peening (ICSP-8)*, pages 53–57, Garmisch-Partenkirchen, Germany.

Fuchi, K., Ware, T. H., Buskohl, P. R., Reich, G. W., Vaia, R. A., White, T. J., and Joo, J. J. (2015). Topology optimization for the design of folding liquid crystal elastomer actuators. *Soft Matter*, 11(37):7288–7295.

Furuhashi, R. and Mura, T. (1979). On the equivalent inclusion method and impotent eigenstrains. *Journal of Elasticity*, 9(3):263–270.

Gardiner, D. S. (2001). *A model for shot peen forming with prestress conditions*. PhD thesis, Cambridge University.

Gariépy, A. (2012). *Finite element modelling of shot peening and peen forming processes and characterisation of peened AA2024-T351 aluminium alloy*. PhD thesis, École Polytechnique de Montréal.

Gariépy, A., Bridier, F., Hoseini, M., Bocher, P., Perron, C., and Lévesque, M. (2013a). Experimental and numerical investigation of material heterogeneity in shot peened aluminium alloy AA2024-T351. *Surface and Coatings Technology*, 219:15–30.

Gariépy, A., Larose, S., Perron, C., Bocher, P., and Lévesque, M. (2013b). On the effect of the orientation of sheet rolling direction in shot peen forming. *Journal of Materials Processing Technology*, 213(6):926–938.

Gariépy, A., Larose, S., Perron, C., Bocher, P., and Lévesque, M. (2013c). On the effect of the peening trajectory in shot peen forming. *Finite Elements in Analysis and Design*, 69:48–61.

Gariépy, A., Larose, S., Perron, C., and Lévesque, M. (2011). Shot peening and peen forming finite element modelling – Towards a quantitative method. *International Journal of Solids and Structures*, 48(20):2859–2877.

Gariépy, A., Miao, H., and Lévesque, M. (2014). Peen forming. In *Comprehensive Materials Processing*, pages 295–329. Elsevier.

Gelineau, M. (2018). *Étude de l'impact du grenaillage sur des composants mécaniques industriels à géométrie complexe*. PhD thesis, École Nationale Supérieure d'Arts et Métiers.

Gladman, A., Matsumoto, E. A., Nuzzo, R. G., Mahadevan, L., and Lewis, J. A. (2016). Biomimetic 4d printing. *Nature Materials*, 15(4):413–418.

Grasty, L. V. and Andrew, C. (1996). Shot peen forming sheet metal: finite element prediction of deformed shape. *Proceedings of the Institution of Mechanical Engineers, Part B: Journal of Engineering Manufacture*, 210(4):361–366.

Hackel, L., Rankin, J., and Rybak, J. (2017). Precision laser peen forming of challenging shapes for aerospace and marine applications. In *Proceedings of the 13th international conference on shot peening*, pages 580–585, Montréal, QC, CA.

Han, K., Owen, D. R. J., and Peric, D. (2002). Combined finite/discrete element and explicit/implicit simulations of peen forming process. *Engineering Computations*, 19(1):92–118.

Harburn, B. and Miller, J. C. (1982). Shot peen forming of compound contours. U.S. Patent No. 4,329,862.

Hill, M. R. (1996). *Determination of residual stress based on the estimation of eigenstrain*. PhD thesis, Stanford University.

Hill, M. R. and Nelson, D. V. (1995). Inherent strain method for residual stress determination and its application to a long welded joint. In *American Society of Mechanical Engineers, Pressure Vessels & Piping Conference (PVP 1995)*.

Homer, S. E. (1989). Aircraft wing skin contouring as a result of residual stress distributions induced by shot peening. Master's thesis, Montana State University, Bozeman, Montana.

Homer, S. E. and VanLuchene, R. D. (1991). Aircraft wing skin contouring by shot peening. *Journal of Materials Shaping Technology*, 9(2):89–101.

Hong, T., Ooi, J., and Shaw, B. (2008). A numerical simulation to relate the shot peening parameters to the induced residual stresses. *Engineering Failure Analysis*, 15(8):1097–1110.

Hornauer, K. P. and Köhler, W. (1990). Development of the peen forming process for spherical shaped components. In *Proceedings of the 4th International Conference on Shot Peening (ICSP4)*, pages 585–594, Tokyo, Japan.

Hu, Y., Han, Y., Yao, Z., and Hu, J. (2010). Three-dimensional numerical simulation and experimental study of sheet metal bending by laser peen forming. *Journal of Manufacturing Science and Engineering*, 132(6):061001.

Hu, Y., Li, Z., Yu, X., and Yao, Z. (2015). Effect of elastic prestress on the laser peen forming of aluminum alloy 2024-T351: Experiments and eigenstrain-based modeling. *Journal of Materials Processing Technology*, 221:214–224.

Hyer, M. W. (1981). Calculations of the room-temperature shapes of unsymmetric laminates. *Journal of Composite Materials*, 15:296–310.

Irschik, H. (2002). A review on static and dynamic shape control of structures by piezoelectric actuation. *Engineering Structures*, 24(1):5–11.

ISO 10360-5:2010 standard (2010). Geometrical product specifications (GPS) – Acceptance and reverification tests for coordinate measuring machines (CMM) – Part 5: CMMs using single and multiple stylus contacting probing systems. Standard, International Organization for Standardization, Geneva, Switzerland.

Jacq, C., Nélias, D., Lormand, G., and Girodin, D. (2002). Development of a three-dimensional semi-analytical elastic-plastic contact code. *Journal of Tribology*, 124(4):653–667.

Johnson, K. L. (2003). *Contact mechanics*. Cambridge Univ. Press, Cambridge, 9th reprint edition.

Johnson, W., Mamalis, A. G., and Ghosh, S. K. (1981). On the peen-forming of metals. In *Proceedings of the Twenty-First International Machine Tool Design and Research Conference*, pages 85–93, Palgrave, London.

Julan, E. (2014). *Simulation numérique du choc laser pour la mise en compression en présence de l'état initial dû au soudage.* PhD thesis, École Polytechnique X, 2014-10-31.

Jun, T.-S. and Korsunsky, A. M. (2010). Evaluation of residual stresses and strains using the Eigenstrain Reconstruction Method. *International Journal of Solids and Structures*, 47(13):1678–1686.

Jun, T.-S., Venter, A., and Korsunsky, A. (2011). Inverse eigenstrain analysis of the effect of non-uniform sample shape on the residual stress due to shot peening. *Experimental Mechanics*, 51(2):165–174.

Khabou, M., Castex, L., and Inglebert, G. (1989). The effect of material behaviour law on the theoretical shot peening results. *European Journal of Mechanics of Solids*, A(6):537–549.

Kittel, S., Linnemann, W., Wüstefeld, F., and Kopp, R. (1999). Tight tolerance peen forming with on-line shape control. In *Proceedings of the 7th International Conference on Shot Peening (ICSP7)*, pages 301–307, Warsaw, Poland.

Koconis, D. B., Kollár, L. P., and Springer, G. S. (1994). Shape control of composite plates and shells with embedded actuators. II. Desired shape specified. *Journal of Composite Materials*, 28(3):262–285.

Kopp, R. and Schulz, J. (2006). Peen Forming. In Semiatin, S., editor, *Metalworking: Sheet Forming*, volume 14B of *ASM Handbook*, pages 429–437. ASM International.

Korsunsky, A. (2017). *A teaching essay on residual stresses and eigenstrains.* Butterworth-Heinemann, Boston, MA, 1st edition edition.

Korsunsky, A. M. (2005). On the modelling of residual stresses due to surface peening using eigenstrain distributions. *The Journal of Strain Analysis for Engineering Design*, 40(8):817–824.

Korsunsky, A. M. (2006). Residual elastic strain due to laser shock peening: modelling by eigenstrain distribution. *The Journal of Strain Analysis for Engineering Design*, 41(3):195–204.

Korsunsky, A. M. (2009). Eigenstrain analysis of residual strains and stresses. *The Journal of Strain Analysis for Engineering Design*, 44(1):29–43.

Korsunsky, A. M., Regino, G., and Nowell, D. (2004). Variational determination of eigenstrain sources of residual stress. In *Proceeding of the 2004 international conference on computational and experimental engineering and sciences*, Madeira, Portugal.

Kulkarni, K. M., Schey, J. A., and Badger, D. V. (1981). Investigation of shot peening as a forming process for aircraft wing skins. *Journal of Applied Metalworking*, 1(4):34–44.

Lee, G. and Kim, S. (2012). Case study of mass customization of double-curved metal façade panels using a new hybrid sheet metal processing technique. *Journal of Construction Engineering and Management*, 138(11):1322–1330.

Lemaitre, J., Chaboche, J.-L., Benallal, A., and Desmorat, R. (2009). *Mécanique des matériaux solides*. Sciences sup. Dunod, Paris, 3rd ed. edition.

Levers, A. (2010). Broughton: From Wellington bombers to the A380. *The International Journal for the History of Engineering & Technology*, 80(1):55–79.

Levers, A. and Prior, A. (1995). Finite element simulation of shot peening. *The Shot Peener Magazine*, 9(3):14–16.

Levers, A. and Prior, A. (1998). Finite element analysis of shot peening. *Journal of Materials Processing Technology*, 80:304–308.

Levy, K. (2018). The 2017 shot peener of the year; Dominic Cimino. *The Shot Peener Magazine*, (Winter):6,8.

Li, K. (1981). Using stress peen-forming process for integrally stiffened wing panels. In *Proceedings of the First International Conference on Shot Peening*, pages 555–563, Paris, France.

Liang, W., Deng, D., and Murakawa, H. (2005). Measurement of inherent deformations in typical weld joints using inverse analysis (part 2); rediction of welding distortion of large structures. *Transactions of the Joining and Welding Research Institute of Osaka University*, 34(1):113–123.

Lundquist, L. K., Kunz, M. A., Pillers, J. E., Castle, J. B., Lin, J. Z., and Nervi, S. (2017). Control feedback loop for real-time variable needle peen forming. U.S. Patent No. 9,539,690.

Luo, Y., Ishiyama, M., and Murakawa, H. (1999). Welding deformation of plates with longitudinal curvature. *Transactions of the Joining and Welding Research Institute of Osaka University*, 28(2):57–65.

Meguid, S. A., Shagal, G., and Stranart, J. C. (2002). 3d FE analysis of peening of strain-rate sensitive materials using multiple impingement model. *International Journal of Impact Engineering*, 27(2):119–134.

Meguid, S. A., Shagal, G., and Stranart, J. C. (2007). Development and validation of novel FE models for 3d analysis of peening of strain-rate sensitive materials. *Journal of Engineering Materials and Technology*, 129(2):271–283.

Merino, J., Patzelt, A., Steinacher, A., Windisch, M., Heinrich, G., Forster, R., and Bauer, C. (2017). Ariane 6: Tanks & structures for the new european launcher. In *Proceedings of the 2017 Deutscher Luft- und Raumfahrtkongress*, page 10, München, Germany.

Merson, J. S., Prime, M. B., Lovato, M. L., and Liu, C. (2016). In-Situ DIC and strain gauges to isolate the deficiencies in a model for indentation including anisotropic plasticity. In *Residual Stress, Thermomechanics & Infrared Imaging, Hybrid Techniques and Inverse Problems, Volume 9*, pages 183–197. Springer International Publishing.

Mesarovic, S. D. and Fleck, N. A. (1999). Spherical indentation of elastic-plastic solids. *Proceedings of the Royal Society A: Mathematical, Physical and Engineering Sciences*, 455(1987):2707–2728.

Meyer, R., Reccius, H., and Schülein, R. (1987). Shot peen-forming of NC-machined parts with integrated stringers using large balls. In *Proceedings of the 3rd international conference on shot peening (ICSP-3)*, pages 327–334, Garmisch-Partenkirchen, Germany.

Miao, H., Demers, D., Larose, S., Perron, C., and Lévesque, M. (2010). Experimental study of shot peening and stress peen forming. *Journal of Materials Processing Technology*, 210(15):2089–2102.

Miao, H., Larose, S., Perron, C., and Lévesque, M. (2011). Numerical simulation of the stress peen forming process and experimental validation. *Advances in Engineering Software*, 42(11):963–975.

Micoulaut, M., Mechkov, S., Retraint, D., Viot, P., and François, M. (2007). Granular gases in mechanical engineering: on the origin of heterogeneous ultrasonic shot peening: Granular gases in mechanical engineering. *Granular Matter*, 9(1-2):25–33.

Mika, D. P., Apostolos, P. K., Dale, R. L., and Steven, R. H. (2006). Method for determining and compensating peening-induced distortion. U.S. Patent No. 7,065,479.

MMPDS-08 (2013). *Metallic Materials Properties Development and Standardization (MMPDS-08) handbook*. Battelle Memorial Institute, Colombus, Ohio.

Mura, T. (1987). *Micromechanics of defects in solids*. Number 3 in Mechanics of Elastic and Inelastic Solids. Springer Netherlands, 2 edition.

Musinski, W. D. and McDowell, D. L. (2015). On the eigenstrain application of shot-peened residual stresses within a crystal plasticity framework: Application to Ni-base superalloy specimens. *International Journal of Mechanical Sciences*, 100:195–208.

Mylonas, G. and Labeas, G. (2011). Numerical modelling of shot peening process and corresponding products: Residual stress, surface roughness and cold work prediction. *Surface and Coatings Technology*, 205(19):4480–4494.

Nervi, S., Louis, S., Bolin, J. L., and Castle, J. B. (2017). Initial stress and eigenstrain computation system and method. US Patent App. 14/988,541.

Nguyen, V. B., Poh, H. J., and Zhang, Y.-W. (2014). Predicting shot peening coverage using multiphase computational fluid dynamics simulations. *Powder Technology*, 256:100–112.

Niku-Lari, A. (1981). Méthode de la flèche. Méthode de la source des contraintes résiduelles. In *Proceedings of the 1st international conference on shot peening (ICSP1)*, pages 237–247, Paris, France.

Nordin, E. and Alfredsson, B. (2016). Measuring shot peening media velocity by indent size comparison. *Journal of Materials Processing Technology*, 235:143–148.

Nyashin, Y., Lokhov, V., and Ziegler, F. (2005). Decomposition method in linear elastic problems with eigenstrain. *Journal of Applied Mathematics and Mechanics/Zeitschrift für Angewandte Mathematik und Mechanik: Applied Mathematics and Mechanics*, 85(8):557–570.

O'Hara, P. (2006). Peen-forming - A developing technique. In Wagner, L., editor, *Shot Peening*, pages 215–226. Wiley-VCH Verlag GmbH & Co. KGaA, Weinheim, FRG.

Pagliaro, P., Prime, M. B., Clausen, B., Lovato, M. L., and Zuccarello, B. (2009). Known residual stress specimens using opposed indentation. *Journal of Engineering Materials and Technology*, 131(3):031002.

Pajot, J. M. and Maute, K. (2006). Analytical sensitivity analysis of geometrically nonlinear structures based on the co-rotational finite element method. *Finite Elements in Analysis and Design*, 42(10):900–913.

Pajot, J. M., Maute, K., Zhang, Y., and Dunn, M. L. (2006). Design of patterned multilayer films with eigenstrains by topology optimization. *International Journal of Solids and Structures*, 43(6):1832–1853.

Paradies, R. and Hertwig, M. (1999). Shape control of adaptive composite reflectors. *Composites Part B: Engineering*, 30(1):65–78.

Penning, L. (2010). A jumbo leap. *Boeing frontiers*, (March):12–21.

Pezzulla, M., Shillig, S. A., Nardinocchi, P., and Holmes, D. P. (2015). Morphing of geometric composites via residual swelling. *Soft Matter*, 11(29):5812–5820.

Pezzulla, M., Smith, G. P., Nardinocchi, P., and Holmes, D. P. (2016). Geometry and mechanics of thin growing bilayers. *Soft Matter*, 12(19):4435–4442.

Prime, M. B. (1999). Residual stress measurement by successive extension of a slot: The crack compliance method. *Applied Mechanics Reviews*, 52(2):75–96.

Prime, M. B. (2013). Anisotropic and pressure-dependent plasticity modeling for residual stress prediction. In *Experimental and Applied Mechanics, Volume 4*, pages 415–427. Springer New York, New York, NY.

Prime, M. B. (2017). Amplified effect of mild plastic anisotropy on residual stress and strain anisotropy. *International Journal of Solids and Structures*, 118-119:70–77.

Prime, M. B. and Hill, M. R. (2002). Residual stress, stress relief, and inhomogeneity in aluminum plate. *Scripta Materialia*, 46(1):77–82.

Prime, M. B. and Hill, M. R. (2006). Uncertainty, model error, and order selection for series-expanded, residual-stress inverse solutions. *Journal of Engineering Materials and Technology*, 128(2):175–185.

Ramati, S., Levasseur, G., and Kennerknecht, S. (1999). Single piece wing skin utilization via advanced peen forming technology. In *Proc. 7th Conf. Shot Peening (ICSP7)*, Warsaw, Poland.

Rankin, J., Campbell, J., and Hackel, L. (2013). Enhancing fatigue lifetimes and precision component shaping by laser peening. JTEG Teleconference.

Robinson, J. S., Tanner, D. A., and Truman, C. E. (2014). The origin and management of residual stress in heat-treatable aluminium alloys. *Strain*, 50(3):185–207.

Roth, M., Bernasconi, J., and Strässler, S. (1984). Residual stress distribution in shot peened plates. In *Proceedings of the 2nd International Conference on Shot Peening (ICSP2)*, pages 293–296, Chicago, USA.

Rouhaud, E., Deslaef, D., Lu, J., and Chaboche, J.-L. (2005). Modeling of residual stress, shot peening. In Lu, J., editor, *Handbook on residual stress*, pages 116–148. Society for Experimental Mechanics.

Rouquette, S., Rouhaud, E., François, M., Roos, A., and Chaboche, J.-L. (2009). Coupled thermo-mechanical simulations of shot impacts: Effects of the temperature on the residual stress field due to shot-peening. *Journal of Materials Processing Technology*, 209(8):3879–3886.

Rueden, C. T., Schindelin, J., Hiner, M. C., DeZonia, B. E., Walter, A. E., Arena, E. T., and Eliceiri, K. W. (2017). ImageJ2: ImageJ for the next generation of scientific image data. *BMC Bioinformatics*, 18(1).

SAE standard J2277 (2013). Shot peening coverage determination. Standard, SAE International.

SAE standard J443 (2010). Procedures for using standard shot peening almen strip. Standard, SAE International.

Salvati, E. and Korsunsky, A. (2018). A simplified FEM eigenstrain residual stress reconstruction for surface treatments in arbitrary 3d geometries. *International Journal of Mechanical Sciences*, 138-139:457–466.

Salvati, E., Lunt, A., Ying, S., Sui, T., Zhang, H., Heason, C., Baxter, G., and Korsunsky, A. (2017). Eigenstrain reconstruction of residual strains in an additively manufactured and shot peened nickel superalloy compressor blade. *Computer Methods in Applied Mechanics and Engineering*, 320:335–351.

Schajer, G. S. and Prime, M. B. (2006). Use of inverse solutions for residual stress measurements. *Journal of Engineering Materials and Technology*, 128(3):375.

Schindelin, J., Arganda-Carreras, I., Frise, E., Kaynig, V., Longair, M., Pietzsch, T., Preibisch, S., Rueden, C., Saalfeld, S., Schmid, B., Tinevez, J.-Y., White, D. J., Hartenstein, V., Eliceiri, K., Tomancak, P., and Cardona, A. (2012). Fiji: an open-source platform for biological-image analysis. *Nature Methods*, 9(7):676–682.

Schulze, V. (2002). Characteristics of surface layers produced by shot peening. In *Proceedings of the 8th international conference on shot peening (ICSP-8)*, pages 143–160, Garmisch-Partenkirchen, Germany.

Seidt, J. and Gilat, A. (2013). Plastic deformation of 2024-T351 aluminum plate over a wide range of loading conditions. *International Journal of Solids and Structures*, 50(10):1781–1790.

Setien, I., Chiumenti, M., van der Veen, S., San Sebastian, M., Garciandía, F., and Echevería, A. (2018). Empirical methodology to determine inherent strains in additive manufacturing. *Computers & Mathematics with Applications*.

Sharp, P. and Clark, G. (2001). The effect of peening on the fatigue life of 7050 aluminium alloy. Technical Report DSTO-RR-0208, Australian Department of Defence; DSTO; Airframes and Engines Division Aeronautical and Maritime Research Laboratory.

Sharp, S., Ashby, M., and Fleck, N. (1993). Material response under static and sliding indentation loads. *Acta Metallurgica et Materialia*, 41(3):685–692.

Sheng, L. (2004). *Finite element analysis and genetic algorithm optimization design for the actuator placement on a large adaptive structure*. Ph.D. Thesis, Virginia Polytechnic Institute and State University.

Simmons, T. C. (1952). Integrally stiffened wing panels formed by shot peening method. *Western metals*.

Skinner, R. D. (1978). Stress-peen straightening of complex machined aircraft parts. In *Formability Topics—Metallic Materials*, pages 100–121. ASTM International.

Stresstech (2018). X-ray diffraction service report; CPO 5753. Test report, American stress technologies.

Stronge, W. J. (2004). *Impact mechanics*. Cambridge University Press, Cambridge.

Terasaki, T., Chen, J., Akiyama, T., and Kishitake, K. (1999). Non-destructive method for estimating residual stress distribution in component due to shot peening. *JSME International Journal Journal Series A Solid Mechanics and Material Engineering*, 42(2):216–223.

Timoshenko, S. (1925). Analysis of bi-metal thermostats. *Journal of the Optical Society of America*, 11(3):233–255.

Timoshenko, S. (1940). *Strength of materials; Part II; Advanced theory and problems*. D. Van Nostrand Company, Inc., 2nd ed. edition.

Tolentino, C. A. (2013). Shot peening/blasting process for part flatness. US Patent App. 13/243,378.

Ueda, Y., Fukuda, K., and Kim, Y. C. (1986). New measuring method of axisymmetric three-dimensional residual stresses using inherent strains as parameters. *Journal of Engineering Materials and Technology*, 108(4):328–334.

Ueda, Y., Fukuda, K., Kim, Y. C., and yamazaki, T. (1984). New measuring method of axisymmetric three dimensional residual stresses using inherent strains as parameters. *Transactions of the Joining and Welding Research Institute of Osaka University*, 13(1):105–114.

Ueda, Y., Kim, Y. C., and Umekuni, A. (1985). Measuring theory of three-dimensional residual stresses using a thinly sliced plate perpendicular to welded line. *Transactions of the Joining and Welding Research Institute of Osaka University*, 14(2):151–157.

Ueda, Y., Kim, Y. C., and Yuan, M. G. (1989). A predicting method of welding residual stress using source of residual stress (report I): characteristics of inherent strain (source of residual stress). *Transactions of the Joining and Welding Research Institute of Osaka University*, 18(1):135–141.

van Rees, W. M., Vouga, E., and Mahadevan, L. (2017). Growth patterns for shape-shifting elastic bilayers. *Proceedings of the National Academy of Sciences*, 114(44):11597–11602.

VanLuchene, R. D. and Cramer, E. J. (1996). Numerical modeling of a wing skin peen forming process. *Journal of materials engineering and performance*, 5(6):753–760.

VanLuchene, R. D., Johnson, J., and Carpenter, R. G. (1995). Induced stress relationships for wing skin forming by shot peening. *Journal of materials engineering and performance*, 4(3):283–290.

Villalva-Braga, A. P. (2011). Análise de ligas de alumínio aeronáuticas conformadas por jateamento com granalhas-caracterização e previsão de deformação. Master's thesis, Universidade de São Paulo.

Wang, M. T., Zeng, Y. S., Bai, X. P., and Huang, X. (2014). Deformation rule of 7150 aluminum alloy thick plate by pre-stress shot peen forming. *Advanced Materials Research*, 1052:477–481.

Wang, T., Platts, J., and Levers, A. (2002). Finite element impact modelling for shot peen forming. In *Proceedings of the 8th international conference on shot peening (ICSP-8)*, pages 540–546, Garmisch-Partenkirchen, Germany.

Wang, T., Platts, M., and Levers, A. (2006). A process model for shot peen forming. *Journal of Materials Processing Technology*, 172(2):159–162.

Xiao, X., Wang, Y., Zhang, W., Wang, J., and Wei, S. (2016). Numerical research on stress peen forming with prestressed regular model. *Journal of Materials Processing Technology*, 229:501–513.

Zarka, J. (2017). Procédé de grenaillage pour formage précis de panneaux métalliques de grande taille. Patent No. FR3034336.

Zeller, R. (1993). Kugelstrahlen unter Zugvorspannung. Verbesserung der Ermüdungseigenschaften von Bauteilen Prüfen. *Materialprufung*, 35(7-8):18–21.

Zhang, S. Y., Venter, A., Vorster, W. J. J., and Korsunsky, A. M. (2008). High-energy synchrotron X-ray analysis of residual plastic strains induced in shot-peened steel plates. *The Journal of Strain Analysis for Engineering Design*, 43(4):229–241.

Zhang, T., Li, L., Lu, S.-h., Zhang, J.-b., Zhou, Z., and Gong, H. (2019). Effect of prestressed ultrasonic peen forming parameters on bending curvature and spherical deformation of plate. *Transactions of Nonferrous Metals Society of China*, 29(2):270–278.

Zimmermann, M., Klemenz, M., and Schulze, V. (2010). Literature review on shot peening simulation. *International Journal of Computational Materials Science and Surface Engineering*, 3(4):289.